

INFORMATION TO USERS

This manuscript has been reproduced from the microfilm master. UMI films the text directly from the original or copy submitted. Thus, some thesis and dissertation copies are in typewriter face, while others may be from any type of computer printer.

The quality of this reproduction is dependent upon the quality of the copy submitted. Broken or indistinct print, colored or poor quality illustrations and photographs, print bleedthrough, substandard margins, and improper alignment can adversely affect reproduction.

In the unlikely event that the author did not send UMI a complete manuscript and there are missing pages, these will be noted. Also, if unauthorized copyright material had to be removed, a note will indicate the deletion.

Oversize materials (e.g., maps, drawings, charts) are reproduced by sectioning the original, beginning at the upper left-hand corner and continuing from left to right in equal sections with small overlaps.

Photographs included in the original manuscript have been reproduced xerographically in this copy. Higher quality 6" x 9" black and white photographic prints are available for any photographs or illustrations appearing in this copy for an additional charge. Contact UMI directly to order.

Bell & Howell Information and Learning
300 North Zeeb Road, Ann Arbor, MI 48106-1346 USA
800-521-0600

UMI[®]

NOTE TO USERS

This reproduction is the best copy available.

UMI

—

Université de Montréal

**Structure inhomogène et dynamique des vents stellaires chauds par
spectroscopie de raies d'émission**

**par
Sébastien Lépine
Département de physique
Faculté des arts et des sciences**

**Thèse présentée à la Faculté des études supérieures
en vue de l'obtention du grade de
Philosophiæ Doctor (Ph.D.)
en physique**

Juin, 1998

© Sébastien Lépine, 1998





National Library
of Canada

Acquisitions and
Bibliographic Services

395 Wellington Street
Ottawa ON K1A 0N4
Canada

Bibliothèque nationale
du Canada

Acquisitions et
services bibliographiques

395, rue Wellington
Ottawa ON K1A 0N4
Canada

Your file Votre référence

Our file Notre référence

The author has granted a non-exclusive licence allowing the National Library of Canada to reproduce, loan, distribute or sell copies of this thesis in microform, paper or electronic formats.

The author retains ownership of the copyright in this thesis. Neither the thesis nor substantial extracts from it may be printed or otherwise reproduced without the author's permission.

L'auteur a accordé une licence non exclusive permettant à la Bibliothèque nationale du Canada de reproduire, prêter, distribuer ou vendre des copies de cette thèse sous la forme de microfiche/film, de reproduction sur papier ou sur format électronique.

L'auteur conserve la propriété du droit d'auteur qui protège cette thèse. Ni la thèse ni des extraits substantiels de celle-ci ne doivent être imprimés ou autrement reproduits sans son autorisation.

0-612-43498-2

Canada

**Université de Montréal
Faculté des études supérieures**

Cette thèse intitulée:

**Structure inhomogène et dynamique des vents stellaires chauds par
spectroscopie de raies d'émission**

présentée par:

Sébastien Lépine

a été évaluée par un jury composé des personnes suivantes:

François Wesemael,	président-rapporteur
Anthony F.J. Moffat,	directeur de recherche
Richard N. Henriksen,	codirecteur
Nicole St-Louis,	membre du jury
Stanley P. Owocki,	examinateur externe

Thèse acceptée le:98....9....11....

SOMMAIRE

Le spectre des étoiles Wolf-Rayet (WR) présente des raies en émission très larges, qui peuvent s'expliquer par l'existence d'un vent stellaire chaud en expansion rapide. Un vent stellaire chaud est généré par la pression de radiation qui agit sur les électrons libres via la diffusion électronique et sur les ions via l'absorption atomique. Les raies d'émission se forment alors que le vent ionisé se refroidit, ce qui provoque la recombinaison atomique. Chaque raie d'émission se forme à un régime de distances donné de l'étoile où l'équilibre d'ionisation et d'excitation est propice à une recombinaison correspondante. La vitesse du vent, la densité et la température du milieu ainsi que leur distribution, de même que la composition chimique, déterminent l'intensité et la forme du profil de chacune des raies d'émission. À l'aide d'un certain nombre d'hypothèses simplificatrices, le *modèle standard* des étoiles WR permet ainsi de prédire la forme et l'intensité des raies observées. Or, la spectroscopie à haute résolution des étoiles WR révèle l'existence de variations stochastiques dans les raies d'émission sur des échelles de temps de quelques minutes à quelques heures, phénomène qui n'est pas reproduit par le modèle standard.

Cette thèse de doctorat présente une étude de la variabilité des raies spectrales en émission des étoiles WR. En particulier, il est montré que cette variabilité peut être reproduite par un vent stellaire *inhomogène*. Un modèle phénoménologique est utilisé pour décrire l'émission d'un vent fragmenté, constitué d'éléments discontinus. Différents paramètres décrivent la structure dynamique (loi de vitesse) et la structure inhomogène (nombre d'éléments discrets, distribution statistique) du vent. Des simulations numériques montrent que ce modèle peut reproduire qualitativement et quantitativement la variabilité stochastique obser-

vée dans les raies des étoiles WR. Des méthodes numériques utilisant l'analyse en ondelettes et les corrélations sont mises au point et adaptées spécialement au problème de la variabilité des raies d'émission. Ces techniques permettent d'effectuer une analyse comparative des simulations avec un ensemble de séries temporelles de spectres de 10 étoiles WR de différents sous-types spectraux.

L'analyse comparative met en lumière les éléments suivants. (1) Afin de reproduire le niveau des variations, il faut utiliser un minimum de 10^4 éléments discrets dans le vent, ce qui implique que la structure inhomogène est extrêmement fine. (2) Le vent doit être animé de fluctuations locales considérables dans le champ de vitesse, correspondant à des vitesses "turbulentes" moyennes sur la ligne de visée $\overline{\sigma_\xi} \sim 100 \text{ km s}^{-1}$. (3) L'intensité des fluctuations locales dans le champ de vitesse doit être *anisotrope*, avec $\sigma_{v_r} \sim 4\sigma_{v_\theta}$, où σ_{v_r} et σ_{v_θ} sont les dispersions en vitesse dans les directions radiales et angulaires, respectivement. (4) L'accélération des structures inhomogènes dans le vent doit être plus lente que l'accélération prédictive pour le vent par le modèle standard. Cependant, (5) le temps caractéristique des variations est cohérent avec le temps de passage des éléments discontinus au travers de la zone d'émission. Tous ces indices suggèrent que la structure inhomogène du vent est constituée de chocs hydrodynamiques se propageant dans la direction radiale, qui peuvent être reliés à des instabilités dynamiques à petite échelle dans un vent poussé par pression de radiation.

L'analyse détaillée des variations spectroscopiques suggère également l'existence de structures inhomogènes dans un régime de dispersions en vitesse plus petites ($\overline{\sigma_\xi} \lesssim 50 \text{ km s}^{-1}$), qui pourraient être la signature de processus chaotiques de dissipation turbulente dans un milieu compressible. L'analyse révèle aussi la présence, dans deux des étoiles de l'échantillon, de structures possédant des dispersions de vitesse plus importantes ($\overline{\sigma_\xi} \gtrsim 200 \text{ km s}^{-1}$), qui résultent possiblement de perturbations à grande échelle dans le vent.

TABLE DES MATIÈRES

SOMMAIRE	iii
TABLE DES MATIÈRES	v
LISTE DES TABLEAUX	x
LISTE DES FIGURES	xi
LISTE DES ABRÉVIATIONS	xvi
CHAPITRE 1: INTRODUCTION	1
1.1 Les Vents Stellaires Chauds	1
1.1.1 Généralités	1
1.1.2 Méthodes d'observation	3
1.1.3 Théorie sommaire des vents radiatifs	6
1.1.4 Le modèle standard des étoiles Wolf-Rayet	8
1.2 La Structure Inhomogène des Vents Stellaires Chauds	10
1.2.1 Instabilités radiatives	10
1.2.2 Variabilité photométrique	11
1.2.3 Variabilité polarimétrique	13
1.2.4 Courbes de lumière des systèmes éclipsants	16

1.2.5	Éclipses momentanées et formation de poussière	19
1.2.6	Excès et variabilité du rayonnement infra-rouge et radio	20
1.2.7	Excès et variabilité du rayonnement X	22
1.2.8	Intensité des ailes de diffusion électroniques	25
1.2.9	Saturation des profils P Cygni	26
1.2.10	Variabilité des profils P Cygni	30
1.2.11	Variabilité des raies d'émission	34
CHAPITRE 2: WIND INHOMOGENEITIES IN WOLF-RAYET STARS.		
I.	SEARCH FOR SCALING LAWS USING WAVELET TRANSFORMS	40
2.1	Introduction: Why Use Wavelets?	43
2.2	The Wavelet Analysis	45
2.3	Scaled Distributions and the Power Spectrum	48
2.4	Data Source	55
2.5	Data Analysis	58
2.5.1	The wavelet power spectrum profile	58
2.5.2	The noise limit	63
2.5.3	Fitting data to the model	64
2.5.4	Discussion	67
2.5.4.1	Dominant scales	67

2.5.4.2 Scaling properties	68
2.6 Summary and Perspectives	71
CHAPITRE 3: WIND INHOMOGENEITIES IN WOLF-RAYET STARS.	
II. INVESTIGATION OF EMISSION-LINE PROFILE VARIATIONS.	74
3.1 Introduction	78
3.2 Spectroscopic Observations	81
3.3 Phenomenological, Clumped Wind Model	90
3.3.1 Discrete wind emission elements	90
3.3.2 The velocity law	92
3.3.3 Line emission from DWEEs	95
3.3.4 Anisotropy	100
3.4 Comparative Analysis	101
3.4.1 Spectroscopic resolution of wind elements	101
3.4.2 Statistical distribution of DWEE fluxes	104
3.4.3 Anisotropic emission	108
3.4.4 Kinematics of the subpeaks	114
3.5 Discussion	120
3.5.1 Physical origin for the variable emission elements	120
3.5.2 The wind velocity structure	122
3.5.3 The size of the LER	125

3.6 Summary and Perspectives	127
3.7 Appendix A: Multi-Scale Wavelet Analysis	130
3.8 Appendix B: The Degradation Function	133
CHAPITRE 4: WIND INHOMOGENEITIES IN WOLF-RAYET STARS.	
III. UNUSUAL EMISSION-LINE PROFILE VARIATIONS	
IN γ^2 VELORUM	135
4.1 Introduction	138
4.2 Observations and reduction	142
4.3 Multi-Scale Analysis	147
4.3.1 Wavelet Spectrum	147
4.3.2 Wavelet Filtering	150
4.4 Comparative analysis	154
4.4.1 Simulations of LPVs from an inhomogeneous wind	154
4.4.2 Multiple LPV modes	160
4.4.3 Kinematics of the inhomogeneities	162
4.4.4 Comparison with the orbital phase	165
4.5 Discussion	167
4.6 Conclusions	170
CHAPITRE 5: CONCLUSIONS	172
5.1 Synthèse des Résultats	172

5.2 Projets Futurs	175
RÉFÉRENCES	178
REMERCIEMENTS	xviii

LISTE DES TABLEAUX

2.1	Liste des raies d'émission observées	58
2.2	Paramètres du modèle de loi de puissance	65
3.1	Caractéristiques des étoiles WR de l'échantillon	82
3.2	Propriétés du vent d'après le profil des raies d'émission	97
3.3	Paramètres des simulations	103
3.4	Propriétés du vent d'après les patrons de variabilité	111
4.1	Paramètres du modèle de vent inhomogène	158

LISTE DES FIGURES

1.1 Formation d'un profil de type P Cygni	5
1.2 Variations photométriques de l'étoile HD 86161	12
1.3 Variabilité dans la polarisation de l'étoile HD 86161	15
1.4 Éclipses du système V444 Cygni dans différents domaines spectraux	18
1.5 Éclipses momentanées des étoiles WR: modèle d'obscurcation par des nuages de poussière	21
1.6 Excès dans le rayonnement infra-rouge de ζ Puppis	23
1.7 Excès de rayons-X dans HD 4004 (=WR1), et variabilité en rayons-X de ζ Puppis.	24
1.8 Modélisation des ailes de diffusion électroniques	27
1.9 Géométrie pour les équations 1.6 et 1.7	28
1.10 Saturation et variabilité d'un profil de raie P Cygni	28
1.11 Composantes discrètes en absorption dans les étoiles ξ Per et HD 34656	31
1.12 Modulations périodiques dans l'absorption du doublet Si IV $\lambda\lambda$ 1400 de l'étoile HD 64760	33
1.13 Variations de type R dans trois raies d'émission de l'étoile EZ CMa	36

1.14 Variation de type S dans la raie d'émission C III $\lambda 5696$ de l'étoile HD192103	38
2.1 Transformée en ondelettes d'un spectre d'étoile WR	49
2.2 Schéma montrant la synthèse d'un signal caractérisé par des lois d'échelles	51
2.3 Spectre en ondelettes de signaux caractérisés par des lois d'échelles	53
2.4 Relation entre la pente du spectre de puissance et les paramètres des lois d'échelles	54
2.5 Profils de raie d'émission des étoiles WR observées	57
2.6 Déviations du profil moyen des raies d'émission en fonction du temps	59
2.7 Exemple de spectre en ondelettes des structures variables dans une raie d'émission	61
2.8 Spectre en ondelettes des variations spectrales observées dans les étoiles de l'échantillon	62
2.9 Modélisation du spectre en ondelettes avec un signal comprenant des lois d'échelles	66
2.10 Comparaison des lois d'échelles déduites de l'analyse en ondelettes avec celles prédites selon d'autres méthodes	70
3.1 Variabilité de la raie d'émission He II $\lambda 5411$ des étoiles HD 191765, HD 192163 et HD 193077	84

3.2 Variabilité de la raie d'émission C III λ 5696 des étoiles HD 192103, HD 192641 et HD 193793	85
3.3 Variabilité de la raie d'émission He II λ 5411 de l'étoile HD 96548, et de la raie d'émission C III λ 5696 des étoiles HD 164270 et HD165763.	86
3.4 Spectre de puissance en ondelettes pour les variations dans les raies d'émission des étoiles de l'échantillon	89
3.5 Représentation schématique de la loi de vitesse de type β	94
3.6 Emissivité relative en fonction de la vitesse radiale par rapport à l'étoile	98
3.7 Variabilité simulée d'une raie d'émission pour différentes valeurs de la vitesse systématique et de la vitesse turbulente d'un vent inhomogène	102
3.8 Spectre de puissance en ondelettes pour les simulations de la figure 3.7	105
3.9 Dépendance de la variabilité induite en fonction des paramètres de la distribution statistique du flux des éléments inhomogènes dans le vent	107
3.10 Variabilité simulée du profil d'une raie d'émission suivant différen- tes distributions statistiques dans le flux des éléments inhomogènes du vent	109
3.11 Spectre de puissance en ondelettes pour les simulations de la figure 3.10	110

3.12 Variabilité simulée d'une raie d'émission pour différentes valeurs de l'anisotropie dans la vitesse turbulente et dans l'émissivité d'un vent inhomogène	113
3.13 Accélérations radiales dans le vent des étoiles WR de l'échantillon obtenues par la fonction de dégradation	116
3.14 Comparaison entre les accélérations mesurées et celle prédites par le modèle standard des étoiles WR	117
3.15 Temps caractéristiques d'apparition des structures dans les raies variables obtenues par la fonction de dégradation	119
4.1 Série temporelle des variations dans la raie d'émission C III $\lambda 5696$ de l'étoile γ^2 Vel	144
4.2 Gradient de variation dans le temps dans la raie CIII $\lambda 5696$ de γ^2 Vel	146
4.3 Spectre de puissance en ondelettes des variations	149
4.4 Spectres de puissance en ondelettes des composantes filtrées en fonction de l'échelle caractéristique	152
4.5 Application du filtre en ondelettes aux données spectroscopiques	153
4.6 Emissivité dans le vent en fonction de la vitesse par rapport au centre de l'étoile	157
4.7 Simulation des variations dans la raie C III $\lambda 5696$ à partir d'un modèle de vent inhomogène	159
4.8 Comparaison des données et des simulations à l'aide du spectre en ondelettes	161

4.9 Estimation de l'accélération radiale dans le vent à l'aide de la fonction de dégradation	164
4.10 Configuration de l'orbite du système γ^2 Velorum	166

LISTE DES ABRÉVIATIONS

Françaises et *Anglaises*

CDA : Composantes Discrètes en Absorption

CFH ou **CFHT** : télescope Canada-France-Hawaii, *Canada-France-Hawaii Telescope*

CIR : *Co-rotating Interacting Region*

DAC : *Discrete Absorption Component*

DWEE : *Discrete Wind Emission Element*

ESO : *European Southern Observatory*

EW : *Equivalent Width*

FP : Fabry-Pérot

HJD ou **JD**: *Heliocentric Julian Date*

IR : rayonnement Infra-Rouge

LBV : étoile Lumineuse Bleue Variable, *Luminous Blue Variable star*

LER : *Line-Emission Region*

LPV : *Line-Profile Variations*

MPA : Modulation Periodique dans l’Absorption

PAM : *Periodic Absorption Modulation*

S/N : *Signal-to-Noise ratio*

TVS : *Temporal Variance Spectrum*

UV : rayonnement Ultra-Violet

WFT : *Windowed Fourier Transform*

WPS : *Wavelet Power Spectrum*

WR : étoile Wolf-Rayet, *Wolf-Rayet star*

À Pascale, qui est mon rayon de soleil,
et à Laurasia, ma petite étincelle.

CHAPITRE 1

INTRODUCTION

1.1 Les Vents Stellaires Chauds

1.1.1 Généralités

Toutes les étoiles perdent de la masse sous la forme d'un *vent stellaire*. Celui-ci est constitué de particules qui s'échappent de la surface, quittant l'attraction gravitationnelle de l'étoile, et s'éloignant avec une vitesse relativement grande. Il peut en résulter des taux de perte de masse substantiels qui peuvent influer significativement sur l'évolution de l'étoile. Un vent stellaire est provoqué par l'existence d'une force radiale orientée vers l'extérieur (le *moteur*) et qui agit sur les particules qui se trouvent près ou au-delà de la surface hydrostatique.

On peut classer les vents stellaires en deux groupes: les vents stellaires dits *froids*, et ceux dits *chauds*. Les vents stellaires froids sont généralement le lot des étoiles de type spectral G, K et M, c'est-à-dire les étoiles dont la température de surface est inférieure à environ 6000K. Il existe plusieurs moteurs aux vents stellaires froids: pulsations, ondes d'Alfvén, pression de radiation sur la poussière, ondes sonores, etc... (cf. Lamers & Cassinelli, 1998). Les vents stellaires froids sont généralement animés de vitesses radiales d'expansion relativement faibles ($v_r \sim 10^1 \text{ km s}^{-1}$).

Les vents stellaires chauds sont le lot des étoiles dont la température de surface est supérieure à environ 6000K (Achmad *et al.* 1997), ce qui comprend

les étoiles de type spectral O, B, et A, ainsi que les étoiles *lumineuses bleues variables* (LBV) et les étoiles *Wolf-Rayet* (WR). Ces dernières présentent des vents particulièrement denses, qui occultent les surfaces de ces étoiles. La vitesse radiale d'expansion des vents chauds est la plupart du temps très élevée ($v_r \sim 10^2 - 10^3$ km s⁻¹) et la densité du vent augmente en général quand on va vers les types spectraux précoces (A → B → O). La densité du vent est à son maximum pour les étoiles WR et LBV, où des taux de perte de masse extrêmes ($\dot{M} \sim 10^{-5} M_\odot$ an⁻¹ pour les WR et, épisodiquement, jusqu'à $\dot{M} \sim 10^{-2} M_\odot$ an⁻¹ pour certaines LBV) sont courants. Le moteur principal des vents stellaires chauds est la pression de radiation, en particulier celle due à l'absorption du rayonnement par les raies atomiques.

Les taux de perte de masse qui caractérisent les vents stellaires chauds des étoiles massives sont tels que l'enveloppe d'hydrogène disparaît progressivement, ce qui réduit considérablement la masse totale de l'étoile au cours de sa vie, et expose graduellement à la surface les produits de fusion du cœur. Ainsi, les modèles évolutifs montrent que les étoiles O sont les *progéniteurs* des étoiles LBV et WR, qui sont les états stellaires résultants de la disparition en tout ou en partie de l'enveloppe d'hydrogène (Langer *et al.* 1994).

Le vent des étoiles de type O, B, et A est relativement ténu, et il est possible de l'étudier en fonction d'un modèle de type cœur-halo, dans lequel on traite séparément la surface de l'étoile, au dessus de laquelle on ajoute ensuite un vent. Il suffit alors de calculer comment ce vent est influencé par les conditions régnant à la surface, et comment la présence du vent modifie ces conditions (e.g. Gabler *et al.* 1989). D'un autre côté, la densité du vent des étoiles WR est telle que le vent est optiquement épais au rayonnement de surface. Il est donc impossible d'utiliser un modèle de type cœur-halo, puisque la surface n'est pas directement accessible à l'observateur, et ne peut donc être modélisée *a priori*. Puisque seul le vent est accessible, la connaissance des propriétés de surface, de la structure et de

l'évolution des étoiles WR dépend donc directement de l'état de nos connaissances de la structure détaillée des vent stellaires chauds.

1.1.2 Méthodes d'observation

Il existe trois méthodes principales pour l'étude de la structure des vents stellaires chauds (cf. Lamers & Cassinelli, 1998): l'observation du rayonnement de type *libre-libre* dans le domaine IR et radio; l'observation de profils de raies spectrales de type P Cygni; l'observation de raies spectrales en émission.

Les vents stellaires chauds sont en partie ionisés jusqu'à des distances relativement grandes de la surface ($\sim 10^2 R_*$). La présence d'électrons libres implique l'émission de rayonnement continu de type libre-libre (émission *Bremmstrahlung*). Les étoiles O, B, WR, et LBV présentent donc des excès importants dans les domaines infra-rouge (IR) et radio (Hartmann & Cassinelli, 1977) dûs à ce rayonnement libre-libre. La taille apparente de l'étoile est nettement plus grande dans les domaines IR et radio, car la photosphère effective se situe alors à une bonne distance dans le vent plutôt que près de la surface. Puisque la température dans le vent décroît avec la distance, les dimensions apparentes augmentent donc avec la longueur d'onde. En mesurant l'excès d'émission en fonction de la longueur d'onde, il est possible d'estimer la densité dans le vent en fonction de la distance à l'étoile, d'où on peut déduire le champ de vitesse ainsi que le taux de perte de masse (Waters & Lamers, 1984). Cependant, l'excès de rayonnement libre-libre peut dépendre de la structure détaillée du vent, en particulier de l'intensité des fluctuations en densité ou en température dans un vent inhomogène (Lamers & Waters, 1984).

Le profil de type P Cygni tient son nom d'une étoile de type LBV dans la constellation du Cygne. Un profil de raie P Cygni comprend généralement une partie en émission flanquée d'une composante en absorption. La partie en émission

est décalée vers le rouge par rapport à la longueur d'onde au repos de la transition atomique, alors que la partie en absorption est toujours nettement décalée vers le bleu. La figure 1.1 illustre la formation d'un profil P Cygni dans un vent stellaire. Il est constitué par trois composantes: (1) le rayonnement thermique continu venant de l'étoile, (2) l'absorption dans le vent due à une transition atomique, et (3) la réémission du rayonnement absorbé. Chaque absorption ou émission s'effectue à une longueur fixe dans le référentiel local. Du point de vue de l'observateur, le continu provenant de l'étoile est aborbé par la partie du vent sur la ligne de visée, dont la vitesse radiale est négative, d'où le décalage vers le bleu. D'un autre côté, les photons réémis vers l'observateur viennent de toutes les régions du vent, d'où la composante en émission qui s'étend sur un large domaine en longueur d'onde correspondant à l'ensemble des vitesses projetées dans le vent. Une partie du rayonnement réémis par le vent est occulté par le disque de l'étoile, ce qui correspond à la fraction des photons qui sont rediffusés vers la surface. L'analyse d'un profil P Cygni permet d'obtenir des informations sur le champ de vitesse, l'équilibre statistique local, et la composition chimique de vent, entre autres. L'extension vers le bleu de la composante en absorption permet d'obtenir une estimation précise de la vitesse terminale v_∞ du vent (Prinja *et al.* 1990; Lamers *et al.* 1997).

Alors que les profils P Cygni peuvent s'apparenter à un phénomène de diffusion, les raies d'émission atomiques se forment dans le cas où l'émission provient directement du vent. Parce que la température décroît en fonction de la distance à l'étoile (Kuhi 1973), l'équilibre d'ionisation d'un élément de plasma qui suit le vent change avec le temps. Il se produit donc des recombinaisons électroniques massives accompagnées de désexcitations vers les niveaux d'énergie fondamentaux. Il en résulte une émission nette de rayonnement à des longueurs d'ondes correspondant aux transitions atomiques concernées. Les profils résultants sont d'autant plus larges dans le spectre que la vitesse radiale du vent est élevée. Les profils des raies d'émission présentent différentes formes: ils sont

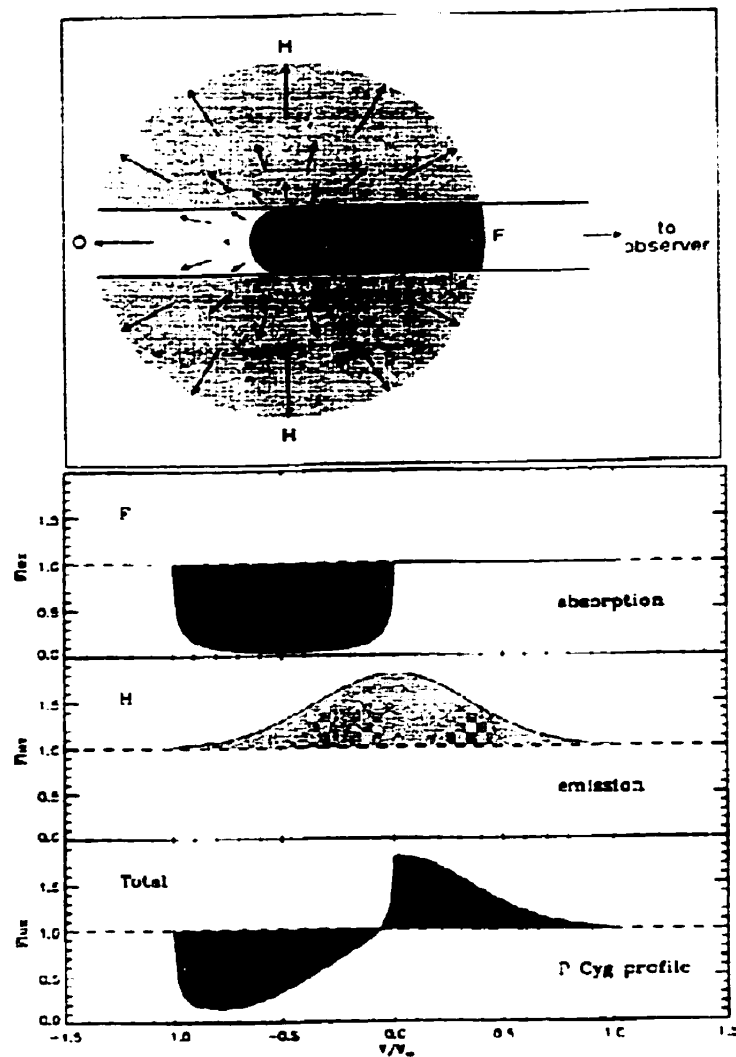


FIGURE 1.1. Schéma montrant la formation d'un profil de type P Cygni. Le rayonnement est absorbé par la partie du vent qui se dirige vers l'observateur, et rediffusé uniformément par toutes les régions du vent, d'où la forme asymétrique du profil autour de la longueur d'onde fondamentale (tiré de Lamers & Cassinelli, 1998)

parfois *plats*, parfois *arrondis*, ou encore flanqués d'un composante faible en absorption de type P Cygni. La forme des profils dépend du champ de vitesse (Brown *et al.* 1997), mais aussi de la profondeur optique dans le vent (Mihalas 1980). Les profils plats impliquent que le vent est optiquement mince, alors que les profils arrondis peuvent s'expliquer par un vent optiquement épais dans la transition atomique donnée (Castor 1970). Il existe différentes méthodes qui permettent de relier la forme et l'intensité des profils à la structure et aux propriétés du vent (e.g. Lamers *et al.* 1987).

1.1.3 Théorie sommaire des vents radiatifs

Un vent stable et de symétrie sphérique est décrit par une densité $\rho(r)$ et un champ de vitesse $v(r)$, fonctions de la distance r au centre de l'étoile. Ces deux expressions sont reliées par l'équation de continuité de la masse:

$$\dot{M} = 4\pi r^2 \rho(r) v(r) , \quad (1.1)$$

où \dot{M} représente le taux de perte de masse par le vent. En général, on caractérise la structure d'un vent stellaire chaud à partir de la forme de son champ de vitesse $v(r)$, aussi appelé *loi de vitesse*. La distribution en densité $\rho(r)$ est alors donnée par l'équation de continuité.

L'équation générale du mouvement pour un vent stellaire est de la forme:

$$\frac{dv}{dt} = v \frac{dv}{dr} = -\frac{1}{\rho} \frac{dp}{dr} - \frac{GM_*}{r^2} + f(r) . \quad (1.2)$$

Le premier terme de l'équation représente la force attribuable au gradient de pression dans le vent et le second terme représente l'attraction gravitationnelle. Le troisième terme représente le moteur du vent, i.e. une force radiale orientée vers l'extérieur de l'étoile. Pour les vents stellaires chauds, $f(r)$ représente la pression de radiation sur les électrons, et la pression de radiation sur les raies atomiques.

Les calculs théoriques et numériques montrent que la pression de radiation

sur les électrons libres, seule, n'est pas suffisante pour pousser les vents stellaires chauds aux vitesses qui sont observées. Le moteur principal des vents stellaires chauds est donc la pression de radiation sur les raies atomiques (Castor *et al.* 1975). Malheureusement, alors que le calcul de la pression de radiation sur les électrons libres est relativement simple, le calcul de la force radiative sur les raies atomiques est extrêmement complexe, car il dépend du détail de la composition chimique et de l'équilibre statistique dans le vent.

On peut cependant supposer que les forces radiatives sont de la forme $f(r) = A(r)r^{-2}$, où $A(r)$ est un facteur de correction qui sert à définir le rayon d'action de la force de rayonnement. Pour une force $f(r)$ inversement proportionnelle au carré de la distance, on peut montrer qu'il existe une solution pour le champ de vitesse $v(r)$ de la forme:

$$v(r) = v_\infty \left(1 - \frac{R_*}{r}\right)^{\frac{1}{2}}. \quad (1.3)$$

La vitesse terminale v_∞ sera fonction de l'intensité du rayonnement qui agit sur les raies atomiques (cf. Lamers & Cassinelli, 1998). Si l'on tient en compte le fait qu'une étoile n'est pas une source ponctuelle, alors la force radiative n'est plus inversement proportionnelle au carré de la distance, du moins près de la surface. En incluant l'effet des dimensions finies de la surface, Friend & Abbott (1986) ont montré que le champ de vitesse prenait la forme:

$$v(r) = v_\infty \left(1 - \frac{0.9983R_*}{r}\right)^{0.83}. \quad (1.4)$$

Dans les faits, le champ de vitesse peut dévier de façon importante par rapport à l'équation 1.4, en fonction de la composition du milieu et du détail des modèles atomiques. Cependant, on peut représenter la loi de vitesse d'un vent stellaire chaud sous la forme dite "loi-bêta", exprimée mathématiquement comme:

$$v(r) = v_\infty \left(1 - \frac{R_*}{r}\right)^\beta, \quad (1.5)$$

où β est utilisé comme paramètre libre (Castor & Lamers, 1979). Les résultats des calculs théoriques et numériques montrent que l'on peut, en première approximation, représenter le champ de vitesse d'un vent stellaire chaud par une loi-bêta. Un valeur de $\beta \simeq 1$ est typique pour les vents d'étoiles de type O et B (Puls *et al.* 1996), alors que le vent des étoile WR requiert apparemment l'utilisation de valeurs $\beta > 4$ (Schmutz 1997).

1.1.4 Le modèle standard des étoiles Wolf-Rayet

La surface des étoiles WR est complètement cachée par le vent très dense qui en émane. Contrairement aux étoiles dont la surface est directement observable, on ne peut pas utiliser l'analyse spectrale classique basée sur l'approximation des atmosphères parallèles planes. En effet, comme l'émission du continu est issue du vent, ont a affaire à une photosphère diffuse et très étendue, qui comporte en plus une stratification importante en température et un gradient d'ionisation.

Afin de procéder à l'analyse spectrale des étoiles WR, et ainsi en déduire des conclusions générales sur les propriétés de l'étoile (masse, luminosité, composition, etc...), il est commode d'utiliser un certain nombre d'hypothèses simplificatrices. Celles-ci sont regroupées dans un cadre que l'on appelle le *modèle standard* des étoiles WR (e.g. Hamann *et al.* 1992; Hillier 1995). Les trois hypothèses principales sont les suivantes.

1. Le vent est de *symétrie sphérique*: ceci implique que la seule variable d'espace à utiliser est la distance r à la surface de l'étoile, ce qui équivaut à travailler le problème en une seule dimension.
2. Le vent est *stationnaire*: c'est à dire que le détail de sa structure ne varie pas dans le temps. Ceci permet e.g. de retirer toute référence explicite au temps dans les équations.

3. Le vent est *homogène*: c'est à dire que les champs de vitesse et de densité sont représentés par des fonctions continues et monotones.

En plus de ces hypothèses de base, on suppose que le vent est en équilibre radiatif, et on applique les équations d'équilibre statistique. De plus, la loi de vitesse est fixée *a priori*, ce qui se traduit communément par le choix d'une valeur du paramètre β (cf. Eq.1.5). Le modèle standard permet d'obtenir, à partir de l'analyse spectrale, une estimation des masses, taux de perte de masse, luminosités et températures effectives des étoiles WR, ce qui permet de les situer dans un cadre évolutif.

Cependant, un nombre croissant d'études ont montré l'existence d'un désaccord important entre les prédictions du modèle standard et les estimations de certains paramètres de l'étoile et du vent mesurés de façon indépendante (Howarth & Schmutz, 1992; Hamann *et al.* 1994; Hillier 1996; Schmutz 1997). Les hypothèses du modèle standard sont apparemment trop simples, et induisent possiblement des erreurs importantes dans les prédictions. Récemment, certains auteurs ont entrepris de mettre au point des modèles théoriques qui tiennent compte d'un certain niveau d'inhomogénéité dans le vent (Schmutz 1997; Hillier & Miller, 1998), ce qui implique l'introduction d'un certain nombre de paramètres libres supplémentaires. Il devient donc important d'utiliser des méthodes d'observation qui permettent d'étudier directement la structure inhomogène des vents stellaires chauds, afin de contraindre les paramètres des modèles de vents inhomogènes.

1.2 La Structure Inhomogène des Vents Stellaires Chauds

1.2.1 Instabilités radiatives

La théorie des vents poussés par la pression de radiation sur les raies spectrales prédit l'existence d'instabilités fondamentales dans les vents stellaires chauds (Lucy & Solomon, 1970). Le principe de base de cette instabilité découle du fait que les raies atomiques sont sensibles au rayonnement d'une longueur d'onde bien définie, auquel se combine des effets Doppler significatifs, vu les vitesses en jeu. Une couche sphérique du vent qui est en expansion radiale à une vitesse v_r agit comme un voile qui absorbe tout le rayonnement de longueur d'onde $\lambda = \lambda_0 + v_r c^{-1}$, où λ_0 est la longueur d'onde correspondant à la transition atomique, et c la vitesse de la lumière. Prenons un élément du vent dont la vitesse s'accroît d'une grandeur δv ; à cause du décalage Doppler, cet élément est maintenant sensible au rayonnement de longueur d'onde $\lambda = \lambda_0 + (v_r + \delta v)c^{-1}$ qui n'est pas voilé par le vent sous-jacent. L'élément perturbé est donc soumis aux forces radiatives, ce qui accroît davantage sa vitesse.

Ainsi, des calculs numériques ont montré que de petites perturbations introduites à la base du vent (inférieures à 1% de l'amplitude du champ de vitesse) s'accroissent de façon non-linéaire et dégénèrent en ondes de choc en aval du vent (Owocki *et al.* 1988). Les calculs des perturbations prédisent des taux de croissance théorique de plus de 40 ordres de grandeur (Gayley & Owocki 1995). Ceci suggère que le vent devient fortement inhomogène, avec des contrastes en densité importants. Le vent se “brise” en un grand nombre de “morceaux” relativement denses, baignés dans un milieu ténu.

Une analyse en trois dimensions, montre que l'effet de la force radiative n'est important que dans la direction *radiale* (Rybicki *et al.* 1990) et que, tandis que les plus faibles perturbations sont amplifiées dans la direction radiale, elle sont en fait

atténues dans toute autre direction. Ceci ne veut pas dire que l'on peut rapporter le problème à une seule dimension, et que le vent prendra la forme de coquilles concentriques. En effet, les simulations montrent que, même si l'on introduit des perturbations strictement périodique à la base du vent, il en résulte malgré tout un comportement stochastique en aval (Owocki *et al.* 1988). La structure globale du vent sera vraisemblablement très fragmentée, dans toutes les directions. La nature hautement chaotique du vent aux petites échelles suggère l'utilisation du formalisme de la turbulence en milieu compressible (Henriksen 1994; Owocki, 1998).

Si l'instabilité et l'inhomogénéité des vents stellaires chauds ne font guère de doute sur le plan théorique, il est difficile de confronter les prédictions des simulations numériques (e.g. Feldmeier 1995) à la structure inhomogène réelle du vent. Il faut pour cela combiner les informations obtenues grâce à diverses méthodes observationnelles, qui sont décrites dans les sections qui suivent.

1.2.2 Variabilité photométrique

Les étoiles massives montrent des variations *périodiques*, qui sont la plupart du temps semblables à celles rencontrées dans tout système binaire, les cas les plus spectaculaires étant les systèmes éclipsants (e.g. Drissen *et al.* 1986). La présence de variations périodiques peut aussi permettre d'identifier la présence d'un compagnon compact (e.g. Antokhin *et al.* 1982), ou encore l'existence de pulsations non-radiales (e.g. Gosset & Vreux, 1987). Cependant, on observe également des variations *stochastiques*, plus ou moins importantes, soit superposées à des variations périodiques, soit apparaissant seules. La photométrie d'échantillons importants d'étoiles WR suggère que toutes présentent des variations stochastiques à des degrés divers (e.g. Moffat & Shara, 1986) sur des échelles de temps de quelques heures à plusieurs jours. La recherche de courtes périodes a donné jusqu'ici des résultats négatifs (e.g. Balona *et al.* 1989), ce qui réfute l'hypothèse

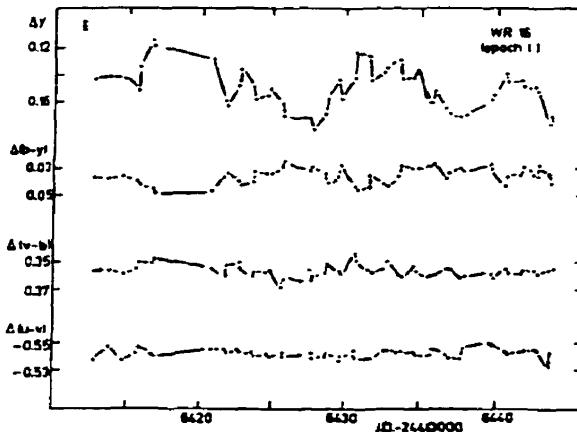


FIGURE 1.2. Variations photométriques dans le système Strömgren (*ubvy*) pour l'étoile HD 86161 (=WR16). On remarque les fluctuations importantes dans la bande *y*, plus ou moins corrélées avec les fluctuations dans les autres bandes (*uvb*). Les fluctuations significatives dans les rapports de couleur *b* – *y*, *v* – *b*, et *u* – *v* impliquent la présence de fluctuations thermiques.

des pulsations rapides.

Pour les étoiles entourées d'un vent stellaire chaud, la présence de nombreuses raies d'émission intenses rend l'interprétation des variations photométriques assez délicate. En effet, la quantité de lumière mesurée dans une bande photométrique large contient parfois une fraction substantielle de rayonnement provenant des raies d'émissions. Il est donc difficile de distinguer entre une variation se produisant dans le continu de l'étoile et une variation dans l'intensité des raies spectrales. Pour ce faire, il convient d'observer simultanément dans plusieurs bandes photométriques et d'identifier, à l'aide d'un spectre détaillé de l'étoile, quelles seront les bandes les plus susceptibles d'être affectées par des raies d'émission et de quelle façon. Une autre méthode consiste à observer dans des régimes spectraux étroits contenant le moins de raies possible, et d'associer les variations résultantes aux variations dans le continu.

Une étude comparative des variations photométriques détectées dans les cinq bandes de couleur du système Walraven (*VBLUW*) a mis en évidence des variations stochastiques dans 4 étoiles WR présumément simples (van Genderen *et al.* 1987). Les variations les plus importantes ont été détectées dans les bandes *L* et *U*, les moins affectées par les raies d'émission, ce qui implique que les variations se produisent en majeure partie dans le continu. On a de plus mis en évidence des variations dans les rapports d'intensité de chaque bande, ce qui implique des fluctuations dans la température. L'interprétation de van Genderen *et al.* (1987) est que cette variabilité photométrique est provoquée par l'apparition momentanée de surdensités plus chaudes que le milieu ambiant. Des observations de l'étoile HD 86161 (=WR16) dans le système photométrique de Strömgren (*uvby*) confirme l'existence de variations dans le continu accompagnées de fluctuations d'origine thermique (van Genderen *et al.* (1989)). Les résultats des ces dernières observations sont présentés à la figure 1.2.

L'examen des temps caractéristiques des variations a conduit van Genderen *et al.* (1990) à proposer deux explications possibles: des pulsations affectant les régions du vent situées près de la surface, ou des inhomogénéités se propageant dans le vent suite à une éruption près de la surface. L'absence de périodicité apparente pose problème pour la première hypothèse, mais selon van Genderen *et al.* (1990) des éruptions devraient occasionner des variations nettement plus irrégulières. Il faut noter cependant que ceci dépend du nombre et de la distribution des inhomogénéités résultantes, un grand nombre de petites structures étant moins susceptible de provoquer des variations détectables qu'un petit nombre de structures plus grandes.

1.2.3 Variabilité polarimétrique

La polarimétrie des étoiles WR montre des variations à des échelles de temps inférieures à une journée (e.g. St-Louis *et al.* 1987). Ceci implique l'existence d'une

polarisation *intrinsèque*, la polarisation par le milieu interstellaire étant stable à des échelles de temps nettement plus longues. Parce que les vents stellaires chauds sont ionisés et comportent un grand nombre d'électrons libres, une partie de la lumière sera polarisée par la diffusion sur les électrons.

Prenons un élément du vent situé à la position (r, θ, ϕ) , dans un système de coordonnées sphériques centré sur l'étoile. La source de rayonnement se trouve à $r = 0$, et $\theta = 0$ est dans la direction de l'observateur. Les photons diffusés en (r, θ, ϕ) et redirigés vers l'observateur seront polarisés dans la direction ϕ . Pour un vent homogène et de symétrie sphérique, cette polarisation *locale* passera inaperçue pour l'observateur qui n'observe qu'un rayonnement intégré sur l'ensemble du vent: les polarisations locales s'annuleront exactement, pour donner une polarisation nulle. Cependant, si le vent n'est pas de symétrie sphérique, ou s'il existe des inhomogénéités, il y aura une polarisation résiduelle non-nulle (Haisch & Cassinelli, 1976). De même, s'il existe une seconde source de rayonnement décentrée par rapport au vent, il y aura une polarisation importante, telle qu'observée dans les systèmes binaires d'étoiles massives (McLean 1980).

La polarisation qui résulte de la présence d'un compagnon varie de façon périodique, en fonction de la phase orbitale (e.g. Drissen *et al.* 1986; Schulte-Ladbeck & van der Hucht, 1989). Ceci est dû au fait que la source de rayonnement qui produit la polarisation (le compagnon) se déplace autour de l'enveloppe. Plus généralement, il existe des variations stochastiques dans la polarisation des étoiles WR (Drissen *et al.* 1987), dont l'intensité varie considérablement d'une étoile à l'autre. La figure 1.3 présente les variations dans la polarisation de l'étoile HD 86161 (=WR16). Ces variations sont interprétées comme étant la signature d'un vent inhomogène dont la structure en densité est variable. On suppose que l'écoulement dans le vent est, en moyenne, de symétrie sphérique, mais qu'à un instant donné, le vent comporte un déséquilibre dans la distribution en ϕ , dû à un excès de surdensités locales d'un côté du vent. Il en résulte une

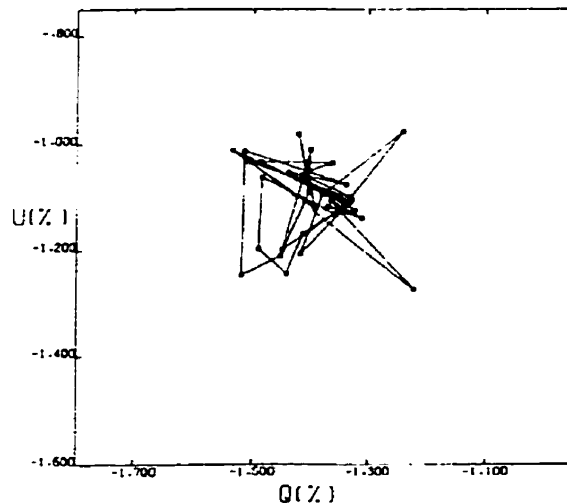


FIGURE 1.3. Polarisation de l'étoile Wolf-Rayet HD 86161 mesurée sur un intervalle de 55 jours. La figure compare les composantes de Stokes Q et U , telles que $Q = \sin 2\phi$ et $U = \cos 2\phi$ où ϕ est l'angle de polarisation dans le plan du ciel. Ces variations stochastiques sont attribuables à l'effet d'un vent inhomogène.

déviation instantanée de la symétrie sphérique (Brown *et al.* 1995). Parce que les fluctuations dans le vent sont stochastiques, la grandeur et l'angle de polarisation varient de façon erratique, comme le montre la figure 1.3.

Une étude des variations polarimétriques dans les étoiles WR de la constellation du Cygne, montre l'existence d'une anti-corrélation du niveau de variabilité avec la vitesse terminale du vent (Robert *et al.* 1989). L'interprétation suggérée est que la structure inhomogène est plus marquée pour les étoiles dont la vitesse du vent est plus faible. Ceci serait une conséquence du fait que les inhomogénéités dans le vent sont générées à partir de la surface, et que leur amplitude croît régulièrement avec le temps. Dans un vent plus rapide, les perturbations s'éloigneraient de l'étoile en un temps plus court, ce qui limiterait d'autant leur croissance. Une autre interprétation pourrait être que le nombre effectif d'éléments inhomogènes est plus petit pour les étoiles à vent lent si, par exemple, l'enveloppe diffusive est également plus petite. En effet, la polarisation résiduelle d'une somme

d'éléments inhomogènes distribués aléatoirement dans un vent est d'autant plus faible que le nombre d'éléments est grand (Richardson *et al.* 1996).

Les variations polarimétriques dans les étoiles WR ont été mises en perspective par rapport aux variations photométriques (Richardson *et al.* 1996). En effet, si les deux phénomènes ont une origine commune, c'est-à-dire l'inhomogénéité du vent, le rapport entre l'amplitude des variations photométriques σ_{phot} et l'amplitude des variations polarimétriques σ_{pol} devrait permettre de contraindre en partie la structure inhomogène. Par exemple, il est en principe possible d'estimer le nombre d'inhomogénéités responsables des variations polarimétriques ainsi que leur densité (Brown *et al.* 1995) à partir du rapport $\sigma_{phot}/\sigma_{pol}$. Or, Richardson *et al.* (1996) ont montré que le rapport $\sigma_{phot}/\sigma_{pol}$ observé pour les étoiles WR ne peut pas être reproduit par un modèle simple de diffusion sur des éléments inhomogènes, car les rapports $\sigma_{phot}/\sigma_{pol}$ observés dépassent la valeur maximale qui est admise par le modèle. Ces résultats suggèrent que les éléments inhomogènes dans le vent n'agissent pas que comme des diffuseurs, et émettent en plus leur propre lumière. Cette conclusion corrobore les résultats de van Genderen *et al.* (1989), qui montrent que les variations photométriques sont accompagnées de fluctuations thermiques. En effet, si les inhomogénéités se comportent comme de simples diffuseurs, on ne devrait pas s'attendre à détecter des variations importantes dans la couleur. Le fait que de telles variations soient observées laisse supposer que les inhomogénéités émettent un excès de rayonnement du fait de leur température plus élevée.

1.2.4 Courbes de lumière des systèmes éclipsants

Lorsqu'une étoile WR se trouve dans un système binaire, et si le plan de l'orbite est suffisamment incliné par rapport à la ligne de visée, le compagnon (généralement de type spectral OB) viendra à passer successivement devant, puis derrière les régions les plus denses du vent de l'étoile WR, situées tout près de

la surface de cette dernière. Le compagnon OB se comporte alors comme une sonde. Lorsqu'il passe derrière l'étoile WR, une partie plus ou moins importante de sa lumière est absorbée en fonction de la densité de colonne (cf. Auer & Koenigsberger, 1994). Lorsque l'étoile OB passe devant, elle occulte à son tour une partie du rayonnement issu du vent de l'étoile WR. Le passage de l'étoile OB permet donc de sonder la profondeur optique du vent à différentes distances de l'étoile WR.

La courbe de lumière d'un système éclipsant WR+OB comporte deux minima (primaire et secondaire), dont l'intensité et la durée varient en fonction de la longueur d'onde. Ceci s'explique par le fait que la température et la densité du vent décroissent en fonction de la distance depuis la surface de l'étoile WR (Hartmann, 1978); le diamètre effectif d'occultation apparaît donc plus petit aux courtes longueurs d'ondes (ultra-violet, optique), alors qu'il est plus grand aux grandes longueurs d'ondes (infra-rouge, millimétrique). À partir des courbes de lumières obtenues sur des bandes étroites allant de l'ultra-violet (UV) à l'infra-rouge (IR), Cherepashchuk *et al.* (1984) ont pu estimer les dimensions du disque effectif de l'étoile WR dans le système binaire V444 Cygni en fonction de la longueur d'onde. Les dimensions dans l'IR (à 2.2μ et 3.5μ) apparaissent effectivement plus grandes que dans l'UV. Mais bien que ce résultat soit en accord qualitatif avec le modèle de Hartmann (1978), le rapport des dimensions mesurées dans l'UV et dans l'IR est beaucoup plus grand que celui prévu par le modèle.

Une étude plus récente par Hamann & Schwartz (1992) confirme le désaccord entre les mesures de l'éclipse de V444 Cygni et un modèle d'éclipse d'un vent stellaire homogène. La figure 1.4 montre la comparaison entre la théorie et les observations. On y voit clairement que les éclipses dans l'infra-rouge (2.2μ et 3.5μ) sont plus larges et plus profondes que celles prédictes par le modèle. Il est cependant possible d'expliquer ce désaccord en supposant que le vent stellaire est inhomogène. En effet, l'opacité dans les régions les plus chaudes du vent est

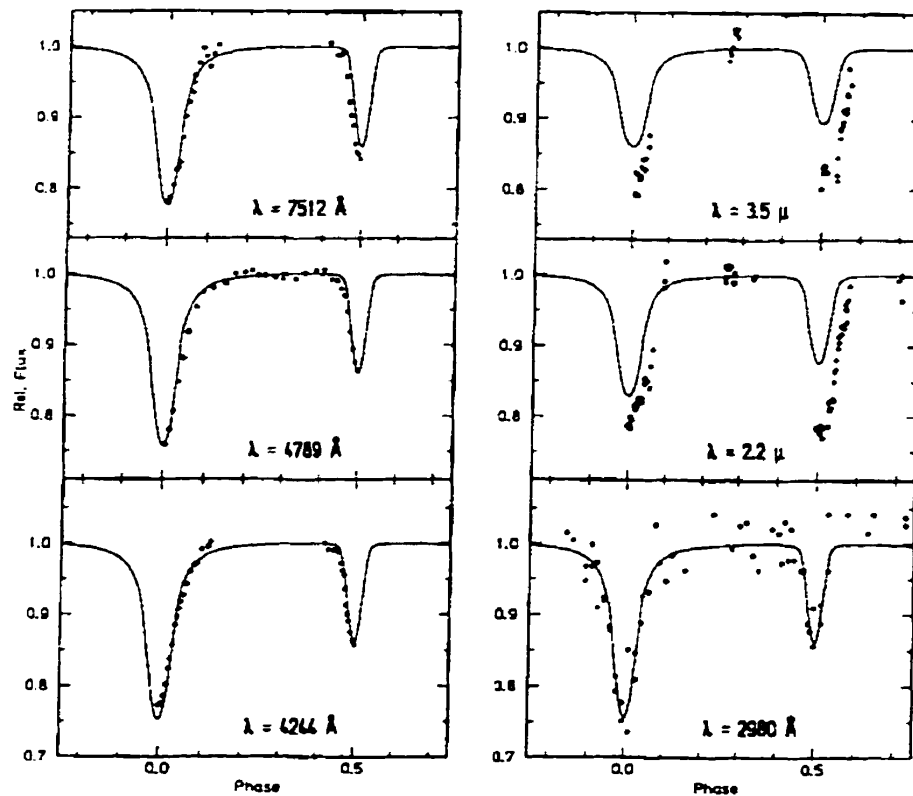


FIGURE 1.4. Comparaison entre la courbe de luminosité observée du système éclipsant V444 Cygni et un modèle d'éclipse d'un vent stellaire homogène. Le système consiste en une étoile WR et une étoile O dont le plan orbital est presque perpendiculaire à la ligne de visée. Le modèle (lignes continues) prédit pour l'infra-rouge (2.2μ et 3.5μ) des éclipses plus étroites et moins profondes que celles observées. Figure tirée de Hamann & Schwarz (1992), d'après les observations de Cherepashchuk *et al.* (1984).

dominée par la diffusion électronique, alors que l'opacité dans les régions plus froides est plutôt dominée par les interactions libre-libre. Or l'opacité de diffusion électronique est directement proportionnelle à la densité, alors que l'opacité libre-libre dépend du carré de la densité locale. Il est donc possible d'accroître l'opacité des régions plus froides sans modifier celle des régions plus chaudes en introduisant des *surdensités locales* dans le vent.

1.2.5 Éclipses momentanées et formation de poussière

Dans l'histoire des observations photométriques des étoiles WR, il existe quelques cas remarquables où l'on a observé une diminution subite dans l'éclat d'une étoile sur un intervalle de temps de quelques jours, et ce sans que le phénomène n'ait été observé précédemment, ni observé à nouveau par la suite. À ce jour, il existe dans la littérature quatre cas répertoriés d'éclipses momentanées, correspondant à des extinctions allant de 0.5 à 1.2 magnitudes photométriques.

La première observation du phénomène a été rapportée par Hjellming & Hiltner (1963), pour l'étoile CV Serpentis (=WR113), une binaire WR+O avec une période de 29,71 jours (Massey & Niemela, 1981). D'abord prise pour une éclipse d'une composante de la binaire par l'autre, le phénomène n'a cependant pas été observé de nouveau dans l'optique, bien qu'il existe un cas rapporté d'une éclipse momentanée dans l'infra-rouge (Williams *et al.* 1977). Le même phénomène a ensuite été observé pour l'étoile HD 164270 (=WR103, réputée sans compagnon) par Lundström & Stenholm (1982). Le phénomène s'est répété de nouveau dans cette étoile, mais seulement 8 ans plus tard (Veen *et al.* 1996). Enfin, une éclipse momentanée a été observée pour l'étoile AS 320 (=WR121) par Veen *et al.* 1998.

Les dernières observations de Veen *et al.* (1998) comportaient des mesures dans cinq bandes de couleurs différentes (photométrie *Walraven*). Les rapports

des extinctions dans ces bandes ont permis de confirmer qu'il s'agissait d'une obscurcation due à de la *poussière*. Veen *et al.* (1998) croient que ces "éclipses" résultent en fait du passage accidentel sur la ligne de visée d'un nuage de poussière se propageant dans le vent. Il y aurait donc un certain nombre de nuages relativement denses de poussière à des distances de l'ordre d'une centaine à un millier de R_{\odot} de la surface de l'étoile. À partir d'un modèle simple de propagation de surdensités locales dans un vent stellaire en expansion, Veen *et al.* (1998) reproduisent assez bien les courbes de lumières des éclipses momentanées (cf. figure 1.5).

La présence de poussière à des distances si courtes de la surface de l'étoile WR est en soi une indication que le vent ne peut pas être homogène. En effet, la formation de poussière ne peut se produire que dans des conditions de densité et de températures qui ne sont pas compatibles avec celles prédictes par les modèles de vent homogène (Cherchneff & Tielens, 1995). Pour que la formation de poussière soit possible, il faut supposer l'existence de surdensités locales importantes, soit sous la forme d'un disque équatorial de compression, soit sous la forme d'inhomogénéités dans le vent (Le Teuff & Cherchneff, 1997).

1.2.6 Excès et variabilité du rayonnement infra-rouge et radio

Une étude détaillée du continu infra-rouge de plusieurs étoiles de type WR, a révélé l'existence d'un désaccord entre l'émission prédicta et celle observée (Rucnacres & Blomme, 1994), sous la forme d'un "excès dans l'excès", c'est à dire une émission IR plus élevée que l'excès prédict par les modèles d'émission libre-libre (voir figure 1.6). Bien que trop faible pour remettre en question l'hypothèse même de l'émission libre-libre, le désaccord est suffisamment important pour que soient révisées les hypothèses secondaires du modèle. En particulier, celle voulant que le vent soit homogène.

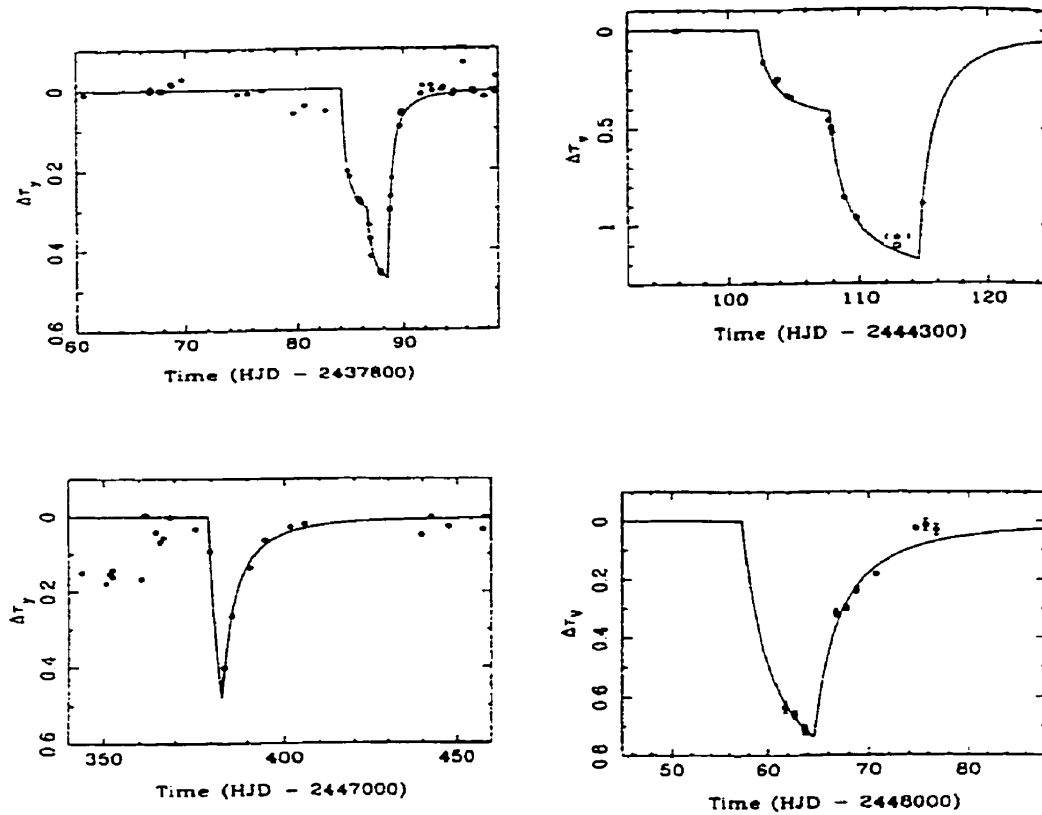


FIGURE 1.5. Éclipses momentanées dans des étoiles WR. Les points montrent les observations de WR113 (en haut à gauche, d'après Hjellming & Hiltner, 1963), WR103 (en haut à droite, d'après Lundström & Stenholm, 1982; en bas à gauche, d'après Veen *et al.* 1996) et WR121 (en bas à droite, d'après Veen *et al.* 1998). Les lignes pleines représentent la modélisation par occultation d'un nuage de poussière passant sur la ligne de visée (Veen *et al.* 1998).

Un modèle d'émission libre-libre dans un vent inhomogène a donc été testé sur les observations (Blomme & Runacres, 1997). Tel que le montre la figure 1.6, ce modèle peut reproduire les déviations dans le continu IR et radio. La raison en est simple: le rayonnement libre-libre dépend du carré de la densité locale du milieu. En introduisant des surdensités, on augmente localement l'émission libre-libre. La fréquence des photons émis étant dépendante de la température locale, et la température étant elle-même fonction de la distance, il suffit d'introduire une surdensité à une distance donnée pour reproduire les petites déviations dans le continu libre-libre (Runacres & Blomme, 1996).

Si l'on croit que les déviations résultent d'un vent inhomogène, on peut également prédire que le continu infra-rouge et radio devraient varier dans le temps. En effet, puisque le vent consiste en une enveloppe de gaz en expansion radiale, les inhomogénéités doivent s'éloigner progressivement de l'étoile. En conséquence, le détail de la structure du vent (densité en fonction de la distance) sera continuellement modifié. On devrait donc s'attendre à observer des variations d'intensité qui soient de l'ordre des déviations observées dans le rayonnement libre-libre. Or, des variations de l'ordre de 20% ont été détectées dans le continu radio (Hogg 1989), sur des intervalles de temps de quelques jours. L'amplitude de ces variations, de même que leur temps caractéristique, sont en accord avec l'existence de structures inhomogènes traversant la zone d'émission du rayonnement libre-libre à une vitesse comparable à la vitesse terminale du vent.

1.2.7 Excès et variabilité du rayonnement X

Les observations en rayons X ont montré que les étoiles O, B et WR émettaient un rayonnement considérable dans ce domaine de longueur d'onde. Wessolowski (1996) a calculé que l'excès du rayonnement X dans l'étoile HD 4004 (=WR1) correspondait à près de 20% de l'énergie totale émise par l'étoile. La spectroscopie en X révèle une courbe d'émission de type corps noir correspondant

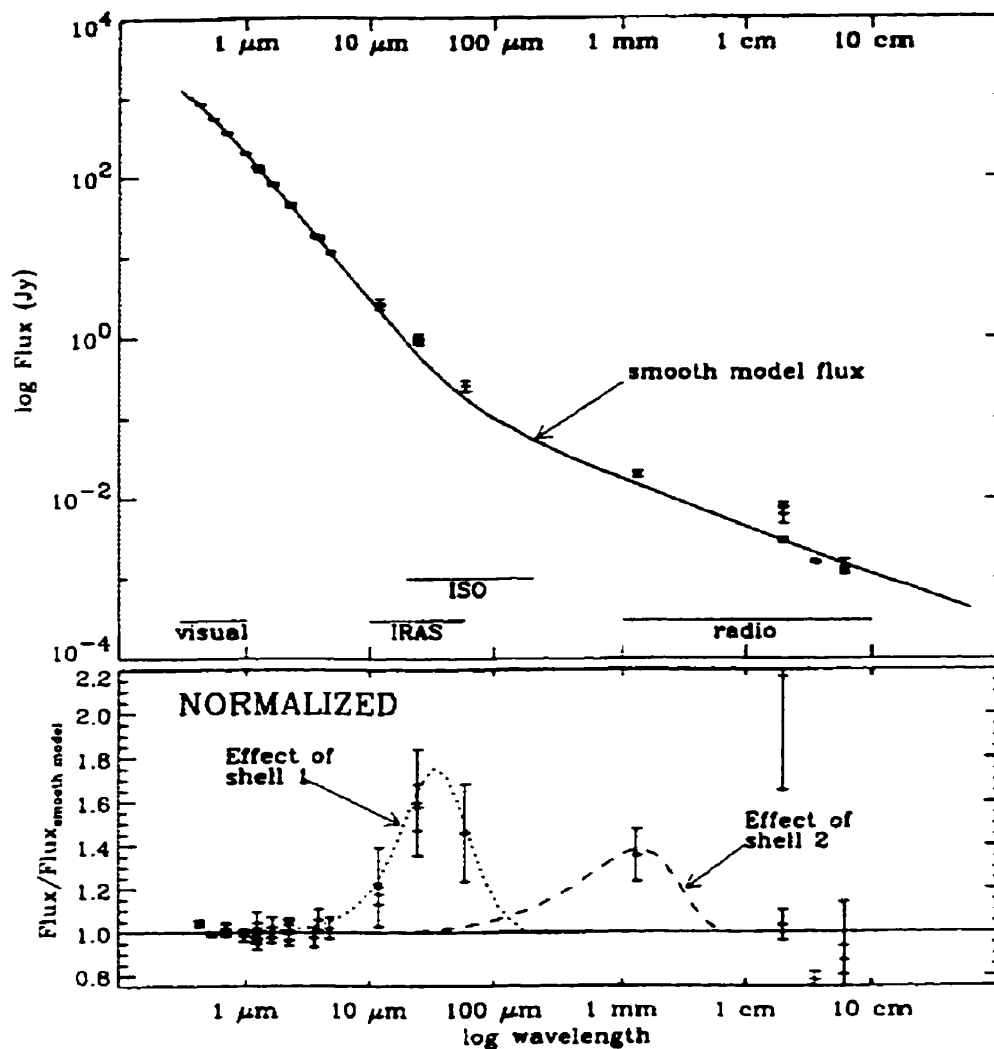


FIGURE 1.6. Excès dans la distribution du rayonnement libre-libre de l'étoile ζ Puppis, de type spectral Of. Les observations montrent un excès dans l'émission IR par rapport à un modèle de vent lisse (schéma du haut). L'excès de rayonnement peut être reproduit si l'on ajoute au vent deux régions en forme de coquille, où la densité est plus élevée ("shell 1" et "shell 2" schéma du bas).

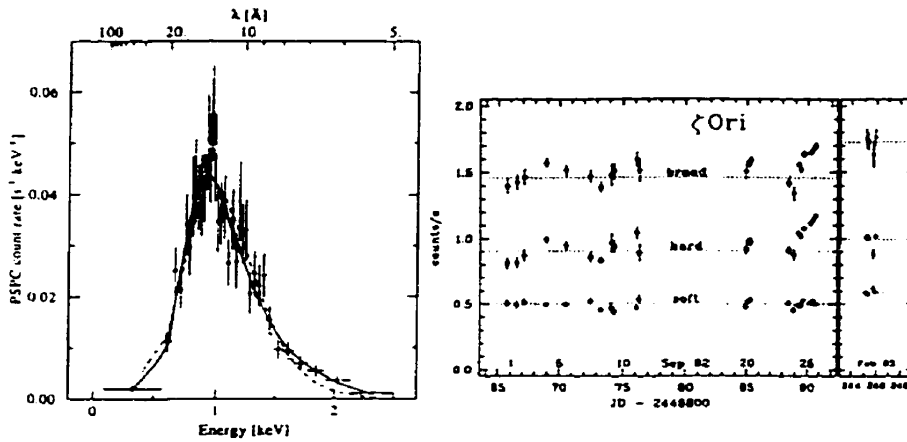


FIGURE 1.7. Excès de rayonnement X observé pour l'étoile HD 4004 (=WR1, panneau de gauche). La courbe montre l'émission attendue pour un corps noir à une température de 2×10^6 K (d'après Wessolowski, 1996). Le panneau de droite montre la variabilité du rayonnement X observée dans l'étoile ζ Puppis, une étoile de type Of (d'après Berghöfer & Schmitt, 1994).

à une température de l'ordre de quelques millions de degrés Kelvins (Wessolowski 1996; cf. figure 1.7). De plus, des séries temporelles d'observations montrent que l'intensité de l'émission X est variable sur des échelles de temps allant de quelques heures à quelques jours (cf. figure 1.7).

Même si l'on sait que la température de surface des étoiles O et WR est probablement très chaude, l'observation de températures de l'ordre de 10^6 K est inattendue. En effet, bien que les régions les plus profondes du vent puissent effectivement être à des températures de cet ordre, les couches supérieures, plus froides, devraient normalement absorber presque complètement le rayonnement X des couches inférieures. Avant que les photons ne puissent s'échapper du vent et se diriger vers l'observateur, ils doivent se trouver à des profondeurs où la température est nettement inférieure à 10^6 K. De plus, s'il s'agissait de l'émission normale du vent, l'on devrait observer un continuum de températures, et non pas un excès à une température fixe.

Un mécanisme proposé pour expliquer les hautes températures associées aux rayons X est la présence d'ondes de choc dans le vent (e.g. MacFarlane & Cassinelli, 1989; Willis & Stevens, 1996), quoique certains modèles théoriques prédisent que de telles ondes de choc produisent des flux en rayons-X insuffisants pour tenir compte des observations (Cooper & Owocki, 1994). Récemment, Feldmeier *et al.* (1997) ont proposé d'expliquer l'excès dans l'émission de rayons-X par la *collision* entre des ondes de choc se propageant dans des directions opposées; leur modèle prédit cependant une variabilité nettement plus importante que celle observée. Cependant, Feldmeier *et al.* remarquent que les simulations en 1D produisent naturellement une variabilité plus élevée que celle à laquelle on peut s'attendre en réalité. En effet, les simulations 1D se ramènent au comportement d'ondes de choc de forme sphérique autour de l'étoile, alors que si l'on suppose que les chocs ont plutôt une extension angulaire $\Delta\Omega$ petite, la variabilité résultante sera d'autant plus réduite que $\Delta\Omega$ est petit. Un plus grand nombre d'arcs de choc distribués aléatoirement a tendance à générer une émission plus uniforme dans le temps que celle associée à quelques ondes de choc sphériques isolées.

1.2.8 Intensité des ailes de diffusion électroniques

Le rayonnement provenant de la recombinaison atomique dans le vent sera en partie diffusé sur les électrons libres. Sous l'effet de la diffusion, une partie de l'énergie du rayonnement sera transférée aux électrons. La lumière diffusée réapparaîtra dans le spectre, mais sera *décalée vers le rouge* à cause de sa perte d'énergie (Castor 1970). Cet effet permet d'expliquer la présence d'*ailes de diffusion électroniques*, qui apparaissent comme une émission résiduelle du côté rouge des raies d'émission des étoiles WR. La diffusion électronique est généralement incluse dans le modèle standard des étoiles WR.

En premier lieu, la diffusion électronique a fourni une explication à certains profils particuliers observés dans les étoiles WR, comme le profil de la raie He

II $\lambda 1640$ de l'étoile HD 50896 (Hillier 1987). Mais alors que la modélisation de raies isolées, dans le cadre du modèle standard, a permis d'obtenir des résultats satisfaisants, la modélisation du spectre en entier a posé certains problèmes. L'utilisation de modèles permettant de simuler un grand nombre de raies d'émission simultanément (analyse spectrale), a montré que les ailes de diffusion électroniques prédictes avaient tendance à être systématiquement plus intenses que dans les spectres observés (e.g. Hillier 1988; Hillier 1989; Hamann *et al.* 1992; Hamann *et al.* 1994). La figure 1.8 montre un exemple tiré de Hamann *et al.* (1994).

Hillier (1991) a montré que l'on pouvait expliquer cet important désaccord dans l'analyse spectrale des étoiles WR en laissant tomber l'hypothèse que le vent est homogène. On l'a vu, la diffusion électronique est proportionnelle à la densité du vent, alors que les processus de recombinaison dépendent du carré de la densité locale. Il en résulte que l'on peut, pour une densité *moyenne* donnée, augmenter l'émission dans la recombinaison en ajoutant des surdensités *locales*, et réduire la fraction de rayonnement diffusée sur les électrons. Cette hypothèse entraîne cependant des conséquences majeures: pour les densités généralement admises pour le vent des WR, l'inclusion des effets d'inhomogénéité pour la modélisation des ailes de diffusion produit des intensités dans les raies d'émission qui sont trop élevées. Il faut donc réduire la densité moyenne du vent (i.e. le taux de perte de masse) par un facteur ~ 3 pour reproduire les spectres observés.

1.2.9 Saturation des profils P Cygni

Un profil de raie d'émission de type P Cygni comporte deux parties principales superposées l'une sur l'autre: une composante large en émission qui est, en première approximation, symétrique autour de la longueur d'onde au repos λ_0 ; une composante en absorption présentant un décalage Doppler vers le bleu par rapport à λ_0 . Pour un vent de symétrie sphérique en expansion radiale avec une vitesse qui croît de façon monotone avec la distance, seul le rayonnement

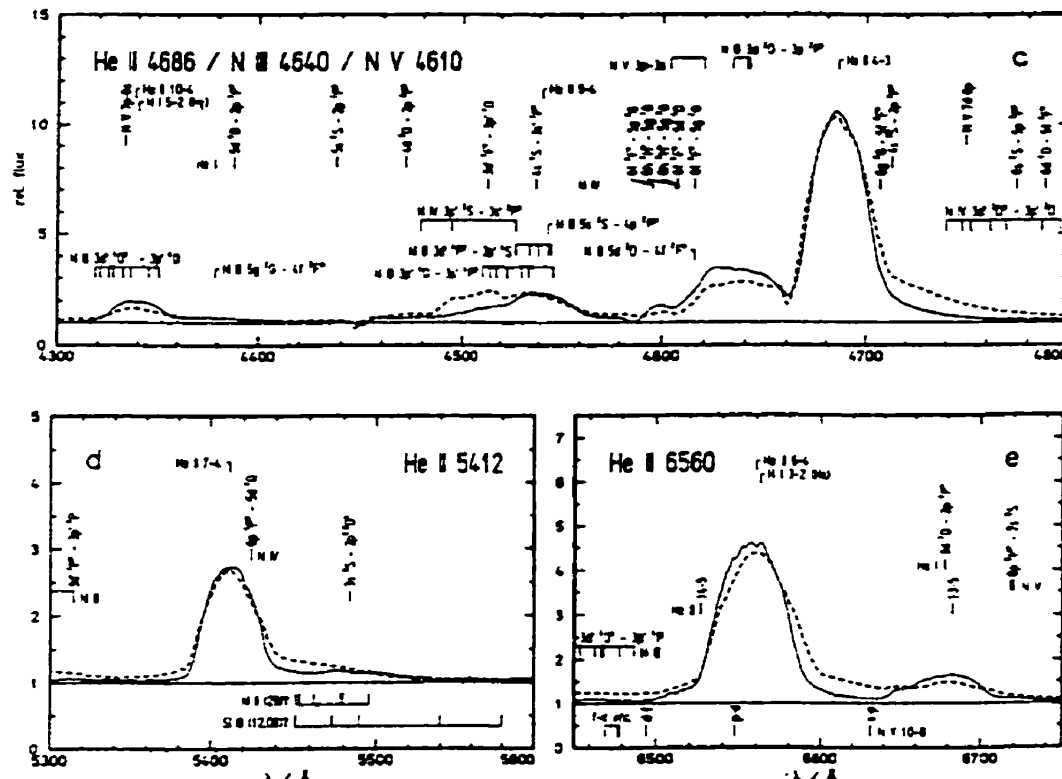


FIGURE 1.8. Comparaison entre le spectre de l'étoile HD 192163 (trait continu) et un spectre synthétique résultant d'un modèle de vent stellaire homogène (trait pointillé). Le spectre synthétique montre des ailes de diffusion électroniques (surélévation à la droite des raies d'émission) qui sont systématiquement plus élevées que dans les observations. Le désaccord peut s'expliquer en postulant l'hypothèse d'un vent inhomogène.

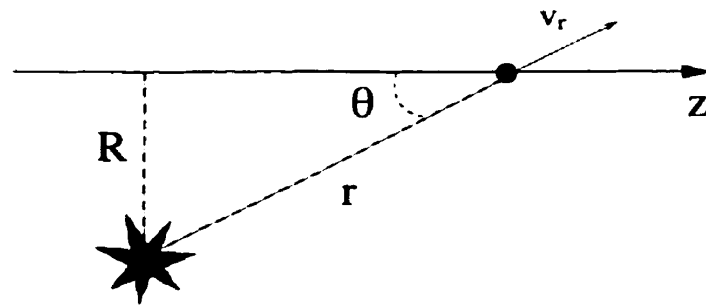


FIGURE 1.9. Géométrie pour les équations 1.6 et 1.7

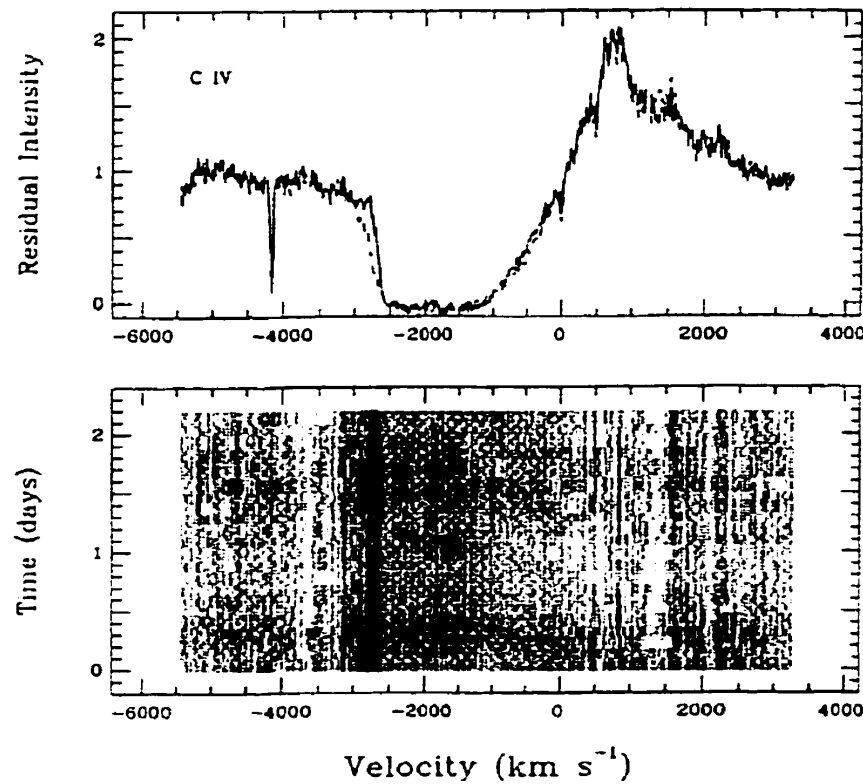


FIGURE 1.10. Saturation dans la partie en absorption d'un profil de type P Cygni (panneau du haut), vraisemblablement dû à l'existence de mouvements turbulents importants dans le vent (tiré de Prinja *et al.* 1992). Le panneau du bas est une série temporelle qui met en évidence des variations dans l'extension vers le bleu de ce profil.

du continu sera affecté par la composante en absorption. En effet, prenons un champ de vitesse $\vec{v}(r, \theta, \phi) = v_r(r)\hat{r}$, pour lequel $v_r(r) > 0$ et la dérivée $v'_r(r) = d/dr v_r(r) > 0$ pour tout $r > 0$. La vitesse projetée sur la ligne de visée $v_\xi(R, z)$, le long d'une droite passant à une distance minimale R de l'étoile (cf. figure 1.9), telle que $z = r \cos \theta$ et $r = \sqrt{R^2 + z^2} = r(R, z)$, est donnée par:

$$v_\xi(R, z) = \frac{z}{\sqrt{R^2 + z^2}} v_r(r(R, z)) . \quad (1.6)$$

Or, la dérivée de la vitesse projetée v_ξ le long de z est:

$$\frac{d}{dz} v_\xi(R, z) = \frac{R^2 v_r(r(R, z))}{(R^2 + z^2)^{3/2}} + \frac{z^2 v'_r(r(R, z))}{R^2 + z^2} \quad (1.7)$$

Sachant que $v_r(r) > 0$ et que sa dérivée $v'_r(r) > 0$, il en résulte que $d/dz v_\xi(R, z) > 0$ et donc que $v_\xi(R, z)$ croît aussi de façon monotone avec z . Ceci implique que, sur une droite parallèle à la ligne de visée, toutes les régions du vent sont *découplées* par rapport au rayonnement monochromatique, dans la limite de Sobolev. La partie en émission d'un profil P Cygni ne devrait donc pas subir l'effet de la composante en absorption. Ceci implique qu'il ne devrait pas y avoir de *saturation* (émission nulle) dans la partie en absorption d'un profil P Cygni car on devrait toujours y détecter une partie de la composante en émission (cf. Lucy 1982).

Or, la spectroscopie des étoiles massives de type O, B et WR montre l'existence de profils P Cygni dont la composante en absorption est saturée (e.g. Prinja *et al.* 1990; Prinja *et al.* 1992), comme le montre la figure 1.10. L'existence de profils P Cygni saturés implique que le champ de vitesse dans le vent n'est pas monotone. En fait, il est possible de reproduire numériquement des profils saturés en incluant dans le modèle une dispersion de vitesse locale de l'ordre de quelques centaines de km s^{-1} (Groenewegen & Lamers, 1989). Selon Owocki (1994), la grandeur de cette vitesse "turbulente" requise pour reproduire les profils saturés est largement supersonique, ce qui doit s'accompagner de fluctuations importantes dans la densité locale du vent. Puls *et al.* (1993) ont montré qu'il était possible de reproduire les profils saturés à partir d'un modèle de vent instable et inhomogène.

1.2.10 Variabilité des profils P Cygni

La composante en absorption des profils P Cygni dépend de la région relativement restreinte du vent qui, du point de vue de l'observateur, est projetée sur le disque de l'étoile. La composante en absorption est donc nettement plus sensible à des fluctuations locales dans la densité que la composante en émission, qui projette une lumière "diluée" sur l'ensemble du vent. Or, alors que des variations dans la composante en émission n'ont pas encore été détectées sans ambiguïté (cf. Kaper *et al.* 1996), la variabilité de la composante en absorption du profil P Cygni des vents stellaires chauds pour des étoiles seules est bien établie. La variabilité des profils P Cygni présente un certain nombre de formes que l'on peut regrouper en quatre classes: les composantes discrètes en absorption (CDA; en anglais DACs, de *Discrete Absorption Components*), les variations dans l'extension vers le bleu, et les modulations périodiques dans l'absorption (MPA; en anglais PAMs, de *Periodic Absorption Modulations*).

Les CDA prennent l'apparence d'un excès dans la partie en absorption, sous forme de composantes étroites se déplaçant systématiquement vers le bleu (Prinja *et al.* 1992). Initialement larges ($\sigma_\xi \sim 1000 \text{ km s}^{-1}$) au moment de leur apparition, elles s'amenuisent à mesure que leur vitesse moyenne s'approche asymptotiquement de v_∞ , la vitesse terminale du vent. Kaper *et al.* (1994) ont montré que les CDA apparaissaient de manière récurrente, sur une échelle de temps de quelques jours. Il semble exister une corrélation entre le temps caractéristique de récurrence τ et la rotation $v \sin i$ de la surface de l'étoile: le temps caractéristique est $1 < \tau < 5$ jours pour les étoiles dont $v \sin i > 250 \text{ km s}^{-1}$, et $10 < \tau < 20$ jours pour les étoiles avec un $v \sin i < 100 \text{ km s}^{-1}$ (Kaper *et al.* 1996). Les CDA réapparaissent donc plus vite pour les étoiles dont la rotation est rapide, ce qui suggère qu'elles résultent de la propagation dans le vent de perturbations générées près de la surface. La figure 1.11 montre un exemple de CDA dans le doublet Si IV $\lambda\lambda 1400$ de l'étoile ξ Per, une étoile de type O.

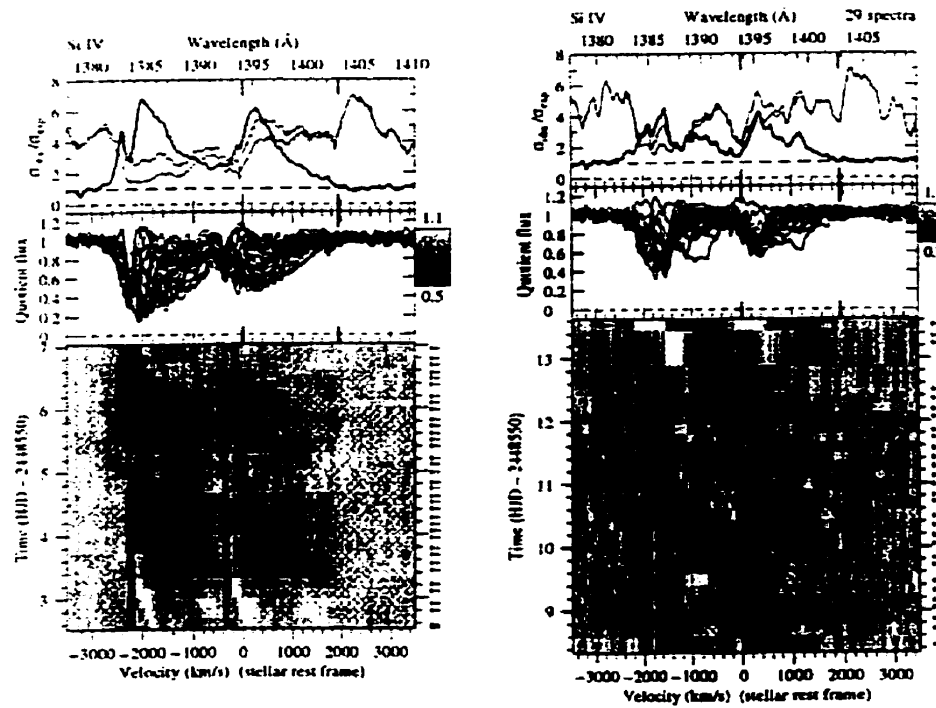


FIGURE 1.11. Composantes discrètes en absorption (CDA) dans les doublets Si IV $\lambda\lambda 1400$ des étoiles ξ Per (à gauche) et HD 34656 (à droite). La figure en tons de gris montre l'excès dans l'absorption en fonction du temps, défini à partir du profil d'absorption minimum. Noter la récurrence du patron sur une période de quelques jours (d'après Kaper *et al.* 1996).

À partir du taux de déplacement $\dot{\xi}$ des CDA dans le spectre, on obtient une estimation de l'accélération radiale dans le vent de la structure responsable de la CDA. Or, les accélération mesurées sont toujours nettement plus faibles que les accélération radiales prédictes par les modèles de vents stellaires (Willis *et al.* 1989). Le désaccord peut s'expliquer par l'idée que la structure responsable de la CDA est constituée de matériaux différents à des temps différents, c'est-à-dire que la structure se déplace par rapport au vent lui-même. Waldron *et al.* (1994) ont montré qu'une *onde de densité* dans un vent stellaire en expansion pouvait reproduire qualitativement le comportement des CDA.

Les variations dans l'extension vers le bleu sont généralement observées dans les profils P Cygni saturés (voir la figure 1.10, panneau du bas). On croit que ce phénomène est tout simplement la signature de CDA dans un profil P Cygni saturé (Prinja *et al.* 1992). Les composantes dans le vent qui provoquent l'apparition des CDA sont invisibles dans la partie saturée du profil, où l'absorption est déjà maximale. Cependant, la limite bleue de la partie en absorption comporte une étroite région non-saturée où la présence d'une CDA peut se faire sentir. De la même façon, certains profils non-saturés, mais où le continu de l'étoile est entièrement absorbé par la composante en émission, peuvent présenter des variations à la limite bleue de l'absorption, sans qu'on y détecte plus directement des CDA (Lamers 1994).

Les MPA n'ont été découvertes que récemment, et grâce à des observations du satellite *International Ultraviolet Explorer*, qui a obtenu des séries temporelles très serrées de spectres ultra-violets de l'étoile HD 64760 (Howarth *et al.* 1995). Il s'agit de fluctuations rapides superposées aux CDA, et qui agissent sur un domaine de longueur d'onde nettement plus grand que ces dernières. Dans la série temporelle des spectres de différence avec le profil maximum (figure 1.12), on voit une perturbation qui apparaît d'abord à des vitesses projetées intermédiaires, avant de se propager rapidement et simultanément vers des vitesses projetées

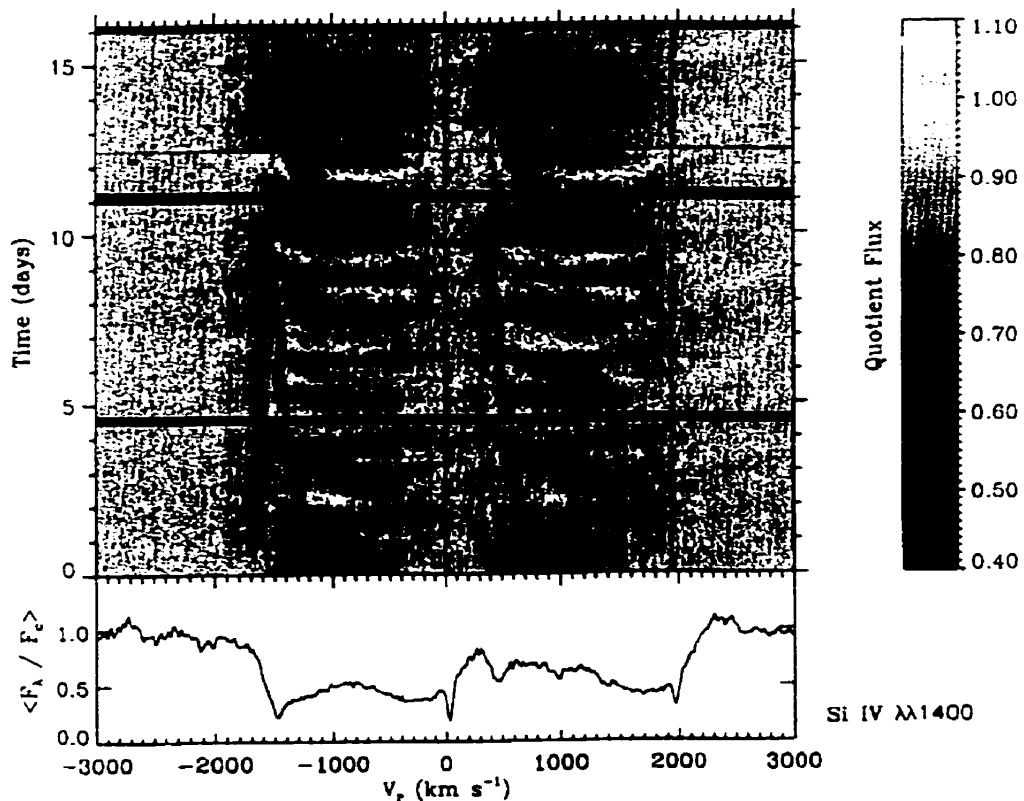


FIGURE 1.12. Modulations périodiques dans l'absorption du doublet Si IV $\lambda\lambda 1400$ de l'étoile HD 64760 (d'après Massa *et al.* 1995). Ces modulations se produisent sur des intervalles de temps plus brefs que les CDA et apparaissent nettement plus larges dans le spectre. Noter la présence d'une CDA étroite se propageant de $v_r = -1000 \text{ km s}^{-1}$ à $v_r = -1500 \text{ km s}^{-1}$.

plus lentes et plus rapides, en laissant une trace ayant vaguement la forme d'un "sourire". Owocki *et al.* (1995), ont émis l'hypothèse que les MPA sont la signature de régions d'interaction en co-rotation (RICs; en anglais CIRs, de *Co-rotating Interacting Regions*). Les RICs seraient le résultat de la propagation dans le vent de perturbations générées au dessus d'un *point chaud* de la surface. La rotation de l'étoile produirait un patron d'ondes de choc en forme de spirale (Cranmer & Owocki, 1996). C'est l'occultation de la surface du disque par une de ces spirales, plus denses que le milieu ambiant, qui produirait les fluctuations rapides des MPA, et qui expliquerait leur forme un peu particulière.

Globalement, on constate que les trois phénomènes (CDA, MPA, variations de la limite vers le bleu de la saturation) peuvent s'interpréter dans le même contexte d'ondes de densité, ou d'ondes de choc, produites à partir de perturbations générées près de la surface de l'étoile. Apparemment, des fluctuations dans la grandeur de la force radiative provoquées par l'alternance de régions plus ou moins chaudes à la surface, dégénéreraient en fluctuations à grande échelle dans le champ de vitesse et de densité du vent.

1.2.11 Variabilité des raies d'émission

Il existe de nombreuses observations montrant l'existence de variations dans les profils de raie d'émission des étoiles de types WR et O. On peut regrouper les variations observées en trois classes phénoménologiques: les variations périodiques (que je désigne sous le nom de type P), les variations récurrentes (type R) et les variations stochastiques (type S).

Les variations de type P sont observées dans les étoiles membres de systèmes binaires, où elles sont modulées avec la phase orbitale. Elles apparaissent sous la forme d'une ou plusieurs composantes en émission qui se superposent au profil "standard" de la raie, et qui se déplacent sur le spectre selon un mouvement de va-

et-vient (Moffat 1996a; Thaller, 1998). La dépendance avec la phase orbitale, et le fait que ces variations apparaissent dans les binaires serrées (i.e. où la séparation entre les composantes est relativement petite), suggère que l'excès d'émission vient d'une région où les vents de chacune des étoiles du système entrent en collision l'un avec l'autre (Marchenko *et al.* 1995). L'analyse de Luehrs (1997) montre que l'on peut reproduire qualitativement la forme des variations de type P en supposant que l'excès d'émission provient d'une région en forme de cône, qui définit la zone de collision entre les vents. La forme particulière des variations dépend alors des paramètres de l'orbite et de l'inclinaison du plan orbital.

Les variations de type R n'ont jusqu'ici été observées que dans 3 étoiles WR apparemment seules: HD 191765 (Vreux *et al.* 1992), EZ CMa (St-Louis *et al.* 1995; Morel *et al.* 1997), et HD 4004 (Morel *et al.* 1998a). Elles prennent la forme de composantes (sous-pics) en émission relativement larges ($\sigma_\xi \sim 200 - 500$ km s $^{-1}$) qui se déplacent sur le profil de la raie, dessinant un patron qui se répète à des intervalles de quelques jours (e.g. McCandliss *et al.* 1994). Un sous-pic en émission persiste généralement pendant ~ 10 heures, période au cours de laquelle il se déplace sur une certaine distance avant de disparaître (voir figure 1.13). Le sous-pic semble ensuite réapparaître de façon récurrente. L'origine de ces variations est encore mal comprise, et diverses hypothèses ont été proposées, allant de l'effet d'un compagnon compact immergé dans le vent (Drissen *et al.* 1989), à l'existence d'un jet bipolaire (Vreux *et al.* 1992). Récemment, Morel *et al.* (1998a) ont suggéré d'interpréter ce type de variation dans le cadre de la rotation d'un *vent structuré*. Cette hypothèse veut que le vent généré à la surface de l'étoile puisse être divisé en secteurs présentant des vitesses et des densités différentes. La rotation du vent fait alors en sorte que l'observateur voie successivement des vents de différentes vitesses et densités sur la ligne de visée. La collision entre un vent plus lent et un vent plus rapide génère possiblement des instabilités à grande échelle.

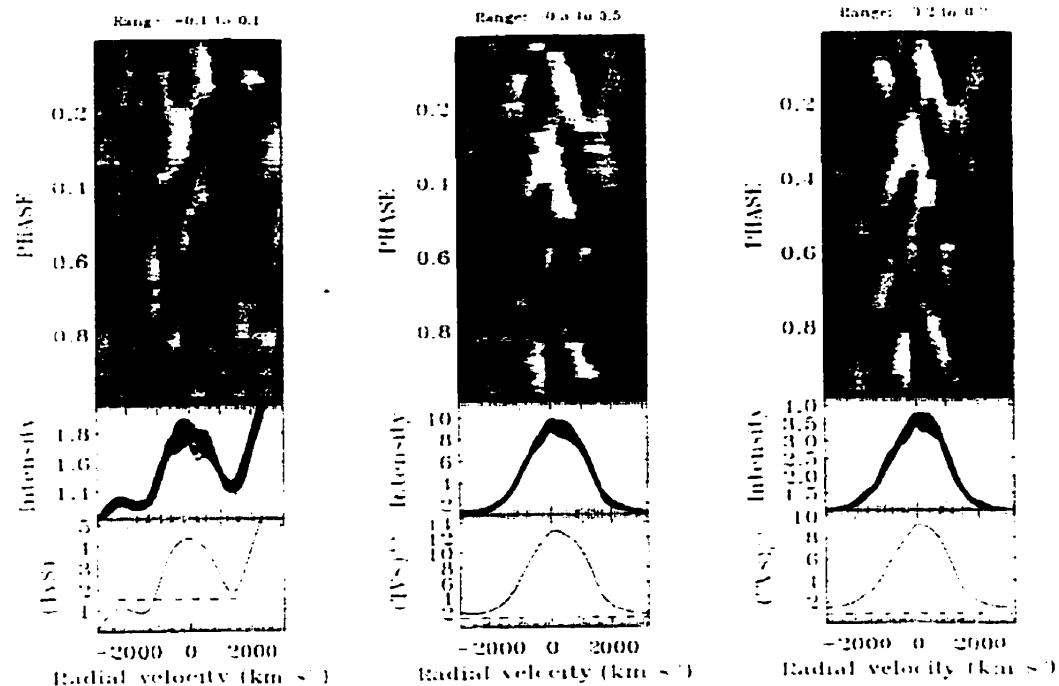


FIGURE 1.13. Variations de type R dans les raies d'émission He II λ 6560, He II λ 4686 (centre) et N IV λ 4058 (droite) de l'étoile EZ CMA. La figure montre une série temporelle de spectres de différence avec le spectre moyen, représentée en fonction de la phase suivant la période de 3,77 jours. Cette figure combine un ensemble de spectres obtenus sur 19 jours, c'est à dire 5 périodes complètes. Noter que le temps s'écoule du haut de la figure vers le bas (d'après Morel *et al.* 1997).

Les variations de type S sont généralement observées dans les profils larges des raies d'étoiles WR, seules ou avec un compagnon (Robert 1992). Récemment, des variations similaires ont été détectées dans le vent de l'étoile ζ Puppis, une étoile de type Of (Eversberg *et al.* 1998a), ainsi que dans le vent de l'étoile BD+30°3639, une étoile centrale de nébuleuse planétaire (Acker *et al.* 1997). Il semble jusqu'ici que ces variations soient systématiquement détectées chaque fois qu'une raie d'émission d'une étoile chaude est observée avec une très haute résolution (typiquement $\Delta\lambda \lesssim 0.1$ Å), et un très haut rapport signal sur bruit dans le continu ($S/B \gtrsim 500$). Les variations de ce type apparaissent sous la forme de sous-pics en émission relativement étroits ($\sigma_\xi \sim 100$ km s⁻¹) qui semblent se déplacer sur le sommet des raies d'émission en se mouvant systématiquement du centre de la raie vers les bords (Robert 1994). Aucune récurrence des patrons de variation dessinés par ces sous-pics n'a encore été mise en évidence. La largeur moyenne des sous-pics en émission dans une raie est toujours approximativement la même, et ne dépend ni de l'étoile, ni de la raie d'émission observée. De plus, les sous-pics semblent être systématiquement plus étroits au centre de la raie que près des bords (Robert 1992). La figure 1.14 montre le détail des variations de type S dans la raie d'émission C III $\lambda 5696$ de l'étoile Wolf-Rayet HD192103.

La cinématique particulière des sous-pics variables est caractéristique d'éléments inhomogènes dans une enveloppe en expansion radiale vue en projection. Moffat *et al.* (1989) ont d'abord proposé que les sous-pics stochastiques soient la signature de nuages denses éjectés à partir de la surface et se propageant dans le vent. Par la suite, sur la base de la théorie des vents stellaires chauds prédisant l'existence d'instabilités dynamiques (Owocki 1994), il a été suggéré d'interpréter les sous-pics stochastiques comme la signature d'inhomogénéités se formant spontanément dans le vent, et possiblement associées à des processus de dissipation turbulente (Moffat *et al.* 1994; Henriksen 1994).

Les raies d'émissions présentent certains avantages sur les profils P Cygni

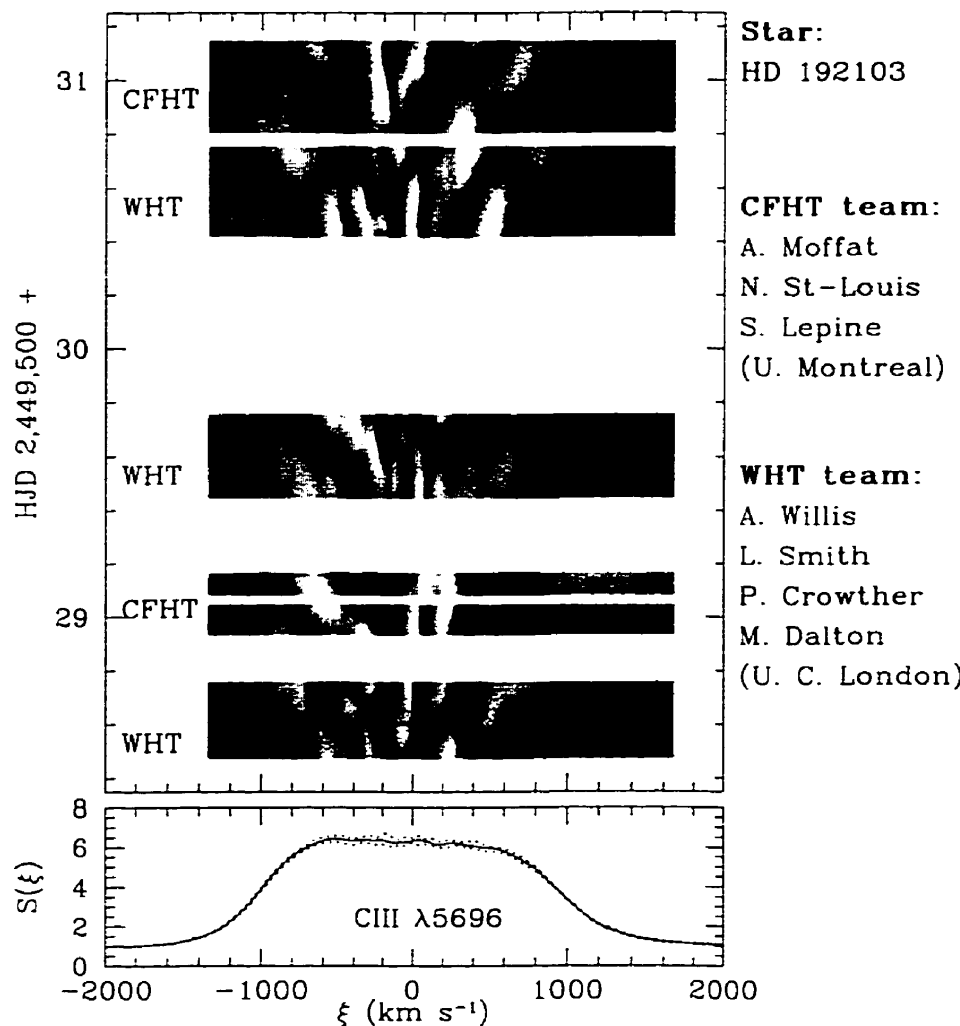


FIGURE 1.14. Séries temporelles montrant des variations de type S dans la raie d'émission C III $\lambda 5696$ de l'étoile HD192103. Cette série combine des observations prises aux télescopes Canada-France-Hawaii (CFHT) et William-Herchel (WHT). Le temps s'écoule du bas de la figure vers le haut. Cette figure est tirée d'un article en préparation par Lépine *et al.* 1998.

pour l'étude de la structure inhomogène du vent. D'abord, elles permettent de sonder le vent dans son ensemble, alors que la partie en absorption des profils P Cygni n'est sensible qu'à une région du vent nettement plus restreinte. D'un autre côté, les grandes vitesses impliquées permettent de résoudre séparément un certain nombre de régions du vent dont les vitesses projetées sont différentes; les raies d'émission donnent une information sur la structure *angulaire* du vent. De plus, chaque raie d'émission dans le spectre d'une étoile se forme à une profondeur particulière dans le vent, à cause de l'existence d'un fort gradient d'ionisation (Schulte-Ladbeck *et al.* 1995). L'observation simultanée des variations stochastiques dans différentes raies d'une même étoile, permet donc d'étudier la structure inhomogène dans la direction *radiale* en plus de pouvoir observer la propagation des éléments inhomogènes à travers le vent (e.g. Paper I).

Cependant, il existe un certain nombre de complications qui limitent l'information que l'on peut tirer de la variabilité des profils en émission. Un des effets majeurs vient de ce que des inhomogénéités se trouvant dans des régions bien distinctes du vent peuvent néanmoins posséder la même vitesse projetée, et ainsi se superposer accidentellement sur le profil de la raie. L'examen systématique des variations de type S et leur interprétation dans le contexte d'un vent stellaire inhomogène sont les sujets de cette thèse de doctorat.

CHAPITRE 2

WIND INHOMOGENEITIES IN WOLF-RAYET STARS. I. SEARCH FOR SCALING LAWS USING WAVELET TRANSFORMS

The Astrophysical Journal, **466**, 392 (1996)

Wind Inhomogeneities in Wolf-Rayet Stars. I. Search for Scaling Laws Using Wavelet Transforms.

Sébastien Lépine,¹ Anthony F.J. Moffat,¹ and Richard N. Henriksen²

Received 1995 December ; accepted 1996 February

Article submitted to the Astrophysical Journal main section.

¹ Département de Physique, Université de Montréal, C.P. 6128, Succ. Centre-Ville, Montréal, Québec, Canada, H3C 3J7; and Observatoire du Mont Mégantic.

² Astronomy group; Dept of Physics, Queen's University, Kingston, ON, K7L 3N6 Canada.

ABSTRACT

We describe a new technique involving wavelet transforms for analyzing discrete stochastic components like those found on the tops of emission lines in Wolf-Rayet stars. A *wavelet power spectrum* is used to characterize the variable component of the emission line we believe to arise from the superposition of many individual gaussian-like subpeaks. This was applied to emission line spectra of eight Wolf-Rayet stars obtained at CFHT and ESO. Where the data show the most power, we identify a *dominant scale*, which is found to be very similar in all but one of the stars in our sample.

We present a phenomenological model where the variable structure on top of the emission line is represented by a sum of individual subpeaks of the same simple shape (gaussian or triangular) and various scales. This model is used to introduce the idea of *scaling laws*. The amplitude A and number density N of subpeaks on a given scale are related to their characteristic width σ (i.e. velocity dispersion) by scaling relations, of which the simplest form is a power law: $A \sim \sigma^\alpha$ and $N \sim \sigma^\beta$. The wavelet power spectrum is used to verify the consistency of this model with the data. Synthetic signals are generated, and their wavelet spectra are compared to those of the data. This provides a constraint on the value of $2\alpha + \beta$, which is found to be $\sim 2.7 \pm 0.5(\sigma)$ for the model involving gaussians, or $\sim 3.4 \pm 0.6(\sigma)$ for the model involving triangles. The implications provided by this new constraint are discussed.

Subject headings: stars: hot, Wolf-Rayet — winds — techniques: wavelets

2.1 Introduction: Why Use Wavelets?

It was already suggested by Antokhin, Kholtynin & Cherepashchuk (1988), on the basis of *indirect* evidence by Cherepashchuk, Eaton & Khaliullin (1984), that the strong stellar winds of Wolf-Rayet stars could be made up of dense clouds immersed in a rarefied inter-cloud medium. Attempts were made by Antokhin, Nugis & Cherepashchuk (1992) to reproduce He line profiles using an inhomogeneous wind model. Likewise, the need for some kind of *clumping* in the wind of Wolf-Rayet stars in order to reproduce electron scattering wings better was pointed out by Hillier (1991). He showed that an inhomogeneous wind required lower mass-loss rates than a homogeneous wind to reproduce line strengths accurately.

Systematic *direct* observation of variable subpeaks on the tops of broad emission lines in Wolf-Rayet stars was first made by Moffat *et al.* (1988) and McCandliss (1988). An extensive study of emission line subpeaks in many Wolf-Rayet stars of different subclass was then carried out by Robert (1992). Careful analysis of individual subpeaks identified in the latter work, combined with simple physical assumptions, led Moffat *et al.* (1994) to suggest a phenomenological model for the inhomogeneous component of the wind using scaling laws. This was used by Moffat & Robert (1994) to suggest a possible factor ~ 3 decrease in mass-loss estimates in Wolf-Rayet winds based on common density-squared dependent emission mechanisms, on the assumption of a fully clumped wind. A review on the observation of inhomogeneities and the information they can provide about the wind was made by Brown *et al.* (1995).

The present work is an attempt to test the assumption of scaling laws in the inhomogeneous component of Wolf-Rayet winds, as revealed by the presence of subpeaks on the tops of emission lines. Wavelet analysis techniques are developed and used to compare the observations to a simple phenomenological model invol-

ving scaling laws.

In previous work that led to the scaling-law hypothesis (Robert 1992; Moffat et al. 1994), individual structures were identified and extracted using multi-gaussian fits and wavelet convolutions, respectively. A statistical analysis of these extracted structures then uncovered relations reminiscent of those used in describing supersonic compressible turbulence in giant molecular clouds (e.g. Henriksen 1991), where full-scale clumping is thought to be the rule. However, because they arise in an optically thin medium (the outer part of the wind) and because they are assumed to be distributed with spherical symmetry around the star, the spectroscopic subpeaks in Wolf-Rayet emission lines are always seen in *projected velocity* space and are subjected to superposition effects. For example, two spatially distinct inhomogeneities could have the same *projected* velocity and thus appear as a single subpeak in the spectrum. This effect can introduce a bias in the statistical analysis involving extracted *apparent* subpeaks, because several spatially distinct inhomogeneities with small velocity dispersion (σ_v) may appear as a single (unresolved) subpeak having larger σ_v in projected velocity space. Possibly, one might benefit from using a technique that avoids the identification of individual structures, being sensitive only to the general profile produced by a collection of subpeaks.

Another problem is the presence of instrumental and statistical *noise*. When extracting individual structures, the noise may artificially introduce a large number of small-scale features. These would be difficult to distinguish from real small-scale subpeaks. Not knowing exactly the threshold for intrinsic small-scale structure identification is a problem, because scaling relations depend critically on the presence of small scale components.

In an attempt to avoid these pitfalls (i.e. noise and superposition effects), a wavelet analysis method is developed to study the variable components of WR emission lines.

The *wavelet transform* is a technique, analogous to the Fourier transform for periodic data, that is well-adapted to the study of non-periodic variable signals. In astronomy, it has found applications in the study of time-series photometry of variable stars (Szatmáry, Vinkó & Gál, 1994), and in the study of hierarchical structures in molecular clouds (Gill & Henriksen, 1990), and galaxy distributions (Slezak, De Lapparent & Bijaoui, 1993; Martínez, Paredes & Saar, 1993). It is also used as an objective, multi-scale structure identifier (Slezak, Durret & Gerbal 1994).

In the present study, the wavelet transform is used to evaluate the *wavelet power spectrum*, which can give valuable statistical information on a random distribution of subpeaks, including any additional feature such as noise. The method leads to a clear identification of the noise threshold. The power spectrum is then used as a comparative tool for testing phenomenological models involving scaling laws. This adds new constraints on the clumping hypothesis for Wolf-Rayet winds. We discuss how new observations should be carried out in order to confront existing models better.

2.2 The Wavelet Analysis

About twelve years ago, wavelet transforms began to be used as an alternative to Fourier transforms in the case of non-periodic signals (see Farge 1992; Daubechies 1992). The advantage of wavelets as analyzing functions is that they are well localized in space, as opposed to Fourier-based functions (sine waves) which oscillate indefinitely over all space. Two conditions must be fulfilled by some real function $\psi(x)$, in order for it to be used as a wavelet: (1) its mean must be zero, i.e.

$$\int_{-\infty}^{\infty} \psi(x)dx = 0,$$

and (2) it must be well localized in space.

A commonly used wavelet (e.g. Argoul *et al.* 1989) is the so-called *Mexican hat*, which is the second derivative of a Gaussian:

$$\psi(x) = (1 - x^2)e^{-x^2/2}.$$

This function satisfies both the above conditions.

From the function $\psi(x)$, also known as the *mother wavelet*, we generate a *wavelet family* $\psi_{b,a}(x)$ by successive *translation* (parameter b) and *dilation* (parameter a) of the mother wavelet, i.e.:

$$\psi_{b,a}(x) = \frac{1}{a}\psi\left(\frac{x-b}{a}\right).$$

This is analogous to the definition of the Fourier function, which is expressed in terms of variations in *phase* and *frequency* in a convolution with a sine wave. The difference is that a wavelet family occupies a two-dimensional parameter space, instead of $\sim 1\frac{1}{2}$ for Fourier parameter space (the phase giving the spatial *origin* only). Thus, precise information about the exact *location* of a feature can be obtained concisely when using a wavelet basis. A Fourier basis needs an infinitely broad spectral regime.

The *continuous wavelet transform* $\tilde{f}(b, a)$ of a one dimensional signal $f(x)$ using a wavelet family $\psi_{b,a}(x)$ is simply:

$$\tilde{f}(b, a) = \int_{-\infty}^{\infty} f(x)\psi_{b,a}(x)dx. \quad (2.1)$$

Its inverse is given by the *wavelet reconstruction theorem*:

$$f(x) = \frac{1}{C_\psi} \int_{-\infty}^{\infty} \int_0^{\infty} \tilde{f}(b, a) \psi\left(\frac{x-b}{a}\right) \frac{dadb}{a}. \quad (2.2)$$

C_ψ is a constant determined by the choice of mother wavelet form:

$$C_\psi = 2\pi \int_0^{\infty} \xi^{-1} |\hat{\psi}(\xi)|^2 d\xi.$$

Here, we denote $\hat{\psi}(\xi)$ as the Fourier transform of $\psi(x)$:

$$\hat{\psi}(\xi) = \frac{1}{\sqrt{2\pi}} \int_{-\infty}^{\infty} e^{-ix\xi} \psi(x) dx.$$

Note that the continuous wavelet transform of a 1D signal is expressed in 2D. As a consequence, there is some redundancy of information in *wavelet space*, i.e. a single subpeak of a given scale shows a wavelet response over neighboring scales (cf. Fig.1). This redundancy turns out to be useful, however, because it makes the wavelet transform almost independent of the form of the mother wavelet. For example, the signal can be reconstructed from its wavelet transform using a different mother wavelet function (cf. Daubechies 1992). For some specific wavelet families, including the Mexican-hat family, the delta function can be used as a reconstruction basis, thus making the reconstruction theorem simpler:

$$f(x) = \frac{1}{C'_\psi} \int_{-\infty}^{\infty} \int_0^{\infty} \tilde{f}(b, a) \delta(x - b) \frac{dadb}{a} = \frac{1}{C'_\psi} \int_0^{\infty} \tilde{f}(x, a) \frac{da}{a}, \quad (2.3)$$

with the normalization constant becoming

$$C'_\psi = 2\pi \int_0^{\infty} \xi^{-1} \hat{\psi}(\xi) \hat{\delta}(\xi) d\xi = \sqrt{2\pi} \int_0^{\infty} \xi^{-1} \hat{\psi}(\xi) d\xi.$$

The wavelet transform is in many ways comparable to the *Windowed Fourier Transform* (WFT), but much more efficient. We recall that the WFT is obtained by using the Fourier transform over some restricted domain of a signal, as defined by some aperture, the so-called *window*. The position of this window can be used as an extra parameter, keeping information about location while a local determination of Fourier coefficients is made. The main problem with the WFT is that the arbitrarily chosen size of the window is kept constant. Obviously, some advantage would be gained if we could automatically adapt the size of the window with the frequency of the analyzing function, for example by optimizing the wavenumber(k)-position(x) uncertainty relation $\Delta x \Delta k = 2\pi$. This is what the wavelet transform achieves; it is an improved WFT in which the size of the window (the scale) is *automatically* adapted to the frequency used.

Wavelet transforms can also be described as pass-band frequency filters. Filtering properties can be inferred from the wavelet reconstruction theorem: instead of integrating over the domain $0 < a < \infty$ (Eq.3), one could integrate

over any interval $a_1 < a < a_2$. This removes the components of the signal having scales outside this interval (see Fig.1). This capacity of zooming in to any given scale, only keeping components relevant to that scale, leads to applications in fractal analysis.

If exact information about location is of no great relevance (e.g. features are randomly distributed), scaling information may be easily obtained using the *Wavelet Power Spectrum* (WPS). We define the wavelet power spectrum $W_{b_1, b_2}(a)$ of any function $f(x)$ over some spatial domain $[b_1, b_2]$ as the integration of the square of the wavelet transform over that domain:

$$W_{b_1, b_2}(a) = \int_{b_1}^{b_2} [\tilde{f}(b, a)]^2 db. \quad (2.4)$$

The dependence of W_{b_1, b_2} on the parameter a will be used to characterize the scaling behavior of the function $f(x)$ over the spatial domain $[b_1, b_2]$.

2.3 Scaled Distributions and the Power Spectrum

Wavelet analysis will be especially efficient when one has a signal made up of discrete components of various sizes. This appears to be the case for the variable component on top of Wolf-Rayet emission lines (Robert 1992). From the data, however, it is unclear if and how these components are organized. We attempt to model the data using the simplest phenomenological approach that comes to mind. Our model describes the signal as arising from a sum of randomly distributed Gaussian-like subpeaks having different widths and amplitudes.

Let $I(x)$ be a signal arising from the superposition of N Gaussian-like structures having some fundamental shape $g(x)$. Let these structures be parameterized by their individual width σ_j , intensity amplitude A_j , and location x_{ij} . If we assume that we have N_j structures of width σ_j then:

$$I(x) = \sum_j \sum_{i=1}^{N_j} A_j g\left(\frac{x - x_{ij}}{\sigma_j}\right). \quad (2.5)$$

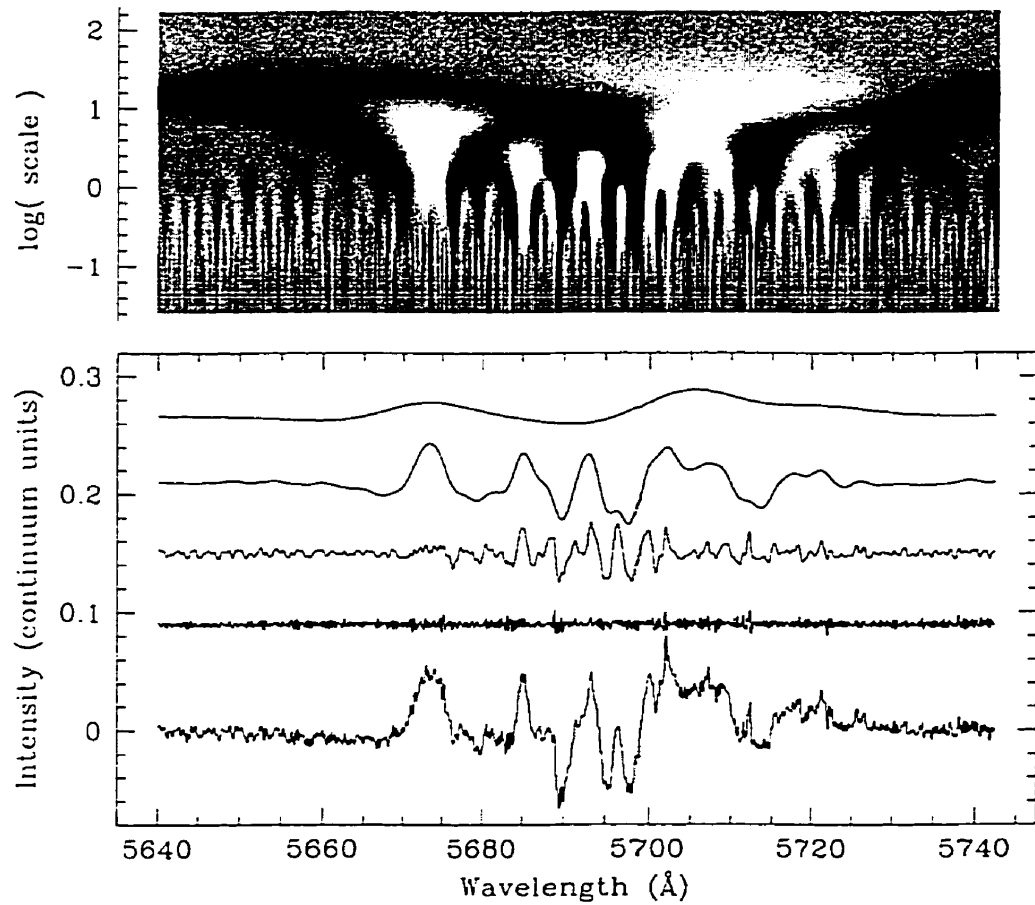


FIGURE 2.1. The top section shows the wavelet transform of a difference spectrum of the star WR137. The bottom section shows the same difference spectrum (bottom curve) decomposed into different scale components by using wavelet filtering. Upwards from the bottom curve are integrations of the wavelet transform over scale intervals (in \AA) $[a_1, a_2] = [0.02, 0.13]$, $[0.13, 0.8]$, $[0.8, 5.0]$, and $[5.0, 32.0]$, respectively.

Here we have made the simplifying assumption that all N_j structures with width σ_j have the same amplitude A_j (e.g. Fig. 2).

It appears plausible to describe this signal using simple, general *scaling relations*. Assuming a continuous distribution over all possible scales σ , we may rewrite $[A_j, N_j]$ as $[A(\sigma), N(\sigma)]$ and use scaling relations such as the power laws:

$$A(\sigma) = K_a \sigma^\alpha \quad (2.6)$$

$$N(\sigma) = K_b \sigma^\beta, \quad (2.7)$$

which are dependent on the four parameters K_a, α, K_b and β .

Given the conclusions from the previous studies of Wolf-Rayet emission line subpeaks (Robert 1992; Moffat *et al.* 1994; Moffat & Robert 1994) this is reasonable as a working model, to the extent that no difficulties have been encountered yet with it. Previous estimates led to $\alpha \sim 1.0$, $\beta \sim -3.6$, for the extracted subpeaks¹. We will now show how α and β can be more objectively constrained using the WPS.

The total flux $F(\sigma)d\sigma$ emitted by all the blobs in the range $[\sigma, \sigma+d\sigma]$ should, according to our model, correspond to:

$$F(\sigma)d\sigma = N(\sigma)A(\sigma)\sigma d\sigma = K_a K_b \sigma^{\alpha+\beta+1} d\sigma. \quad (2.8)$$

However, we do not expect the piling up of a large number of structures in a signal to be directly detected by the wavelet analysis, only the resulting deviations from the mean. This can be understood by noticing that the wavelet transform of a single gaussian has zero mean. Because it is a linear transformation, the wavelet transform of a set of superposed gaussians is the sum of their individual wavelet

¹From the scaling relations $f \sim \sigma^{2.0 \pm 0.4(s.d.)}$ (Moffat *et al.* 1994) and $N(f) \sim f^{-2.3 \pm 0.8(s.d.)}$ (Robert 1992), where $f = A\sigma$. The standard deviation (s.d.) is based on the scatter for a typical star for $f(\sigma)$ and among several stars for $N(f)$. One finds $A \sim \sigma^{1.0 \pm 0.4(s.d.)}$ and $N(\sigma) \sim \sigma^{-3.6 \pm 0.8(s.d.)}$, i.e. $\alpha = 1.0 \pm 0.4(s.d.)$; $\beta = -3.6 \pm 1.6(s.d.)$.

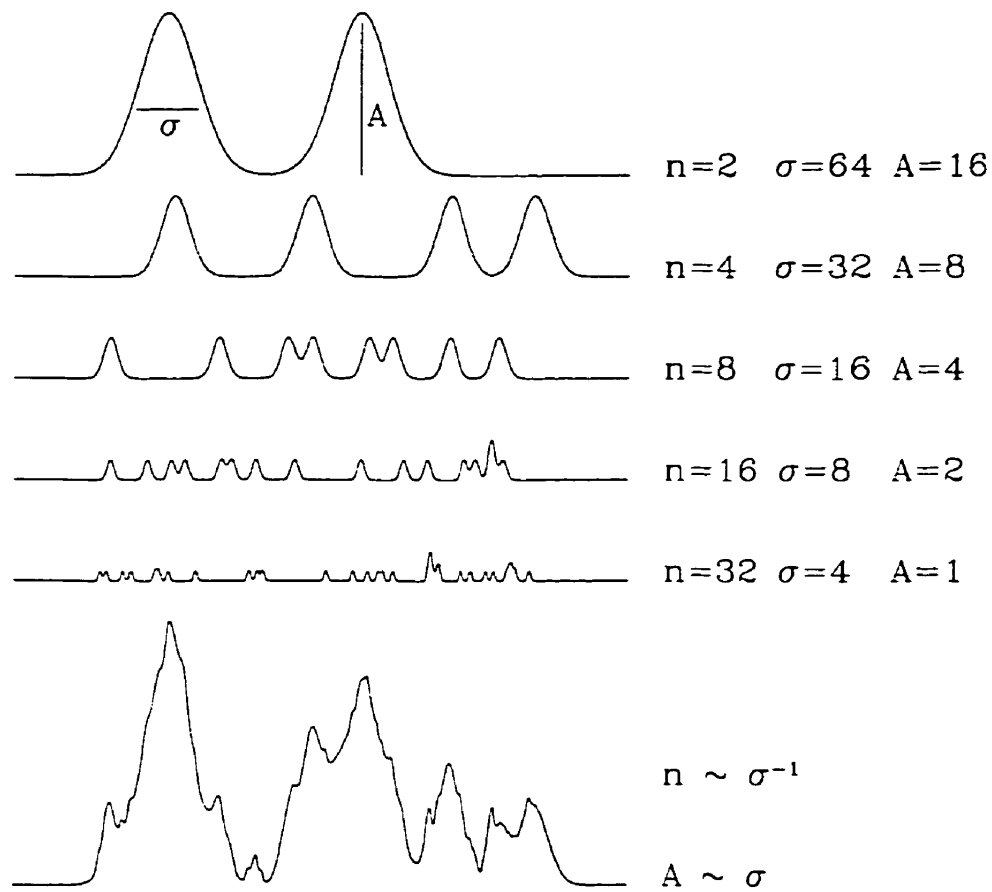


FIGURE 2.2. Example construction of a synthesized subpeak profile (bottom) using simple scaling relations. At different scales, gaussians are randomly placed, with their number n and intensity amplitude A determined by the scaling relations. The resulting profile is the sum of the individual scales. This example corresponds to parameters $\alpha = 1$ and $\beta = -1$ (see text).

transforms. So the overall wavelet transform should also have zero mean, with a mean deviation proportional to the square root of the number of gaussians involved. This mean deviation is what the wavelet transform will be sensitive to.

Thus, the WPS (Eq. 4) gives us information about the squared amplitude of the *mean deviation* at some scale σ . In the range of scales $[\sigma, \sigma + d\sigma]$, this should be directly proportional to the square of (1) the intensity amplitude $A(\sigma)$ of individual structures at that scale and (2) the square root of $N(\sigma)$, the number density of structures at the same scale. Naively, we might expect the WPS to show a dependence such as:

$$W(\sigma)d\sigma \sim (A(\sigma)\sqrt{N(\sigma)})^2d\sigma = K_a^2 K_b \sigma^{2\alpha+\beta} d\sigma.$$

In fact, the WPS also includes information about the fundamental shape $g(x)$ of individual elements, since each element is itself a superposition of different scales. Strictly speaking, the WPS is a convolution of the general scaling laws with the WPS of an individual structure. Thus, the dependence on the parameters α and β will be more generally given by:

$$W(\sigma) \sim \sigma^{\phi(2\alpha+\beta)}, \quad (2.9)$$

where $\phi(2\alpha + \beta)$ is some non-trivial, but monotonic function that depends on the fundamental shape of the structures involved.

In order to check these ideas, we generated numerous signals with known scaling parameter values, according to the model described in Eqs. 5,6,7. For each synthetic signal, the WPS was evaluated and the power index $\phi = \phi(2\alpha + \beta)$ was determined (see Fig. 3,4). Simulations were done using both gaussians and triangles as the fundamental shape. The function ϕ is shown to be significantly dependent on the choice of the fundamental shape $g(x)$, and this should be kept in mind.

In principle, we now have a way of obtaining the value of $2\alpha + \beta$ from the

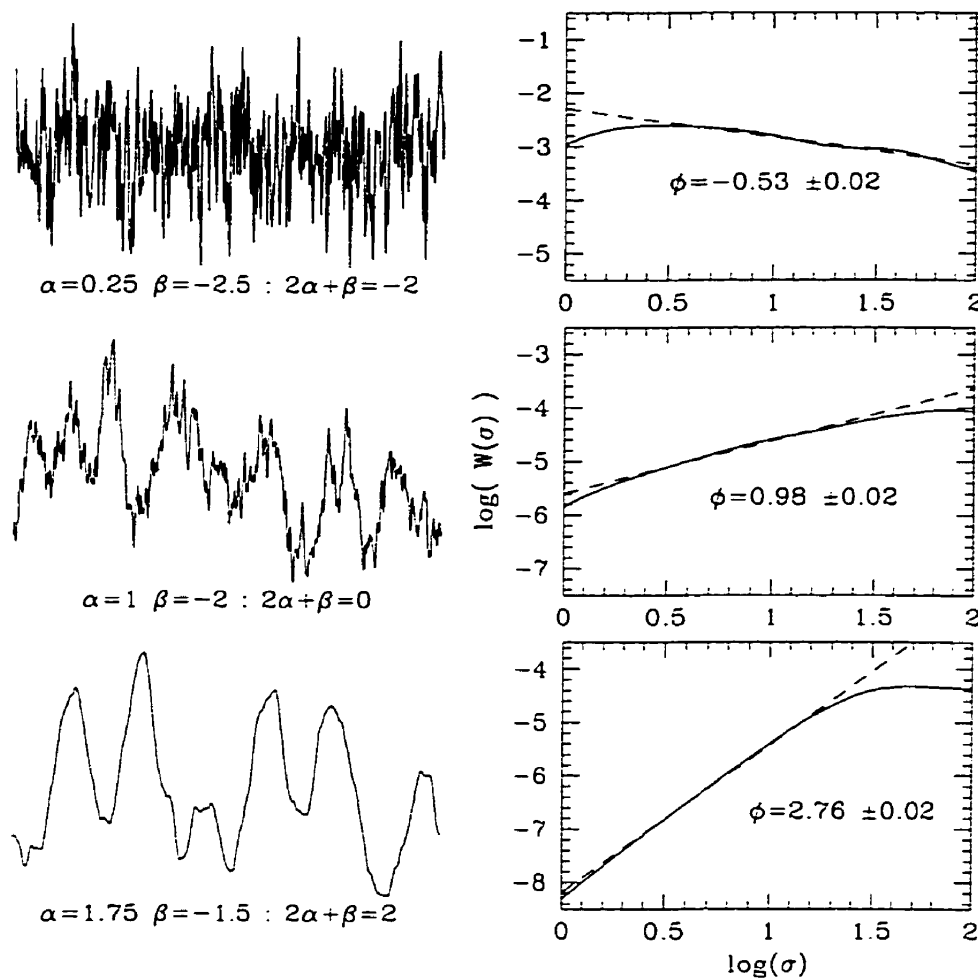


FIGURE 2.3. The Wavelet Power Spectrum $W(\sigma)$ (right, full line) is plotted for each set of simulated multi-gaussian signals depicted as examples on the left. These simulated subpeak distributions are scaled with different values of the parameters α and β . Notice that $W(\sigma)$ is very sensitive to these parameters: the power dependence of the WPS changes accordingly, giving different slopes ϕ (linear regression, dotted line), which can be used to obtain an estimate of $2\alpha + \beta$ (see Fig.4). With this technique, it is not possible to decouple α and β .

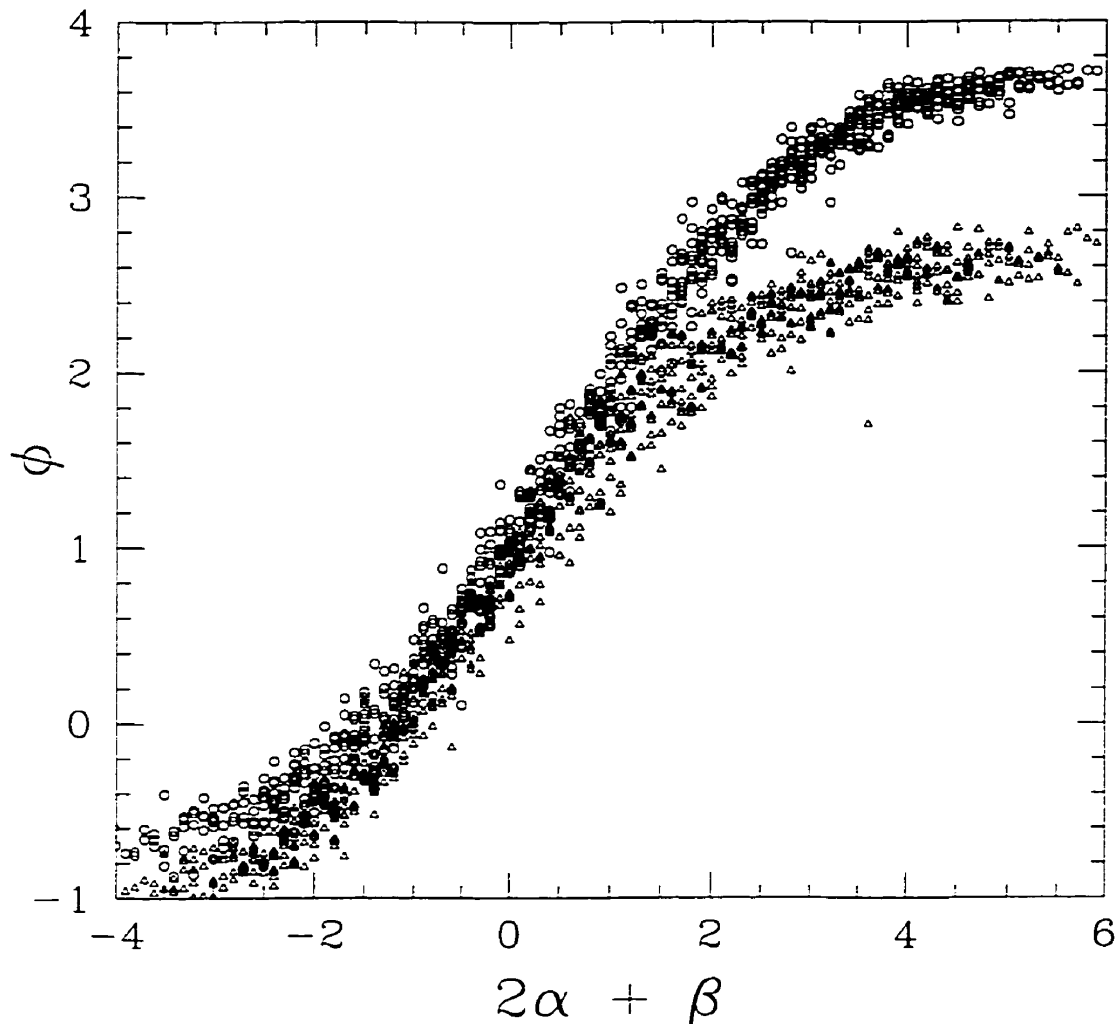


FIGURE 2.4. The power dependence of the WPS (slope ϕ in Fig.3) given for different values of $2\alpha + \beta$, as obtained from simulations using the model described in the text. Results are shown for the use of gaussians (open circles) and triangles (open triangles) as the fundamental shape of individual structures. Signals were generated using model parameters within the range $-1 < \alpha < 3$ and $-2 < \beta < -0.1$, each with a 0.1 step (2 x 820 models are thus shown here).

power spectrum by evaluating ϕ . There is some uncertainty in the evaluation of ϕ that arises from the fact that we are dealing with signals extended over a limited spatial domain, because subpeaks are then finite in number, and subjected to statistical variations. This explains the dispersion of the points in Fig.4 (simulated signals from which this figure was made, had a limited spatial extension of 500 units, to match that of the data). Another uncertainty arises from our poor knowledge of the fundamental shape of the structures in the data. This effect is rather limited for small values of $2\alpha + \beta$, but is far from negligible for large values, as seen in Fig. 4. Other fundamental shapes (e.g. lorenzians; rectangular profiles) were tested and found to give results similar to, or intermediate between, triangles and gaussians.

Notice also that very large absolute values of $2\alpha + \beta$ lead to asymptotic behavior in $\phi(2\alpha + \beta)$. An infinite value of $2\alpha + \beta$ would actually correspond to a case for which no scaling laws are present (absence of small-scale elements). However, we see that it is not possible, with this method, to distinguish between that specific case and a case where $2\alpha + \beta \gtrsim 5$ (gaussians) or $\gtrsim 4$ (triangles). Thus, we can say that evidence for scaling laws is only compelling when $|2\alpha + \beta|$ is found to be $\lesssim 4$.

2.4 Data Source

In order to test for consistency with the hypothesis of scaling laws in the subpeaks of observed emission line profiles, it is necessary to have time-resolved, high spectral resolution, high signal-to-noise (S/N) data, to detect coherent structures over at least an order of magnitude in scale. We focus our attention on the best bank of high resolution spectra to date: those obtained by AFJM & C. Robert in 1987, 1988, and 1989 (Robert 1992). These data consist of time-resolved, high resolution, high S/N emission line spectra from (a) CFHT(normal diffraction grating + Reticon at the coudé focus), showing mainly HeII $\lambda 5412$ in

the WN stars HD191765 (WN6), HD192163 (WN6), and HD193077 (WN5+OB), and CIII $\lambda 5696$ for the WC stars HD192103 (WC8), HD192641 (WC7+abs), and HD193793 (WC7+O4-5V), and (b) ESO (échelle + CCD at the Cassegrain focus), also showing CIII $\lambda 5696$ (among other lines) for the stars HD164270 (WC9) and HD165763 (WC5). These Wolf-Rayet stars are also designated as WR134, WR136, WR138, WR135, WR137, WR140, WR103, and WR111 respectively (van der Hucht *et al.* 1988); the latter names will be used hereafter in this article. ESO spectra of the stars HD96548 (WN8) and HD113904 (WC6+O9.5Iab) from the same observing run, were not included in this study: most emission lines of the former are perturbed by P Cygni edges, while emission lines of the latter are strongly diluted by the supergiant companion. These effects made the identification of variable subpeaks more problematic. CFHT observations of the two remaining bright WR stars in Cygnus, WR133(WN5+O9Iab) and WR139(WN5+O6), were not included either: their emission lines are also heavily diluted or perturbed by their bright O-companions. WR137, 138 and 140 are also binaries, but of very long period (Annuk 1991) and dilution effects are less important, especially for WR137 and WR138.

All the spectra have a dispersion of $\sim 0.1 \text{ \AA/pixel}$ and a S/N per pixel in the continuum between 150 and 380 (see Table 1). Figure 5 shows a typical profile obtained for each star. The observations were made over an interval of 3-4 consecutive nights. Four to twelve spectra spaced by ~ 1 hour were obtained each night for each star. All spectra have been rectified.

The presence of subpeaks on the lines is obvious on the top of all flat-top emission lines (see Fig. 5). However, in the sloping part of a line profile, it is often difficult to distinguish these narrow features. As a way to enhance the presence of discrete variable subpeaks, we have therefore subtracted the smoothed mean profile (based on the data from all 3 or 4 nights) from each line in each star, as was done by Robert (1992). In order to avoid degradation of the base profile in

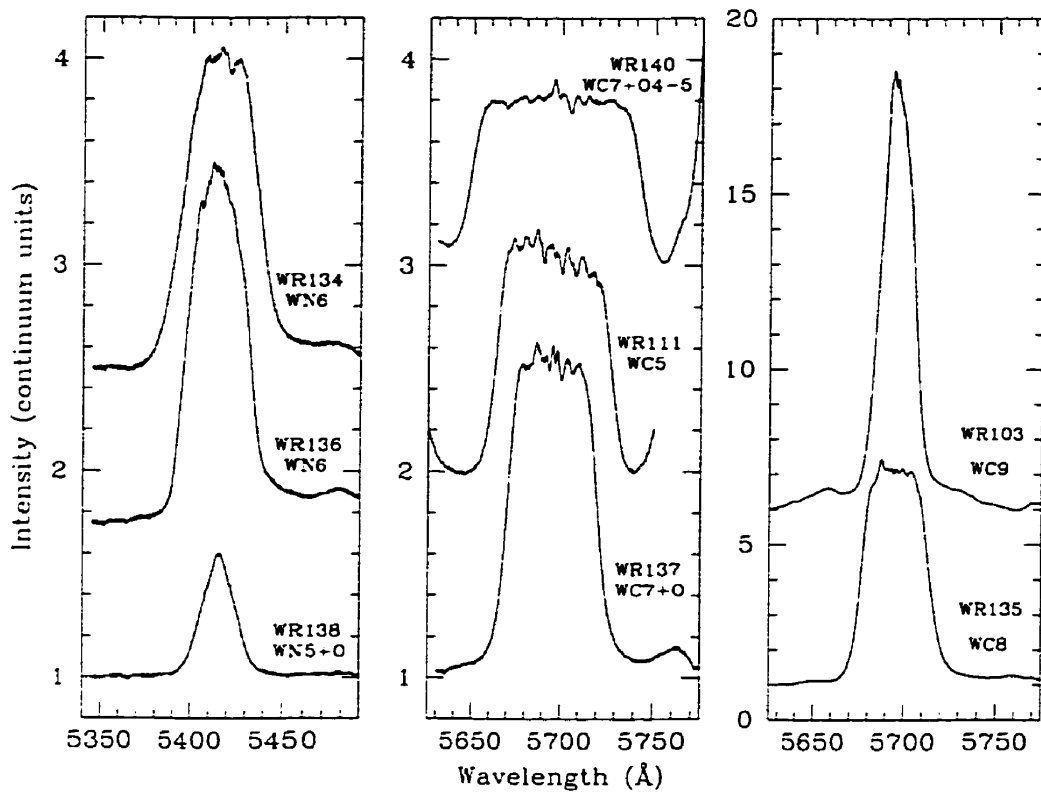


FIGURE 2.5. Individual sample spectra of emission lines in 8 stars observed at ESO (WR103, WR111) and CFHT (rest). The He II $\lambda 5412$ line was observed in the WN stars, CIII $\lambda 5696$ in the WC stars. All these lines show variable subpeaks, which are more obvious on flat-top lines.

TABLEAU 2.1. List of Observed Emission Lines

Star	HD	Sub-type	v_{∞}^a	No. Spectra	S/N_{cont}	Line	$\langle EW \rangle (\text{\AA})^b$
WR103	164270	WC9	1190	30	210	C III 5696	-294.2
WR111	165753	WC5	2415	28	150	C III 5696	-67.9
WR134	191765	WN6	1905	36	190	He II 5411	-69.6
WR135	192103	WC8	1405	26	180	C III 5696	-247.6
WR136	192163	WN6	1605	26	200	He II 5411	-62.8
WR137	192641	WC7+OB	2550	25	240	C III 5696	-83.8
WR138	193077	WN5+OB	1345	18	230	He II 5411	-13.3
WR140	193793	WC7+O4-5	2900	23	380	C III 5696	-77.6

^a From Prinja *et al.* (1990).

^b Time-averaged equivalent width from Robert (1992).

the smoothing process, we used optimized 6th-order Savitzki-Golay smoothing filters. The time dependence of the resulting difference profiles is shown as an example in Fig. 6 for one night's data. The persistence and slow evolution of the most obvious discrete features makes it extremely unlikely for them to be the result of instrumental or statistical noise.

2.5 Data Analysis

2.5.1 The wavelet power spectrum profile

For each individual line (CIII 5696 in WC stars, and HeII 5411 in WN stars) in each spectrum of our eight Wolf-Rayet stars, we have evaluated the WPS of the structures observed on top of the bright emission lines. From the spectroscopic signal $I(\lambda)$ obtained after subtracting off the mean, we first calculate the wavelet transform $\tilde{I}(\lambda', \sigma)$. Then for an emission line at location λ_0 with a FWHM of $\Delta\lambda$, we evaluate $W(\sigma)$ over the restricted domain $[\lambda_0 - \Delta\lambda/2, \lambda_0 + \Delta\lambda/2]$, in order

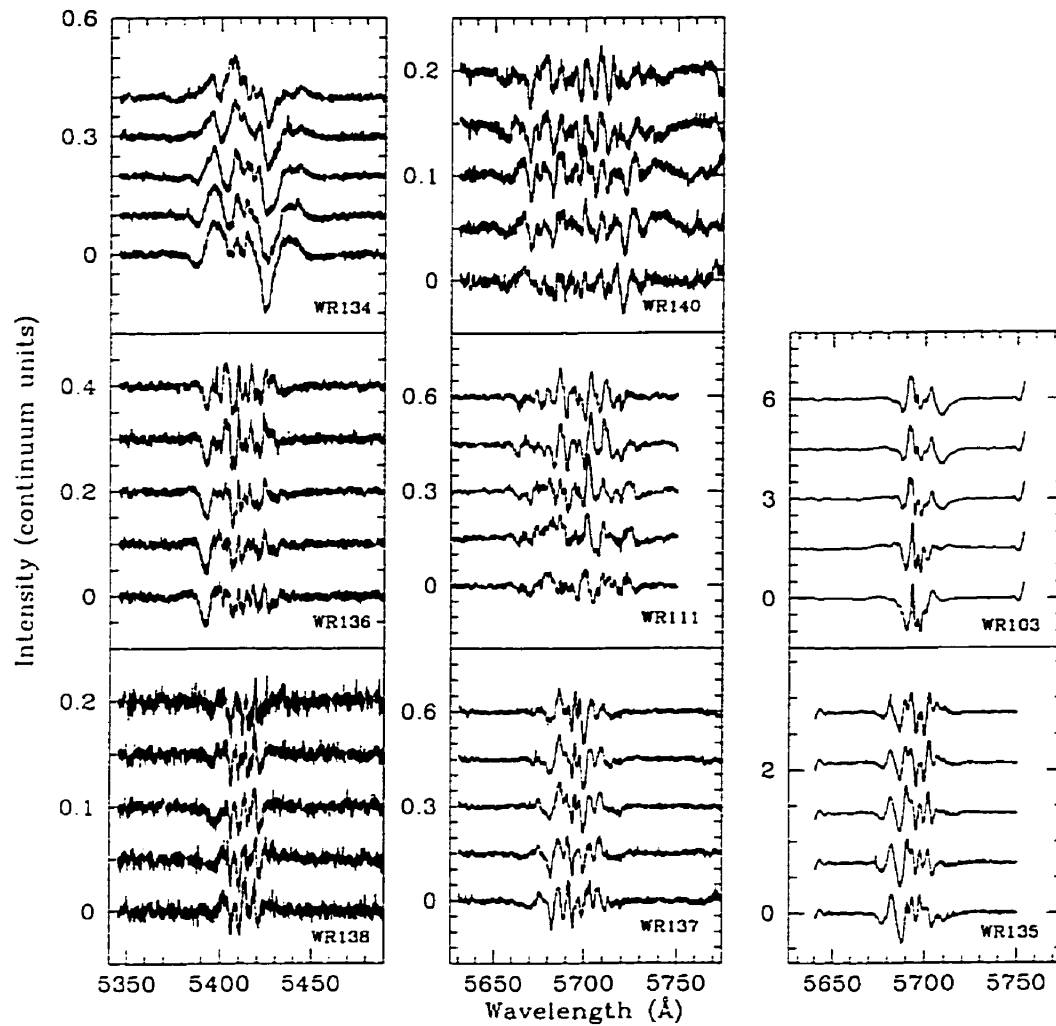


FIGURE 2.6. A set of 5 consecutive spectra taken from the same single night as the spectra in Fig. 5 is shown for each star. In each case, an average, smoothed line profile was subtracted in order to enhance the presence of the subpeaks. The average time separation is ~ 1 hour between successive spectra with time increasing upwards. Some subpeaks appear to move slightly and change intensity with time.

to avoid edge effects. For a given line in a given star we obtain the average WPS ($\bar{W}(\sigma)$) from each of the different spectra. Then we normalize $\bar{W}(\sigma)$ by dividing by the mean line equivalent width for that star, in order to facilitate a comparison among different objects.

A sample average WPS so obtained for the CIII 5696 line in the star WR137 is shown in Fig. 7. The smallest scales are usually dominated by instrumental or photon statistical noise, appearing as high frequency components. The noise sets a minimal value for the power at a given scale. Intrinsic subpeaks in the signal may only be detected with confidence if they amount to a power greater than this minimal value set by the noise.

Beyond the region where noise dominates, we observe an increase in amplitude as the scale increases. A noise-only signal cannot produce such an increase in power for larger scales since it is always dominated by small scale components. *This is the principal diagnostic for the presence of discrete structures distinct from the noise.* The rate of increase can be used to determine the presence of scaled distributions, as described in the previous section. However, one must be very careful to remove the possible effects that might arise from the presence of noise (see section below).

The WPS usually reaches a maximum at some scale we designate as the *dominant scale*. This usually corresponds to the scale at which the structures have the highest intensity amplitude in the signal. In our model of a scaled distribution, this dominant scale may be introduced by setting an upper limit for the width of any intrinsic individual structure. The shape of the WPS is very similar for all stars in our sample (Fig.8). These are all consistent with the presence of intrinsic subpeaks, with various levels of superposed instrumental and statistical noise.

In this paper, we have neglected possible variations in the WPS across the emission line. This restriction was added only for the sake of our simple model,

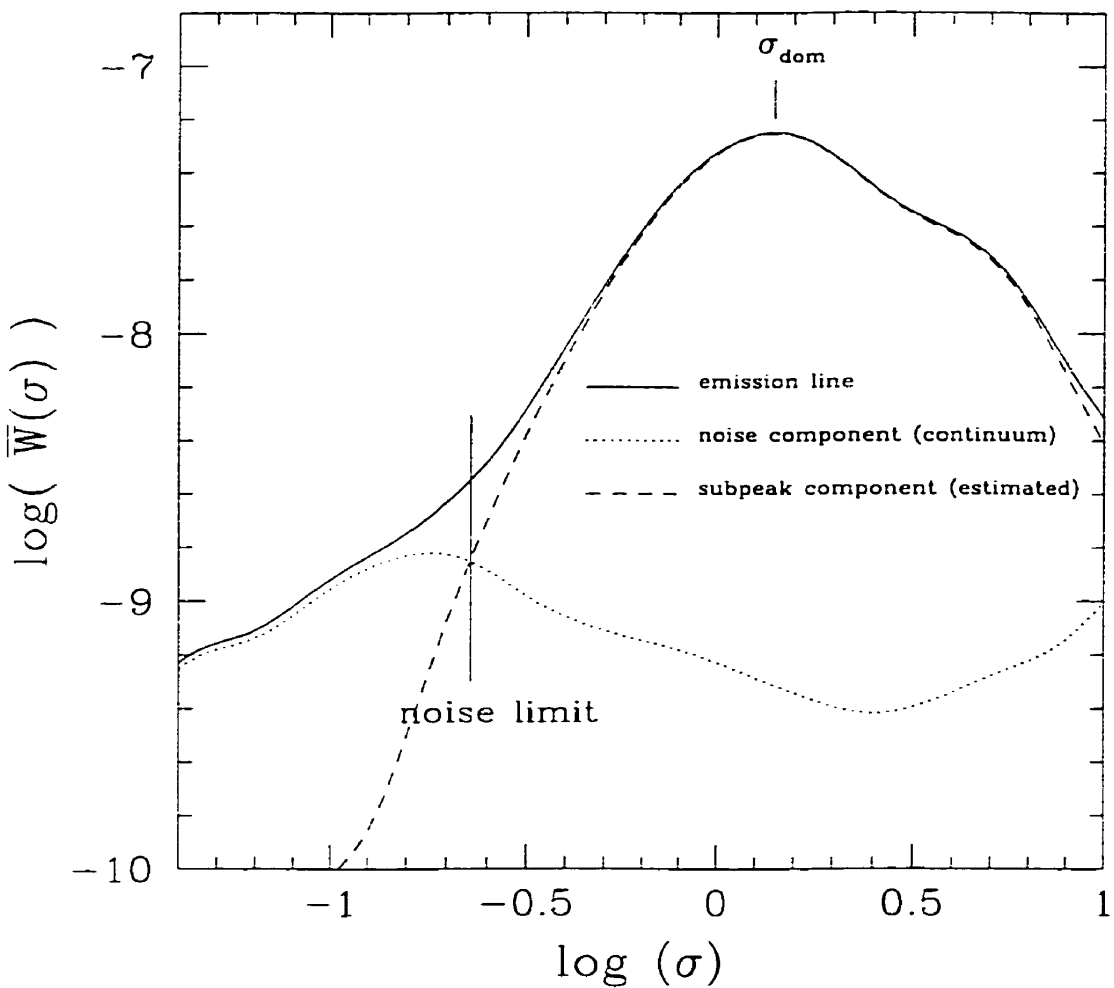


FIGURE 2.7. WPS for the subpeaks in the CIII emission line of the WC7 star WR137. The dominant scale σ_{dom} (see text) is defined as the scale σ where a maximum is reached. A WPS evaluated in the continuum region next to the line is used to determine the power contribution of the noise. This contribution is then subtracted from the subpeak power spectrum. The *noise limit* is defined as the lowest scale where the power contribution from the subpeaks can be evaluated with confidence. (Note: $\log[\sigma]$ is plotted with σ expressed in Å.)

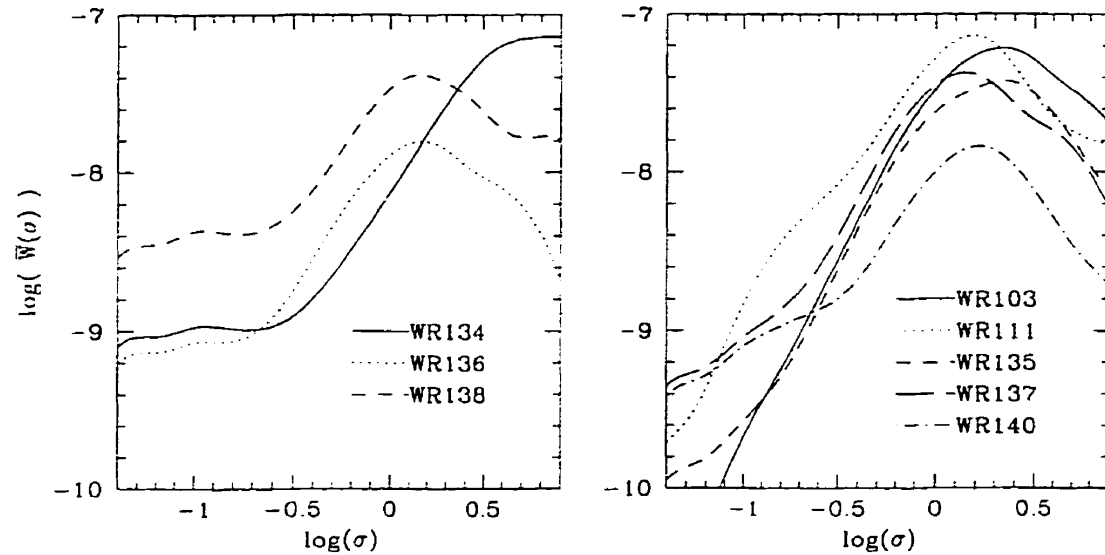


FIGURE 2.8. WPS from subpeaks of all WR stars in the sample. The left panel refers to subpeaks observed in the HeII $\lambda 5412$ line; the right panel is for those observed in CIII $\lambda 5696$. The amplitudes were normalized in overall emission line amplitude units, so that a comparison can be made between different stars. Notice the distinct shape of the WPS from star WR134, and the various levels introduced by the noise in the low scale region. (Note: $\text{Log}[\sigma]$ is plotted with σ expressed in \AA .)

which does not include this behavior. However, such variations in the power spectrum were actually observed. These will be analyzed, along with the time dependence, in an upcoming paper (Lépine *et al.* 1998, paper II).

2.5.2 The noise limit

Noise effects appear in the WPS as an excess on smaller scales. As a good approximation, the noise can be said to be independent of the behavior of the structures we are interested in since it arises mainly from photon statistics (dependent mainly on the amplitude in the emission line, which is large relative to the subpeaks) and from instrumental, signal-independent read-out noise. It is possible statistically to remove these noise effects by subtracting their power contribution from the WPS. This contribution can be evaluated by using the adjacent continuum emission of the star, which normally should be devoid of any significant intrinsic structure (i.e. it should be flat). However, both the photon count and the Poisson noise arising from it are lower in the continuum than in the line peak, so that the noise must be scaled accordingly. However, we need not evaluate any multiplicative factor, since it can be obtained directly from the WPS. If we assume that the noise has more or less the same scaling behavior in both the line and continuum, we need only scale the WPS of the continuum with that of the line *at the smallest scales* where the noise also dominates in the line. The normalized WPS so obtained for the continuum is then subtracted from the emission line WPS. An example of such noise correction is shown in Fig.7.

The small-scale part of the WPS is very dependent on the noise in the data (cf. Fig.8). The amount of noise is critical in our ability to identify *intrinsic* small scale structures. Below some limiting scale, subtraction of noise effects becomes increasingly unreliable in determining the exact, intrinsic WPS, because intrinsic structures become indistinguishable from the noise. This *noise limit* is defined as the scale for which the noise component and the intrinsic component of the

data reach the same amplitude in the WPS (cf. Fig.7). The noise limit clearly identifies the scale below which any interpretation about the presence or behavior of intrinsic structures becomes hazardous.

If we are specifically looking for scaling laws, we must sample the largest possible significant range in scale, in order to derive anything useful. This significant range is set between the dominant scale and the noise limit. Therefore, increasing the accuracy in the detection and determination of scaling laws requires one to improve *both* the spectral resolution *and* the signal-to-noise ratio of the data, in order to have the noise limit set to smaller scales. Future observations should emphasize this goal, as well as providing better time resolution, in order to avoid any smearing out of the small scale features due to their dynamical behavior.

2.5.3 Fitting data to the model

To test for the hypothesis of scaling behavior in emission line subpeaks, we compare WPS obtained from the data to those of simulated profiles generated in accordance with the model described by Eqs. 5-7, and to which a large scale cutoff was included, in order to reproduce the presence of a dominant scale.

Three aspects of the observed and model wavelet spectra are compared: (1) the dominant scale σ_{dom} , (2) the power at the dominant scale $\bar{W}(\sigma_{dom})$, and (3) the scaling parameter $2\alpha + \beta$. The parameters σ_{dom} and $\bar{W}(\sigma_{dom})$ affect the WPS in the simplest way. In log-log space, they correspond to horizontal and vertical shifts. Only the scaling parameter $2\alpha + \beta$ directly reflects the *shape* of the WPS.

We have already shown the distinct scaling behavior we get by using triangles instead of gaussians. Since other tested shapes led to a behavior intermediate between gaussian and triangles, we restricted ourselves to two series of models, one using gaussians, the other triangles. For each pre-assigned value of the parameter

TABLEAU 2.2. Best Fit Subpeak Model Parameters

Star	σ_{dom} (Å)	σ_v (km/s)	$P(\sigma_{dom})$	$2\alpha + \beta$ (gaussians)	$2\alpha + \beta$ (triangles)
WR103	2.0 ± 0.1	105 ± 5	0.029	2.5 ± 0.2	3.3 ± 0.5
WR111	2.0 ± 0.1	105 ± 5	0.033	2.3 ± 0.2	2.9 ± 0.3
WR134	8.0 ± 1.5	440 ± 80	0.032	1.2 ± 0.1	1.7 ± 0.3
WR135	1.8 ± 0.1	95 ± 5	0.021	2.6 ± 0.2	3.5 ± 0.5
WR136	1.5 ± 0.2	83 ± 11	0.015	2.8 ± 0.2	3.2 ± 0.5
WR137	1.5 ± 0.2	79 ± 11	0.025	3.4 ± 0.4	4.5 ± 1.0
WR138	1.6 ± 0.2	88 ± 11	0.025	2.5 ± 0.6	3.0 ± 0.5
WR140	1.9 ± 0.2	100 ± 11	0.014	> 4	> 5

$2\alpha + \beta$ and for each fundamental shape (gaussian or triangular), a set of synthetic signals was constructed. Individual values of α and β do not matter here, since only the combined parameter $2\alpha + \beta$ dictates the behavior of the associated WPS. For each set, the power spectrum was evaluated and compared to that previously found for the data. Synthetic power spectra were translated in log-log space based on least-squares fit procedures. For each star, we determined the model that fitted best the observed WPS (e.g. Fig.9). Table 2 shows the parameters for the best-fitted model for each star. Gaussian and triangular models were treated separately and results are given for each type. Because moderately high values of $\phi(2\alpha + \beta)$ are found, the two models do not lead to the same value of $2\alpha + \beta$ (cf. Fig.4).

We note here that decoupled values of α and β cannot be determined using the current WPS technique. So far, we know of no way to determine their individual values other than by extracting and analyzing individual features in the data, a procedure we believe to suffer from various biases. We will therefore restrict ourselves to the determination of $2\alpha + \beta$, from which useful information can still be inferred.

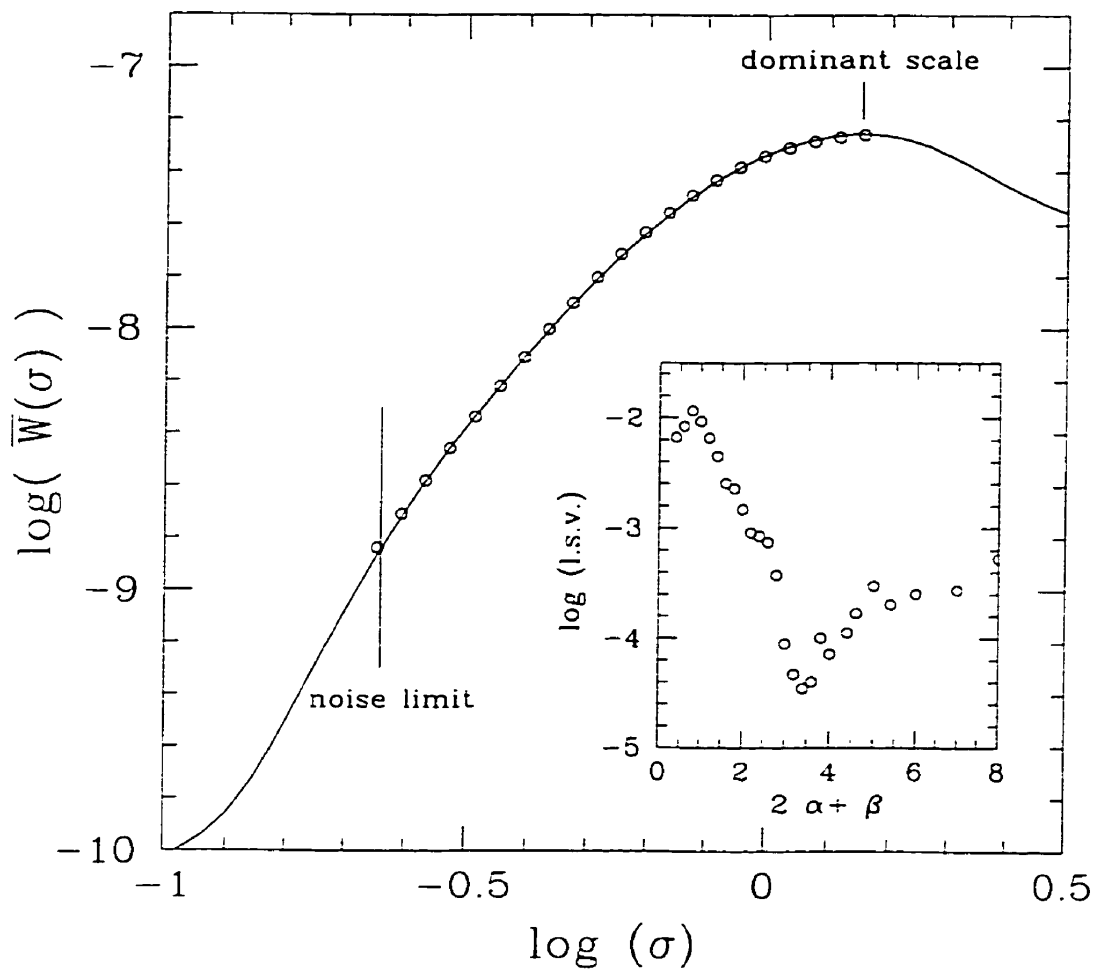


FIGURE 2.9. WPS of a subpeak model (circles) that best fits the WPS of subpeaks on the CIII line in WR137 (corrected for noise, full line) between the noise limit and the dominant scale. The model uses a set of gaussians (fundamental shape) with 1.7 \AA ($\sim 90 \text{ km/s}$) as the dominant scale and a scaling parameter $2\alpha + \beta = 3.4$. The subplot shows the least-square value (l.s.v.) obtained by fitting the WPS of similar models with given values of $2\alpha + \beta$; it clearly shows a minimum around $2\alpha + \beta = 3.4$.

2.5.4 Discussion

2.5.4.1 Dominant scales

Table 2 shows the dominant scale σ_{dom} and its corresponding velocity dispersion σ_v found for the substructures in each star. The value of σ_v for the largest individual substructures present in the line tends to be relatively similar for most stars ($94 \pm 11(s.d.)$ km/s), except for WR134.

The dominant scale for WR134 is *much* larger, with $\sigma_v \sim 440$ km/s. This suggests that at least some (i.e. the largest) of these subpeaks might have a different origin. Actually, it was already noticed by Robert (1992) and McCandliss *et al.* (1994) that the *largest* subpeaks in the lines of WR134 move in a periodic fashion, in contrast to the apparently stochastic nature of all the subpeaks seen in other stars of the sample. This periodic behavior might be the result of asymmetry in a single rotating star or a binary system. This distinct-origin hypothesis is corroborated by the wavelet analysis.

The outstanding nature of WR 134 serves as supplemental evidence that there is no *a priori* reason for observing the same dominant scale in each of the other stars. The observed dominant scale seems to be an intrinsic property of WR stars as a whole, rather than some purely numerical phenomenon. Moreover, there is some evidence that a general stochastic phenomenon similar to that of the other stars is *also* present in WR134, but superposed on the variations generated by the large scale periodic behavior. The scaling parameter $2\alpha + \beta$ for WR134 is small, indicating a significant subpeak component on smaller scales. We suggest that this arises in an additional subpeak distribution similar to that seen in other stars, that is superposed on the large periodic structures.

2.5.4.2 Scaling properties

The interpretation of our results in terms of scaling laws is complicated by the fact that we are dealing with structures seen in projected velocity space. The widths of the subpeaks observed in the emission lines cannot be directly associated with the physical sizes of the corresponding wind inhomogeneities. Any density enhancement should have a minimal velocity dispersion because of its internal temperature. For a gas of (helium) ions in a hot (10^4 K) wind, this would be of the order of ~ 5 km/s (~ 0.1 Å in our lines), and no subpeak having smaller width should be observed. This makes our simple model, where σ can take any arbitrarily small value, unsuited to the observed phenomenon. However, since the resolution in our data is also 0.1 Å, our model can be used as a good approximation in the corresponding spectral regime, but a more complete physical model is still needed in order to relate the velocity dispersion σ_v to the real, physical extension of the subpeaks.

The most we can do with the current, oversimplified model, is to speculate about the total flux emitted by the intrinsic variable component in the line. According to our model, with a scaled distribution described by Eqs. 6 and 7, the total flux emitted by any given scale $F(\sigma)d\sigma$ is proportional to $\sigma^{\alpha+\beta+1}d\sigma$ (Eq. 8). Hence, if the coefficient $\alpha + \beta + 1$ is greater than 0, then most of the flux will arise in the largest structures, but if it is smaller than 0, then most of the flux will be emitted by the small structures. In the latter case, the large subpeaks observed are seen as the “tip of the iceberg”, and a much larger part of the flux in the emission line might come from (smaller) density enhancements; this has already been suggested by Moffat & Robert (1994). In the former case however, the small density enhancements (if any) are not bright enough or numerous enough to make a significant contribution as a whole. In this case, most of the observed line flux would arise in another (likely *smooth*) component of the wind.

These possibilities are illustrated in Fig. 10, where the previous (biased, i.e. not allowing for superposition effects) values obtained for the parameters α and β and the current range of estimates are plotted. Note that the range of old values does not agree with the current estimates, which means that, assuming the present analysis to be viable, the various biases we suspected to be present effectively led to an erroneous evaluation of the scaling parameters. Fig.10 also shows the zones for which these parameters would indicate a large-scale or small-scale flux-dominated distribution. We observe that values of $\alpha \lesssim 4$ and $\beta \gtrsim -5$ that lie within the allowed shaded regions, would lead to a large-scale flux-dominated regime, where the (undetectable) small-scale part of the distribution does not contribute enough flux to account for a significant fraction of the line flux. The converse is possible, though, if $\alpha \gtrsim 4$ and $\beta \lesssim -5$ within the allowed region. However, the latter case makes the model appear to be somewhat *ad hoc*, and a different model might be more appropriate. In any case, this raises doubts about the hypothesis of a fully clumped wind which assumes that most (or all) of the line flux arises in an inhomogeneous component (Moffat & Robert 1994). We speculate that more sophisticated subpeak models, perhaps involving no scaling laws, could also be consistent with the data. The wavelet technique presented here could be used as an objective test for these alternative models.

Further investigations should be carried out by gathering spectra with finer spectral resolution in order to test for scaling properties of the line structure to smaller scales. The intrinsic velocity dispersion arising in thermal broadening might, however, set an inescapable low-scale limit to such a detection. New observations should be made with a simultaneous increase in spectral and time resolution as well as signal-to-noise. From the current wavelet power spectra, we estimate that gaining, say, an additional threefold in scale can only be achieved by increasing the spectral resolution by a factor 3, and the signal-to-noise ratio by a factor 10. In order to increase the time resolution by a factor 3 as well (see paper II), this would require observing bright stars ($m < 3$) with a large telescope

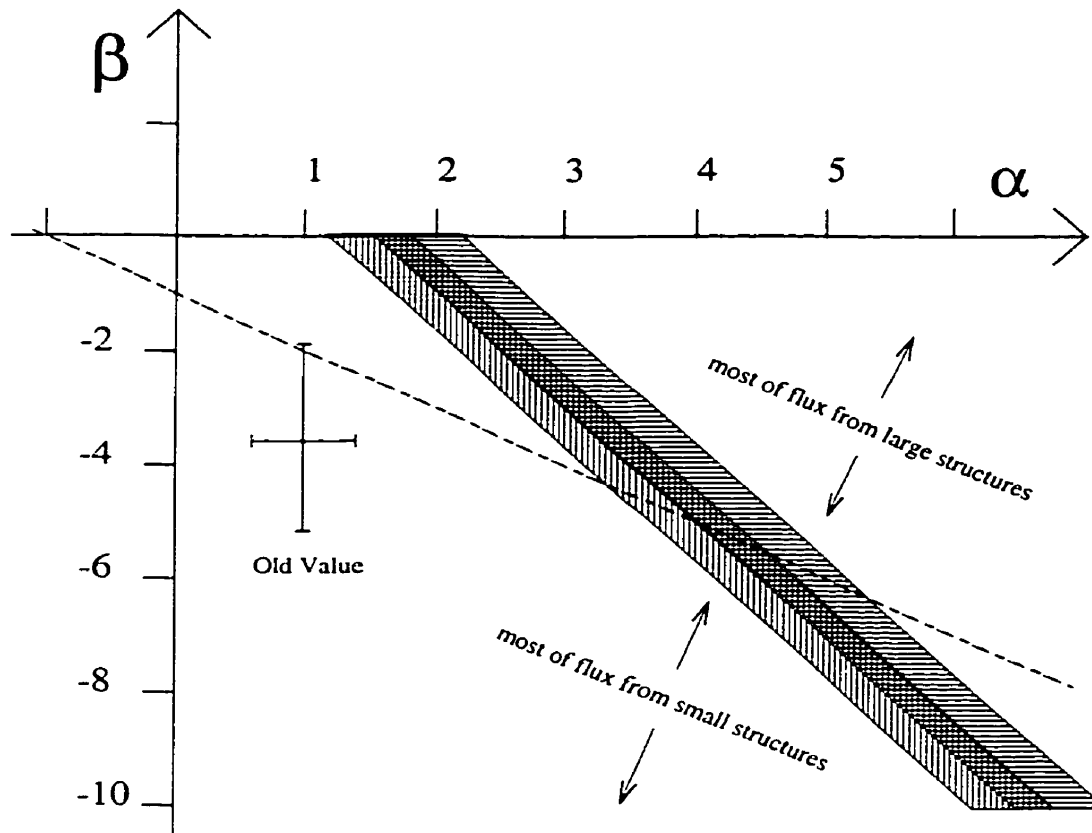


FIGURE 2.10. Plot showing the range of model parameters α and β that are consistent with the data. Vertical shading shows the results obtained when using the model with gaussian subpeaks, horizontal shading for the model with triangular subpeaks. The dashed line separates parameter space in regions where the flux contribution is dominated by small and large scale structures, as indicated. The error bars shows the range of values obtained with previous techniques (extracted subpeaks), which are believed to suffer from various biases.

($\phi > 3$ m).

2.6 Summary and Perspectives

We have presented a new objective technique to analyze the stochastic, variable, emission component in line spectra of Wolf-Rayet stars, involving the use of a *wavelet power spectrum* (WPS). This technique was used to quantify the intrinsic variable component in the line and to test for consistency with the idea of scaling laws.

The data were found to be increasingly affected on smaller scales by instrumental and statistical noise. The WPS was used to determine a *noise limit*, defining the scale below which the data became unreliable because of the noise. The effects of the noise on the WPS were evaluated and statistically removed.

We have identified a scale where the WPS reaches a maximum, the *dominant scale*, which is presented as a new parameter to characterize the variable subpeak component in the emission line. The dominant scale is found to be similar in most of the stars of our sample, suggesting that the variable subpeaks in these stars have a similar origin. The only exception is in the star WR134, where a larger dominant scale corroborates previous results indicating a distinct nature for the observed subpeaks (Robert 1992; McCandliss *et al.* 1994). Further studies should include a larger sample of Wolf-Rayet stars, where the dominant scale should be checked in lines of various ionization levels. This is required to search for any correlation between the dominant scale and the most obvious stellar parameters, such as the wind terminal velocity, the spectral sub-class or the mass-loss rate.

We have introduced a simple phenomenological model for the variable subpeak component, describing it as a sum of Gaussian-like features of various scales σ (Eq. 5). The model allows for the presence of scaling laws, in the form of power

laws parameterized by the powers α and β (Eqs. 6,7). We have shown that only the combined parameter $2\alpha + \beta$ can be safely estimated from the WPS. We have found the data to be consistent with our model, providing $2\alpha + \beta \sim 2.7 \pm 0.4$ (*s.d.*) for gaussian subpeaks, and $2\alpha + \beta \sim 3.4 \pm 0.6$ (*s.d.*) for triangular subpeaks, neglecting WR134 and WR140 in both cases. Other subpeak shapes are believed to give intermediate results. We have noted the possibility that other models might give slightly different scaling properties, including the possibility that no scaling laws are present. The WPS technique is expected to be a good way to test for other (more physical) subpeak models.

So far, the information contained in the time evolution of the subpeaks has not been considered, as well as systematic variations in the behavior of the subpeaks across a single emission line. This will be considered in a forthcoming paper (Lépine *et al.* 1996, paper II).

In order to increase our confidence in the above results, an increase in the range of scales over which subpeaks can be identified (roughly between the dominant scale and the noise limit) is required. So far, because of noise limitations, we are not able to observe scaling behavior over more than an order of magnitude in scale. Improved, but difficult observations are necessary, using increased spectral and time resolution combined simultaneously with better signal-to-noise ratio, in order to push the noise limit several factors lower. High time resolution may also be required for a better identification of individual subpeaks, in order to determine their fundamental shape. We would then expect to obtain more significant results for the scaling properties of emission line subpeaks in Wolf-Rayet stars. This would place us in a better position to evaluate the true impact of clumping on basic key quantities such as the mass-loss rate.

Acknowledgements

The authors are grateful to J.C. Brown, A. Conway and L. Richardson from

Glasgow University, for useful, constructive comments and discussions related to this work.

SL acknowledges the support provided by a Post-Graduate Scholarship from NSERC of Canada. AFJM & RNH are grateful to NSERC of Canada (AFJM also to FCAR Québec) for financial aid.

CHAPITRE 3

WIND INHOMOGENEITIES IN WOLF-RAYET STARS. II. INVESTIGATION OF EMISSION-LINE PROFILE VARIATIONS.

The Astrophysical Journal, *accepted* (1998)

**WIND INHOMOGENEITIES IN WOLF-RAYET
STARS. II. INVESTIGATION OF EMISSION-LINE
PROFILE VARIATIONS.**

Sébastien Lépine¹, and Anthony F.J. Moffat,^{1,2}

Article submitted to the Astrophysical Journal main section.

¹ Département de Physique, Université de Montréal, C.P. 6128, Succ. Centre-Ville, Montréal, Québec, Canada, H3C 3J7; and Observatoire du Mont Mégantic.

² Killam Research Fellow of the Canada Council for the Arts

ABSTRACT

We present high-resolution spectroscopic monitoring of the line profile variations (LPV) in the He II $\lambda 5411$ emission-line of 4 Wolf-Rayet (WR) stars of the WN sequence (HD96548, HD191765, HD192163, and HD193077), and in the C III $\lambda 5696$ emission-line of 5 WR stars of the WC sequence (HD164270, HD165763, HD192103, HD192641, and HD193793). The LPV are shown to present systematic patterns: they all consist of a number of relatively narrow emission subpeaks which tend to move from the line center towards the line edges.

We introduce a phenomenological model which depicts WR winds as being made up of a large number of randomly distributed, radially propagating, discrete wind emission elements (DWEES). This working model is used to simulate LPV patterns in emission-lines from a clumped wind. General properties of the LPV patterns are analyzed with the help of novel numerical tools (based on multi-scale, wavelet analysis), and simulations are compared to the data. We investigate the effects on the LPV of local velocity gradients, optical depths, various numbers of discrete wind elements, and a statistical distribution in the line-flux from individual elements. We also investigate how the LPV patterns are affected by the velocity structure of the wind, and by the extension of the line-emission region (LER).

Eight of the stars in our sample are shown to possess strong similarities in their LPV patterns, which can all be explained in terms of our simple model of local wind inhomogeneities. We find, however, that a very large number ($\gtrsim 10^4$) of DWEES must be used to account for the LPV. Large velocity dispersions must occur within DWEES, which give rise to the $\overline{\sigma_\xi} \sim 100$ km s $^{-1}$ line-of-sight velocity dispersions. We find evidence for anisotropy in the velocity dispersion within DWEES with $\sigma_{v_r} \sim 4\sigma_{v_\theta}$, where σ_{v_r} and σ_{v_θ} are the velocity dispersions in the radial and azimuthal directions, respectively. We find marginal evidence for optical depth effects within inhomogeneous features, with the escape probability

being slightly smaller in the radial direction. The kinematics of the variable features reveals lower-than-expected radial accelerations, with $20 < \beta R_*(R_\odot) < 80$, where β and R_* are parameters of the commonly used velocity law $v(r) = v_\infty(1 - R_*r^{-1})^\beta$, with v_∞ the terminal wind velocity. The mean duration of subpeak events, interpreted as the crossing time of DWEEs through the LER, is found to be consistent with a relatively thin LER. As a consequence, the large emission-line broadening cannot be accounted for by the systematic radial velocity gradient from the accelerating wind. Rather, emission-line broadening must be dominated by the large “turbulent” velocity dispersion σ_{v_r} suggested by the LPV patterns.

The remaining WR star in our sample (HD191765) is shown to present significant differences in its LPV pattern. In particular, the associated mean velocity dispersion is found to be especially large ($\overline{\sigma_\xi} \sim 350 \text{ km s}^{-1}$ compared to $\overline{\sigma_\xi} \sim 100 \text{ km s}^{-1}$ in other stars). Accordingly, the LPV patterns in HD191765 cannot be satisfactorily accounted for with our model, requiring a different origin.

Subject headings: *Instabilities – line: profiles – methods: data analysis – stars: Wolf-Rayet*

3.1 Introduction

The spectra of Wolf-Rayet (WR) stars are dominated by broad emission-lines of Helium, with lines of Nitrogen in stars of the WN sequence, or Carbon and Oxygen in stars of the WC/WO sequence. These lines are sometimes accompanied by blue-shifted P Cygni absorption features. The generally accepted interpretation is that the lines are formed in extended regions of a fast ($\sim 10^3$ km s $^{-1}$), dense ($\sim 10^{-5}$ M $_{\odot}$ yr $^{-1}$) stellar wind (e.g. Willis 1991). The spectral analysis of WR stars is made difficult by the fact that the usual assumptions of local thermodynamic equilibrium and plane-parallel atmospheres do not apply. Moreover, WR winds are believed to be stratified in ionization (e.g. Schulte-Ladbeck *et al.* 1995), which means that emission-lines from different atomic transitions are formed at different depths in the wind.

Current models of WR atmospheres rely on a set of simplifying assumptions within the framework of the so-called *standard model* (e.g., Hillier 1995, Hamann 1995, and references therein), which describes the formation of emission-lines in a dense wind photo-ionized by a hot core. In the standard model, it is assumed that the wind is spherically symmetric, homogeneous, and stationary. Radiative and statistical equilibrium are adopted, and a monotonic wind velocity law is fixed *a priori*. These assumptions have been used to perform spectral analyses of WR spectra and to predict effective temperatures and luminosities. However, several systematic deficiencies have been observed (e.g. Howarth & Schmutz, 1992; Hamann *et al.* 1994; Hillier 1996; Schmutz 1997), which suggest that at least some assumptions in the standard model are invalid.

The picture of a smooth, homogeneous wind in WR stars is being challenged by several lines of observational evidence (cf. Moffat 1996b). Since it is believed that inhomogeneous winds might lead to a downward revision of the mass-loss rate (Moffat & Robert 1994), this would have important implications for evolutionary

models of massive stars (Maeder 1991). Recently, some attempts have been made to relax certain assumptions of the standard model (Hillier 1996, and references therein), and spectral analysis using clumped wind models has been attempted (Schmutz 1997; Hillier & Miller, 1998).

The difficulty in establishing realistic, inhomogeneous wind models is that clues about the degree of clumping have mainly come from indirect observational methods. For example, continuum emission excess in the infra-red and radio was observed in 18 early-type stars (Runacres & Blomme, 1996), which is interpreted as excess free-free emission due to wind over-densities (Lamers & Waters, 1984). Though models of inhomogeneous winds were shown to reproduce the IR and radio excess well (Blomme & Runacres, 1997), only limited constraints on the *detailed* density structure could be obtained, since observations mostly depend on the *global* effects of clumping. Stochastic variations in polarization and photometry of single WR stars was also interpreted in terms of residuals from a clumped wind (Robert *et al.* 1989). Other examples include measures in the intensity of the electron scattering wings in some WR emission lines (Hillier 1991), the relative intensity of the IR lines of He I and He II (Nugis & Niedzielski, 1995), and λ -dependence in the secondary eclipse in V444 Cyg (Cherepashchuk *et al.* 1984).

Although we can directly observe details in the clumpy structure of wind-blown bubbles around Wolf-Rayet stars (cf. Marston 1997), we cannot yet directly resolve regions close to the star, where emission-lines are formed and the wind is presumably driven by the intense radiation field. In the near future, it might be possible to resolve this wind region in γ^2 Vel, the closest WR star at ~ 250 pc (van der Hucht *et al.* 1997; Schaerer *et al.* 1997), using optical interferometric imaging techniques (cf. Vakili *et al.* 1997). Still, most WR stars will remain out of reach, at least initially.

Another technique which can provide *limited* resolution of the inhomogeneous structure of the wind, and which is independent of the distance, is high-

resolution spectroscopy of broad emission lines. Because of the large Doppler-shifts induced by the high wind velocity, regions in the wind having large differences in their *line-of-sight* velocity can be resolved on the emission-line spectrum. Early observations showed rapidly fluctuating features in the broad C III $\lambda 5696$ emission-line profile of the WC7 component in the binary star HD152270 (Schumann & Seggewiss 1975). These were interpreted as spectroscopically resolved, moving clouds or knots in the expanding wind. Later, high resolution spectroscopic monitoring of the He II $\lambda 5412$ emission-line in the WN6 star HD191765 revealed many narrow, moving, emission features superposed on the emission-line profile (Moffat *et al.* 1988). These appeared to be the trace signature of clumps being accelerating along with the wind, and emitting for a few hours as they passed through the line-emission region (LER). Extensive monitoring of 9 WR stars of various subtypes showed this phenomenon to be present in each star observed (Robert 1992; Robert 1994), and to be apparently stochastic. Similar, but periodic LPV were also observed in some apparently single stars: e.g. in HD191765 (Vreux *et al.* 1992; McCandliss *et al.* 1994), and in EZ CMa (Robert *et al.* 1992; St-Louis *et al.* 1995; Morel *et al.* 1997). It is suspected that these periodic variations are linked either to the presence of a compact companion, or to the rotation of global wind structures. But whereas such a periodic behavior is observed only in a few stars, stochastic variations seem to be present in every WR star observed so far.

A phenomenological model has been suggested to explain the LPV patterns in terms of local over-densities (termed *blobs* or *clumps*) in WR winds, as being related e.g. to compressible, supersonic turbulence (Robert 1992; Moffat *et al.* 1994). Each clump presumably follows the general wind expansion, giving rise to one emission-line subpeak as it moves in, through, and out of the LER. A similar inhomogeneous wind model had previously been investigated (cf. Antokhin *et al.* 1992) in relation to deviations in the shape of an emission-line profile for a clumped wind. A review of the simultaneous photometric, spectroscopic,

and polarimetric variations expected from such a clumped wind model has been presented elsewhere (Brown *et al.* 1995).

In the first paper of this series (Lépine *et al.* 1996, hereafter Paper I) we performed a preliminary analysis of LPV in emission-lines of WR stars using the clumped wind hypothesis as a working model. We investigated the effects on the LPV patterns of a hierarchy of inhomogeneous elements in WR winds, which might result from the presence of self-structured chaos (e.g., compressible turbulence) in the wind (Robert 1994, Henriksen 1994). This involved a study of the LPV in a static situation (i.e. snapshots of the emission line).

In this second paper, we investigate the LPV patterns in a more general way, in terms of a complete, phenomenological model of radially propagating, discrete wind elements. We first present a database which comprises sets of high-resolution spectra of optical emission-lines from 9 WR stars (§2). Our phenomenological formalism is then presented, which allows for a simplified but general description of the inhomogeneous structure from a WR wind (§3). We use this working model to generate synthetic spectral time-series, which are analyzed in order to determine which information can be obtained from the LPV patterns (§4). We are helped in this by the introduction of two numerical tools which provide a systematic analysis of the LPV pattern. We perform a comparative analysis between the data and the simulations, and obtain various constraints on the inhomogeneous wind structure of the WR stars in our sample. The results are discussed in §5. A summary is presented in the final section (§6).

3.2 Spectroscopic Observations

A set of high signal-to-noise ($S/N > 200$), high-resolution ($\lambda/\Delta\lambda \sim 30,000$) spectra of emission lines from 9 WR stars, was obtained from two observing runs at CFHT in 1987 and 1988, and one at ESO in 1989. Reduction and preliminary

TABLEAU 3.1. Sample of Wolf-Rayet stars observed.

HD	WR ^a	Sub-type	Orb. Period	v_∞ (km s ⁻¹) ^b	# Spectra	S/N_{cont}
96548	40	WN8	-	975	16	350
164270	103	WC9	-	1190	30	210
165763	111	WC5	-	2415	28	150
191765	134	WN6	-	1905	36	190
192103	135	WC8	-	1405	26	180
192163	136	WN6	-	1605	26	200
192641	137	WC7+OB	12.6 yr ^c	1885	25	240
193077	138	WN5+OB	4.2 yr ^d	1345	18	230
193793	140	WC7+O4-5	7.94 yr ^e	2900	23	380

^a WR number from the van der Hucht *et al.* (1981) catalog.

^b Terminal wind velocities from Prinja *et al.* (1990).

^c From Williams *et al.* (1996).

^d From Annuk (1990).

^e From Williams *et al.* (1990).

analysis was carried out by C. Robert as part of her Ph.D. thesis (Robert 1992). Basic characteristics of the selected targets are presented in Table 1. The CFHT spectra cover the optical region around the C III $\lambda 5696$ line for the WC stars WR135, WR137, and WR140, and around the He II $\lambda 5411$ line for the WN stars WR134, WR136 and WR138. The ESO spectra of stars WR40, WR103, and WR111, cover a broader range with several emission lines (5200Å-5900Å), but here we chose to study the same lines in each case as observed at CFHT, since these lines are the strongest, isolated emission lines in the spectra of WC and WN stars. The temporal resolution and coverage (one spectrum every hour or so over an interval of ~ 8 hours in each of 3 or 4 consecutive nights) make these spectral time-series well suited for a comprehensive study of the LPV on short time-scales.

We present a compact display of the observed LPV: time-wavelength grey-

scale plots of the residuals after subtracting off the mean line profile are shown in Figs.1-3. These clearly reveal the presence of moving spectral features (subpeaks). The most apparent subpeaks have full widths at half maximum (FWHM) ranging from $\sim 2\text{-}10 \text{ \AA}$, with a typical amplitude of about 2-8% of the line intensity. Residuals show subpeaks with positive (negative) amplitudes, which most likely indicate excess (lack) of emission. Absorption is unlikely, since subpeaks are exclusively observed in the spectral range spanned by the line-emission profile (Robert 1992). Subpeaks systematically move from line center towards line edges (Moffat *et al.* 1988; Robert 1992). This behavior rules out both non-radial pulsations, or any rotation/orbital motion hypothesis, since half the subpeaks on average would then be expected to move *towards* the line center. Rather, these data are consistent with wind features accelerated outward along radial trajectories.

The central wavelength of a subpeak corresponds to the mean line-of-sight velocity of one local wind feature (via the Doppler effect). The subpeak width presumably reflects a dispersion in velocity within the feature. Such internal velocity dispersions may arise from thermal or turbulent motions, but also from a systematic velocity gradient throughout the feature (e.g. from a shock discontinuity). Subpeaks near the edges on the emission-line profile have the largest apparent line motion (i.e. line-of-sight acceleration), whereas subpeaks near the center appear to be almost stationary. This can be naturally explained as a consequence of the radial motion of wind features. With line-of-sight velocity $\xi = v\mu$, where $\mu = \cos(\theta)$ is the projection factor relative to the line of sight ($\theta = 0$), one sees that a radial motion having $\mu = \text{const}$ implies a spectral motion $\dot{\xi} = \dot{v}\mu$. In a shell-like region centered on the star, the wind has approximately constant radial velocity v and acceleration \dot{v} , which yields $\dot{\xi} \propto \xi$, similar to what is observed.

On the grey-scale plots in Figs.1-3, the eye catches what appear to be a few

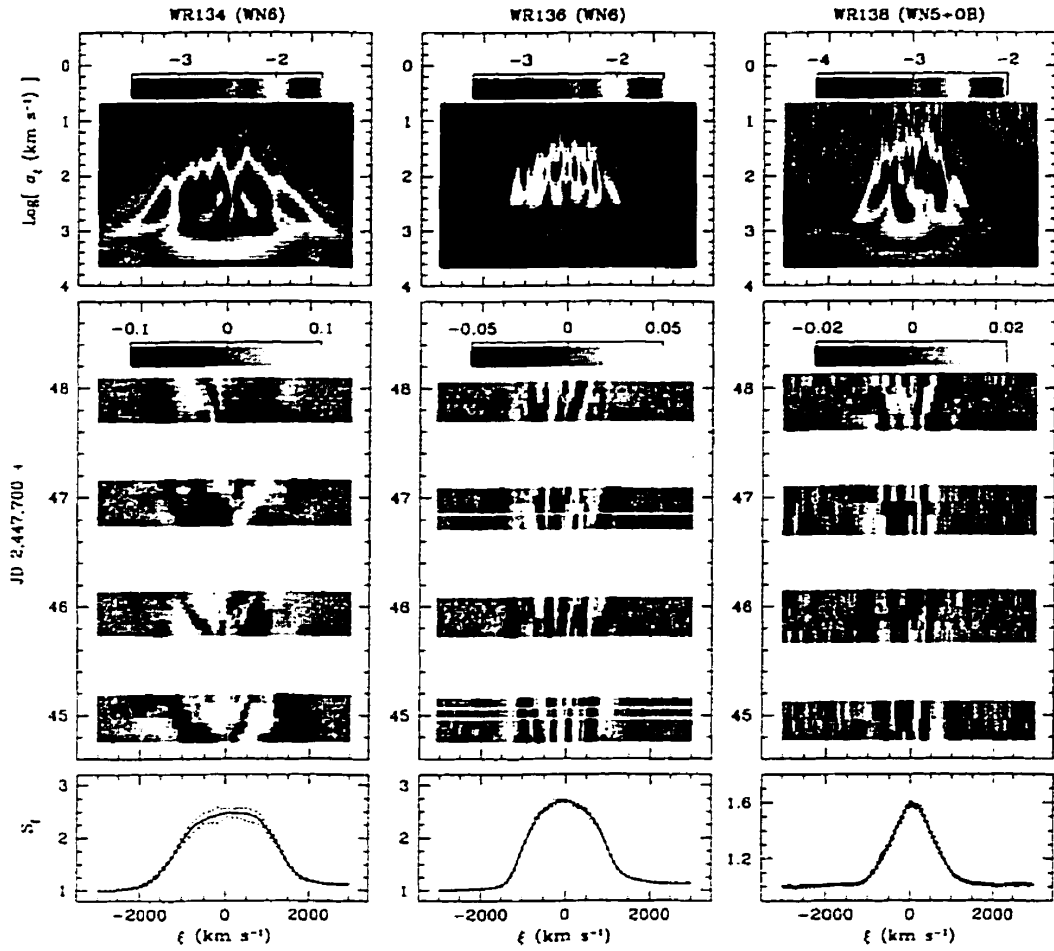


FIGURE 3.1. Plot of the LPV observed in HD191765 (= WR134), HD192163 (= WR136), and HD193077 (= WR138). Bottom panels show the minimum, mean, and maximum measured values in the intensity in the He II $\lambda 5411$ emission line for the whole observing run. Center panels show time-resolved plots of the residuals after subtracting off the mean profile. The color displays show the wavelet spectrum from each time-series. The wavelet spectrum identifies the typical location (ξ) and scale (σ_ξ) of the variable features in the LPVs. Note the outstanding behavior of WR134, where the variable subpeaks are broader and a 2.3 day period occurs. Narrow subpeaks in the other stars appear to be stochastic.

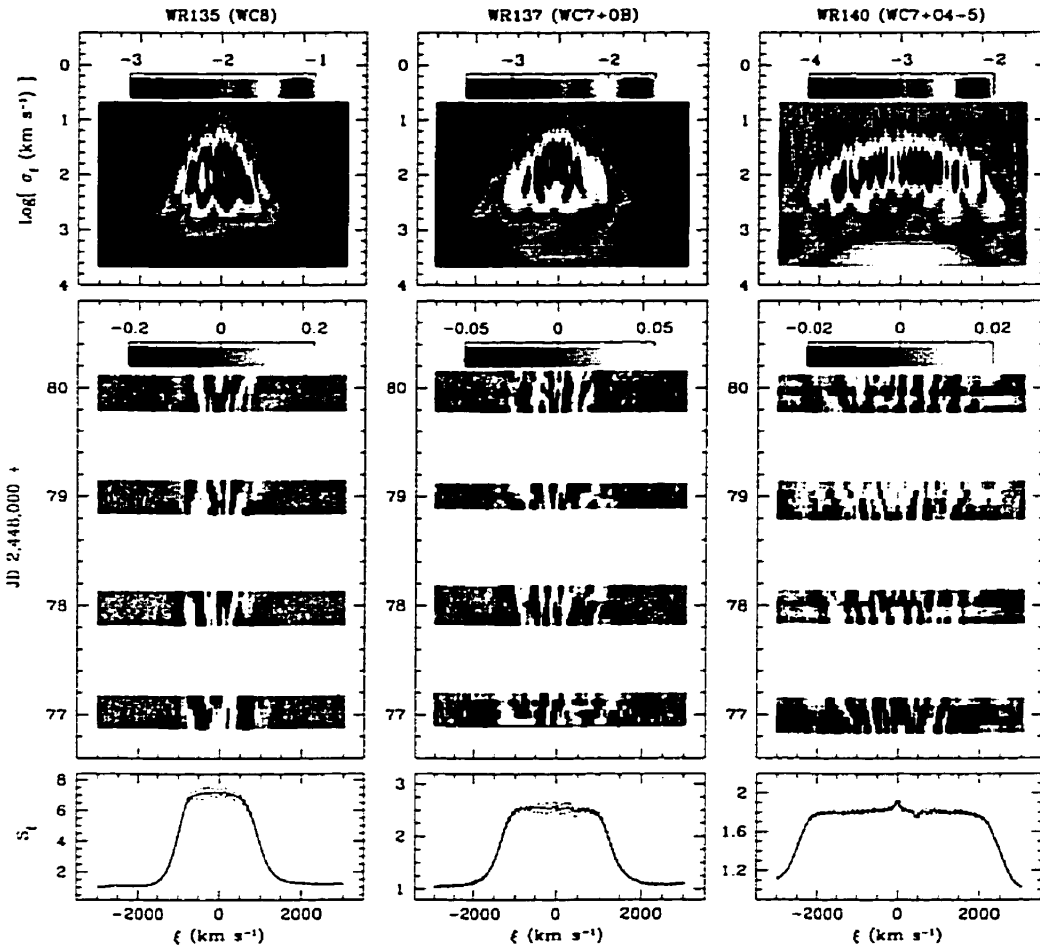


FIGURE 3.2. Plot of the LPV observed in the C III $\lambda 5696$ emission line in HD192103 (= WR135), HD192641 (= WR137), and HD193793 (= WR140), with the same display as in Fig.1. One can see that subpeaks tend to propagate from lower to higher $|\xi|$. Note how the number of apparent subpeaks increases with the emission line width, an artifact which is explained in §4.1.

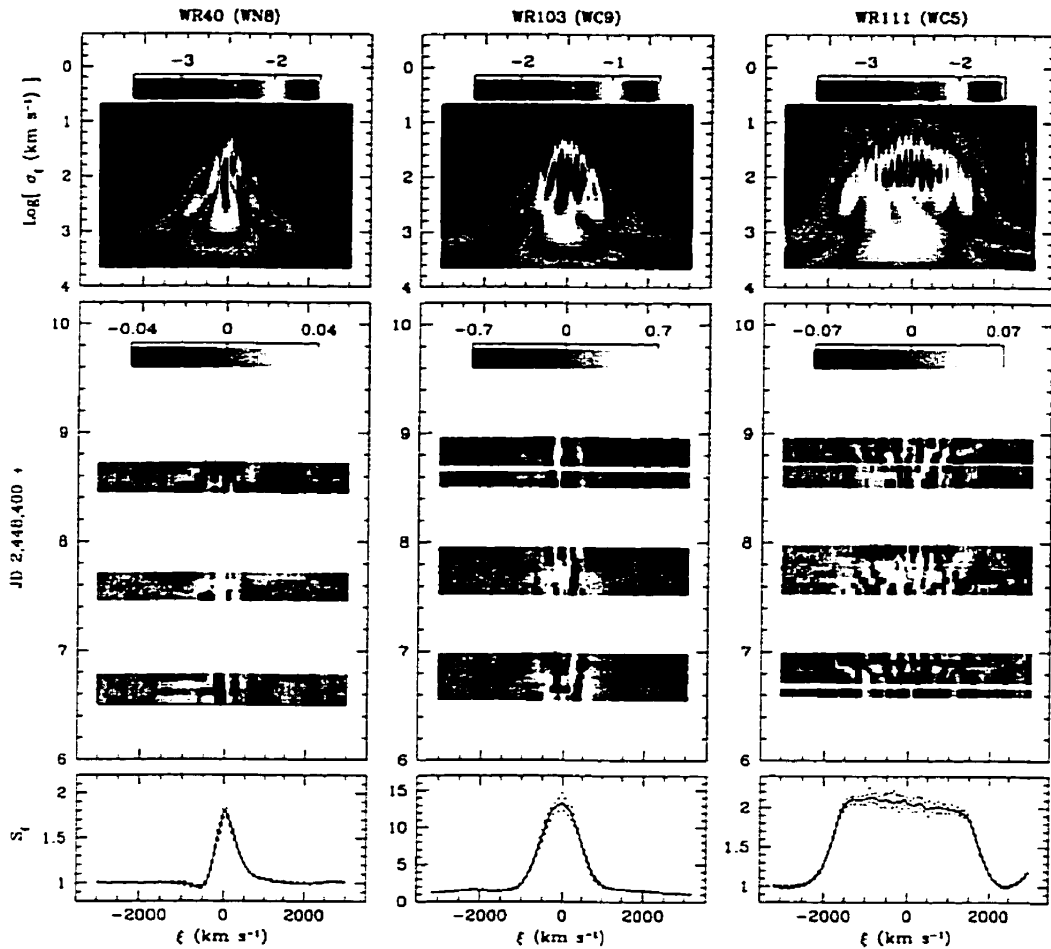


FIGURE 3.3. Plot of the LPV observed in the He II $\lambda 5411$ emission line in HD96548 (= WR40), and in the C III $\lambda 5696$ emission line in HD164270 (= WR103) and HD165763 (= WR111), with the same display as in Figs.1-2. The wavelet spectra reveal that, in all 9 WR stars, the scale σ_ξ of variable subpeaks is smaller near the line center $\xi = 0$ and larger near the edges.

moving subpeaks. It is tempting to assume each of these apparent features to arise in a single wind event (cloud or clump). It then appears possible to enumerate how many clump events instantaneously occur in the LER. Unfortunately, this is an overly simplistic interpretation of the data. In Paper I, we have shown that the few apparently individual subpeaks uncovered either by eye or by any other kind of structure identifier (such as multi-gaussian fitting), may actually result from the sum of a large number of independent wind events. Only a few features actually appear because of superposition and blending effects. Therefore, the characteristics of apparent subpeaks *extracted* from the data can be biased, because they depend on the way in which subpeaks superpose in line-of-sight velocity space. This is why we have introduced numerical tools, such as the wavelet transform, which analyze the LPV pattern as a whole, instead of a few apparently independent components.

Wavelet analysis is analogous to a windowed Fourier transform in that it yields simultaneous information on both the *scale* and *location* of features in a signal. We have already discussed the advantages of the wavelet transform over Fourier transform (cf. Paper I). We provide in appendix A a brief review of our wavelet analysis method. One powerful tool is the *wavelet spectrum* which is like a multi-scale analyzer. We present in Figs.1-3 the mean wavelet spectrum $\langle \hat{R}(\xi, \sigma_\xi) \rangle$ of the residual spectra from each star. The wavelet spectra show striking patterns which can be interpreted as consisting of two components: (1) a more or less uniform response over location ξ , which gradually decreases from small to medium scale σ_ξ , on which is superposed (2) a triangular-like pattern with maximum response near $\sigma_\xi \sim 10^2 \text{ km s}^{-1}$ (except for WR134 where the maximum is nearer to $\sigma_\xi \sim 10^{2.5} \text{ km s}^{-1}$) and centered on $\xi = 0$. The first component is the wavelet response to instrumental noise, which is uniform over the spectrum, and yields the highest response at the smallest scales (pixel-to-pixel variation). The second component is the wavelet response to intrinsic LPV, as evidenced from the fact that the response correlates strongly with the emission-line profile, and

shows up on scales which are much larger than pixel-to-pixel variations.

The mean wavelet spectra provide clear evidence that the scale (width) of emission subpeaks depends on their location on the line; LPV are made up of narrow subpeaks near the line center, and broader ones near the edges. This behavior shows up especially well for the broadest emission lines (cf. WR140). We note that the location where the narrowest intrinsic subpeaks are found coincides with $\xi = 0$. The pattern is also symmetrical around $\xi = 0$, indicating that the width of a subpeak does not depend on the sign of its line-of-sight velocity.

The general, multi-scale properties of LPV can be studied with the *mean wavelet power spectrum*. We have plotted in Fig.4 the mean wavelet power spectrum $\langle \tilde{R} \rangle_{LPV}$ of the residuals averaged over the spectral domain ξ (see appendix A). The maximum in $\langle \tilde{R}(\sigma_\xi) \rangle_{LPV}$ yields an approximate measure for the mean line-of-sight velocity dispersion $\overline{\sigma_\xi}$ of LPV subpeaks. Most stars show a maximum in the range $80 < \sigma_\xi < 150 \text{ km s}^{-1}$. Stars WR134 and WR40 show broader features, with $\overline{\sigma_\xi} \simeq 350 \text{ km s}^{-1}$. We suspect that the broad subpeaks in WR40 might result from variations in the whole line profile which can be confused, on residual spectra, with broad subpeaks having the width of the emission line. In any case, the wavelet spectrum of WR40 in Fig.4 suggests the occurrence of narrow features on a scale similar to that found in other stars. On the other hand, the LPV in WR134 seem to be dominated by broad subpeaks; there is no clear evidence for a distinct population of narrow subpeaks. Thus, WR134 appears to be a special case. Indeed, whereas observations suggest that LPV in the other WR stars are stochastic, recurrence in the LPV patterns have been detected for WR134 (McCandliss *et al.* 1994), confirmed and interpreted as being related to the rotation of a structured wind (Morel *et al.* 1998).

We note that the small-scale behavior of $\langle \tilde{R}(\sigma_\xi) \rangle_{LPV}$ depends on the observing run. In the first CFHT run (WR134, WR136, and WR138), the wavelet power in the range $0.5 < \text{Log}[\sigma_\xi (\text{km s}^{-1})] < 1.2$ is more or less uniform,

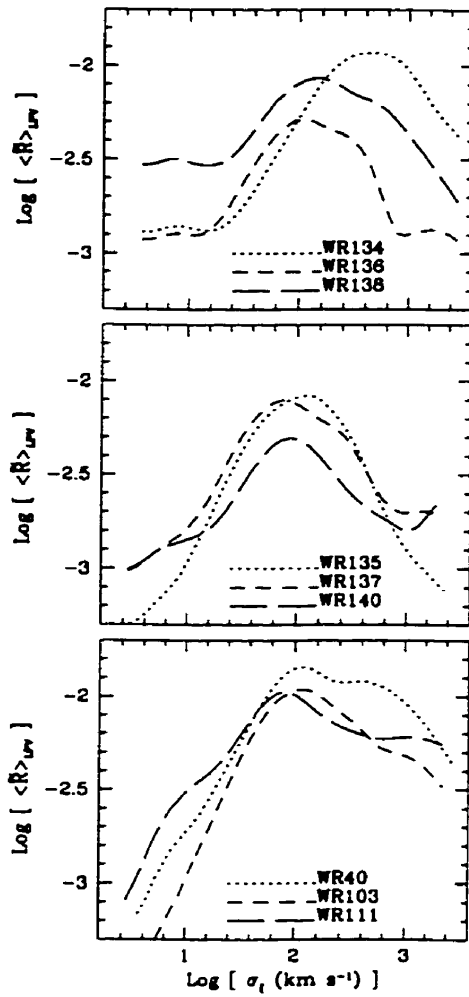


FIGURE 3.4. Mean wavelet power spectrum $\langle \tilde{R}(\sigma_\xi) \rangle_{LPV}$ for all the spectral time-series in our data set. All stars show a maximum at $\sigma_\xi \simeq 100 \text{ km s}^{-1}$, except for WR134 which has a maximum near $\sigma_\xi \simeq 350 \text{ km s}^{-1}$. The width of the stochastic subpeaks is apparently independent of the star observed, but the periodic subpeaks in WR134 are significantly broader. Note how the behavior of $\langle \tilde{R}(\sigma_\xi) \rangle_{LPV}$ at small σ_ξ depends on the observing run, indicating variable noise quality and statistics.

whereas in the second run (WR135, WR137, and WR140), the wavelet power increases proportionally with σ_ξ . It appears that the scaling properties of the CFHT instrumental noise are epoch dependent. In the ESO run (WR40, WR103, and WR111), there is a sharp drop in power below $\text{Log}[\sigma_\xi \text{ (km s}^{-1}\text{)}] \sim 0.8$; this arises because a smoothing procedure was applied to this particular data set in the reduction procedure, to remove a contaminating high-frequency signal (Robert 1992).

Our wavelet analysis technique has some advantages over other methods for the identification of intrinsic variability, such as the temporal variance spectrum (TVS) technique (Fullerton 1990, Robert 1992). The TVS compares the variability at each pixel with that expected from instrumental noise, accounting for the quality of each individual spectrum. But while TVS works on pixel elements individually, the wavelet analysis separates the variable features according to their scale (in wavelength space), and thus can make use of the fact that some intrinsic subpeak features may occupy several neighboring pixels. The wavelet spectrum may thus effectively separate the generally small-scale instrumental noise from the intrinsic large-scale features, yielding a straightforward detection of the latter.

3.3 Phenomenological, Clumped Wind Model

3.3.1 Discrete wind emission elements

The intrinsic, stochastic subpeaks can be described as statistical fluctuations arising in a distribution of discrete emission features. The amplitude of the fluctuations should depend on the number of discrete elements as well as on their individual flux. Assume that the line emission can be represented as arising in a finite number N_e of “discrete wind emission elements” (DWEEs). Line emission from a single DWEE arises as the associated wind feature passes through the LER, where the ionization balance is such as to stimulate the emission from the

given atomic transition. The LER is expected to span some well-defined range from the underlying WR star. Line variability is expected to occur because the discrete wind elements will successively move in and out of this LER. Our model of LPV is therefore very simple: every DWEE has an assigned location in the wind; as this location changes (according to the wind velocity law) the DWEE enters the LER, and yields a discrete subpeak on the emission-line profile; this subpeak vanishes as the DWEE leaves the LER. This is sufficient to reproduce the observed LPV patterns with reasonable fidelity.

Let $[r_i, \mu_i, \phi_i]$ be the coordinates of the i^{th} DWEE, in a spherical coordinate system centered on the star, with $\mu_i = \cos \theta_i$. We assume that the wind is radially expanding, and that the expansion follows a monotonically increasing velocity-law $v(r)$. It simplifies things to calculate the problem in the directly observable bulk wind velocity space, and use the coordinates $[v_i, \mu_i, \phi_i]$, with $v_i = v(r_i)$. Let $s_i = s_i(\xi)$ be the spectral emission (subpeak) arising from the i^{th} DWEE, where we use the line-of-sight Doppler velocity $\xi \equiv \lambda_0^{-1}(\lambda - \lambda_0)c$, with λ_0 the rest wavelength of the line radiation and c the speed of light. We assume that $s_i(\xi)$ is of the form:

$$s_i(\xi) = \frac{F_i}{\sigma_{\xi_i} \sqrt{\pi}} \exp \frac{-(\xi - \xi_i)^2}{\sigma_{\xi_i}^2}. \quad (3.1)$$

Here, F_i is the integrated emission-line flux from the DWEE; ξ_i and σ_{ξ_i} are the spectral location and width of the subpeak feature, respectively.

The parameter ξ_i corresponds to the mean line-of-sight velocity of the emitting material in the DWEE: i.e. $\xi_i = \mu_i v_i$. Since the DWEE is moving, it is implicitly assumed that $v_i = v_i(t)$. The value for v_i at any given time can be obtained from the wind velocity law $v = v(r)$ (see §3.2 below). Since we assume that DWEEs only move radially, μ_i is a constant. The velocity dispersion σ_{ξ_i} reflects the motion of atoms associated with the DWEE. This includes thermal and turbulent motions, as well as possible systematic velocity gradients within the element. Values for σ_{ξ_i} might vary with distance from the star, and velocity

dispersion might be anisotropic. As we will show (§3.3), the LER does not usually span a large domain in wind bulk velocity, and possible variations in σ_{ξ_i} with depth can be neglected. However, we do need to consider possible anisotropic effects (§3.4).

The observed global emission-line profile $S(\xi)$ will result from the combination of a large number N_e of DWEEs:

$$S(\xi) = \sum_{i=1}^{N_e} s_i(\xi) . \quad (3.2)$$

We expect the resulting emission-line profile to be variable, depending on the mean number of DWEEs. An inhomogeneous wind with a very large $\overline{N_e}$ should yield a line profile very close to that of a smooth wind, whereas a wind with a small $\overline{N_e}$ will result in high levels of variability. The patterns of LPV, however, will be critically dependent on the wind velocity law and on the geometry of the LER, as well as on the statistical distribution of fluxes from individual DWEEs.

3.3.2 The velocity law

The velocity-law describes the bulk motion of the accelerated wind material as a function of distance from the star. The most popular velocity-law typically used in models of hot-star winds is the so-called β -law (Castor & Lamers, 1979):

$$v(r) = v_\infty \left(1 - \frac{R_*}{r}\right)^\beta , \quad (3.3)$$

which is given here in its simplest version, with v_∞ the terminal velocity of the wind and R_* some spatial dimension of the order of the stellar radius. This law is a parameterized generalization of a law that arises from the theory of radiation-driven winds (Castor *et al.* 1975, the so-called CAK model). Different values of β , typically in the range [0.5, 4.0], have been used in the literature for different models and stars.

In the approximation of point source stars, the CAK theory predicts a velocity law with $\beta = 0.5$. When finite disk effects are considered, the CAK theory yields $\beta = 0.8$ (Friend & Abbott, 1986). In modeling the winds of OB and WR stars, the velocity field is usually assumed to follow the β -law, but the value of β is left as a free parameter. A value of $\beta \simeq 1$ has been successfully used for models of stellar winds from OB stars (Puls *et al.* 1996), while observations of LPV subpeaks in WR winds suggest much larger values of β (Robert 1994). This is supported by recent spectral analysis of WR spectra with a clumped wind model (Schmutz 1997), which yields fits of the velocity law with $\beta \simeq 4 - 8$.

The β -law yields an “acceleration law” in the form:

$$a(r) \equiv \frac{dv}{dt} = v \frac{dv}{dr} = \frac{v_\infty^2}{R_*} \left(\frac{R_*}{r} \right)^2 \beta \left(1 - \frac{R_*}{r} \right)^{2\beta-1}. \quad (3.4)$$

The acceleration a can also be expressed as a function of the local, bulk wind velocity v :

$$a(v) = \beta \frac{v^2}{R_*} \left[\left(\frac{v}{v_\infty} \right)^{-\frac{1}{2\beta}} - \left(\frac{v}{v_\infty} \right)^{\frac{1}{2\beta}} \right]^2. \quad (3.5)$$

It turns out that the function $\beta a(v)$ converges very fast for $\beta \rightarrow \infty$ such that, for $\beta > 1$, we may use the approximation:

$$\beta a(v) \simeq \lim_{\beta \rightarrow \infty} \beta a(v) = R_*^{-1} [v \ln(v/v_\infty)]^2. \quad (3.6)$$

Fig.5 shows the $a(r)$ and $\beta a(v)$ functions for different values of the parameter β . One sees that the approximation in Eq.6 yields values of $\beta a(v)$ to better than $\sim 5\%$ for all $\beta \gtrsim 2$. This result has important implications, because it means that unless there exists a reliable estimate of R_* (which is usually *not* the case for WR stars), it is not possible to determine β from the magnitude of the acceleration alone, since we have $a(v) \propto \beta^{-1} R_*^{-1}$. A measure of the wind acceleration as a function of the velocity, combined with a knowledge of v_∞ , only yields a constraint on βR_* . On the other hand, any large divergence from the very specific $a(v)$ function rules out the β -law as an adequate representation of the motion of inhomogeneous wind features.

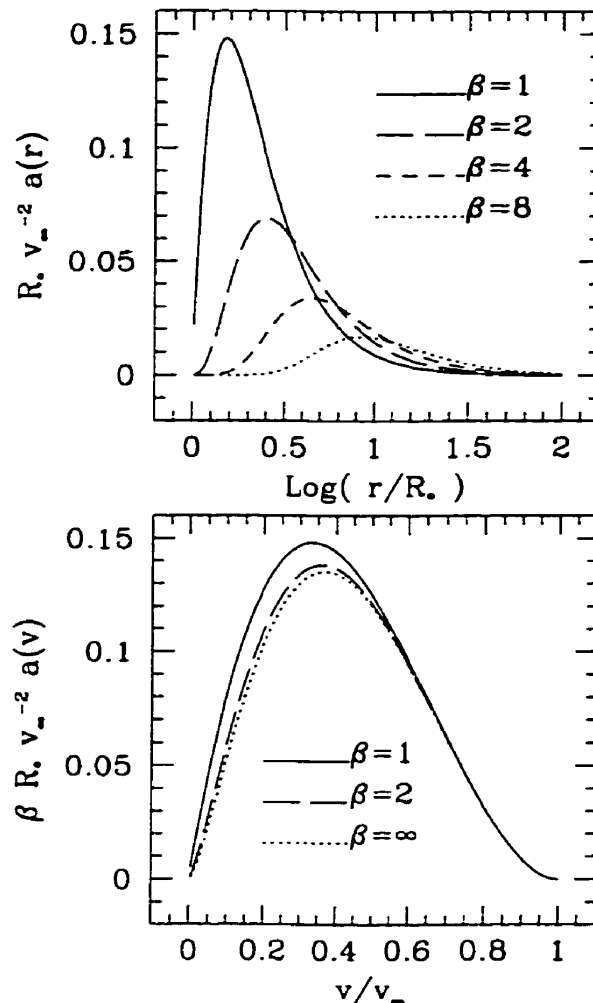


FIGURE 3.5. Illustration of the β -law, the commonly adopted velocity law used in hot star wind models. The upper panel shows the dimensionless acceleration plotted as a function of radius. In *velocity space*, however, the β -law has the same general shape for all relevant values of β (lower panel). This is crucial in the interpretation of our data, since spectroscopy only measures events in velocity space.

3.3.3 Line emission from DWEEs

The line flux F_i from each DWEE depends on its distance from the star or, equivalently, on its velocity v_i . The DWEE will be emitting line-radiation while being accelerated through the LER. Letting F_i be the emission-line flux from a DWEE, we may write $F_i = f_i f_e(v_i)$, where $f_e(v_i)$ is the dependence of the line flux with the location v_i of the DWEE in the wind, and f_i a constant which allows for the relative emission from that DWEE (no two are alike).

The most rigorous way to obtain $f_e(v_i)$, or more generally $f_e(v)$, would be to use reliable theoretical WR models. In standard models of WR winds, recombination-line emission in WR winds arises in concentric “shells”, whose depth and thickness depend on the particular line transition (e.g. Hillier 1988; Hillier 1989). The classical approach to obtain an estimate of $f_e(v)$ for one specific line transition would be to perform standard spectral analysis, and derive $\Phi_e(r)$, the emission as a function of distance from the star, from which one gets $f_e(v) \simeq \Phi_e(r(v))$, where $r(v)$ is obtained by inversion of the velocity-law $v(r)$.

But here, we are interested in obtaining the most information from observations alone. It is possible to derive an approximate expression for the *total* line flux $F_e(v)$ as a function of the radial velocity v from the shape of the emission-line profile (cf. Brown *et al.* 1997). The technique is based on the assumptions that the wind is roughly homogeneous, spherically symmetric, and optically thin. An emission-line profile can be imagined to consist of a sum of profiles arising from infinitesimally thin, concentric wind shells. It is easily shown that the emission dF of such a shell formed by wind material having velocity between v and $v + dv$ yields a spectral profile $dS(\xi, v)$ in the form:

$$dS(\xi, v) = \begin{cases} F_0 \frac{F_e(v)}{a(v)} dv, & -v < \xi < v \\ 0, & \text{otherwise,} \end{cases} \quad (3.7)$$

where $a(v)$ is the “acceleration law” (cf. Eq. 5), and F_0 some normalization con-

stant. The global line-profile $S(\xi)$ is the sum of all shells:

$$S(\xi) = \int_{v=0}^{v=v_\infty} dS(\xi, v) . \quad (3.8)$$

It is possible to solve the inverse problem (see Brown *et al.* 1997), to obtain $F_e(v)$ from the shape of the line profile $S(\xi)$:

$$F_e(v) \propto a(v) v^{-1} \left[\frac{dS}{d\xi} \right]_{|\xi|=v} . \quad (3.9)$$

This is equivalent to performing a “spherical deprojection” of the line emission, starting with the emission as a function of line-of-sight velocity ξ to obtain emission as a function of radial velocity v . We note that the observed $F_e(v)$ is expected to deviate from the theoretical $f_e(v) = \Phi_e(r(v))$, because $F_e(v)$ is affected by the existence of “turbulent” motions, which tend to increase the apparent range of line-emission in *velocity space*, whereas $f_e(v)$ should reflect the extension of the LER in *distance space* only. Both sides of the emission line profile ($\xi < 0$ and $\xi > 0$) can in principle be used to estimate $F_e(v)$. However, the red-shifted side of the emission-line ($\xi > 0$) may be affected by stellar occultation (see Ignace *et al.* 1998), and the blue-shifted side may also be affected by P Cygni-type absorption. We therefore use either the blue-shifted or red-shifted side of the line, depending on whether these biases are assumed to be significant or not.

In Fig.6 we plot $F_e(v)$, as obtained from Eq.9, for the emission-lines of the WR stars in our sample, using $a(v)$ from Eq.6 as the velocity law. We then fitted the $F_e(v)$ using a gaussian-like function, which appears to be quite appropriate:

$$F_e(v) \propto \exp \frac{-(v - v_e)^2}{\Delta v_e^2} , \quad (3.10)$$

with the free parameters v_e , the velocity regime where maximum emissivity occurs, and Δv_e , the extension of the LER in velocity space. Although this parameterization is, at best, a crude approximation of the actual emissivity function, it serves our purpose reasonably well here, since we are mainly interested in the approximate size of the region where *most* of the emission occurs, and not

TABLEAU 3.2. Wind properties from the shape of the emission-line profiles.

WR star	Transition	EW (km s $^{-1}$)	v_e (km s $^{-1}$)	Δv_e (km s $^{-1}$)
WR40	HeII $\lambda 5411$	- 460	315 ± 10	175 ± 10
WR103	CIII $\lambda 5696$	- 15500	545 ± 10	280 ± 10
WR111	CIII $\lambda 5696$	- 3580	1610 ± 10	255 ± 10
WR134	HeII $\lambda 5411$	- 3860	1090 ± 10	430 ± 20
WR135	CIII $\lambda 5696$	- 13040	890 ± 10	240 ± 10
WR136	HeII $\lambda 5411$	- 3480	905 ± 10	360 ± 15
WR137	CIII $\lambda 5696$	- 4410	1220 ± 10	260 ± 10
WR138	HeII $\lambda 5411$	- 740	620 ± 10	350 ± 15
WR140	CIII $\lambda 5696$	- 4090	2310 ± 10	265 ± 10

The line equivalent width (EW) is translated into km s $^{-1}$ units, as the line is plotted in projected velocity space ξ . Parameters v_e and Δv_e are derived from the shape of the line profile, and correspond to the mean wind velocity of line-emitting material, and to the emission-line broadening (dispersion in velocity space), respectively.

on the detailed line-emission e.g. in regions closer to the star where it is relatively small. Best fits are plotted in Fig.6 and results are listed in Table 2. For the C III $\lambda 5696$ line (WC stars), the values obtained should be reliable estimates of the size and extension of the LER (within the validity of the β -law), since the line is optically thin. On the other hand, the He II $\lambda 5411$ line in the WN stars is likely not to be optically thin, which means that the estimated size and location of the LER will be biased by the fact that optically thick lines tend to be naturally rounded (Castor *et al.* 1970). In this case, Δv_e will overestimate the actual extension in velocity space of the LER. As it turns out, the Δv_e obtained from the WN stars are significantly larger (except for the WN8 star WR40) than those measured in the WC stars.

Since the velocity dispersion Δv_e reflects the radial extension of the LER in bulk wind velocity space as well the turbulent motions within the LER region,

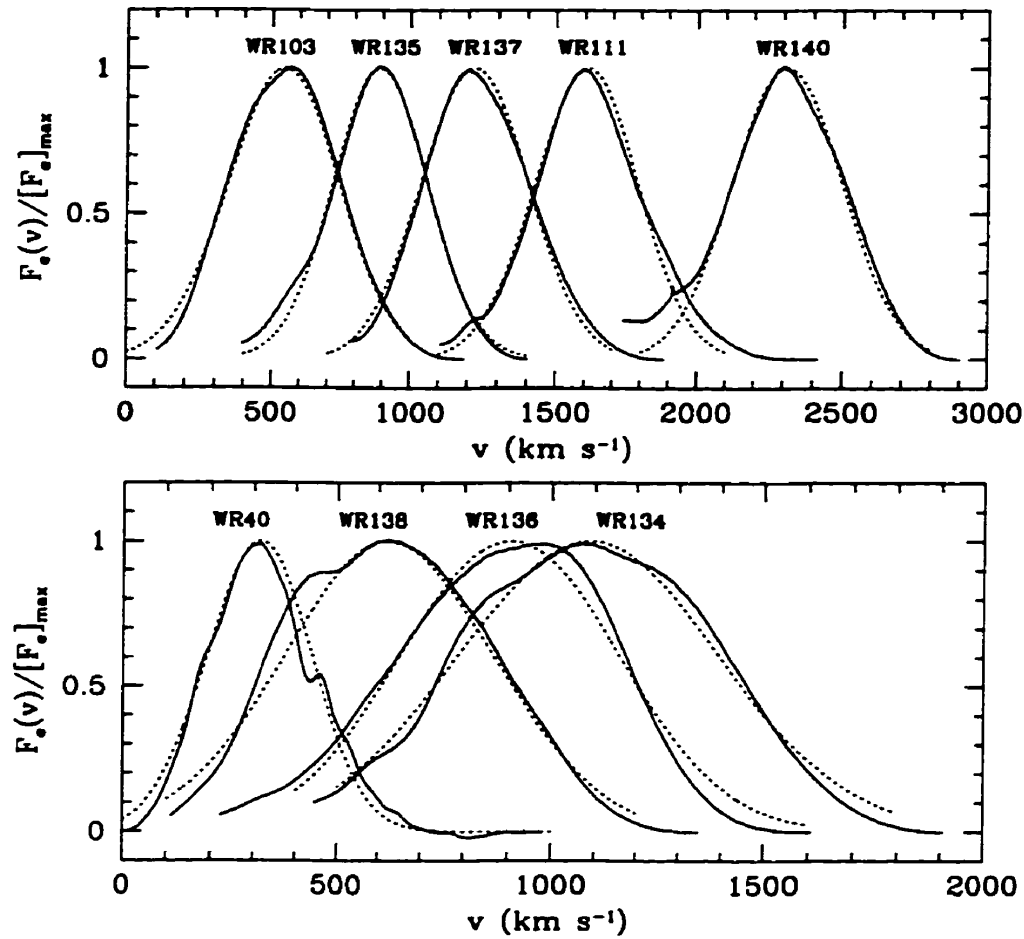


FIGURE 3.6. Deprojected emission function $F_e(v)$ for the WR stars in our sample, obtained with the method discussed in §3.3. This yields the relative emission from discrete wind elements as a function of their radial velocity. Dotted lines show the best-fit gaussian profiles, whose parameters are listed in Table 2. The mean emission-line profiles (cf. Figs.1-3) were smoothed with a low-pass filter before computation of $F_e(v)$, in order to reduce instrumental noise effects. Normalization to the maximum value $[F_e]_{max}$ facilitates the comparison between stars.

we use the relation:

$$\Delta v_e \simeq \sigma_{v_r} + \sigma_{v_e}, \quad (3.11)$$

where σ_{v_r} is a measure of the radial “turbulent” motions within the LER, and σ_{v_e} is the spatial extension of the LER translated in bulk wind velocity space. We may estimate σ_{v_r} from the widths of LPV subpeaks, assuming these to be a reliable measure of local velocity dispersions in the wind. The effective emission function $f_e(v)$ for individual DWEEs becomes:

$$f_e(v) \propto \exp \frac{-(v - v_e)^2}{\sigma_{v_e}^2}. \quad (3.12)$$

As we will show in §4.4, we can obtain an independent estimate of σ_{v_e} from an analysis of LPV patterns. This will allow us to verify the consistency of σ_{v_e} as estimated from the shape of the emission-line profile.

DWEEs are assumed not to have the same relative emission. For practical purposes, and inspired by previous studies (cf. Paper I), we will use a statistical power law distribution in the form $n(f)df \sim f^{-\alpha}df$, and let the individual fluxes f be in a range $f_0 < f < \eta f_0$, with $\eta > 1$. For F_e the mean total flux in the line-emission and N_e the mean number of DWEEs in the LER (i.e. clumps in the $v_e - \sigma_{v_e} < v < v_e + \sigma_{v_e}$ velocity regime, where most of the flux is found), we get the statistical distribution function:

$$n(f) = K_f \left(\frac{f}{f_0} \right)^{-\alpha}, \quad (3.13)$$

where K_f and f_0 are functions of the parameters F_e , N_e , α and η . These are determined with the relations:

$$N_e = \int_{f_0}^{\eta f_0} n(f) df, \quad (3.14)$$

$$F_e = \int_{f_0}^{\eta f_0} f n(f) df. \quad (3.15)$$

The flux distribution is therefore defined by four independent parameters (F_e , N_e , α , η). Of these, the total line-flux F_e is determined by the emission-line equivalent width. The distribution therefore uses three free parameters (N_e , α , η).

3.3.4 Anisotropy

The wavelet analysis has revealed that the widths of emission subpeaks depend on their location on the line profile. This suggests that DWEEs have anisotropic velocity dispersions. We model this anisotropy by expressing the velocity dispersion of DWEEs as a vector $\vec{\sigma}_v$:

$$\vec{\sigma}_v(\vec{r}) = \sigma_{v_r} \hat{r} + \sigma_{v_\theta} \hat{\theta} + \sigma_{v_\phi} \hat{\phi}, \quad (3.16)$$

where σ_{v_r} , σ_{v_θ} , and σ_{v_ϕ} , are the velocity dispersions in the radial, latitudinal, and longitudinal directions r , θ , ϕ , respectively. The scalar, line-of-sight velocity dispersion σ_ξ of one DWEE will be:

$$\sigma_\xi = \sqrt{\mu_i^2 \sigma_{v_r}^2 + (1 - \mu_i^2) \sigma_{v_\theta}^2}, \quad (3.17)$$

where we assume $\sigma_{v_\theta} = \sigma_{v_\phi}$. Consider a spherical shell confining a region of approximately constant wind expansion velocity v_c . Within this region, we get a relation between σ_ξ and ξ , namely:

$$\sigma_\xi(\xi) = \sqrt{\frac{\xi^2}{v_c^2} (\sigma_{v_r})^2 + (1 - \frac{\xi^2}{v_c^2}) (\sigma_{v_\theta})^2}. \quad (3.18)$$

Moffat & Robert (1992) already surmised this in their preliminary analysis of emission-line subpeaks of the WR star WR140, supporting evidence for anisotropic local velocity dispersion.

Similarly, we may allow for the emission from individual DWEEs to be anisotropic as well. This can happen e.g. because of optical depth effects. Following the same reasoning as for σ_ξ , we will now write the flux F_i from the i^{th} DWEE as:

$$F_i = f_i f_e(v_i) \sqrt{\mu_i^2 f_r^2 + (1 - \mu_i^2) f_\theta^2}, \quad (3.19)$$

where f_r and f_θ define escape probabilities in the directions r and θ . In the optically thin case, we use $f_r = f_\theta = 1$, whereas the optically thick case can be modeled with $f_r \neq f_\theta$.

3.4 Comparative Analysis

3.4.1 Spectroscopic resolution of wind elements

The large velocities of spherically expanding WR winds, combined with the Doppler effect, generate very broad line-profiles. Spectroscopy therefore allows the observer to resolve parts of the wind in emission-line radiation, i.e. to observe wind regions having different line-of-sight bulk velocities separately. However, a practical limit is set by local velocity dispersions (such as atomic thermal motions or turbulence) which blend the emission from regions having different spatial locations, but similar line-of-sight velocities. Let an emission line arise in a spherically expanding LER with mean radial velocity v_e , and mean local line-of-sight velocity dispersion $\bar{\sigma}_\xi$ (cf. §3). We define the *spectroscopic wind resolving power* $R_w \equiv v_e \bar{\sigma}_\xi^{-1}$. Higher values of R_w mean that a larger number of wind regions can be resolved with spectroscopy. The best results should therefore be obtained for winds having large bulk velocities and relatively small turbulent motions.

We present in Fig. 7 simulations of LPV patterns obtained from the phenomenological model presented in §3. Values of the parameters used in each simulation are listed in Table 3. The first series (SIM1, SIM2, SIM3) shows how the LPV pattern is affected by a change in v_e . All three simulations used exactly the same distribution of DWEES; only the values of v_∞ and R_* were adjusted. One notices that the number of apparent subpeaks is proportional to the width of the line (i.e. to v_e). Note how the apparent subpeaks in SIM1 break up into many resolved components in SIM3. Similar effects on the LPV patterns can be obtained by varying $\bar{\sigma}_\xi$. One example is shown by the other three simulations (SIM4, SIM5, SIM6) where, again, the same spatial distribution of DWEES was used, but with different values for their σ_ξ .

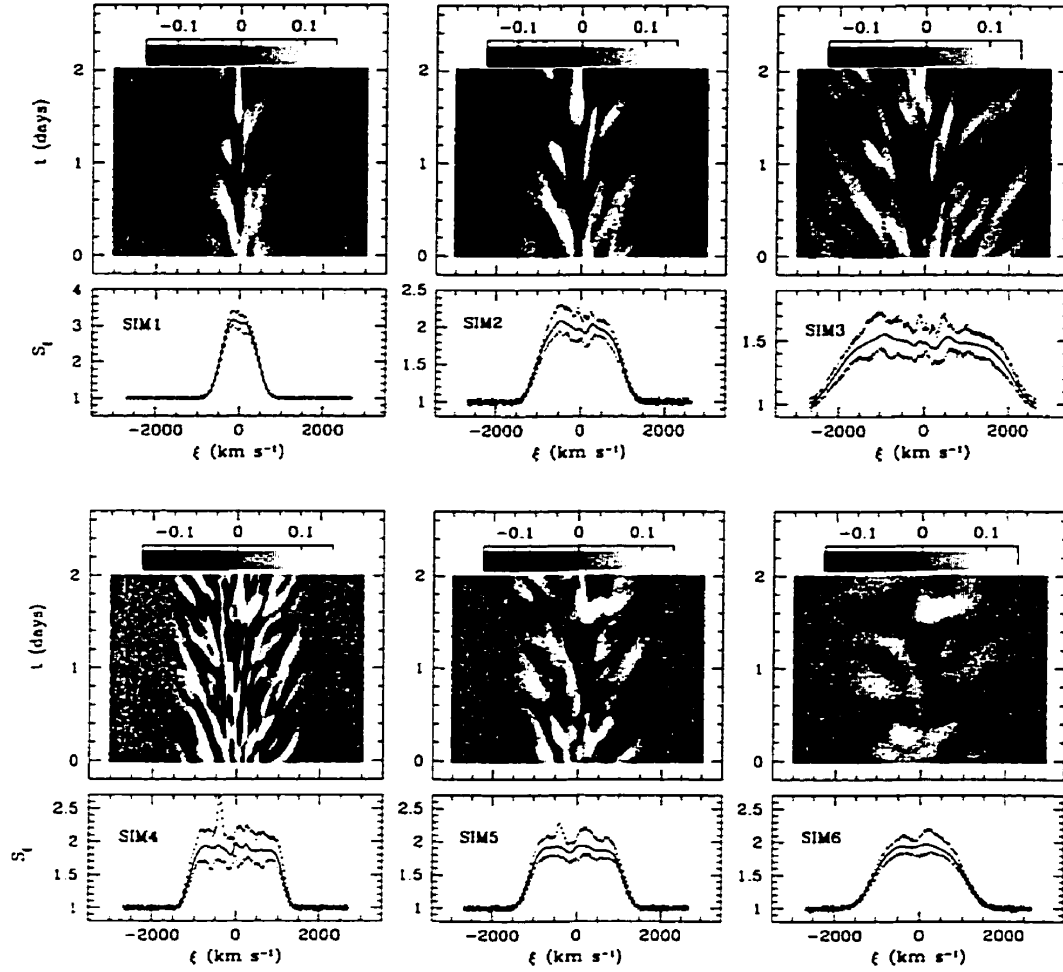


FIGURE 3.7. Simulations of LPV from our model of radially propagating DWEEs. The LPV pattern from one DWEE distribution is shown to depend on the wind terminal velocity v_∞ (top), and on the average width of emission subpeaks σ_ξ (bottom). Note how the number of apparent subpeak features is proportional to the v_∞/σ_ν ratio. Simulated spectral time-series include 60 spectra spread over a 48h time-base. The minimum, mean, and maximum line profiles are shown. Grey-scale plots show the residuals obtained after subtracting off the mean profile. The same DWEE distribution was used in SIM1, SIM2, and SIM3, and another one in SIM4, SIM5, and SIM6. Model parameters are listed in Table 3.

TABLEAU 3.3. Parameters of the simulations.

Sim #	R_*	v_∞	β	v_e	σ_{v_e}	F_e	N_e	α	η	σ_{v_r}	σ_{v_θ}	f_r/f_θ
	(R_\odot)	(km s $^{-1}$)		(v_∞)	(v_∞)	(km s $^{-1}$)				(km s $^{-1}$)	(km s $^{-1}$)	
SIM1	2.5	750	4	.65	.15	2000	10^3	4	10^4	200	75	1
SIM2	5	1500	4	.65	.15	2000	10^3	4	10^4	200	75	1
SIM3	10	3000	4	.65	.15	2000	10^3	4	10^4	200	75	1
SIM4	5	1700	4	.65	.10	2000	10^3	4	10^4	100	50	1
SIM5	5	1700	4	.65	.10	2000	10^3	4	10^4	200	100	1
SIM6	5	1700	4	.65	.10	2000	10^3	4	10^4	400	200	1
SIM7	5	2000	4	.65	.10	2000	10^4	2	10^3	200	100	1
SIM8	5	2000	4	.65	.10	2000	10^4	2	10^2	200	100	1
SIM9	5	2000	4	.65	.10	2000	10^4	2	10^1	200	100	1
SIM10	5	2000	4	.65	.10	2000	10^4	3	10^3	200	100	1
SIM11	5	2000	4	.65	.10	2000	10^4	4	10^3	200	100	1
SIM12	5	2000	4	.65	.10	2000	10^4	6	10^3	200	100	1
SIM13	5	2000	4	.65	.10	2000	10^2	3	10^3	200	100	1
SIM14	5	2000	4	.65	.10	2000	10^3	3	10^3	200	100	1
SIM15	5	2000	4	.65	.10	2000	10^5	3	10^3	200	100	1
SIM16	5	2000	4	.65	.10	2000	10^3	3	10^2	100	100	3
SIM17	5	2000	4	.65	.10	2000	10^3	3	10^2	130	65	3
SIM18	5	2000	4	.65	.10	2000	10^3	3	10^2	160	40	3
SIM19	5	2000	4	.65	.10	2000	10^3	3	10^2	100	100	1
SIM20	5	2000	4	.65	.10	2000	10^3	3	10^2	130	65	1
SIM21	5	2000	4	.65	.10	2000	10^3	3	10^2	160	40	1
SIM22	5	2000	4	.65	.10	2000	10^3	3	10^2	100	100	0.3
SIM23	5	2000	4	.65	.10	2000	10^3	3	10^2	130	65	0.3
SIM24	5	2000	4	.65	.10	2000	10^3	3	10^2	160	40	0.3

Parameter key: R_* , wind velocity-law parameter (\sim stellar core radius); v_∞ , terminal wind velocity; β , velocity-law power index; v_e , location of the LER in wind velocity space; σ_{v_e} , extension of the LER in wind velocity space; F_e , mean emission-line flux (equivalent width in units of projected Doppler velocity); N_e , mean number of DWEEs in the LER; α , power index in the statistical distribution of DWEE fluxes; η , total range in the flux from individual DWEEs; σ_{v_r} , velocity dispersion in the direction of propagation (radial); σ_{v_θ} , velocity dispersion perpendicular to propagation; f_r/f_θ , escape probability ratio.

In previous studies of LPV patterns in WR emission-lines (Robert 1994), it was found that the number of subpeaks observed on the emission-line was proportional to the terminal velocity v_∞ of the wind. In the light of our current investigation, this correlation finds an easy explanation. Because $\overline{\sigma_\xi}$ is approximately the same in all WR stars (see Fig.4), the number of apparent subpeaks should be proportional to the line width, which in turn is proportional to v_∞ . We wish to emphasize that *the number of apparent subpeaks in LPV patterns is not related to the actual number of DWEEs in the LER*; it simply reflects the spectroscopic resolving power for the emission-line. Both v_e and $\overline{\sigma_\xi}$ are intrinsic to the star. Therefore, one cannot hope to get higher R_w by instrumental means; there is a *fundamental limit* in the spectroscopic investigation of inhomogeneous wind structure. Since $\overline{\sigma_\xi}$ is apparently independent of the stellar subtype, the best WR candidates for a study of the wind structure are those with the largest v_∞ .

If N_e is the mean number of DWEEs in the emission-line region, the R_w spectroscopically resolved sectors consist of the emission from $N_e R_w^{-1}$ wind elements. Let $\overline{F_j}$ be the mean emission-line flux from the j^{th} sector. The mean flux variation σ_{F_j} induced by the statistical variation in the number of DWEEs in this sector will be:

$$\sigma_{F_j} \propto \overline{F_j} N_e^{-\frac{1}{2}} R_w^{\frac{1}{2}} . \quad (3.20)$$

We can verify this relation by comparing the wavelet spectra for the simulations shown in Fig.7. In Fig.8, we present the normalized, mean wavelet power averaged over the emission-line region $\langle \tilde{R}(\sigma_\xi) \rangle_{LPV}$. These show that, for similar values of N_e , the magnitude of the variability in the emission-line is proportional to $v_e^{\frac{1}{2}} \overline{\sigma_\xi}^{-\frac{1}{2}} = R_w^{\frac{1}{2}}$ as predicted in Eq.20.

3.4.2 Statistical distribution of DWEE fluxes

Let an emission line with total line-flux F_e be made up of a mean number N_e of DWEEs. If $n(f)$ is the statistical distribution in flux of individual DWEEs,

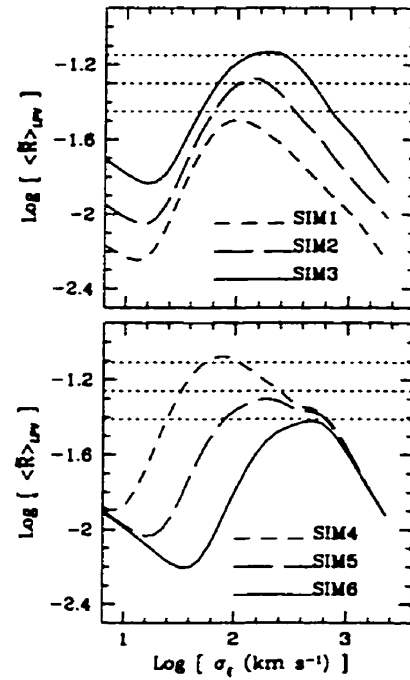


FIGURE 3.8. Wavelet power spectrum $\langle \tilde{R}(\sigma_\xi) \rangle_{LPV}$ for the six simulations in Fig.7. Dotted horizontal lines, spaced by $1/2 \log(2)$ intervals, show that the LPV amplitude is proportional to $v_\infty^{1/2}$ and inversely proportional to $\sigma_v^{1/2}$. Note that the locations of the maxima in $\langle \tilde{R}(\sigma_\xi) \rangle_{LPV}$ depend on the mean scale σ_ξ of LPV subpeaks.

the standard deviation σ_{F_e} in the total line flux will be given by:

$$\sigma_{F_e}^2 = \int_{f_0}^{\eta f_0} f^2 n(f) df . \quad (3.21)$$

Under the power law distribution given in Eq.13, σ_{F_e} has the general form:

$$\sigma_{F_e} = F_e N_e^{-\frac{1}{2}} \sigma(\alpha, \eta) . \quad (3.22)$$

We can calculate the function $\sigma(\alpha, \eta)$ from Eqs.13-15:

$$\begin{aligned} \sigma(\alpha, \eta) &= \left(\frac{\eta^{1-\alpha} - 1}{1 - \alpha} \right)^{\frac{1}{2}} \left(\frac{\eta^{2-\alpha} - 1}{2 - \alpha} \right)^{-1} \left(\frac{\eta^{3-\alpha} - 1}{3 - \alpha} \right)^{\frac{1}{2}}, \quad \alpha \neq 1, 2, 3 ; \\ \sigma(1, \eta) = \sigma(3, \eta) &= \left(\frac{\ln \eta}{2} \frac{\eta + 1}{\eta - 1} \right)^{\frac{1}{2}} ; \quad \sigma(2, \eta) = \left(\frac{\eta - 1}{\sqrt{\eta} \ln \eta} \right) . \end{aligned} \quad (3.23)$$

In the case where all the DWEES have approximately the same flux (e.g. if $\eta \rightarrow 1$), $\sigma(\alpha, \eta)$ converges to 1, and we get the familiar relation $\sigma_{F_e} = F_e N_e^{-\frac{1}{2}}$.

A plot of $\sigma(\alpha, \eta)$ as a function of α for different η is presented in Fig.9. One sees that significant deviations from the $\sigma_{F_e} = F_e N_e^{-\frac{1}{2}}$ relation occur for small positive values of α and for large η . Deviations occur when the statistical distribution is such that the total flux F_e is dominated by low-flux elements, while the fluctuations are mainly caused by high-flux elements making a small, but non-negligible contribution to F_e . Thus, $\sigma(\alpha, \eta)$ converges to 1 for small values of η and for large values of α , because these cases represent situations where the number of high-flux elements is negligible.

For an emission line profile $S(\xi)$ the standard deviation in the amplitude σ_S will be proportional to σ_{F_e} , but will also depend on the spectroscopic wind resolution:

$$\sigma_S \propto \sigma(\alpha, \eta) N_e^{-\frac{1}{2}} R_w^{\frac{1}{2}} . \quad (3.24)$$

So far, we have used the normalized wavelet power spectrum $\langle \tilde{R}(\sigma_\xi) \rangle_{LPV}$ to measure the amplitude in the LPV. We used a large number of simulations to calibrate the relation between the maximum $\langle \tilde{R}(\bar{\sigma}_\xi) \rangle_{LPV}$ and σ_S , leading to:

$$\left[\langle \tilde{R}(\bar{\sigma}_\xi) \rangle_{LPV} \right]_{max} \simeq 0.3 \sigma(\alpha, \eta) N_e^{-\frac{1}{2}} R_w^{\frac{1}{2}} . \quad (3.25)$$

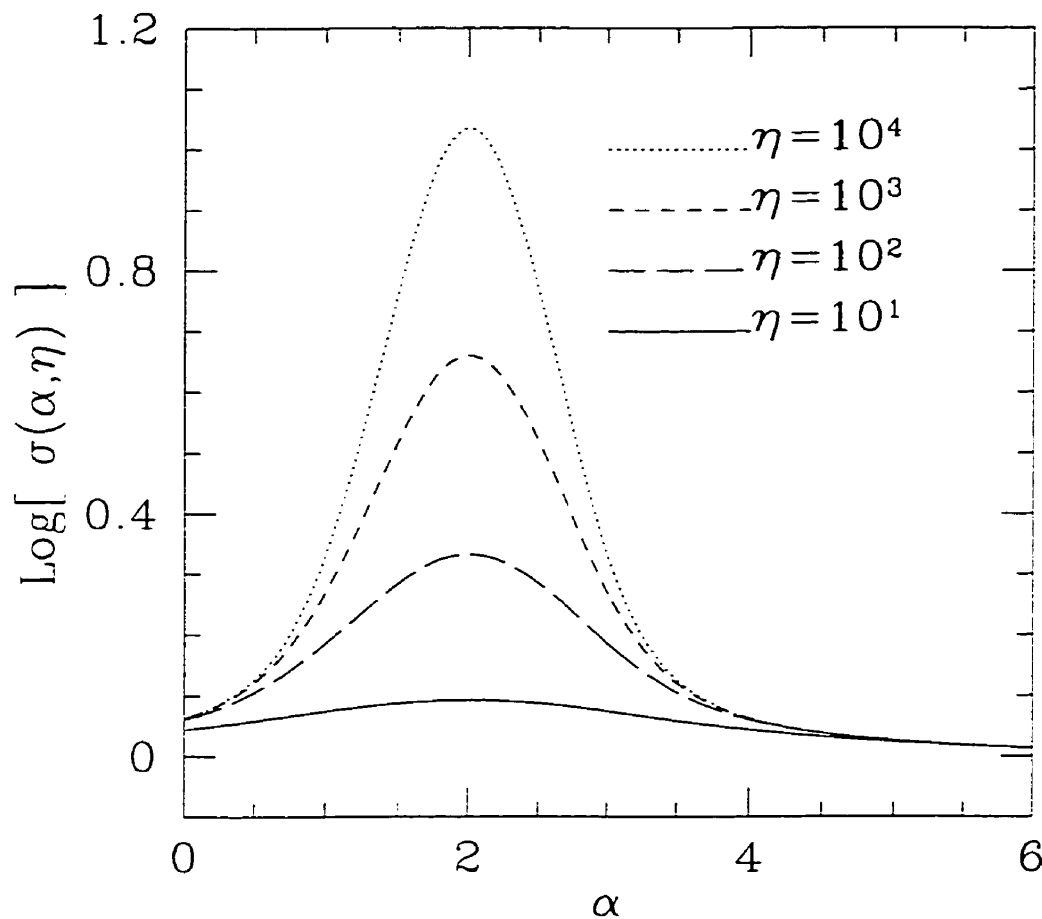


FIGURE 3.9. The variability induced by a distribution of DWEEs with a power law-distribution in their individual flux will depend on the power index α and flux range η . This is demonstrated here with a plot of $\sigma(\alpha, \eta)$ as a function of α , for different values of η , where $\sigma(\alpha, \eta)$ is a correction factor used in determining the total flux variability σ_{F_e} from a set on N_e individual DWEEs (see §4.2).

We present a synthesis of these results with simulations of LPV patterns from inhomogeneous winds obtained with various values of α , η , and N_e . Some of the resulting LPV are shown in Fig.10. In Fig.11, we plot the wavelet power spectrum $\langle \tilde{R}(\sigma_\xi) \rangle_{LPV}$, obtained from each of the simulations. The maxima in the wavelet spectra are compared with the values predicted from Eq.25, shown as dotted lines. The amplitudes of the maxima fall within $\sim 10\%$ of the predicted values. However, except for the amplitude of the LPV, the patterns look extremely similar. It is virtually impossible to guess which pattern comes from which simulation. This strongly suggests that *specific values of α , η , and N_e cannot be estimated from the LPV patterns alone*; only an estimate of $\sigma(\alpha, \eta) N_e^{-\frac{1}{2}}$ can be obtained. This is a serious limitation to the study of inhomogeneous structure based on emission-line variability, although we may obtain constraints on possible ranges of values of α , η , and N_e .

We have used the wavelet power spectrum $\langle \tilde{R}(\sigma_\xi) \rangle_{LPV}$ obtained from the data for our 9 WR stars (cf. Fig.4), combined with estimates of R_w , to evaluate $N_e \sigma(\alpha, \eta)^{-2}$ for each star (cf. Table 4). They indicate that one would need at least $10^3 \lesssim N_e \lesssim 10^4$ DWEEs in the LER at any time to account for the LPV in these WR stars. If there is a power-law distribution in the flux of individual DWEEs such that $\sigma(\alpha, \eta) > 1$, several orders of magnitude more DWEEs might be required to account for the LPV. We note that N_e only represents DWEEs that lie in the LER, i.e. a relatively small fraction of the whole wind. We conclude that the structure of WR winds is probably extremely fragmented.

3.4.3 Anisotropic emission

We have run several simulations of line emission from inhomogeneous winds, with various values of the radial to angular velocity dispersion ratio $\sigma_{v_r}/\sigma_{v_\theta}$, and of the radial to angular flux emission ratio f_r/f_θ . Nine simulations were performed with combinations of $\sigma_{v_r}/\sigma_{v_\theta} = [1, 2, 4]$ and $f_r/f_\theta = [3.3, 1, 0.3]$. White noise was

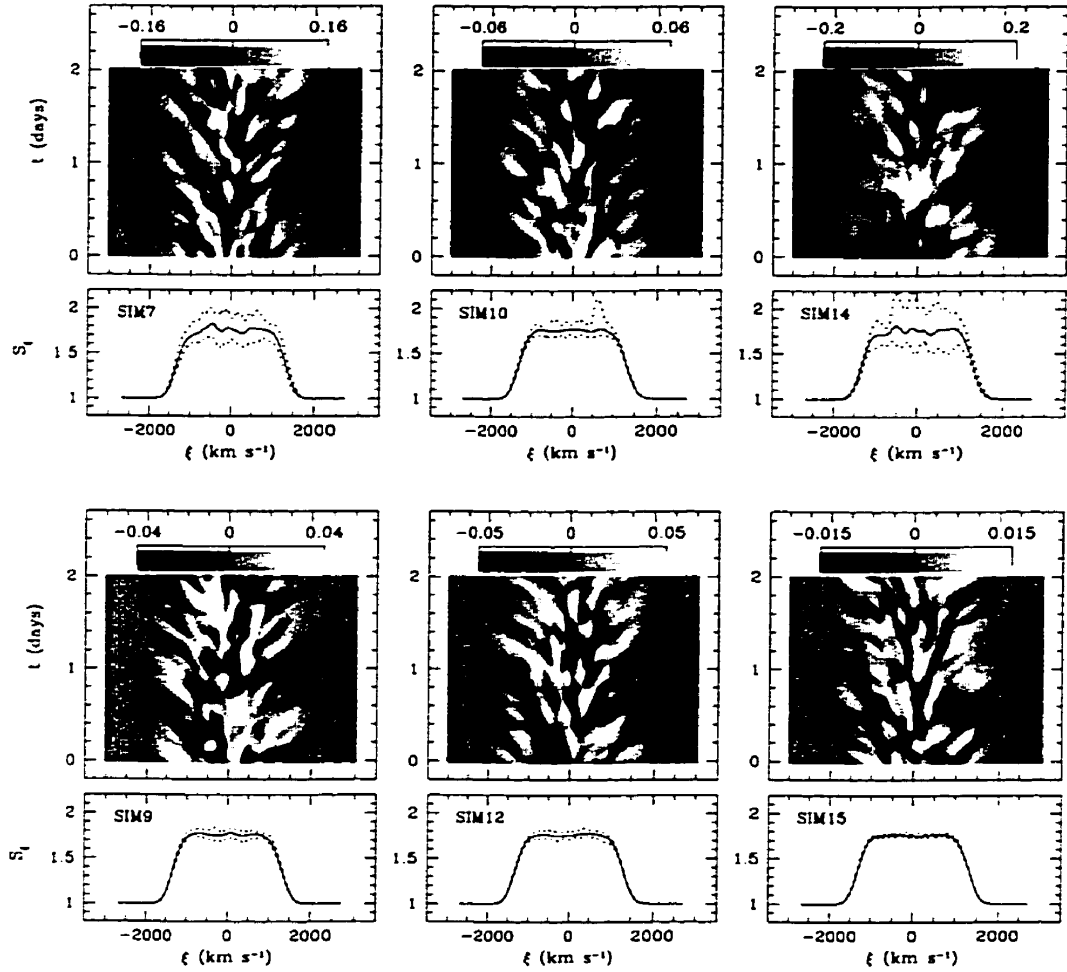


FIGURE 3.10. Simulations of LPVs, showing the dependence of the LPV patterns on the mean number N_e , power-law flux index α and flux range η of DWEES. Model parameters used in these simulations are listed in Table 3. The general patterns of the LPVs are indiscernible: unique determinations of N_e , α , and η cannot be obtained from such a spectral time-series. Only the amplitude in the LPV varies, yielding constraints on a *combination* of these parameter values.

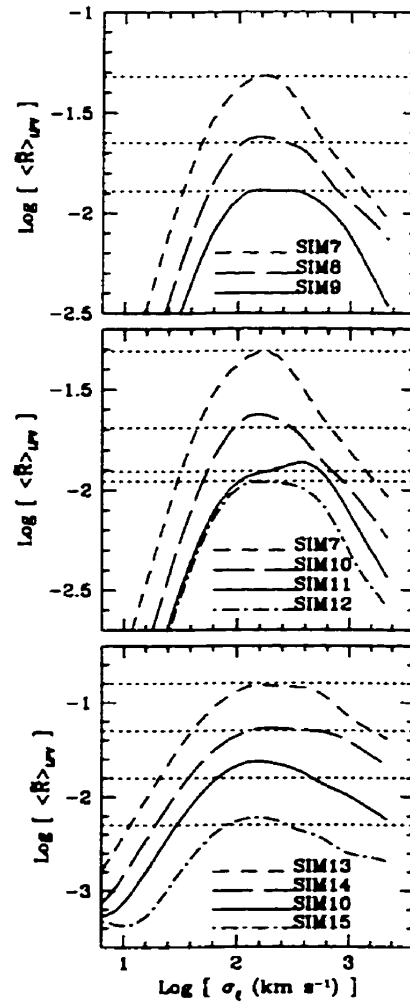


FIGURE 3.11. Wavelet power spectrum $\langle \tilde{R}(\sigma_\xi) \rangle_{LPV}$ for the simulations SIM7 to SIM15, which were made using different numbers and flux distributions of DWEEs (cf. Table 3). Top: η is varied while N_e and α are fixed. Center: α is varied, η and N_e fixed. Bottom: N_e is varied, α and η fixed. Horizontal lines show the amplitude of the maxima in $\langle \tilde{R}(\sigma_\xi) \rangle_{LPV}$ predicted from Eq.25. All measurements fall within 10% of the predictions.

TABLEAU 3.4. Wind properties from the LPV patterns.

WR #	$\bar{\sigma}_\xi$ (km s $^{-1}$)	$N_e \sigma(\alpha, \eta)^{-2}$	a_e (m s $^{-2}$)	σ_{v_e} (km s $^{-1}$)	σ_{v_r} (km s $^{-1}$)
WR40	90 ± 20	$1.6 \pm 0.6 \cdot 10^3$	3.5 ± 1.5	60 ± 15	115 ± 18
WR103	120 ± 25	$3.5 \pm 1.4 \cdot 10^3$	4.5 ± 1.5	70 ± 15	210 ± 22
WR111	90 ± 20	$1.5 \pm 0.6 \cdot 10^4$	20.0 ± 5.0	120 ± 20	135 ± 22
WR134	350 ± 75	$2.0 \pm 0.8 \cdot 10^3$	25.0 ± 3.0	285 ± 40	145 ± 49
WR135	120 ± 25	$9.5 \pm 3.8 \cdot 10^3$	11.0 ± 1.5	100 ± 25	140 ± 27
WR136	90 ± 20	$4.1 \pm 1.7 \cdot 10^4$	5.5 ± 1.0	80 ± 20	280 ± 25
WR137	75 ± 15	$2.4 \pm 1.0 \cdot 10^4$	8.5 ± 3.5	95 ± 20	165 ± 22
WR138	110 ± 25	$6.9 \pm 2.7 \cdot 10^3$	9.0 ± 1.5	135 ± 30	215 ± 34
WR140	90 ± 20	$3.6 \pm 1.4 \cdot 10^4$	12.0 ± 2.5	90 ± 25	175 ± 27

All values are estimated from the LPV patterns: $\bar{\sigma}_\xi$ is the average width of subpeak features, N_e is the mean number of DWEEs in the LER (cf. §4.2), a_e is the radial acceleration of DWEEs, σ_{v_e} is the estimated size of the LER for one DWEE. The values listed for σ_{v_r} are the radial velocity dispersions needed to account for the large Δv_e (see Table 2) provided that σ_{v_e} are reliable measures for the size of the LER.

added to simulate the presence of some instrumental noise. In Fig.12, we show the mean profiles obtained from a 48h spectral time-series, along with the maximum and minimum spectrum profiles; the 2D wavelet spectrum of the residuals is also plotted for each of the nine simulations.

The shape of the line-profile is found to be strongly affected by the f_r/f_θ ratio, but seems almost unaffected by a reasonable degree of anisotropy in σ_v . The profile is especially sensitive to $f_r/f_\theta > 1$, where it yields something reminiscent of a profile generated by an emission ring. In the case where $f_r/f_\theta = 1$ the profile is “flat-topped”, whereas it looks somewhat rounded when $f_r/f_\theta < 1$. This works in the sense expected from optically thick line-emission in a spherical, radial wind flow. Comparison with the observed mean profiles confirms that the shape of the C III $\lambda 5696$ line is consistent with optically thin emission ($f_r/f_\theta = 1$), whereas the He II $\lambda 5411$ line could be affected by optical thickness effects.

The wavelet spectrum appears to be mainly sensitive to the $\sigma_{v_r}/\sigma_{v_\theta}$ ratio, but it is also affected by changes in the f_r/f_θ ratio. One has to be careful in discriminating both effects. The f_r/f_θ ratio affects the *amplitude* of the wavelet response as a function of ξ , whereas the $\sigma_{v_r}/\sigma_{v_\theta}$ ratio affects both the *amplitude* and *scale* of the wavelet response. Statistical fluctuations also arise because of the limited sampling of the time-series. The wavelet spectra from SIM21 and SIM24 are those which resemble most the wavelet spectra obtained from the data. Overall, we have found that the best fits are obtained with $3 < \sigma_{v_r}/\sigma_{v_\theta} < 5$, and with $f_r/f_\theta \lesssim 1$.

The fact that we obtain $f_r/f_\theta \lesssim 1$ from fitting the wavelet spectra of the LPV seems to be in contradiction with the impression that the C III line is optically thin. However, this could be explained if individual DWEEs have different f_r/f_θ ratios. For example, high-flux DWEEs may arise from wind elements with higher column density, and might be more subject to opacity effects than low-flux DWEEs. As mentioned in §4.2 one can have a line whose global emission is

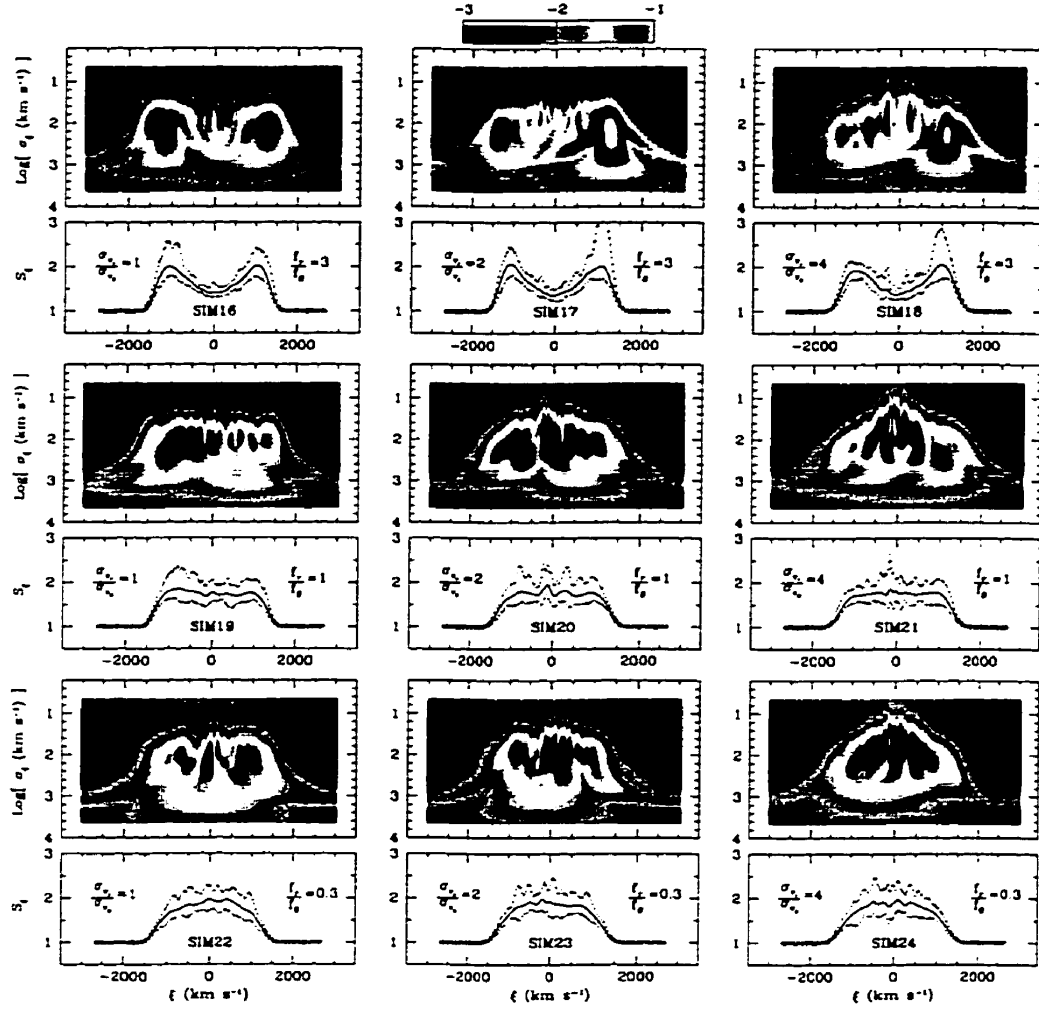


FIGURE 3.12. Simulated LPV showing the effects of anisotropic velocity dispersions and photon escape probabilities. The parameters of the simulation are listed in Table 3. The minimum, mean and maximum profiles from 48h long spectral time-series are shown. The shape of the mean profile is sensitive to the emissivity ratio f_r/f_θ , especially when $f_r/f_\theta > 1$. The mean wavelet spectrum of the spectral time-series (top panels) is sensitive to the $\sigma_{v_r}/\sigma_{v_\theta}$ ratio. A comparison with Figs.1-3 suggests that inhomogeneous features in WR winds have $\sigma_{v_r}/\sigma_{v_\theta} \approx 4$. We can rule out the possibility that $f_r/f_\theta > 1$ in WR stars, because of the shape of WR emission-line profiles. The LPV patterns seem to be consistent with $f_r/f_\theta \lesssim 1$, though the flat-top C III profiles seem to argue against this possibility (see. §4.3).

dominated by the low-flux DWEEs, while the LPV arises because of the high-flux DWEEs. This would explain the observed effect on the wavelet spectra.

The addition of white noise in the simulations does not critically affect the wavelet response to the LPV. Since the noise varies on a pixel-to-pixel level, it consists only of very narrow features which show up in the WPS as a response near the smallest scale (in Fig.12; this is the uniform response near $\text{Log}[\sigma_\xi(\text{km s}^{-1})] \sim 1$). The noise is not a serious problem in our analysis, because the spectral resolution is such that intrinsic features are at least several pixels in size. On the other hand, since the quality of the WPS depends on the size of the sample, larger spectral time-series would improve the quality of the wavelet spectra, which could be used to investigate more subtle effects such as occultation of DWEEs by the stellar disk.

3.4.4 Kinematics of the subpeaks

We have seen that variable subpeaks tend to persist on emission line profiles for a certain period of time, and that subpeak features show a systematic motion from the line center to the line edges. This behavior is suggestive of radial expansion of wind features. The general evolution in time of the LPV pattern depends on the wind dynamics and line-emission structure. The simplest interpretation for the characteristic time-scale of a subpeak event relates it to the time it takes for the wind feature to cross the LER, whereas subpeak motion reflects the wind acceleration in the LER.

In order to keep the analysis as objective as possible (i.e. without having to rely on the identification of “individual” subpeak events), we introduce the *degradation function* as an analysis tool. The degradation function, noted $\sigma_D(a, \Delta t)$ (see appendix B) is similar to a correlation function, and is used to estimate the mean radial acceleration a_e of DWEEs in the LER, and the velocity range

σ_{v_e} of this LER from the LPV pattern. The quality of $\sigma_D(a, \Delta t)$ is proportional to the size of the data sample, which must include pairs of spectra with temporal separation shorter than the subpeak lifetime. This requirement is necessary to obtain a reliable estimate for a_e .

The minimal degradation value of $\sigma_D(a, \Delta t)$ is obtained when parameter a is set to $a = a_e$. More reliable estimates can be obtained from $\langle \sigma_D(a) \rangle_{\Delta t < t_e}$, i.e. the mean degradation obtained from all pairs of spectra separated by $\Delta t < t_e$, where t_e is shorter than the estimated duration of subpeak events. We present in Fig.13 the mean degradation $\langle \sigma_D(a) \rangle$, estimated from pairs of spectra separated by $\Delta t < 3$ h, for each of the WR stars in our data set. The locations of the minima yield estimates of a_e , which are listed in Table 4; they range from ~ 3.5 m s $^{-2}$ in WR40 to ~ 25 m s $^{-2}$ in WR134. To facilitate the comparison between the stars, we have plotted in Fig.13 the normalized $\langle \sigma_D(a) \rangle / \langle \sigma_D(a_e) \rangle$.

We summarize the results in Fig.14, where we plot the non-dimensional stellar wind acceleration $a_e R_\odot v_\infty^{-2}$ as a function of the normalized wind velocity $v_e v_\infty^{-1}$. This plot indicates the relative wind acceleration as a function of wind depth, where we use the relative radial wind velocity $v_e v_\infty^{-1}$ as a depth measure. We compare the measurements from the stars to the values expected from idealized β -type wind velocity laws having different values of the parameter βR_* . (see §3.2). The estimates all correspond to β -laws with $20 < \beta R_* R_\odot^{-1} < 80$.

The duration of subpeak events can be estimated from a plot of $\sigma_D(a_e, \Delta t)$ (e.g. Fig.15). One sees in Fig.15 that $\sigma_D(a_e, \Delta t)$ increases steadily with Δt until it asymptotically reaches some constant level. From that moment onwards, any correlation is lost, which indicates that the time interval has become larger than the subpeak duration. All structures initially present in the signal have disappeared, which explains the loss of correlation.

Using the estimated values of βR_* obtained from the accelerations a_e , we

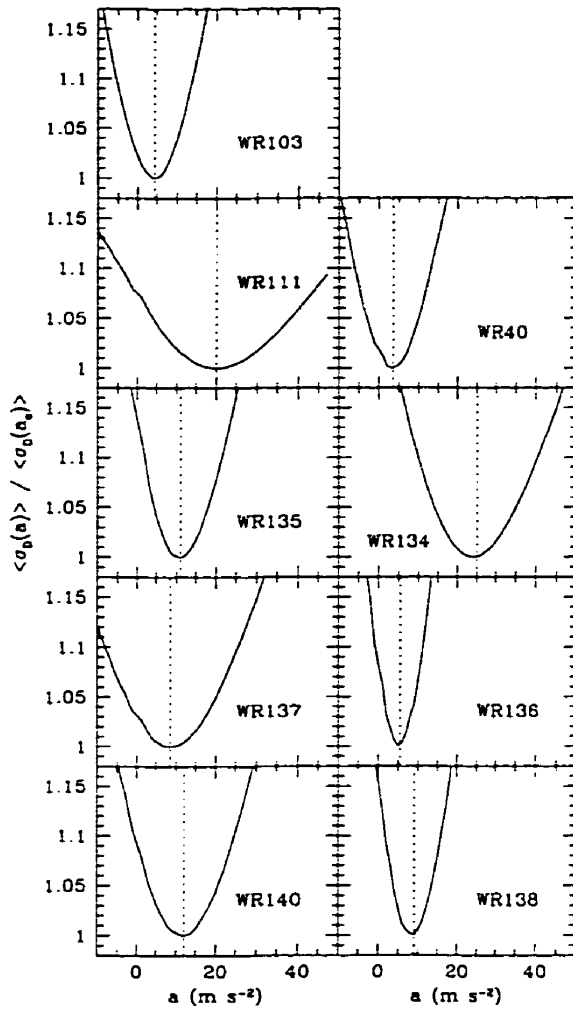


FIGURE 3.13. Radial acceleration a_e of wind inhomogeneities, as obtained from the mean degradation function $\langle \sigma_D(a) \rangle$ of LPV patterns, from pairs of spectra separated by $\Delta t < 3h$. The minima yield estimates of the radial wind acceleration a_e in the LER (see appendix B). We obtain estimates in the range $4 < a_e < 25$ m s⁻² (see Table 4).

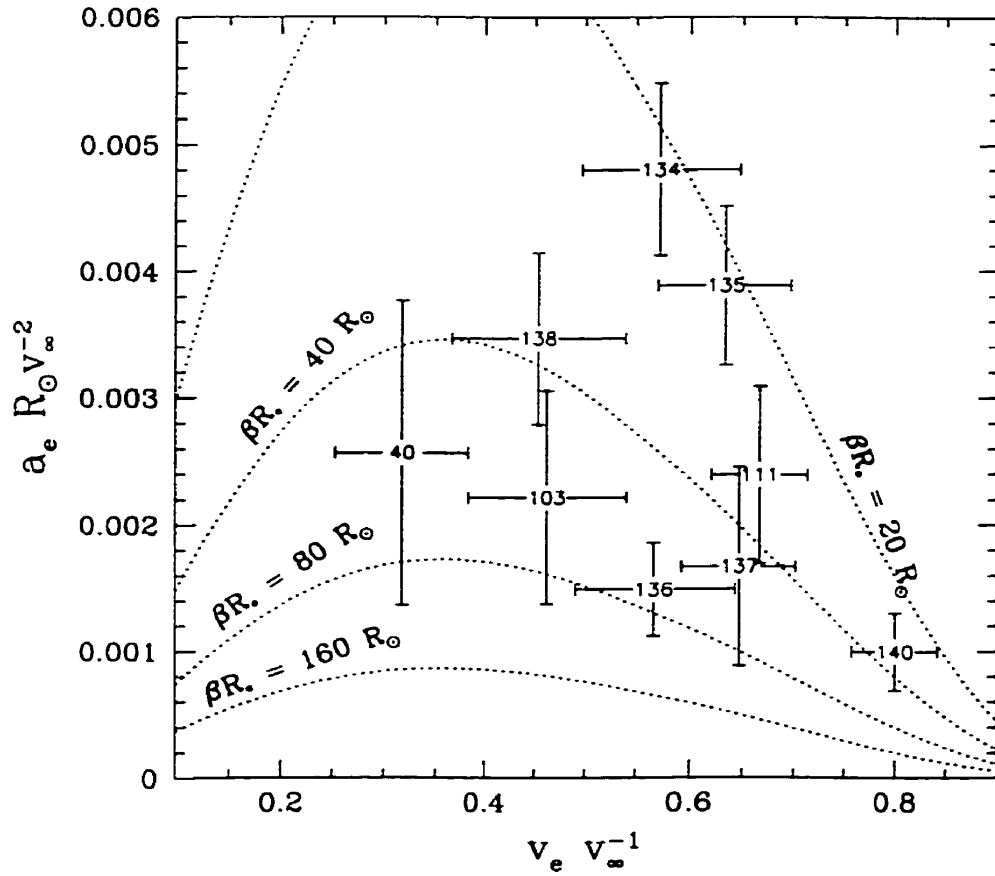


FIGURE 3.14. Comparison between the dimensionless acceleration $a_e R_\odot v_\infty^{-2}$ and the relative velocity range $v_e v_\infty^{-1}$ in the wind, as estimated from the LPV in the WR stars of our sample. Dashed lines show the ratios expected from β -laws for various values of the combined βR_\star parameter. The kinematics of the WR LPV subpeaks are consistent with $20 < \beta R_\star R_\odot^{-1} < 80$, much larger than the values typically used in theoretical WR wind models. The large dispersion in βR_\star for the stars in the sample might reflect either different values in their core radii, or simply indicate the inadequacy of one general β -law as a good representation of WR wind velocity fields.

performed simulations of LPV using the model described in §3. For each star in our data set, we performed independent simulations using the same time-base, and selecting values of a_e to match those obtained from Fig.13. For each star the degradation function $\sigma_D(a_e, \Delta t)$ from the data was compared to that obtained from the matching simulation; the results are shown in Fig.15. We performed the simulations by first trying $\sigma_{v_e} = \Delta v_e$ (i.e. neglecting the turbulent broadening σ_ξ , cf. Eq.11), as the extension of the LER expressed in wind velocity space (short-dashed line). This attempt resulted in poor agreement with the data, the longer lifetime of the subpeak features revealing that the size of the LER had been overestimated. Better fits were obtained with smaller values for σ_{v_e} (long-dashed lines), which are listed in Table 4. From these, we evaluated the radial wind velocity dispersion σ_{v_r} which would account for the dispersion Δv_e in the emission-line profile (cf. Eq.11).

For most of the stars, the estimated σ_{v_r} are consistent with what has been suggested from the wavelet analysis, namely that $\sigma_{v_r} \sim 4\sigma_{v_\theta}$. Wavelet analysis of simulations made with these values typically yield $\overline{\sigma_\xi} \approx \sigma_{v_r}/2$. The star WR134 again makes the exception, having $\sigma_{v_r} < \overline{\sigma_\xi}$ instead. One also sees that σ_{v_e} is apparently much larger for this star, although the emission line-profile is not very different from that in other WR stars. This is further evidence that the LPVs in WR134 cannot be accounted for by radially propagating wind features. The large, apparent σ_{v_e} would be consistent with a wind structure having a motion in $\hat{\theta}$ as well as in \hat{r} . For the other WN stars, because of the possible optical depth effects, we suspected that Δv_e would overestimate the actual dispersion in the line emission (cf. §3.3). One sees that this might indeed be the case for some of the WN stars: e.g. for WR136, we find $\sigma_{v_r} \sim 3\overline{\sigma_\xi}$, which can be reproduced with a $\sigma_{v_r}/\sigma_{v_\theta} \sim 9$ ratio, much larger than what is inferred from the wavelet spectrum.

The flat-topped C III line in the WC stars stands out as the line which is best suited for a comparison with our simulations. We note that the size of the

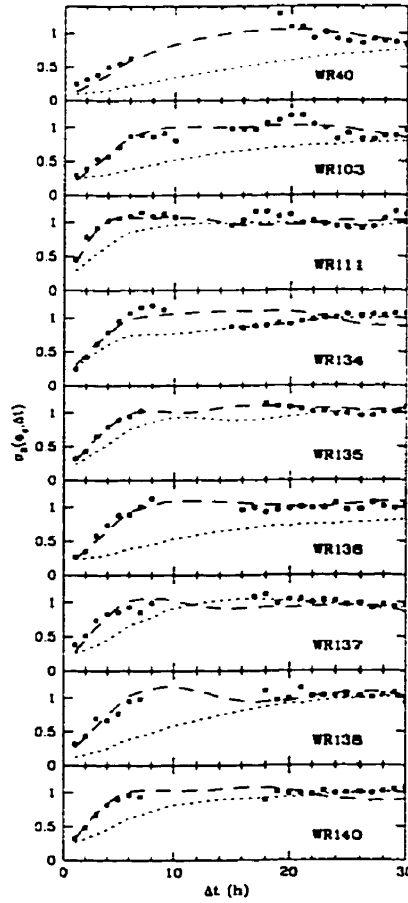


FIGURE 3.15. Comparison between the degradation function $\sigma_D(a_e, \Delta t)$ obtained from the data (squares) with that from simulated LPV. For each star, we present one simulation which uses Δv_e as the full range σ_{v_e} of the LER (dotted lines), i.e. which assumes that there are no turbulent broadening in the profile, and that Δv_e yields a correct estimate of the DWEEs velocity range (cf. §3.3). The $\sigma_D(a_e, \Delta t)$ for these simulations are found to disagree with the data. A better fit was obtained using much smaller depths for the LER (dashed lines). These smaller values suggest a radial turbulent broadening $\sigma_{v_r} \sim 2\bar{\sigma}_\xi$. This is consistent with the results obtained from the wavelet analysis which suggested anisotropic velocity dispersion (see §4.3).

LER only contributes a minor part of the emission-line broadening Δv_e . It is the “turbulent” motions, as revealed by the width of variable subpeaks, which dominate the line-broadening. It appears that the size of the LER would be relatively small, at least for the C III transition.

3.5 Discussion

3.5.1 Physical origin for the variable emission elements

Our analysis of the LPV in WR emission lines strongly suggests that a very similar phenomenon is at work in all the stars, independent of the spectral sequence and subclass. Except for the peculiar (and periodic) case of HD191765, the LPV can be reproduced using the same model of radially propagating, stochastic inhomogeneities. The fact that the physical aspect of the subpeaks, i.e. their velocity dispersion, does not depend on the geometry of the LER, the magnitude and acceleration of the wind velocity, or the depth in the wind at which the line is formed, is suggestive of some universal process within the inhomogeneous WR wind structure.

One conclusion to be drawn is that variable subpeaks must reflect strong, *local* velocity gradients. One cannot explain easily the large σ_v in terms of the extension in space of an over-dense region, for which the velocity dispersion would simply reflect the range in radial bulk wind velocity within the region. One reason is that one would then expect to observe different σ_v in different stars, depending on the wind velocities and accelerations. Another reason is that the very large number ($>> 10^3$) of wind elements which are required to model the LPV suggests that individual DWEEs occupy relatively *small* volumes. The large velocity dispersions are more easily explained in terms of large local *random* motions such as from macro-turbulence, or large local *systematic* motions such as from shocks in large-scale stream interactions (cf. Cranmer & Owocki, 1996).

We believe that the observed $\sigma_{v_r}/\sigma_{v_\theta} \sim 4$ reflects a true anisotropy in the velocity dispersion. The large ratio might be reproducible from radiative transfer effects in optically thick wind clumps, but such effects would likely show up in the shape of the emission-line profile as well, in the form of deviations from a flat-top profile. Since we do not see any such large deviations, at least for the C III $\lambda 5696$ line in the WC sequence, the only possibility would be that only *some* DWEE (likely in the high-flux regime) would show these optical depth effects. But in this case, we should also detect narrow (although weaker) subpeaks near the edges of the line; this is apparently not the case. Thus, although we believe that optical depth effects might be affecting some DWEEs, yielding $f_r/f_\theta \lesssim 1$, the $\sigma_{v_r}/\sigma_{v_\theta}$ ratio most likely depends on the real velocity dispersion within DWEEs.

Anisotropic turbulence is believed to exist in the chromospheres of some stars (e.g. Carpenter & Robinson, 1997). However, the latter imply motions of $\sigma_v \sim 20 - 30 \text{ km s}^{-1}$, substantially lower than what we measure (we note that our observed σ_v correspond to highly supersonic motions). It is not clear how coherent wind features with such large internal random motions can persist for long enough to be observed as discrete wind features. Should hydrodynamical viscous dissipation occur, a hierarchy of clumps will also be expected to form, governed by specific *scaling laws* (Henriksen 1991). This means that smaller clumps, i.e. shocks having smaller velocity dispersion, should be present in the wind. This makes the analysis of the variable subpeak patterns still more complex, since our assumption that all clumps have the same velocity dispersion would only be approximate. This specific problem of scaling relations in the clumps was investigated in Paper I, where we presented marginal observational support for the existence of such scaling laws, and obtained constraints on the possible scaling properties. One consequence of supersonic turbulence, or self-structured chaos (see Henriksen 1994), is that coherent wind features could survive for only a limited time, possibly yielding a subpeak time-scale that is shorter than expected from the crossing-time through the LER.

The supersonic/anisotropic behavior could also be accounted for by the existence of radially propagating shocks. It has been shown that the radiation line-driving mechanism is unstable, and that strong shocks can form and propagate in a radiatively-driven wind (Owocki *et al.* 1988). These shocks are usually thought to be initiated by hydrodynamical perturbations at the base of the wind, such as stellar pulsations or surface inhomogeneities in conjunction with stellar rotation (Owocki *et al.* (1995)). These mechanisms may account for the periodic wind fluctuations such as in the DAC phenomenon in OB stars (Cranmer & Owocki, 1996), but could be hard to reconcile with the stochastic behavior of the WR LPV. However, it has been shown that the growth rates of instabilities in WR winds are likely to be extremely large, such that small, random fluctuations could grow into the stochastic shocks that we observe (Gayley & Owocki 1995).

However, it has been claimed that shock propagation in winds driven by line scattering should be “polarized” in the radial direction (Rybicki *et al.* 1990), i.e. damped in other directions. Our results provide direct evidence supporting this claim. We note, however, that even though wind perturbations are such that $\sigma_{v_\theta} \ll \sigma_{v_r}$, we might still get relatively large *apparent* measures of σ_{v_θ} due to the finite angular extension of the perturbation. For example, a radially propagating shock with angular size $\Delta\Omega \simeq 0.2$ steradian and radial velocity dispersion σ_{v_r} would yield an apparent $\sigma_{v_\theta} \simeq \sigma_{v_r}/4$ when observed to propagate perpendicular to the main propagation axis. Such large angular sizes (about 1/50th of a spherical shell) could be reconciled with a large N_e , since shocks could be relatively shallow in the radial direction. It is not clear, however, why shocks would then tend to have similar angular sizes.

3.5.2 The wind velocity structure

The wind acceleration is a crucial quantity for testing the velocity law. This test is critical for the reason that the velocity law is usually *assumed* in modeling

the winds and atmospheres of WR stars (see Hillier 1996). The degradation function provides reliable estimates of a_e , the radial acceleration of DWEES. However, a_e might not be equal to the radial acceleration of the wind material: if DWEES arise e.g. from shock compressions, the corresponding density enhancements (compressions patterns) might be moving *relative to the mean motion* of wind material. The question is whether this motion relative to the bulk wind velocity would bias the a_e measures. If we believe this effect to be unimportant (or non-existent), there is still a basic uncertainty in the determination of the velocity law from emission subpeaks. Spectroscopy only provides information in velocity space, and because the magnitude of the acceleration depends linearly on the product βR_* , it is not possible to evaluate β or R_* separately.

Nevertheless, our estimates of βR_* may provide interesting constraints on the β -law in WR winds. So far, we obtain βR_* values which are not consistent with the values commonly used in WR wind models. For instance, values of $\beta = 1$ and a core radius $R_* = 3R_\odot$ have been used to model the wind from WR111 (Hillier 1989), whereas we find $\beta R_* \sim 30$ for this same star. Non-LTE spectral analysis of the WN star WR136 yielded $R_* = 6.4R_\odot$ with $\beta = 1$ (Hamann *et al.* 1994), whereas we find $\beta R_* \simeq 70$. These results were obtained from using the “standard model” hypotheses, including homogeneity. More recently, Schmutz (1997) has performed a spectral analysis of HD50896, this time using a clumped wind model. He obtained a velocity law which was fitted (in the outer wind regions) with $\beta = 8$, $R_* = 3.5R_\odot$. This appears to be in better agreement with our analysis, though a study of the LPV in HD50896 would be required to confront this result. Still, the βR_* that we measure in some stars is significantly larger than what is obtained from most models.

The source of this discrepancy might reside in the fact that the parameter R_* in the β -law is not related to the stellar core radius. Close binary systems provide upper limits for the core radii of the components, since the size of the

orbit must always be larger than the sum of the radii of the component stars. There exist a few WR stars in very short period WR+O binaries, such as CQ Cep with a period of 1.6 days. Upper limits to the core radii of 6 WN stars (including CQ Cep) in close binary systems have been estimated to be in the range $2 - 10R_{\odot}$ (Moffat & Marchenko 1996). It is not clear whether the results from binary stars should apply to our sample of single WR stars, since single WR stars may have evolved differently from WR stars in binary systems (Dalton *et al.* 1995; see however Moffat 1995). Therefore, either we adopt large values for β , or we abandon the idea that R_* is related to the core radius. Using values of R_* which are larger than the core radius will result in a failure for the β -law to describe the velocity field close to the stellar radius.

In any case, we can still attempt to fit the velocity structure at larger v with a β -law. Depending on the actual velocity structure near $v = 0$, we will obtain R_* values which can be either larger or smaller than the core radius. The analysis of HD50896 by Schmutz (1997) appears to be consistent with this view, and suggests that there is a divergence from the β -law form at small distances from the stellar surface. On the other hand, models of radiation-driven winds (e.g. Gayley *et al.* 1995; Springmann 1994) suggest a more extended wind acceleration region than that from the β -law, which could actually result in a smaller than expected acceleration near to the star for a given terminal velocity.

There remains the possibility that the apparent motion of DWEEs in velocity space does not reflect the actual mean hydrodynamical wind flow. If the inhomogeneous structure is in the form of radially propagating shocks, and if we rely on the smaller, theoretical estimates of βR_* , this implies that shocks have *smaller* radial acceleration than the wind material. This might be explained with shocks propagating towards the star, in the wind rest frame, like the “reverse shocks” found by Owocki *et al.* (1988) in 1D simulations of radiatively driven winds. In this hydrodynamical model, it was found that shocks of different sizes seemed to

propagate at different rates, denser shocks having a lower radial acceleration. Such a behavior might eventually be verified, by testing whether the LPV subpeaks are consistent with intense DWEEs having low acceleration (high βR_*), and weaker DWEEs having higher accelerations (low βR_*).

3.5.3 The size of the LER

We have interpreted the time-scale of LPV subpeaks as the crossing of one DWEE through the LER. Using our estimates for the radial acceleration of DWEEs, we have estimated the size in velocity space σ_{v_e} of the LERs for the WR stars in our sample. We have found relatively small values, which suggest that σ_{v_e} is not the main factor responsible for the emission-line broadening Δv_e .

The large Δv_e , estimated from the shape of the emission-line profiles (cf. §3.3), can be accounted for by the large radial velocity dispersion σ_{v_r} within the DWEEs, provided that $\sigma_{v_r} \sim 2\bar{\sigma}_\xi$, where $\bar{\sigma}_\xi$ is the mean velocity dispersion measured from the LPV subpeaks. This is consistent with the conclusions from the wavelet analysis, which suggest large anisotropies in the velocity dispersion, with $\sigma_{v_r} \sim 4\sigma_{v_\theta}$.

A small σ_{v_e} , however, does more than just corroborate the anisotropic velocity dispersion hypothesis; it also supports the view that the whole line emission comes from DWEEs having large σ_{v_r} . We have assumed in our model that the whole line arose from DWEEs, and that the velocity dispersion vector $\vec{\sigma}_v$ (cf. §3.4) was the same for all DWEEs. However, the LPV patterns could not provide any support to this view, because one cannot know whether the LPV subpeaks reflect the physical properties of all DWEEs, or only a few, especially large ones.

For example, in the case where there is a power-law distribution in the DWEE fluxes, most of the line-emission F_e might arise from the low-flux DWEEs, while the variability σ_{F_e} is dominated by the high-flux components. In Paper I,

we have investigated the possibility that there could be a proportionality relation between the flux and the velocity dispersion of DWEEs. If this were the case, then the large $\bar{\sigma}_\xi$ might only reflect the velocity dispersion of the high-flux DWEEs. However, the small values of σ_{v_e} indicate that large σ_{v_e} must prevail for the whole wind emission.

One could blame the small σ_{v_e} on a systematic bias in the degradation function, such as effects of standing but variable features (e.g. atmospheric lines, noise). These might bias the measure of the acceleration to smaller values, in turn leading to underestimates in σ_{v_e} . The degradation in the signal might also be “accelerated” by the noise, which might induce underestimates in the characteristic time duration. However, we verified the effect of synthetic noise on the simulations, and did not find significant deviations in the measure of σ_{v_e} .

On the other hand there are physical effects which would yield an underestimate of σ_{v_e} from the degradation function. These would be responsible for the short time-scale of variable subpeaks while accounting for the large Δv_e in the line-profile without having to rely on the existence of large *local* turbulent motions: (1) a large random motion of DWEEs relative to one another, (2) variable location of the LER for individual DWEEs, (3) rapid fluctuations in the density structure.

The width of one LPV subpeak depends on the velocity dispersion within the region occupied by the corresponding DWEEs. Large random motions could exist which would not be reflected in the width of LPV subpeaks, e.g. the motion of one clump relative to others. These “macro-turbulent” motions would affect the shape of the emission line profile, increasing the Δv_e , but would not be detectable from the LPV pattern.

We have assumed so far that each and every DWEE has the same emissivity function, i.e. that the location of the LER was an independent quantity. However, the emissivity of one DWEE as a function of wind depth might depend on its

density. Since DWEEs represent stochastic wind fluctuations, it is reasonable to assume that inhomogeneous components will not all be emitting from the same wind region. While individual subpeaks could emit only within a narrow region from the star, they could, as a whole be emitting from a much larger region.

Finally, the inhomogeneous wind structure might be rapidly fluctuating, as in models of self-structured chaos, or turbulent energy dissipation. The relative density of DWEEs may also be changing because of pressure gradients. It is therefore possible that our σ_{v_e} would not measure the crossing-time of one DWEE through the LER, but rather measure the *lifetime* of inhomogeneous wind features. The actual size of the LER could therefore be larger, while we may still account for the small σ_{v_e} measured from the degradation function method.

3.6 Summary and Perspectives

We have presented a set of high-resolution spectra for 9 WR stars. The spectra show time-series of the C III $\lambda 5696$ emission-line for 5 stars of the WC sequence, and the He II $\lambda 5412$ emission-line for 4 stars of the WN sequence. The time series each cover 3-4 consecutive nights, with spectral sampling every hour or so. The time series reveal the presence of line profile variations (LPV) on the order of 5 % of the line intensity. The LPV show characteristic patterns, with narrow emission subpeaks moving from line center toward line edges on both halves of the line. The universality of the phenomenon is supported by recent detection of similar LPVs in an O-star wind (Eversberg *et al.* 1998a).

We have investigated the hypothesis that these LPV could be due to radially propagating wind inhomogeneities. We developed a simple phenomenological model which uses a random distribution of discrete wind emission elements (DWEEs). These DWEEs are assumed to propagate radially according to some monotonically increasing velocity law $v(r)$, and to be emitting line radiation as they cross

a corresponding line emission region (LER) which has the form of a spherical shell with some arbitrary thickness. We used the so-called β -law in the form $v(r) = v_\infty(1 - R_*r^{-1})^\beta$, with v_∞ the terminal wind velocity. Both the location of individual DWEEs and the location/thickness of the LER are expressed in wind velocity space. The DWEEs are assigned a certain velocity dispersion, which represents the local deviations from the wind velocity law, such as turbulent motions or shocks. The model also allows for some optical depth effects within individual DWEEs, although these are assumed to be optically thin to one another.

We used this model to generate time-series of synthetic emission-line spectra, which were shown to reproduce well the observed LPV patterns. Synthetic spectra were used to investigate how model parameters affect the shape of the emission-line profile and the pattern of LPV. We found that a finely structured inhomogeneous wind, requiring a huge number of DWEEs, could yield LPV patterns where only a few apparent subpeak events are observed. The actual number of subpeak events detected at any time was shown to depend on $R_w \equiv v_e \overline{\sigma_\xi}^{-1}$, the ratio of the wind velocity v_e (related to the emission-line width) to the mean line-of-sight velocity dispersion $\overline{\sigma_\xi}$ of variable subpeaks.

We used the continuous wavelet transform as a multi-scale analysis tool for the study of LPV patterns. This numerical tool is shown to be very useful in many ways, in that it can also be used to distinguish intrinsic, variable features in the signal (large-scale response) from instrumental noise variability (small-scale response). We found intrinsic features with mean velocity dispersions $\overline{\sigma_\xi} \sim 100 \text{ km s}^{-1}$, with only one exception (HD191765, where $\overline{\sigma_\xi} \simeq 350 \text{ km s}^{-1}$). Wavelet analysis showed that LPV subpeaks are narrower near the line center than near the edges, i.e. that the velocity dispersion is larger for DWEEs which are propagating along the line-of-sight. This suggests that the velocity dispersion of DWEEs is larger in the radial direction than in the azimuthal direction, with

$\sigma_{v_r} \sim 4\sigma_{v_\theta}$. Wavelet analysis also provided marginal evidence for optical depth effects, with an escape probability within DWEEs possibly smaller in the radial direction. However, the flat-top shape of the C III $\lambda 5696$ line in stars of the WC sequence suggests that only *some* of the DWEEs might be affected by optical thickness effects.

Systematic temporal variations in the LPV patterns were investigated with the use of the so-called degradation function, which finds correlations between different spectra in the time series. The degradation function is used to determine the magnitude of the radial acceleration of DWEEs, and the characteristic duration of the subpeak events. These sources of information are used to investigate both the velocity law (from the acceleration) and the size in velocity space of the LER (relating it to the duration of subpeak events). Data analysis revealed smaller accelerations than expected. We found that the data could be fit with a β -law with $20 < \beta R_* R_\odot^{-1} < 80$, an order of magnitude larger than predicted by homogeneous models of WR winds.

We compared the data to simulations, to determine the size of the LER which best reproduced the duration of subpeak events. These fits resulted in relatively small sizes for the LER, much smaller than the observed line-profile broadening Δv_e . This suggests that most of the line-broadening arises from a large, “turbulent” radial velocity dispersion, which must be $\sigma_{v_r} \sim 2\bar{\sigma}_\xi$. Simulations show this result to be consistent with large anisotropic velocity dispersion with $\sigma_{v_r} \simeq 4\sigma_{v_\theta}$. This result thus yields independent evidence for anisotropy, while suggesting that σ_{v_r} must be affecting the whole line-emission, and not just a few intense DWEEs. Other possible interpretations were also discussed (§5.3).

One of the stars (HD191765) is shown to yield results that are inconsistent with our model of radially propagating wind features. The large-scale, LPV pattern from this star was already known to be somehow peculiar, being recurrent rather than stochastic, as in other WR stars. A better model for this peculiar star

might involve the rotation of a structured wind (Morel *et al.* 1997; Morel *et al.* 1998b).

Overall, this new method for the analysis of LPV patterns has yielded several new constraints on the inhomogeneous and dynamical structure of WR winds. Since our numerical tools use statistical measures which combine the information from several consecutive spectra, we expect that the precision and quality of the constraints should increase with the number of spectra obtained. Continuous observations of bright WR stars, such as from multi-site spectroscopy or from space, could provide a data sample allowing for more precision on the acceleration and clump duration. Furthermore, an in-depth investigation of the wind velocity structure would necessitate measuring the acceleration in different regions of the wind. This could be provided by detailed, simultaneous spectroscopy of many emission-lines from the same star, since the LER from different species occur at different distances from the star.

Acknowledgements

The authors wish to thank the referee, Dr. W. Schmutz, whose suggestions and comments have stimulated a substantial improvement of the manuscript. SL acknowledges the support provided by Post-Graduate Scholarships from NSERC of Canada and from FCAR Québec. AFJM is grateful to the same two organizations, as well as the Killam program of the Canada Council for the Arts, for financial aid.

3.7 Appendix A: Multi-Scale Wavelet Analysis

Wavelet analysis is in many ways analogous to Fourier analysis: it provides information about the *scale* of certain features in a signal. However, its advantage over Fourier analysis with periodically repetitive trigonometric functions is that,

due to their discrete nature, wavelets also provide information about the *location* of features in the signal (see Paper I, and references therein).

Wavelets are defined as functions which follow two specific criteria. First of all, a wavelet function $\psi(\xi)$ must be such that it has zero mean i.e.:

$$\int_{-\infty}^{\infty} \psi(\xi) d\xi = 0. \quad (3.26)$$

Furthermore, the wavelet must be *localized* in space, a condition which is satisfied if:

$$\int_{-\infty}^{\infty} [\psi(\xi)]^2 d\xi = C, \quad (3.27)$$

where C is some *finite* value. One very simple, popular wavelet function is the so-called *Mexican-hat wavelet*, which comes from the second derivative of a gaussian:

$$\psi(\xi) = (1 - \xi^2)e^{-\xi^2/2}. \quad (3.28)$$

The *continuous* wavelet transform uses, as a basis, a *wavelet family*, denoted $\psi_{\xi, \sigma_\xi}(\xi')$, which is obtained by continuous translation (parameter ξ) and dilation (parameter σ_ξ) of one wavelet function:

$$\psi_{\xi, \sigma_\xi}(\xi') \equiv \frac{1}{\sigma_\xi} \psi\left(\frac{\xi' - \xi}{\sigma_\xi}\right). \quad (3.29)$$

Let $R(\xi, t)$ be some emission-line time-series of residual spectra plotted in line-of-sight velocity space ξ . The continuous wavelet transform $\tilde{R}(\xi, \sigma_\xi, t)$ is obtained by convolution of each spectrum in the series with the wavelet family, e.g.:

$$\tilde{R}(\xi, \sigma_\xi, t) \equiv \frac{\pi}{8} \int_{-\infty}^{\infty} R(\xi, t) \psi\left(\frac{\xi' - \xi}{\sigma_\xi}\right) \frac{d\xi'}{\sigma_\xi}. \quad (3.30)$$

The wavelet transform as defined in Eq.30 yields a simple form for the inverse transformation, the so-called *wavelet reconstruction theorem*, which gives back the data from its *wavelet transform*. It is possible to show that if we use the Mexican-hat as the wavelet in Eq.30, the reconstruction is obtained from:

$$R(\xi, t) = \int_0^{\infty} \tilde{R}(\xi, \sigma_\xi, t) \frac{d\sigma_\xi}{\sigma_\xi}. \quad (3.31)$$

This relation considerably simplifies the interpretation of the wavelet transform. One now sees that the original signal is recovered from its wavelet transform by a simple sum over the scale parameter σ_ξ . This suggests that the wavelet transform is simply a representation of the data where signal features have been separated according to their characteristic scale σ_ξ . This is very similar to a scale-decomposition using a pass-band Fourier filter.

We may synthesize the results obtained from the wavelet analysis of the spectral time-series to get a statistical measure of the mean scaling properties. We call this the *mean wavelet power spectrum*, denoted $\langle \tilde{R}(\xi, \sigma_\xi) \rangle$. If the time-series consists of n measures at times t_i , the mean wavelet power spectrum is given by:

$$\langle \tilde{R}(\xi, \sigma_\xi) \rangle^2 \equiv \sum_i^n \frac{1}{n} (\tilde{R}(\xi, \sigma_\xi, t_i))^2 , \quad (3.32)$$

This will be useful in determining the *general* location and scale of variable subpeak components in the spectra, and especially for uncovering any relation between the width (scale) and position of emission features on the line profile, for an ensemble of data.

We may also be interested in obtaining a measure for the amplitude of signal features as a function of their location but independent of their scale, or as a function of their scale but independent of their location. We obtain these by integration over one independent parameter or the other:

$$[\langle \tilde{R}(\xi) \rangle_{[\sigma_{\xi_1}, \sigma_{\xi_2}]}]^2 \equiv \int_{\sigma_{\xi_1}}^{\sigma_{\xi_2}} \langle \tilde{R}(\xi, \sigma_\xi) \rangle^2 d\sigma_\xi ; \quad (3.33)$$

$$[\langle \tilde{R}(\sigma_\xi) \rangle_{[\xi_1, \xi_2]}]^2 \equiv \frac{1}{\xi_2 - \xi_1} \int_{\xi_1}^{\xi_2} \langle \tilde{R}(\xi, \sigma_\xi) \rangle^2 d\xi . \quad (3.34)$$

We call the latter measure (Eq.34) the *wavelet power spectrum*, by analogy with the Fourier power spectrum of a signal, since it yields an average measure over ξ in the scale σ_ξ of signal features.

For an emission-line arising in a spherical shell from a radially expanding

wind, we will use a normalization:

$$\langle \bar{R}(\sigma_\xi) \rangle_{LPV} = 2(v_e + \sigma_{v_e}) E W_\xi^{-1} \langle \bar{R}(\sigma_\xi) \rangle_{[-v_e - \sigma_{v_e}, v_e + \sigma_{v_e}]} , \quad (3.35)$$

where $E W_\xi$ is the line equivalent width (in units of the Doppler line-of-sight velocity), and $2(v_e + \sigma_{v_e})$ is the characteristic width of a line arising in a wind region with mean radial velocity v_e and velocity dispersion σ_{v_e} (see §3.3). This normalization allows for a comparison in the variability from lines with different $E W_\xi$; $\langle \bar{R} \rangle_{LPV}$ yields a measure of the absolute emission-line variability as a function of the scale of the variable subpeak features.

3.8 Appendix B: The Degradation Function

Consider a measure of the *degradation* of the LPV pattern in a spectral line with time, i.e. a measure of the changes in the pattern induced by the evolution of DWEEs. We will characterize this measure by defining a *degradation function* in the following way. Let $\sigma_D(\Delta t)$ be a measure for the degradation in a time-series of residuals $R(\xi, t_i)$, with LPVs in the spectral region $-v_e < \xi < v_e$:

$$[\sigma_D(\Delta t)]^2 = \sum_{i=1}^{n-1} \sum_{j=i}^n \int_{-v_e}^{v_e} [R(\xi, t_j) - R(\xi, t_i)]^2 [R(\xi, t_j)]^{-2} d\xi , \quad (3.36)$$

comparing all pairs of spectra with $\Delta t = t_j - t_i$. One can select specific intervals of Δt , and use the average $\sigma_D(\Delta t)$ obtained for all the pairs ij which have $t_j - t_i$ falling in this interval.

The function σ_D is expected to increase with Δt as the pattern slowly changes, and reaches an asymptotic maximum value after some characteristic time for the whole pattern to have changed completely. Spectra which have a time-separation larger than the characteristic time differ in the same way as randomly generated signals. Mainly two effects will yield a pattern degradation with time: (1) the appearance and disappearance of emission subpeaks and (2) the motion of the subpeaks on the line. Both effects should be distinguished,

since they have different physical origins. The first effect is related to the time t_e necessary for a wind feature to cross the emission-line region. The second effect is related to the radial acceleration a of wind features.

It is however possible to estimate the radial acceleration of the inhomogeneous wind components from the LPV pattern. Consider the function $\sigma_D(a, \Delta t)$ defined as:

$$[\sigma_D(a, \Delta t)]^2 \equiv \sum_{0 < t_j - t_i < \Delta t} \int_{-v_e}^{v_e} [R(\xi + a(t_j - t_i)v_e^{-1}\xi, t_i) - R(\xi, t_j)]^2 [R(\xi, t_j)]^{-2} d\xi, \quad (3.37)$$

which finds the mean standard deviation between pairs of spectra separated by a time interval Δt , when the former spectrum in the pair is “stretched” in order to imitate the effects on the LPV of features radially accelerating at a rate a in a wind region with mean radial velocity v_e . The minimum value of $\sigma_D(a, \Delta t)$ should be obtained for a matching the actual mean radial acceleration of the wind features. One drawback of this technique is that the shapes of individual subpeak features are distorted by the stretching. This distortion may become especially important for broad features, or for pairs of spectra with large Δt separations. This is why one has to be careful not to compare spectra separated by too large Δt , and to account for possible biases in LPV where broad features are found.

One assumption made here is that the acceleration is approximately constant in the LER; most observations suggest this to be the case. Since the LER occupies a relatively narrow region of the wind, the acceleration does not vary by a significant amount (e.g. Eversberg *et al.* 1998a). Thus, the assumption of a constant acceleration should not introduce large biases in σ_D .

CHAPITRE 4

WIND INHOMOGENEITIES IN WOLF-RAYET STARS.

III. UNUSUAL EMISSION-LINE PROFILE VARIATIONS IN γ^2 VELORUM

The Astronomical Journal, *soumis* (1998)

**WIND INHOMOGENEITIES IN WOLF-RAYET
STARS. III. UNUSUAL EMISSION-LINE PROFILE
VARIATIONS IN γ^2 VELORUM**

Sébastien Lépine^{1,2}, T. Eversberg^{1,2}, and Anthony F.J. Moffat,^{1,2,3}

Article submitted to the Astronomical Journal.

¹ Département de Physique, Université de Montréal, C.P. 6128, Succ. Centre-Ville, Montréal, Québec, Canada, H3C 3J7; and Observatoire du Mont Mégantic.

² Visiting astronomer, Canada-France-Hawaii Telescope.

³ Killam Research Fellow of the Canada Council for the Arts

ABSTRACT

We present very high resolution, very high signal-to-noise spectra from the 3.6m CFH telescope for the strong C III $\lambda 5696$ emission line in γ^2 Velorum, the brightest Wolf-Rayet (WR) star in the sky. From two nights of spectroscopic monitoring, we have detected line-profile variations (LPVs) in the form of moving emission features (subpeaks) on the broad, “flat-topped” underlying profile.

We use the working model from Lépine & Moffat (1998, Paper II) to study these LPVs in terms of inhomogeneities in the radially expanding stellar wind. A comparison between simulations and the data suggests the variable subpeaks to consist of a superposition of two distinct components: (1) narrow moving subpeaks with a mean line-of-sight velocity dispersion $\bar{\sigma}_\xi \simeq 80 \text{ km s}^{-1}$, and (2) broad moving subpeaks with $\bar{\sigma}_\xi \simeq 200 \text{ km s}^{-1}$. Both narrow and broad subpeak components are seen to move systematically in a direction from the line center ($\xi = 0$) towards the line edges. This motion is found to be consistent with a radial wind expansion at a mean acceleration rate $a_r = 13 \pm 3 \text{ m s}^{-2}$.

The narrow subpeaks are found to be similar to the stochastic subpeaks seen in the LPVs from several single and long-period binary WR stars. On the other hand, the broad features are reminiscent of the recurrent subpeaks observed in the LPVs from a few peculiar WR stars (HD4004, HD191765, and EZ CMa), although in γ^2 Vel, we find no evidence for a recurrent behavior.

We investigate the possibility that, in γ^2 Vel, these broad variable subpeaks arise from the shock-cone region, at the interface where the wind from the WR star collides with that of its O companion. We find no convincing evidence to support this hypothesis, although we suspect that there could be a relation between the existence of broad LPV subpeaks and the presence of the more massive O companion.

Subject headings: Line: profiles — methods: data analysis — stars: individual

(γ^2 Vel) — stars: Wolf-Rayet

4.1 Introduction

Wolf-Rayet (WR) stars are believed to be the evolved counterparts of massive OB stars (Pasquali *et al.* 1997). They are characterized by intense mass-loss occurring through dense, fast winds ($\dot{M} \sim 10^{-5} M_{\odot} \text{ yr}^{-1}$; $v_{\infty} \sim 10^3 \text{ km s}^{-1}$), consisting mainly of products from the CNO cycle for stars in the WN sequence (Hamann *et al.* 1994), and of products from the triple- α cycle for stars of the WC sequence (Grafener *et al.* 1998). The optical spectra of WR stars typically show broad emission lines from these elements. The broad recombination lines are believed to arise from the radial expansion and subsequent cooling of the wind (e.g. Schmutz 1997).

For simplicity, hot winds from WR stars have traditionally been modeled as steady, homogeneous flows. Until recently, models used in the spectral analysis of WR winds depended on a set of simplifying assumptions grouped under the name of *standard model* for WR stars (see Langer 1989). In this standard model, the wind is assumed to be (1) spherically symmetric, (2) radially expanding with a monotonic velocity law, (3) homogeneous, and (4) time independent, or steady. However, the theory of radiation driven winds predicts that WR winds should be hydrodynamically unstable (e.g. Owocki & Rybicki 1991), and theoretical models suggest that this leads to the development of strong wind clumping (Gayley & Owocki 1995).

Investigation of wind clumping mainly comes from indirect observational evidence. This includes the low intensity in the electron scattering wings of wind emission-lines (Hillier 1991), IR emission-line ratios (Nugis & Niedzielski, 1995), stochastic variations in polarized light (Robert *et al.* 1989), and continuum excess in IR and radio free-free emission (Runacres & Blomme, 1996). In all cases the

inhomogeneity is observed by the way it *globally* affects the emission from the stellar wind. Although such observations may provide estimates of the *clumping factor* or the mean density contrast between overdense and rarefied zones, they provide little information on the detailed geometry of the inhomogeneous structure.

Though it might be possible in the near future to resolve the inhomogeneous wind structure using optical interferometry (e.g. Vakili *et al.* 1997), no direct optical imaging of detailed WR wind structure is currently available. Details about the clumpy structure can however be obtained from high-resolution spectroscopy of wind emission-lines. Because the wind velocity in WR stars is very high ($v_\infty \sim 10^3 \text{ km s}^{-1}$), wind regions having different line-of-sight velocities can be spectroscopically resolved (cf. Lépine & Moffat, 1998; hereafter paper II). Monitoring of optical lines in several WR stars has revealed the presence of significant levels of line-profile variations (LPVs) on time-scales of minutes to days, which can be interpreted as variations in the wind density structure. We can classify the observed LPVs in three types: narrow, stochastic subpeaks (hereafter S-type); broad, recurrent subpeaks (R-type); and periodic line modulations (P-type).

Type-S LPVs show up as variable subpeak features with mean line-of-sight velocity dispersion $\overline{\sigma_\xi} \sim 100 \text{ km s}^{-1}$ (Robert 1992; Paper I). These are systematically observed to move away from the line center, i.e. features on the $\xi < 0$ side of the line move toward the blue edge, while features on the $\xi > 0$ side move towards the red edge (Moffat *et al.* 1988). Variable features were shown to persist on time-scales of ~ 8 hours (paper II) but any search for periodic or recurrent behavior has so far been negative. The subpeaks are therefore assumed to be stochastic in nature, and are believed to be the trace signature of local wind inhomogeneities. This type of LPV seems to be omnipresent in hot stellar winds. Apart from their detection in at least 8 other WR stars, either single or in long-period binaries

(Robert 1992; paper II), type-S LPVs have also been detected in central stars of planetary nebula (BD+30°3639: Acker *et al.* 1997; NGC40: Balick *et al.* 1996) and in one Of star (ζ Pup: Eversberg *et al.* 1998a).

Type-R LPVs appear as broader ($\sigma_\xi \sim 200 - 500 \text{ km s}^{-1}$) subpeak features, which move across the line profile and typically persist for ~ 10 hours. Apart from their larger width, they sometimes look like S-type LPVs. However, their variation patterns are found to be *recurrent* on time-scales of a few days (McCandliss *et al.* 1994). They have been found in a few apparently peculiar WR stars: HD191765 (Vreux *et al.* 1992; Morel *et al.* 1998a), EZ CMa (St-Louis 1995; Morel *et al.* 1997), and HD4004 (Morel *et al.* 1998a). Several interpretations have been suggested to explain this phenomenon, including the presence of a compact companion hidden in the wind (Drissen *et al.* 1989), a bipolar jet (Vreux *et al.* 1992), or a wind-surface connection (Morel *et al.* 1997).

Type-P LPVs occur in the form of dramatic ($> 10\%$ of line emission) variations in the shape of the line profile, which are correlated with the orbital period in binary WR+O systems (St-Louis *et al.* 1996; Moffat 1996a). Some of these phase-dependent LPVs can be modeled as excess line emission from the wind-wind collision zone between the two hot-star components (Marchenko *et al.* 1995; Lührs 1997). Other periodic variations were explained as selective eclipses of one star by the wind of its stellar companion (St-Louis *et al.* 1993).

In the previous two papers in this series, we have investigated S-type LPVs with the use of a simple phenomenological model in which the LPVs arise from local inhomogeneities in a radially expanding stellar wind (Lépine *et al.* 1996, hereafter Paper I; paper II). This working model uses the idea that an emission line arising from a clumped wind can be thought of as arising from the sum of a large number of discrete wind emission elements (DWEEs). With a few assumptions about the statistical distribution and relative emission of individual DWEEs as a function of time, we have obtained simulations which agree with the

data remarkably well.

A comparison of these synthetic LPV patterns with observations of LPVs in optical WR emission-lines yielded several constraints on the inhomogeneous structure of WR winds. We found that the wind must consist of a huge number ($N_e \gtrsim 10^{4-5}$) of DWEEs. These DWEEs must have large, intrinsic velocity dispersions $\overline{\sigma_v} \sim 100 \text{ km s}^{-1}$, to account for the size of variable subpeaks in the line-of-sight velocity space ξ . There is strong evidence for the local velocity dispersion within DWEEs to be anisotropic, with $\sigma_{v_r} \sim 4\sigma_{v_\theta}$, where σ_{v_r} is the velocity dispersion along the propagation axis (radial), while σ_{v_θ} is the velocity dispersion perpendicular to the propagation axis. The radial acceleration rates of DWEEs, $a_r \sim 5 - 30 \text{ m s}^{-2}$, are found to be smaller than the wind acceleration predicted from the standard model of WR stars ($a_r \gtrsim 50 \text{ m s}^{-2}$). The duration of subpeak events is found to be consistent with the time it takes for a local wind inhomogeneity to pass through the line-emission region.

We also reported in papers I and II on observational limits in the study of inhomogeneous WR wind structure from LPVs in their optical emission-lines. We suggested that one would benefit from using very high spectral-resolution and signal-to-noise ratio, combined with very tight and extensive time-sampling, in order to uncover important details in the patterns of LPVs. It turns out that the best star for such a study is the very bright WR star γ^2 Velorum, with apparent visual magnitude $V \simeq 1.82$. Even though γ^2 Vel owes this brightness partly to its O-type companion, it is still by far the closest WR star (van der Hucht *et al.* 1997; Schaefer *et al.* 1997). If it were a single WR star, it would shine with $V \simeq 3.2$.

This paper presents series of very high-resolution spectra of γ^2 Vel obtained from the CFH telescope (§2). The observed LPV patterns are analyzed with the help of a multi-scale analysis method involving the wavelet transform (§3). The data are compared to LPV simulations from a model of radially propagating

inhomogeneous wind features (§4). It is shown that the data can be accounted for by the existence of two separate LPV modes, one consisting of the usual stochastic, narrow emission subpeaks, the other one arising from an additional component of broad subpeaks, which are similar to type-R LPVs, although no recurrent behavior has been confirmed yet. The results are discussed in §5, where we discuss the possible origin of the broad LPV subpeaks. A summary follows in §6.

4.2 Observations and reduction

On heliocentric Julian dates (JD) 2,450,061 and 2,450,063 we observed γ^2 Velorum at the Coudé focus of the Canada-France-Hawaii 3.6 meter telescope on Mauna Kea. We used the 1800 mm^{-1} holographic grating to project spectral images with the f/8 camera onto a Reticon 1872 array detector with $75\mu\text{m} \times 15\mu\text{m}$ pixels. We monitored the strong C III $\lambda 5696$ optical emission-line with successive, short (300 seconds) exposures, achieving a signal-to-noise ratio $S/N \sim 2000$ per pixel, and a 2.5 pixel resolution of $\Delta\lambda \sim 0.08 \text{ \AA}$. This was equivalent to monitoring at $\lambda 5696 \text{ \AA}$ with a line-of-sight velocity resolution $\Delta\xi \simeq 4.2 \text{ km s}^{-1}$.

Reduction was carried out using IRAF with the Reticon reduction package developed by D. Bohlender and G. Hill, which includes the baseline reduction, flat-fielding, heliocentric correction and wavelength calibration with a Th-Ar comparison spectrum. The whole C III $\lambda 5696$ emission-line is so broad in γ^2 Vel that it could not all fit in the full 58 \AA range available at the detector. Thus, the extreme blue and red line wings do not appear in the data images. The absence of a flat continuum region means that we had to rectify the spectra by fitting a straight line passing through fixed wavelength regions on the blue and red edges, where contributions from the line emission are minimal. Although this means that precise estimates of equivalent widths cannot be obtained from our data, our analysis of LPVs should not be significantly affected.

One single night of data consists of N spectra taken at times t_i ($i = 1, N$). The spectra can be denoted as a spectral time-series $S(\xi, t_i)$, where $\xi = (\lambda - \lambda_0)\lambda_0^{-1}c$ is the line-of-sight Doppler velocity of line-emitting atoms, with $\lambda_0 = 5696 \text{ \AA}$. We define the residual spectra $R(\xi, t_i)$ as the instantaneous deviation from the mean profile:

$$R(\xi, t_i) = S(\xi, t_i) - \frac{1}{N} \sum_{i=1}^N S(\xi, t_i). \quad (4.1)$$

The time-series of residual spectra are presented for each night in Fig.1, along with the mean profile and the maximum and minimum values recorded in $S(\xi, t_i)$ for each pixel element. We detect variability in the line on time-scales of minutes to hours, with a mean amplitude $\sim 5\%$ of the continuum level, i.e. about 50 times larger than the expected instrumental noise. Fluctuations do not occur independently from pixel to pixel, but rather appear in the form of extended features in line-of-sight velocity space ξ .

The variations also seem to follow a systematic trend. The intensity in some sectors seems to increase systematically during the night, whereas it apparently decreases in other sectors. This gives one the impression that the variations occur in the form of excess features which are either in emission or absorption, and that emission features gradually turn to absorption in the course of the night and vice versa. However, we can show these apparent reversal patterns to be numerical artifacts. Although the level of reference $\bar{S}(\xi)$ is well defined for each night, it is still arbitrary; the fact that one feature appears in emission or absorption in $R(\xi, t_i)$ has no direct physical meaning. The procedure in Eq.1 can also introduce spurious features in $R(\xi, t_i)$ if $\bar{S}(\xi)$ is not perfectly smooth. Furthermore, values of $R(\xi, t_i)$ always add up to zero at any wavelength when summed over t_i , as is evident from Eq.1. This means that slow, systematic variations in the line profile will always produce inversion patterns like those observed in Fig.1. For example, an excess emission feature at the start of the series will always be followed by an apparent absorption trough.

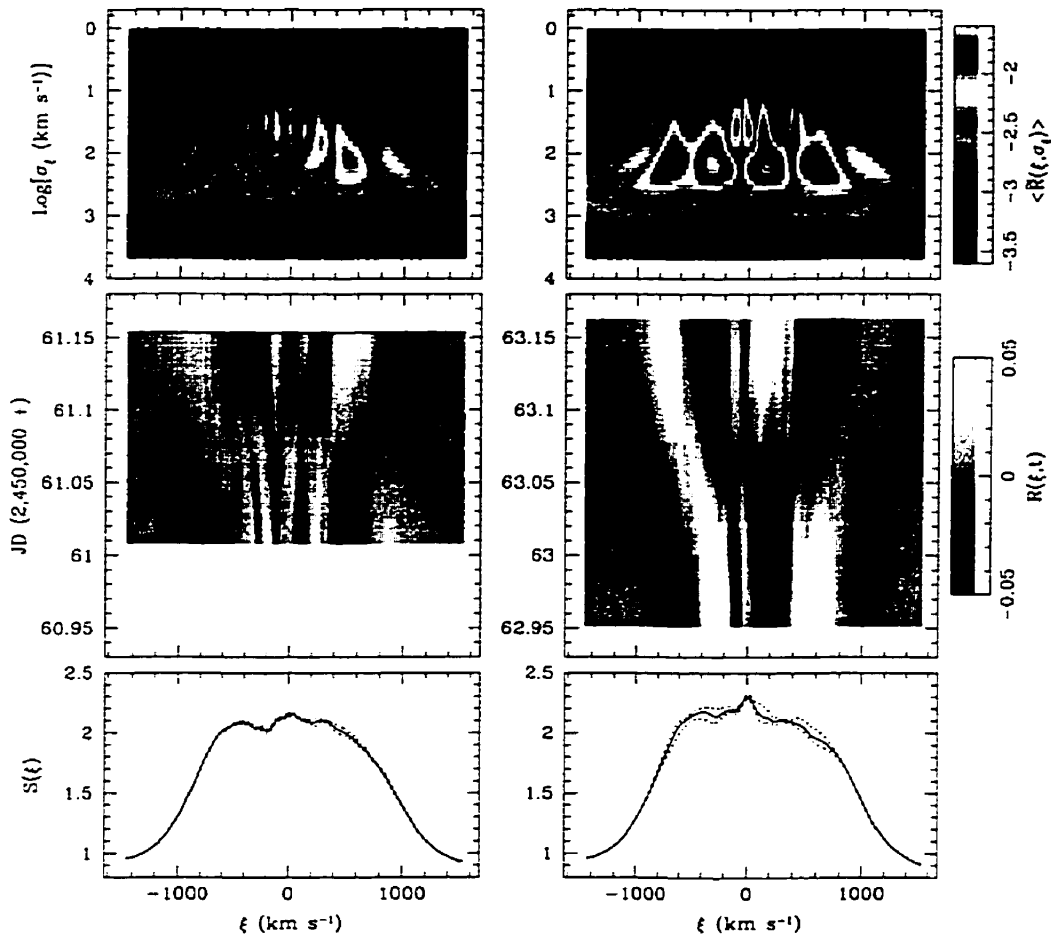


FIGURE 4.1. Spectral time-series of the residuals $R(\xi, t_i)$ in the C III $\lambda 5696$ emission line (greyscale plots, central panels) obtained after subtracting off the mean line profile, which is shown at bottom (full line) along with the maximum and minimum measured values (dashed lines). The color displays at the top show the mean wavelet spectrum for each time-series (see §3.1). The wavelet spectrum indicates the characteristic location (ξ) and scale (σ_ξ) of the variable line subpeaks.

Systematic variations in the spectrum can be better appreciated if we plot the *instantaneous* line variation gradient at any time. We define an instantaneous spectral variation gradient time-series $T(\xi, t_j)$ as:

$$T(\xi, t_j) \equiv \frac{S(\xi, t_p) - S(\xi, t_q)}{t_p - t_q}, \quad \forall t_j = \frac{t_p + t_q}{2}; \quad \Delta t_{min} < t_p - t_q < \Delta t_{max}, \quad (4.2)$$

i.e. the difference between all pairs of spectra in the time-series which are separated by a time interval $\Delta t_{min} < \Delta t < \Delta t_{max}$. This time interval should be selected in such a way that Δt_{max} is not too large as compared to Δt_{min} , e.g. in order that one compares spectrum 1 with 3, 2 with 4, 3 with 5, etc... One drawback of this method is that it emphasizes the effects of instrumental noise, especially the random pixel-to-pixel variations. One way to minimize these effects is to use a Δt_{min} such that the mean amplitudes of LPVs after an interval $\Delta t \simeq \Delta t_{min}$ are significantly larger than the standard deviation from the noise. Alternatively, we may use the wavelet filtering technique, described in §3.2, to reduce the amplitudes of the pixel-to-pixel variations in the spectra. Fig.2 shows the $T(\xi, t_j)$ of the data (with $[\Delta t_{min}, \Delta t_{max}] = [6, 12]$ minutes), after having performed a wavelet filtering procedure with combined filters B and C (cf. §3.2).

The resulting $T_{BC}(\xi, t_j)$ reveal that the LPV features systematically move from line center towards line edges. This pattern is consistent with LPVs arising from radially accelerating emission elements (see Moffat *et al.* 1988; Robert 1992; and paper II). The LPV patterns in γ^2 Vel therefore behave similarly to the stochastic subpeaks observed in single and long-period binary WR stars, which are interpreted in terms of inhomogeneities in a radially expanding stellar wind. The reason why we did not need to calculate the $T(\xi, t_j)$ in most previous studies is due to the greater time-coverage leading to a more robust time average $\bar{S}(\xi)$.

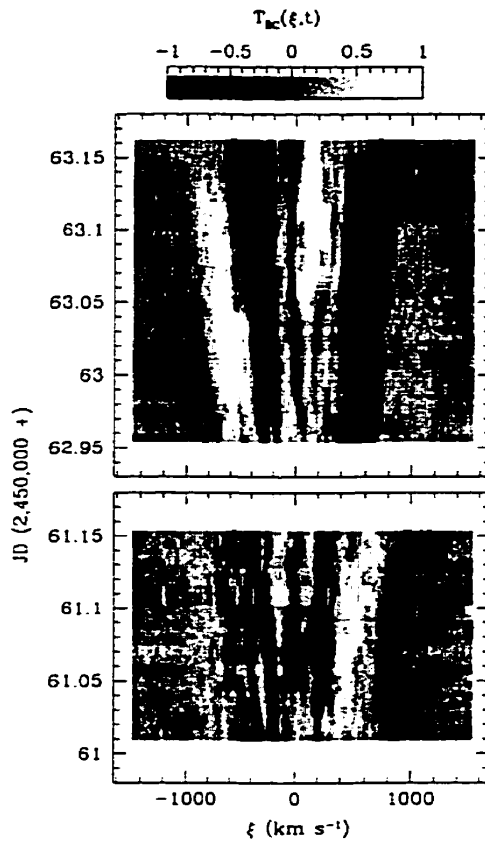


FIGURE 4.2. Instantaneous variation with time, $T(\xi, t_i)$, in the spectral time-series, obtained by comparison of successive spectra. This yields a more objective representation for the time-variability in the emission-line than does the residuals, because $R(\xi, t_i)$ is dependent on the arbitrary choice of the mean spectrum. The plots clearly shows that LPVs consist of features which systematically move from the line center ($\xi = 0$) towards the line edges, whereas the greyscale plots in Fig.1 did not show this behavior unambiguously.

4.3 Multi-Scale Analysis

4.3.1 Wavelet Spectrum

We use wavelet analysis to quantify the characteristic scale and location of variable features in the spectra. A mathematical formulation and interpretation for the wavelet technique applied to spectral time-series can be found in papers I and II. The continuous *wavelet transform* over ξ of a data set $R(\xi, t_i)$, denoted $\tilde{R}(\xi, \sigma_\xi, t_i)$ is defined as:

$$\tilde{R}(\xi, \sigma_\xi, t_i) \equiv \frac{\pi}{8} \int_{-\infty}^{\infty} R(\xi', t_i) \psi\left(\frac{\xi' - \xi}{\sigma_\xi}\right) \frac{d\xi'}{\sigma_\xi}, \quad (4.3)$$

where we use $\psi(x) = (1 - x^2) \exp(-x^2/2)$, the so-called *Mexican-Hat* function, as the wavelet. We also define the *mean wavelet power spectrum*, denoted $\langle \tilde{R}(\xi, \sigma_\xi) \rangle$, which combines the information from N individual spectra in the time-series:

$$\langle \tilde{R}(\xi, \sigma_\xi) \rangle^2 \equiv \sum_{i=1}^N \frac{1}{N} (\tilde{R}(\xi, \sigma_\xi, t_i))^2. \quad (4.4)$$

The mean wavelet spectrum $\langle \tilde{R}(\xi, \sigma_\xi) \rangle$ shows the typical amplitude of variable features with a characteristic scale σ_ξ at each location ξ .

The mean wavelet spectrum for each of the two spectral time-series from γ^2 Vel is displayed in Fig.1. The small scale regime ($0 \lesssim \text{Log}[\sigma_\xi(\text{km s}^{-1})] \lesssim 1$) shows a more or less uniform response over ξ , and is the scale domain for pixel-to-pixel fluctuations. On intermediate scales ($1 \lesssim \text{Log}[\sigma_\xi(\text{km s}^{-1})] \lesssim 3$), one sees a response in ξ whose intensity is correlated with the intensity of the emission-line; this is the realm of *intrinsic* variable line features. The largest scale domain ($3 \lesssim \text{Log}[\sigma_\xi(\text{km s}^{-1})] \lesssim 4$) is sensitive to variations on a scale comparable to the data interval, such as global line variations, or continuum variations. Because of the normalization procedure in the data reduction, these latter variations have been attenuated, which might explain the negligible wavelet response on that scale domain.

The wavelet spectrum reveals the existence of relatively narrow variable features near the line center ($\xi \sim 0$), which are absent near the line edges. This makes the wavelet spectra in Fig.1 look like semi-circles centered on $\xi = 0$. This particular behavior has been observed to occur systematically in WR emission-lines with S-type LPVs (see paper II). It was interpreted as evidence for anisotropic velocity dispersion in the wind, with velocity dispersions in the radial direction larger than in the azimuthal direction ($\sigma_{v_r} \sim 4\sigma_{v_\theta}$). The LPVs in γ^2 Vel therefore show similarities with the S-type phenomenon. On the other hand, these other WR stars showed no evidence for broad features near their line center, whereas in γ^2 Vel, the wavelet spectrum suggests the existence of a uniform distribution of broad features (at a scale $\text{Log}[\sigma_\xi(\text{km s}^{-1})] \simeq 2.3$) over the whole profile. The scale of these features is reminiscent of the type-R LPVs found in the star HD191765 (cf. paper II), although we have no indication of a recurrent behavior in γ^2 Vel.

The scaling properties of the variable components over the line profile are combined with the *wavelet power spectrum*, which yields the mean power in the wavelet spectrum within some interval $[\xi_1, \xi_2]$. The wavelet power spectrum, denoted $\langle \tilde{R}(\sigma_\xi) \rangle_{[\xi_1, \xi_2]}$ is obtained from:

$$\left[\langle \tilde{R}(\sigma_\xi) \rangle_{[\xi_1, \xi_2]} \right]^2 \equiv \frac{1}{\xi_2 - \xi_1} \int_{\xi_1}^{\xi_2} \langle \tilde{R}(\xi, \sigma_\xi) \rangle^2 d\xi , \quad (4.5)$$

and is analogous to the Fourier power spectrum. We present in Fig.3 the wavelet power spectrum of LPVs in γ^2 Vel in the interval $[\xi_1, \xi_2] = [-900, 900] \text{ km s}^{-1}$. The combined wavelet power spectrum from the two nights is compared to the wavelet power spectra from the LPVs in the C III $\lambda 5696$ emission-line in HD192103, and from the LPVs in the He II $\lambda 5411$ emission-line in HD191765 (see paper II). The star HD192103 is a single star with the same WR subtype as γ^2 Vel (WC8), and shows typical S-type LPVs as seen in most WR spectra. The star HD191765, on the other hand, is a prototype, along with EZ CMa, for the rare class of WR stars with R-type LPVs.

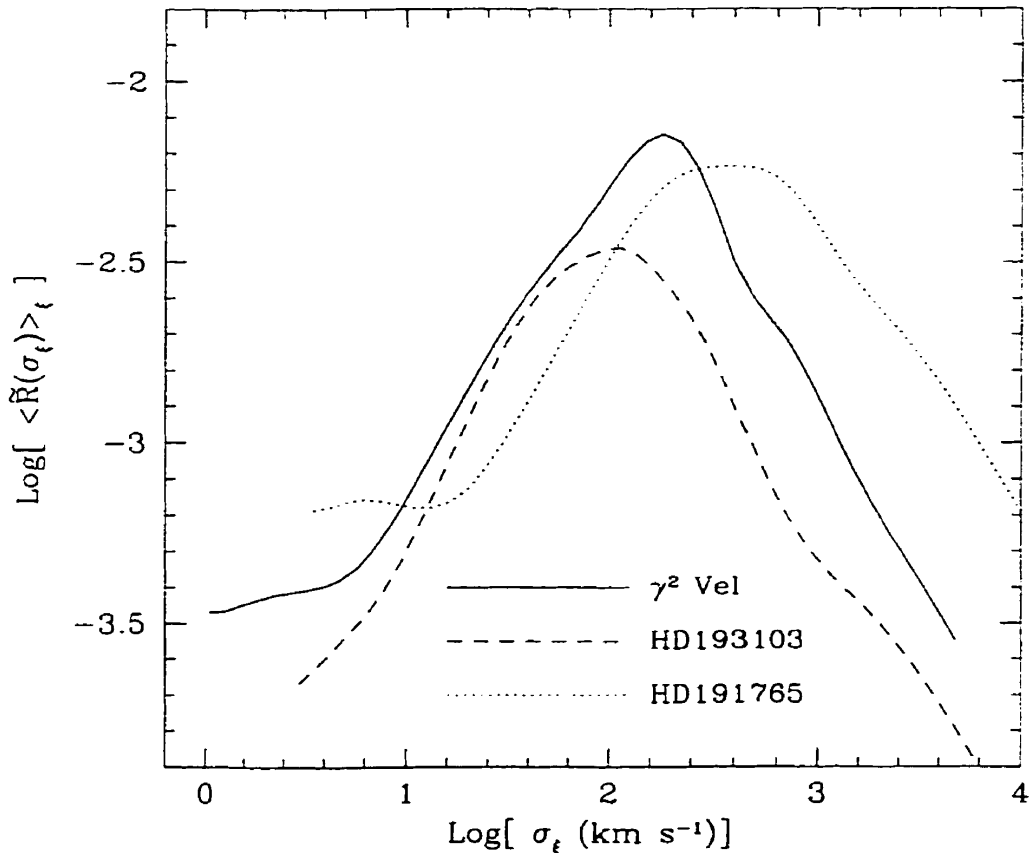


FIGURE 4.3. The wavelet power spectra from the LPVs found in the C III $\lambda 5696$ emission line in γ^2 Vel (for both nights) are compared to the power spectra from the stochastic LPVs (narrow emission subpeaks) in the C III $\lambda 5696$ from HD192103, and the power spectra from the recurrent LPVs (broad emission subpeaks) found in the He II $\lambda 5411$ of HD191765. The wavelet power spectrum from γ^2 Vel is apparently intermediate between these two other stars, suggesting the presence of both narrow and broad components.

One sees that γ^2 Vel seems to be intermediate between HD192103 and HD191765. Compared to HD192103, γ^2 Vel definitely shows an excess of large-scale components ($\text{Log}[\sigma_\xi(\text{km s}^{-1})] \simeq 2 - 3$). The star HD191765 shows more power at the large-scale end, but has a deficit in small-scale intrinsic features ($\text{Log}[\sigma_\xi(\text{km s}^{-1})] \simeq 1 - 2$) at the same time. This is not the case for γ^2 Vel, whose subpeak features show high levels of variability on both small and large scales.

4.3.2 Wavelet Filtering

The wavelet transform can be used to devise a very efficient scale-filtering tool. A spectral time-series $R(\xi, t_i)$ can be recovered from its wavelet transform $\tilde{R}(\xi, \sigma_\xi, t_i)$ from the so-called *wavelet reconstruction theorem* which, for our specific choice of wavelet and normalization, can be shown to be obtained easily from:

$$R(\xi, t_i) = \int_0^\infty \tilde{R}(\xi, \sigma_\xi, t_i) \frac{d\sigma_\xi}{\sigma_\xi}. \quad (4.6)$$

A scale filtering of the signal is obtained if, instead of rebuilding the signal from all its scale components, one integrates over a finite scale domain $[\sigma_{\xi 1}, \sigma_{\xi 2}]$:

$$R_{[\sigma_{\xi 1}, \sigma_{\xi 2}]}(\xi, t_i) = \int_{\sigma_{\xi 1}}^{\sigma_{\xi 2}} \tilde{R}(\xi, \sigma_\xi, t_i) \frac{d\sigma_\xi}{\sigma_\xi}. \quad (4.7)$$

This procedure effectively filters out all signal components with characteristic scales out of the range $\sigma_{\xi 1} < \sigma_\xi < \sigma_{\xi 2}$.

We have defined four scale domains, each spanning a factor of 8, for the analysis of the γ^2 Vel spectral time-series: A = [0.78, 6.3] km s⁻¹, B = [6.3, 50] km s⁻¹, C = [50, 400] km s⁻¹, and D = [400, 3200] km s⁻¹. These domains were not selected arbitrarily, but defined in such a way as to obtain a *natural* separation of the apparent scale components in the signal, as suggested from the wavelet power spectrum. We have plotted in Fig.4 the mean wavelet power spectrum for each night, along with the power spectrum for each of the four filtered components obtained with filters A, B, C, and D. One sees that the wavelet power spectrum

of the original data can be viewed as a combination of four “bumps”, which are separated from one another with our choice of wavelet filters. Note that the wavelet power spectrum of each filtered component does not fall abruptly at the band limits, although the filter bands are strictly defined. This is actually a very interesting by-product of the wavelet transform: it minimizes the numerical artifacts which can arise in Fourier band-pass filtering. This is made at the expense of the scale-resolution, and results in some leaking of power from one scale component to the next.

The time-series for the filtered LPV patterns are presented in Fig.5. Note that the sum of the four scale components R_A , R_B , R_C and R_D yields back the unfiltered time-series. From examination of the variation patterns for each scale regime, it seems that we have achieved a reasonably good separation between instrumental fluctuations (scale domains A and D) and intrinsic stellar variability (scale domains B and C).

Spectral variations in scale domain A comprise the pixel-to-pixel variations which arise from photon-counting statistics, but also from other instrumental effects, and contamination by cosmic rays and telluric lines. In the first night, one also sees the emergence of a weak Fabry-Perot (FP) pattern, which must have resulted from internal reflections in the instrument. The fact we detect this FP pattern in these difference spectra suggests that the pattern *varied* during the first night, for reasons which are still unclear. The FP pattern probably remained stable in the second night, which explain why it does not show in $R(\xi, t_i)$. Finally, one can also see a trace of narrow *intrinsic* features near the center of the emission-line, which are absent from the edges. Their presence is more conclusive in the data from the second night which is not contaminated by a variable FP pattern.

Variability in scale domain D reveals the presence of global, random variations in the line-amplitude during the first night. These are likely due to errors in spectral rectification. As mentioned in §2, we were obliged to define a pseudo-

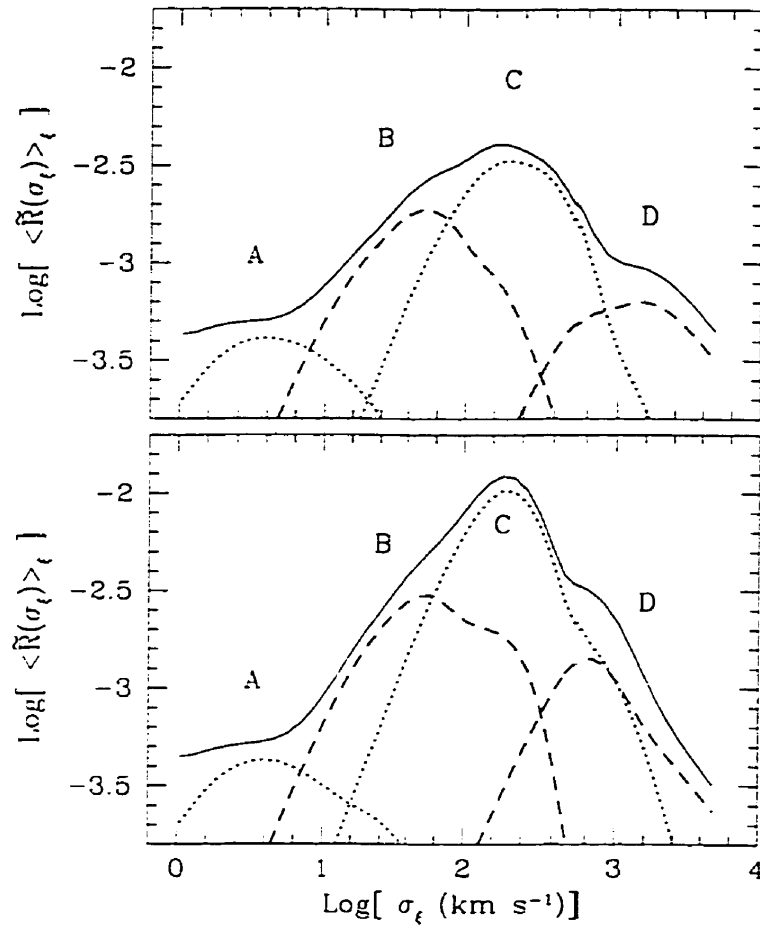


FIGURE 4.4. Wavelet power spectrum from each of the spectral time-series (upper: first night; lower: second night) of residuals from γ^2 Vel (full line), and from each of the corresponding, scale-filtered time-series (cf. Fig.5). The four filters separate the power spectrum in a seemingly *natural* way, i.e. along the four apparent bumps. The difference in the scaling properties of the LPV between the two time-series can be explained mainly by a change in the amplitude of components sensitive to filter C. Note how the wavelet filtering yields a smooth separation of the scale components.

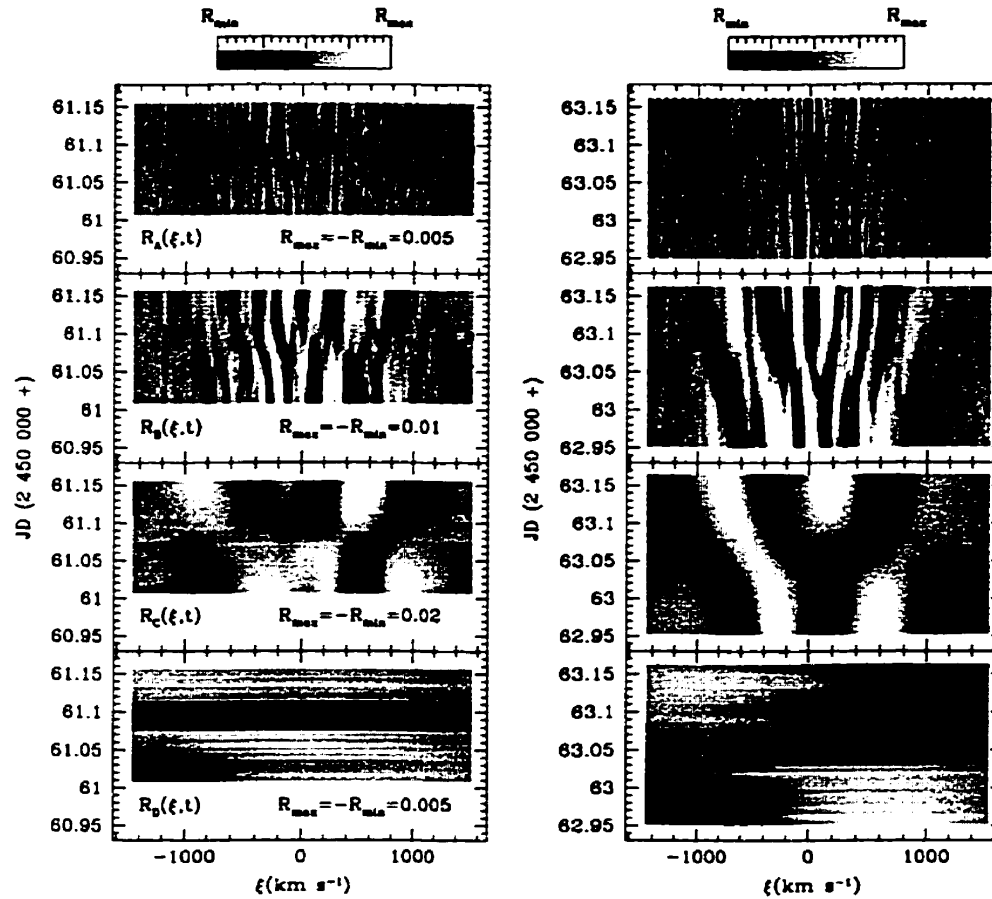


FIGURE 4.5. Wavelet filtering of the residuals using the four filters A, B, C, and D (from top to bottom, respectively), defined in §3.2. The small-scale residuals R_A emphasize instrumental noise features, while R_B and R_C show the narrow and broad intrinsic moving subpeaks, respectively. The larger scale residuals R_D show what appear to be global variations in the emission-line profile.

continuum using narrow spectral regions near the edges of the detector array. Apparently, these regions were affected either by intrinsic line variability or, more likely, by instrumental fluctuations, which resulted in spurious, vertical shifts in this pseudo-continuum. As a result, the intensity in the emission-line seems to vary abruptly in the course of the night. In the second night on the other hand, the filtered component $R_D(\xi, t)$ suggests a systematic shift in the radial velocity of the emission-line during the night, which might be real or arise in small, systematic errors in the wavelength calibration. In any case, all these effects are relatively small compared to the intrinsic LPVs which are obvious in scale domains B and C.

The regularity in the behavior of variable features at scale domains B and C: their strong correlation with location on the emission-line profile; and their symmetrical distribution around $\xi = 0$, all point to the intrinsic nature of these variable components. We note that the kinematics of broad (scale C) and narrow (scale B) features are not significantly different. Both components exhibit a behavior which is consistent with the same rate of motion on the line, suggesting that they arise from wind components having the same radial acceleration. This suggests that both narrow and broad line-features are formed in similar dynamical regions of the wind. We will now show that these LPVs can be reproduced with a model of inhomogeneities in a radially expanding wind.

4.4 Comparative analysis

4.4.1 Simulations of LPVs from an inhomogeneous wind

We model the C III $\lambda 5696$ LPVs in γ^2 Vel using the phenomenological working model introduced in paper II, which describes the LPVs in terms of inhomogeneities in a radially expanding stellar wind. We provide here a brief summary of the model; the reader should refer to paper II for more details.

The emission-line is assumed to arise from a number of *discrete wind emission elements* (DWEEs). We assume the DWEEs to propagate radially along a monotonically increasing velocity law of the form:

$$v_r(r) = v_\infty \left(1 - \frac{R_*}{r}\right)^\beta , \quad (4.8)$$

i.e. the so-called β -law, which is commonly used in models of WR winds (e.g. Schmutz 1997; Hillier & Miller, 1998; Hamann & Koesterke 1998). The parameter R_* should be of the order of the stellar hydrostatic core radius, while β values in the range $0.5 < \beta < 4$ are typically used in the literature.

The relative emission f_e from one DWEE depends on its distance from the star, which can be expressed by the magnitude of its velocity v_r relative to the center of the star, yielding an emission function:

$$f_e(v_r)dv \propto \exp \frac{-(v_r - v_e)^2}{\sigma_{v_e}^2} dv . \quad (4.9)$$

The parameters v_e and σ_{v_e} define the mean location and extension of the line emission region (LER) in wind velocity space, respectively.

We have shown in paper II (see also Brown *et al.* 1997) that, in the optically thin case, we can use the shape of the emission-line profile to estimate the line emission as a function of the radial velocity in the wind. The mean line profile $\bar{S}(\xi)$ gives the emission as a function of projected velocity ξ . From $\bar{S}(\xi)$, we can obtain the spherical deprojection, i.e. the emission as a function of radial velocity $F_e(v_r)$ as:

$$F_e(v_r) \propto \left[-\xi \frac{d}{d\xi} \bar{S}(\xi) \right]_{\xi=v_r} . \quad (4.10)$$

This function is distinct from the function $f_e(v_r)$, because it depends on the radial velocity dispersion σ_{v_r} (“turbulent” motions) in the wind as well as on the extension of the LER, σ_{v_e} , in the wind *mean* velocity space:

$$F_e(v_r)dv \propto \exp \frac{-(v_r - v_e)^2}{\sigma_{v_e}^2 + \sigma_{v_r}^2} dv . \quad (4.11)$$

This can yield an estimate of σ_{v_e} , provided that σ_{v_r} can be evaluated by other means. The function $F_e(v_r)$ computed from the C III $\lambda 5696$ emission line in γ^2 Vel is shown in Fig.6, where it can be compared to $F_e(v_r)$ obtained from the same emission-line in the star HD192103 (cf. paper II). The range in radial velocity appears to be broader for γ^2 Vel. This suggests either the presence of larger perturbations (σ_{v_r}) in the velocity field, or a larger extension (σ_{v_e}) of the LER in mean bulk velocity space. Since both stars are of the same subtype (WC8) and have almost identical terminal wind velocities ($v_\infty \simeq 1415$ km s⁻¹ for γ^2 Vel, and $v_\infty \simeq 1405$ km s⁻¹ for HD192103, according to Prinja *et al.* 1990), then it is reasonable to assume that the location and size of the LER should be very similar. Therefore, the larger emission-line broadening in γ^2 Vel should be interpreted as evidence for larger σ_{v_r} . This interpretation is consistent with the observation of broader LPV subpeaks on the line profile, suggesting the existence of larger “turbulent” motions in some regions of the wind.

In our model, we assume a statistical distribution in the relative fluxes from DWEEs in the form of a power law:

$$n(f) \propto f^{-\alpha}, \quad f_0 < f < \eta f_0. \quad (4.12)$$

We define N_e as the mean number of DWEEs that lie in the velocity regime $v_e - \Delta v_e < v_r < v_e + \Delta v_e$, where most of the emission occurs, and F_e as the mean value of the total emission from all DWEEs.

The DWEEs are assumed to have large intrinsic velocity dispersions, which are assumed to be anisotropic. We define a radial velocity dispersion σ_{v_r} and an azimuthal velocity dispersion σ_{v_θ} . The resulting line-of-sight velocity dispersion σ_ξ from one DWEE therefore depends on its projection angle $\mu = \cos \theta$:

$$\sigma_\xi^2 = \mu^2 \sigma_{v_r}^2 + (1 - \mu^2) \sigma_{v_\theta}^2. \quad (4.13)$$

Because DWEEs with different values for μ will appear at different locations on the emission-line profile, the anisotropic velocity dispersion means that the width

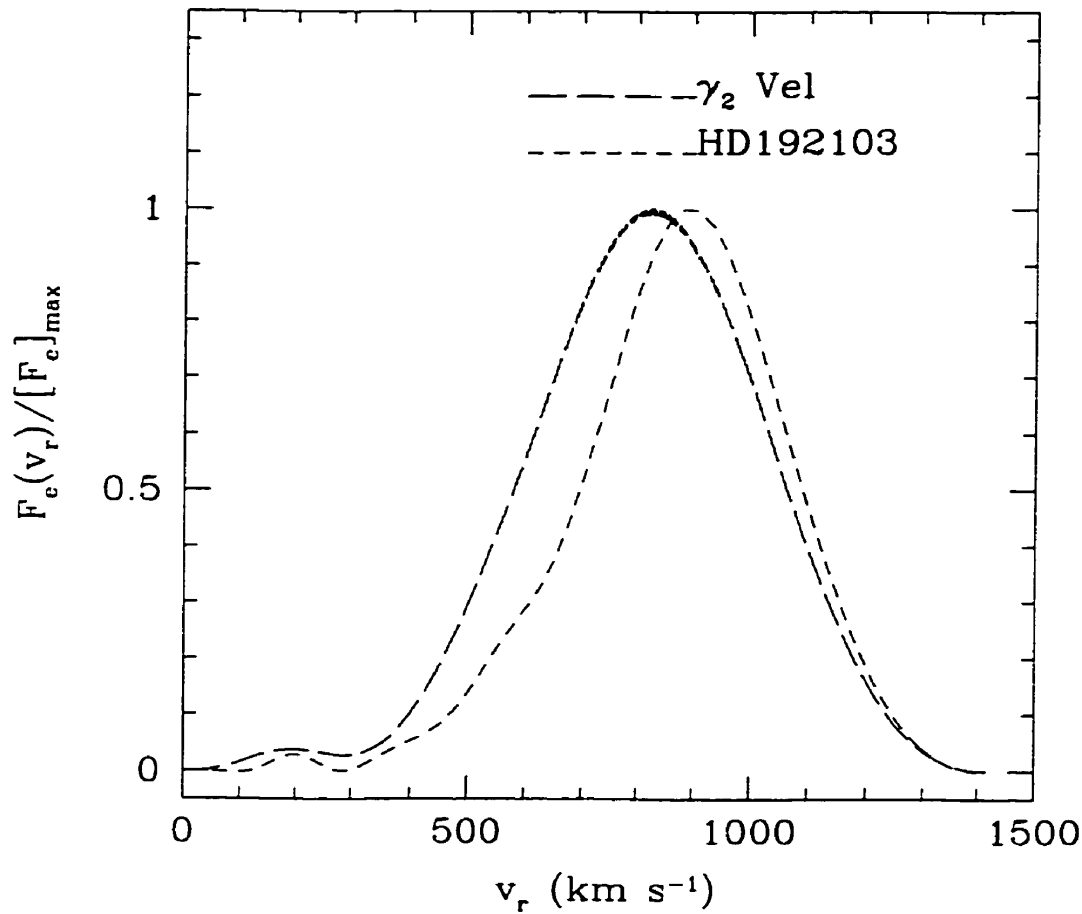


FIGURE 4.6. Estimated emission $F_e(v_r)$ from the C III $\lambda 5696$ line as a function of the expansion velocity of emitting wind material, as estimated from the shape of the emission-line profile. The function $F_e(v_r)$ for γ^2 Vel (long-dashed line) is compared to $F_e(v_r)$ obtained from the same line in the WR star HD192103 (short-dashed line), which is of the same WR subtype (WC8). The C III line emission apparently arises from a slightly broader velocity regime in γ^2 Vel.

TABLEAU 4.1. Parameter of the inhomogeneous wind model and best-fit values.

Parameter	Definition	Component (a)	Component (b)
v_∞	terminal wind velocity	1400 km s ⁻¹	1400 km s ⁻¹
R_*	velocity law parameter (physical size)	10 R_\odot	10 R_\odot
β	velocity law parameter (β -law index)	4	4
v_e	location of emission region (in radial velocity space)	850 km s ⁻¹	850 km s ⁻¹
σ_{v_e}	extension of emission region	150 km s ⁻¹	150 km s ⁻¹
F_e	total flux (equivalent width)	1500 km s ⁻¹	400 km s ⁻¹
N_e	mean number of discrete elements	5,000	25
α	flux distribution parameter (power index)	3	3
η	flux distribution parameter (range)	10^2	10^3
σ_{v_r}	local velocity dispersion (to propagation)	160 km s ⁻¹	200 km s ⁻¹
σ_{v_θ}	local velocity dispersion (\perp to propagation)	40 km s ⁻¹	200 km s ⁻¹
f_r/f_θ	escape probability ratio	0.7	1.0

of the resulting LPV subpeaks will depend on their location on the line profile. Similarly, we separately define f_r as the escape probability in the radial direction, and f_θ as the escape probability in the azimuthal direction. The relative escape probability f becomes:

$$f^2 = \mu^2 f_r^2 + (1 - \mu^2) f_\theta^2 . \quad (4.14)$$

The LPVs in other WR stars were found in paper II to be consistent with $\sigma_{v_r} \simeq 4\sigma_{v_\theta}$, and with $f_r \lesssim f_\theta$.

We present in Fig.7 a model simulation which is in qualitative agreement with the data. Values for the model parameters used in these simulations are listed in Table 1. We used the same template as the data for sampling of the time-series, in order to facilitate the comparison with the data, and to avoid sampling biases in the comparative analysis. Instrumental noise was implemented in the simulations in the form of random fluctuations according to Poisson-statistics. One sees that the general appearance of the LPVs is reproduced remarkably well.

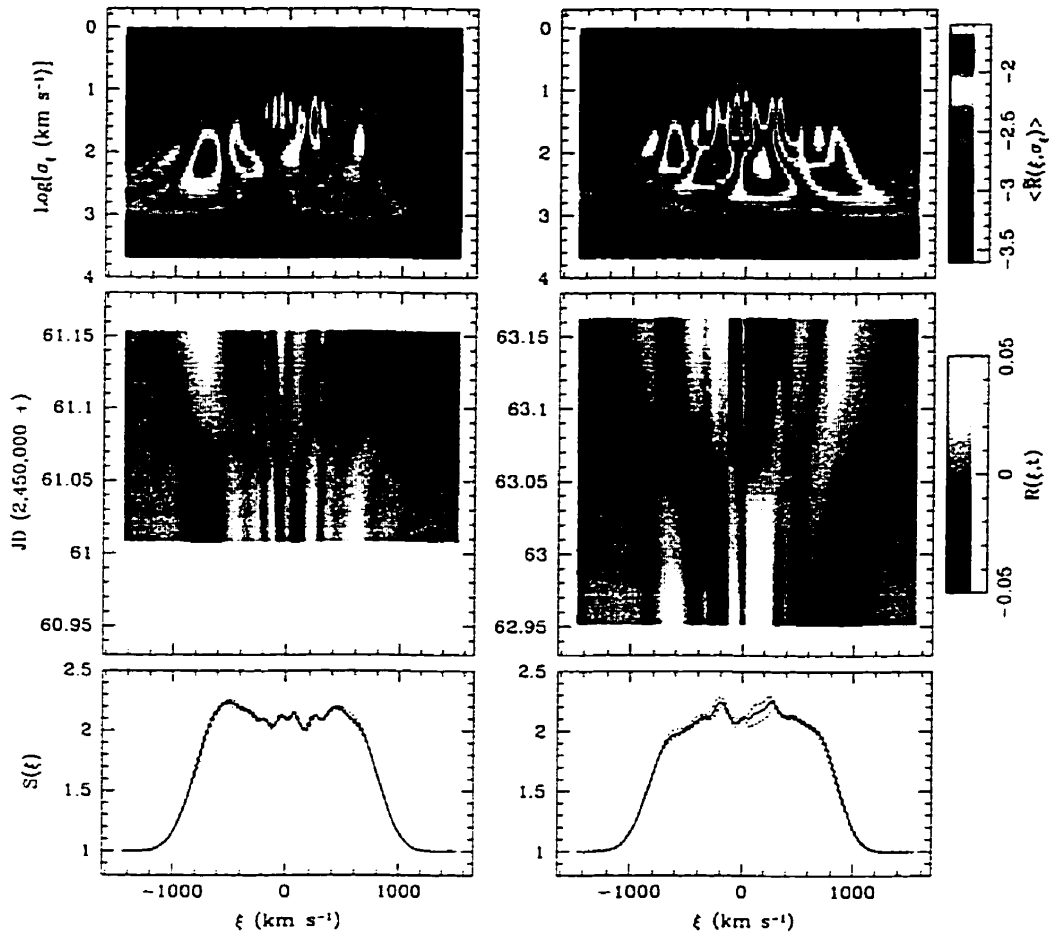


FIGURE 4.7. Simulation of the variability in the C III $\lambda 5696$ emission-line from an inhomogeneous wind, using the same time-series template as the data. Values of the model parameters are listed in Table 1. The greyscale plots shows the residuals obtained after subtracting off the mean profile (bottom); the color-plots show the corresponding mean wavelet spectrum. The resulting LPV patterns are very similar to those seen in the data in both general appearance and scaling properties (cf. Fig.1).

4.4.2 Multiple LPV modes

We have performed several simulations using different values for the scale and amplitude of the wind fluctuations. We used the wavelet power spectrum $\langle \tilde{R} \rangle_\xi$ to compare the scaling properties of the LPVs from the simulations with that of the data. The upper panels in Fig.8 show the $\langle \tilde{R} \rangle_\xi$ from simulations made with a single population of low velocity dispersion DWEEs (a) with $\bar{\sigma}_\xi = 80 \text{ km s}^{-1}$. Although there is considerable scatter in $\langle \tilde{R} \rangle_\xi$, it is clear that these simulations cannot fully reproduce the $\langle \tilde{R} \rangle_\xi$ from the data. The simulations definitely lack some power in the scale range $2 < \log[\sigma_\xi(\text{km s}^{-1})] < 3$. This can be compensated for if we add an extra population of high velocity dispersion DWEEs (b) with $\bar{\sigma}_\xi = 200 \text{ km s}^{-1}$. The LPVs resulting from population (b) cannot account for the observed $\langle \tilde{R} \rangle_\xi$ alone (central panels). However, simulations made by summing patterns from populations (a) and (b) result in wavelet power spectra which are in good agreement with those from the data (bottom panels).

This two-component solution is not unique: the shape of the wavelet spectrum could be reproduced using a more complex distribution of subpeaks on many more different scales. However, the 2-component solution provides an easy explanation for the fact that the LPVs from γ^2 Vel differ from those of other WR stars: the difference is in the existence of an extra component of high velocity dispersion DWEEs. Moreover, whereas we used the same amplitude for component (a) to fit the wavelet power spectrum from each of the two data sets, we had to use a different amplitude for component (b). This suggests that the first population is relatively stable, while the second population is subjected to a significant night-to-night change in amplitude.

We note that the amplitude of the variability resulting from one population of DWEEs can be increased in at least two independent ways: (1) by increasing the mean flux F_e arising from this component, (2) by decreasing the mean number

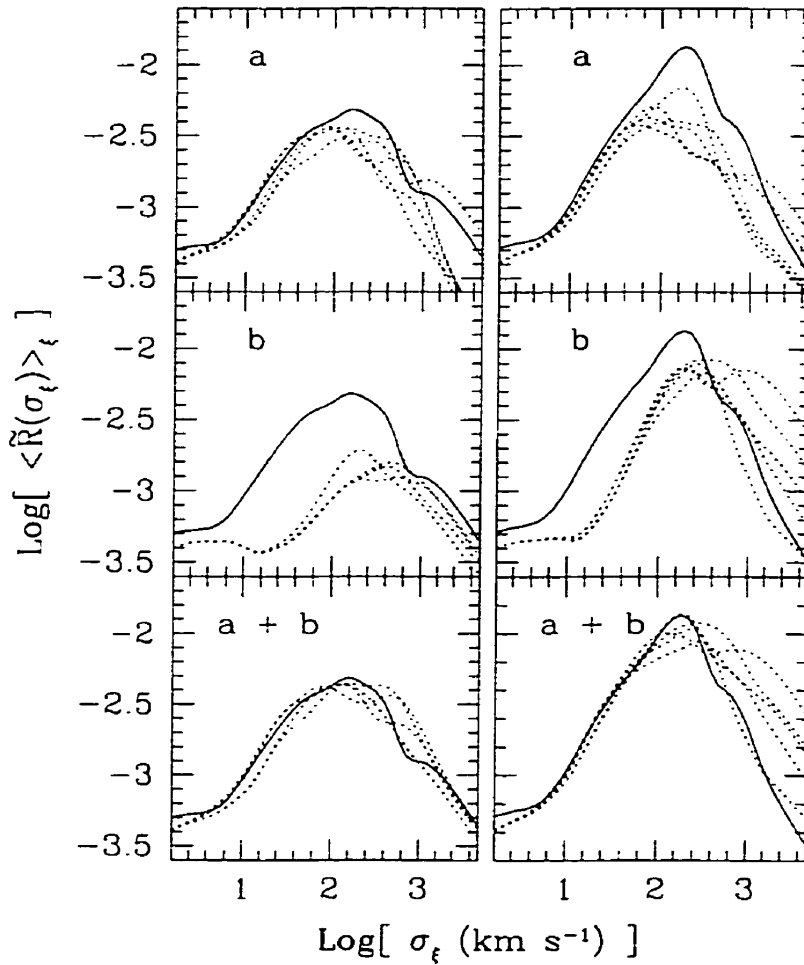


FIGURE 4.8. Comparison between the wavelet power spectrum from the γ^2 Vel data (full lines), with the wavelet power spectra from simulations (dotted lines). Upper panels compare the data with simulations made to generate LPV patterns similar those seen in most WR stars, showing narrow ($\bar{\sigma}_\xi \simeq 80 \text{ km s}^{-1}$) stochastic subpeaks (a). Middle panels show the resulting wavelet power spectra from a set of broader ($\sigma_\xi \simeq 200 \text{ km s}^{-1}$) subpeak features (b). Best fit of the wavelet power spectra from γ^2 Vel is obtained from the superposition of the usual component with a extra set of broad emission features (a + b). Left column is for the first night of observation, right column for the second night. The apparent disagreement between data and simulations on large scales ($\text{Log}[\sigma_\xi] \gtrsim 3$) for the second night can be attributed to a filtering out of large scale features in the data reduction after the spectral rectification procedure.

N_e of DWEEs responsible for the emission. For a given statistical flux distribution of DWEEs (i.e. fixed values of η and α ; cf. §4.1), the amplitude σ_{LPV} of the LPV is expected to be $\sigma_{LPV} \propto F_e N_e^{-1/2}$. For a single population of DWEEs, it is possible to get an estimate of N_e from measured values of F_e and σ_{LPV} . However, in the case where there are two distinct components responsible for line the emission, although we may estimate the σ_{LPV} from each component with $\langle \tilde{R} \rangle_\xi$, we know only the sum of the mean flux from each component $F_{ea} + F_{eb}$. Therefore, it is not possible to estimate N_{ea} and N_{eb} from σ_{LPV} , even with the help of the wavelet power spectrum.

If we assume that the mean flux from individual DWEEs is constant over time, then we have $F_e \propto N_e$, which also means that $\sigma_{LPV} \propto N_e^{-1/2}$. Therefore we might expect to find a correlation between the total flux from one component (say F_{eb}) and the amplitude of the LPVs arising from this component. As it turns out, we observe that the apparent night-to-night change in the amplitude of component (b) correlates with the change in line equivalent width (EW), which is significantly larger in the second night. Though the correlation is only anecdotal, it is consistent with the idea that an increase in the amplitude of the (b) component is responsible for both higher σ_{LPV} and increase in EW. This effect could actually be used to estimate the F_{ea}/F_{eb} ratio, which would yield an estimate of N_{ea}/N_{eb} , although observations over many more nights would be required to test for this trend.

4.4.3 Kinematics of the inhomogeneities

We have introduced in paper II the *degradation function*, a numerical tool which can be used to estimate the radial acceleration of the wind from the systematic motion of LPV features. The degradation function $\sigma_D(a, \Delta t)$ of a

spectral time-series $R(\xi, t_i)$ is obtained from:

$$[\sigma_D(a, \Delta t)]^2 \equiv \sum_{0 < t_j - t_i < \Delta t} \int_{-v_e}^{v_e} [R(\xi + a(t_j - t_i)v_e^{-1}\xi, t_i) - R(\xi, t_j)]^2 [R(\xi, t_j)]^{-2} d\xi. \quad (4.15)$$

The degradation function compares one spectrum with another occurring at a subsequent time Δt after “stretching” the first spectrum in a way which mimics the motion in line-of-sight velocity component ξ of wind features having *radial* acceleration a with respect to the star. The minimum value for $\sigma_D(a, \Delta t)$ at a given Δt is obtained when $a \simeq a_r$, where a_r is the effective radial acceleration in the LER for the observed star (see appendix B in paper II). Experience shows that the best results are obtained when the intrinsic features in the signal are relatively narrow. This is because a motion at a given rate is more easily detected for narrow features. Experiments with the simulations have shown that better results are obtained if we use $R_B(\xi, t_i)$ to perform the degradation function, i.e. if we filter out all scales except those sensitive to the narrow components in the LPV patterns.

We present in Fig.9 the mean degradation functions $\langle \sigma_D(a) \rangle$ obtained from all spectra separated by $\Delta t \leq 4$ hr. We compare the $\langle \sigma_D(a) \rangle$ for the LPV patterns in γ^2 Vel to the $\langle \sigma_D(a) \rangle$ from four simulations generated with different values of βR_* . We computed $\langle \sigma_D(a) \rangle$ on the wavelet filtered time series $R_B(\xi, t_i)$, and separately for each of the two nights for γ^2 Vel. We find that the motions of variable subpeaks in γ^2 Vel are consistent with radial accelerations $a_r \simeq 13 \pm 3 \text{ m s}^{-2}$. The comparison with simulations reveals that such an acceleration in the CIII 5696 emission-line is consistent with velocity laws having $25 < \beta R_* R_\odot^{-1} < 35$. One notes that $\langle \sigma_D(a) \rangle$ is broader for the first night (short-dashed line) than for the second one (long-dashed line). This reflects the larger uncertainty in estimating a_r in the first night, because of the smaller sample for a shorter time-interval. We believe that one could get a very precise estimate of a_r from a larger sample.

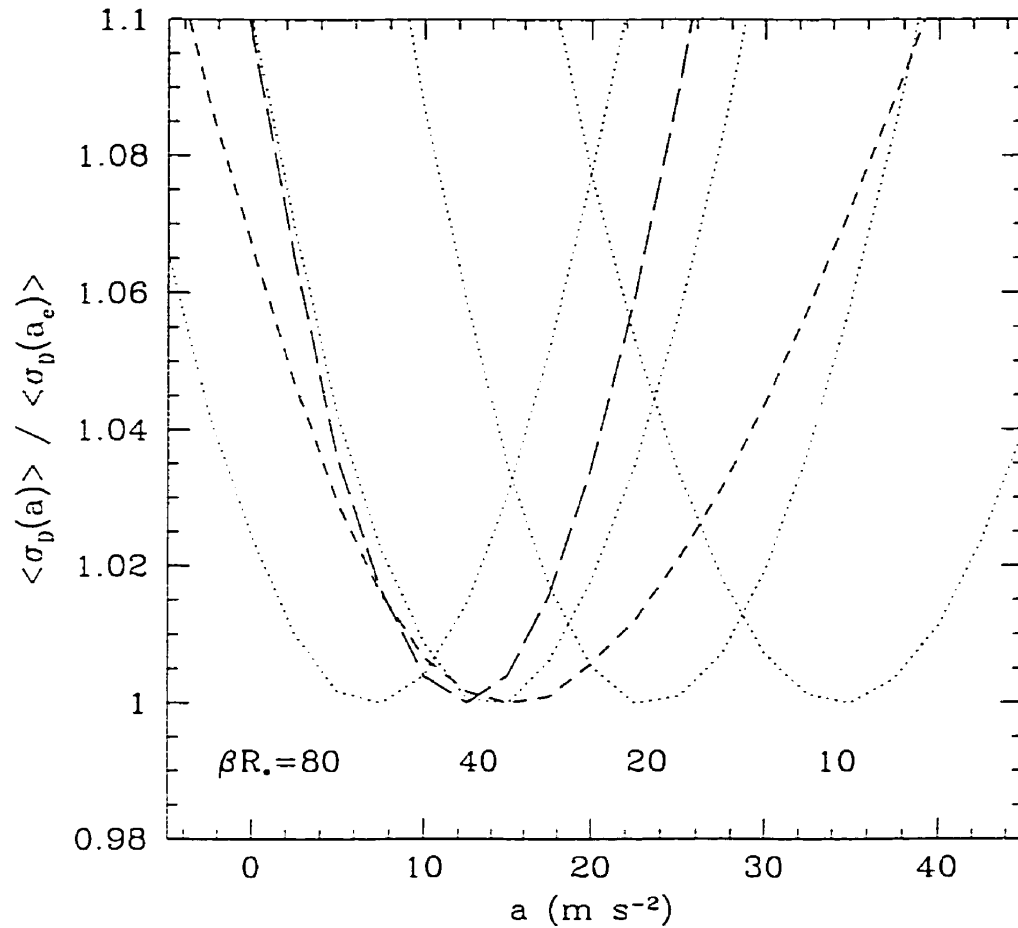


FIGURE 4.9. Estimate of the radial acceleration of inhomogeneous wind features from the degradation function $\langle \sigma_D(a) \rangle$ of the spectral time-series (see §4.3). The LPVs in γ^2 Vel (dashed lines) are consistent with propagating wind features with a radial acceleration $a = 13 \pm 3 m s^{-2}$, which can be fitted with β -type velocity laws having $\beta R_* \approx 40 R_\odot$. Dotted lines show the degradation functions from simulations of LPVs arising in radially propagating wind inhomogeneities, and velocity fields defined by β -laws, with the indicated values of βR_* . The short dashed line is the degradation function for the JD2,450,061 time-series, while the long-dashed line is that for JD2,450,063.

In paper II, we have used the degradation function to estimate the characteristic time-scale of the subpeak features. We have tried to perform the same analysis on our γ^2 Vel spectral time series, but we could not obtain reliable estimates of the subpeak duration. The main reason for this failure is that the characteristic time-scale of subpeak events is on the order of, or larger than the size of our nightly samples.

4.4.4 Comparison with the orbital phase

We use the most recent ephemeris calculated for γ^2 Vel (Schmutz *et al.* 1997) to estimate the orbital phase at which our observations were performed. From a time of periastron passage $T_0 = 2,450,119.1$ (HJD) and an orbital period $P = 78.53$ days, we find orbital phases $\phi \simeq 0.26$ and $\phi \simeq 0.29$ for the first and second night of observation, respectively. The O star passes in front at phase $\phi = 0.03$, the WR star at phase $\phi = 0.61$. Since the orbit is eccentric ($e \simeq 0.33$) the WR star is then slightly in front of the O star at phases $\phi \simeq 0.26 - 0.29$ (see fig.10).

Because the momentum flux in the WR wind is much larger than that of its companion the colliding-wind shock cone region wraps around the O star. At phase $\phi \simeq 0.27$, the mean flow in the shock cone region will be oriented \sim perpendicular to the line-of-sight (or slightly deviating if we take coriolis effects into account). Therefore any line emission from the shock cone at phase $\phi \simeq 0.27$ should appear in spectral region centered on $\xi \cong 0$. The opening angle θ of the shock cone has been evaluated based on X-ray observation of γ^2 Vel (Willis *et al.* 1995) as $20^\circ < \theta < 30^\circ$. The maximum spread $\Delta\xi$ in line-of-sight velocity of elements in the shock cone will be $\Delta\xi \simeq 2 \sin(25^\circ) v_\infty \simeq 0.85 v_\infty$, where v_∞ is the terminal wind velocity, and might be lower depending on the orbital inclination. Thus, assuming the flow in the shock cone to be similar to the mean wind flow, the effects of the shock cone on the emission-line profile should be restricted to a

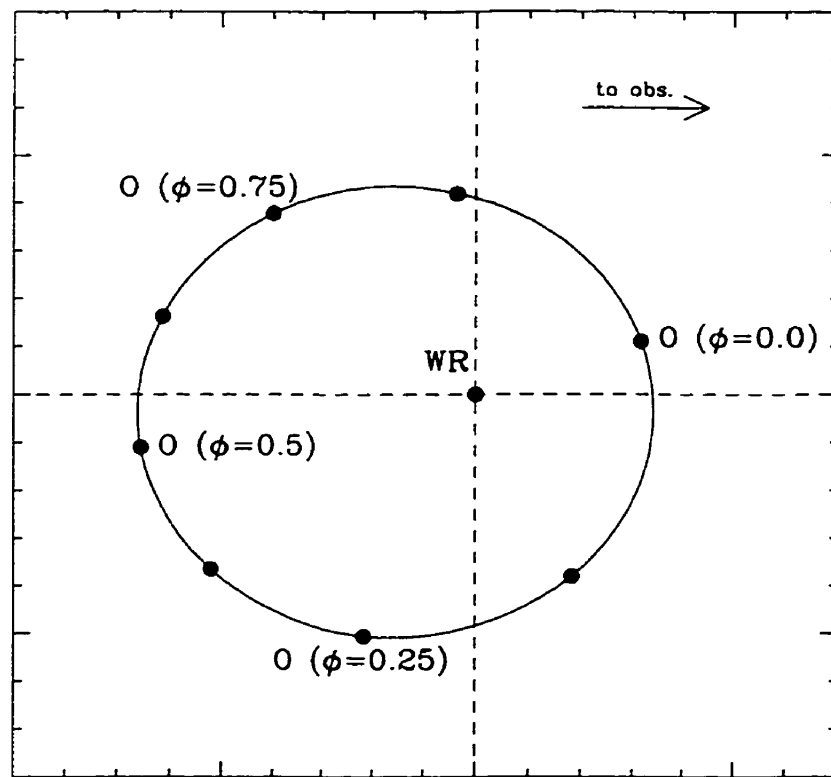


FIGURE 4.10. Schematic representation in the WR star rest frame of the orbital configuration of the γ^2 Vel system. The orbital inclination is not represented here. Spectroscopic observations presented in this paper were performed in the phase interval $0.26 < \phi < 0.29$.

region no larger than $\Delta\xi \approx 1200 \text{ km s}^{-1}$.

However, we detect broad features in the range $-900 \text{ km s}^{-1} < \xi < 900 \text{ km s}^{-1}$ (cf. Fig.1), which yields a $\Delta\xi \simeq 1800 \text{ km s}^{-1}$. Even if we account for the large velocity dispersion associated with the variable subpeak components ($\sigma_\xi \simeq 200 \text{ km s}^{-1}$), the observed range in ξ is too large to be accounted for by emission features in the shock cone region. Therefore, the bulk of the line variability we see in $\gamma^2 \text{ Vel}$ must be intrinsic to the wind.

4.5 Discussion

A first review on the observations showing evidence for line-strength variability in $\gamma^2 \text{ Vel}$ was presented more than ten years ago (Jeffers *et al.* 1985). At that time, these were interpreted as evidence for the presence of a compact companion, a hypothesis which has not been confirmed. Evidence for variability in the He II $\lambda 4686$ line has been interpreted as evidence for irregular mass ejections (Taylor 1990). In this same work, observations of the C III $\lambda 5696$ line strength were also presented, but unfortunately, the signal-to-noise ratio was not high enough to detect any variations on the scale we observed here. Line profile variations have been detected in UV lines of $\gamma^2 \text{ Vel}$ (Brandi *et al.* 1989; St-Louis *et al.* 1993). However we have found no report in the literature on the detection of LPV in optical emission-lines, although their presence was rather suggestive in one study of the orbital variations using optical spectra (Moffat 1977), which included the C III $\lambda 5696$ region.

There is little doubt that the variations we have detected in the C III emission-line profile in $\gamma^2 \text{ Vel}$ are intrinsic to the WR wind. Three observational arguments support this view: (1) the variability coincides with the whole spectral domain occupied by the C III $\lambda 5696$ line emission, (2) the variability takes the form of intense emission subpeaks, which are significantly broader than pixel-to-

pixel variations expected from instrumental noise and other contaminating effects, and (3) these subpeaks show organized patterns with a clear characteristic time-behavior (motion from line center towards line edges). Possible causes of extrinsic variations are insignificant. Instrumental noise is low ($S/N \sim 2000$) since we have observed a very bright star at a 3.6m telescope. Line-shifts can be ruled out, since they would only generate residual features near the line edges, whereas we also detect subpeaks near the line center. Only intrinsic variations in the line emission can explain the observed LPV patterns.

We believe that the observed LPVs arise primarily from inhomogeneities in the WR wind of γ^2 Vel. This is supported by the fact that (1) the LPVs occur in the same spectral domain as the line itself and (2) the systematic motion center \rightarrow edges is consistent with a radial expansion. To verify this hypothesis, we have used the working model presented in paper II, and showed that it is possible to reproduce the LPV patterns in γ^2 Vel from a radially expanding, inhomogeneous wind, represented as the sum of a large number of discrete wind emission elements.

However, comparison between simulations and the data suggests that the LPVs cannot be modeled using a single population of narrow discrete wind elements (with mean line-of-sight velocity dispersion $\overline{\sigma_\xi} \sim 80 \text{ km s}^{-1}$), as is usually sufficient for most other WR stars. To reproduce the scaling properties of the LPV patterns in γ^2 Vel, we must use an extra set of broader ($\overline{\sigma_\xi} \simeq 200 \text{ km s}^{-1}$) variable subpeaks, whose scale is reminiscent of the broad R-type LPVs observed in a few peculiar WR stars. The detection of these unusual, broad components comes as a surprise, because of their co-existence with the regular, narrow LPV subpeaks. In the stars where R-type LPVs were detected, there was no convincing evidence for the existence of narrow features.

One interpretation is that variable features of S-type and R-type always co-exist, but their amplitude ratio changes from one star to another in such a way that one type usually dominates, while the other type remains unnoticed.

Systematic spectroscopic monitoring of a larger sample of WR stars and their classification according to the scaling properties of their LPVs could shed more light on this idea. On the other hand, we have no evidence that the broad features in γ^2 Vel have a recurrent behavior, and it may be that this phenomenon is unrelated to the R-type LPV phenomenon. As it turns out, recent spectroscopic monitoring of γ^2 (Eversberg *et al.* 1998b) over several days has shown no evidence for any periodicity in the LPVs.

Another possible origin for the broad subpeak features of γ^2 Vel in C III $\lambda 5696$ could be in the region where the wind from the WR star collides with that of its O companion (cf. St-Louis *et al.* 1993). We cannot attribute the broad component directly to LPVs of the P-type, because they occur on time-scales much shorter than the 78.53d orbital period. However, we believe that P-type LPVs arise from excess emission from the shock cone region, because of a correlation found between the equivalent width of the C III $\lambda 5696$ emission-line and orbital phase (St-Louis 1995). It seems likely that the shock cone region should be unstable and inhomogeneous (Stevens *et al.* 1992). In this case, the shock-cone emission could well be variable on time-scales of minutes to hours, and arise in the form of moving LPV subpeaks. Nevertheless, we have shown in §4.4 that a shock-cone origin for the broad variable components is unlikely mainly because the range in line-of-sight velocities over which these features are observed is inconsistent with the predicted geometry of the shock-cone.

However, we find anecdotal evidence which suggests that the amplitude of the broad LPV subpeaks is correlated with changes in the line equivalent width. Since St-Louis (1995) has found a correlation between EW and orbital phase, we are tempted to suggest that either: (1) these EW variations with phase are not due to the shock cone emission, but rather to the broad LPV subpeaks, whose effects are amplified when the orbital separation is low, or (2) that there are significant variations in EW associated with the broad LPV subpeaks, which are

not phase dependent, but which are superposed on the excess from the shock cone. This should be checked with high-resolution spectroscopic monitoring of γ^2 Vel spanning most of an orbital phase.

4.6 Conclusions

We have monitored the C III $\lambda 5696$ emission-line in the bright WR star γ^2 Velorum, in a search for line-profile variations (LPVs) on short time-scales (minutes to hours), at a very high signal-to-noise ratio. Observations reveal the presence of LPVs in the form of narrow moving subpeaks having a mean amplitude $\sim 5\%$ of line intensity. These variable features appear to move systematically from line center towards line edges.

We have shown that the observed LPVs can be reproduced from a model of inhomogeneous features in a radially expanding stellar wind. We have used the working model presented in paper II to make simulations of the LPVs in the C III emission-line. A comparison between the data and the simulations reveals the LPVs in γ^2 Vel to be unusual. Whereas the LPVs in most WR star winds are in the form of relatively narrow ($\overline{\sigma_\xi} \simeq 80 \text{ km s}^{-1}$), stochastic features (S-type), the LPVs in γ^2 Vel show the existence of an additional component of broader ($\overline{\sigma_\xi} \simeq 200 \text{ km s}^{-1}$) variable features. These broad features are reminiscent of the broad recurrent LPV features (R-type) occurring in a few peculiar WN stars (HD4004, EZ CMa, and HD191765), although it is not possible to verify the existence of a recurrent behavior with this data set. Independent longer time monitoring of γ^2 Vel has shown no evidence of a recurrent behavior so far (Eversberg *et al.* 1998b).

The C III $\lambda 5696$ emission-line variability from γ^2 Vel is found to be affected by a larger broadening effect than the same line in the star HD192103, a WR star with the same subtype (WC8) and terminal velocity ($v_\infty \simeq 1400 \text{ km s}^{-1}$). This is consistent with the existence of larger wind perturbations yielding higher

velocity dispersions in γ^2 Vel, as reflected by the existence of the broad variable features.

We find that the motion of the narrow (S-type) features is consistent with a radial wind acceleration $a_r = 13 \pm 3 \text{ km s}^{-1}$. If we assume that the wind has a velocity-law in the form $v(r) = (1 - R_* r^{-1})^\beta$, the observed a_r is consistent with laws having $\beta R_* \simeq 40 R_\odot$.

Acknowledgements

SL acknowledges the support provided by scholarships from NSERC of Canada and from FCAR of Québec. AFJM is grateful to the same two organizations and the Killam program of the Canada Council for the Arts for financial aid. TE thanks the Evangelisches Studienwerk/Germany for a 3 year student bursary.

CHAPITRE 5

CONCLUSIONS

5.1 Synthèse des Résultats

Les travaux qui ont mené à cette thèse de doctorat comportaient trois objectifs principaux: (1) mettre au point des méthodes numériques permettant l'analyse systématique de la variabilité des raies d'émission issues des vents stellaires chauds, (2) vérifier l'hypothèse voulant que la variabilité soit dûe à la présence d'inhomogénéités dans un vent en expansion, et (3) extraire le maximum d'information sur la structure du vent directement à partir des observations. Ces trois objectifs ont été atteints.

Les méthodes d'analyse en ondelettes appliquées à des séries temporelles de spectres variables de raies d'émission a permis de montrer qu'il était possible d'identifier et de classifier différents modes de variation dans les raies des étoiles WR. On a ainsi montré que cette technique permet de vérifier l'existence de lois d'échelles dans la partie variable du profil, en tenant compte des effets du bruit instrumental sur le signal (chapitre 2). Grâce aux propriétés des ondelettes, qui permettent de conserver l'information sur la position en même temps que d'extraire une information sur les échelles caractéristiques, on a pu démontrer de façon objective que les propriétés des structures variables dépendaient de leur position exacte sur le profil de la raie d'émission (chapitre 3). On a aussi montré comment on pouvait mettre au point des filtres multi-échelles permettant de séparer, dans une certaine mesure, les variations se produisant à certaines échelles

particulières. Enfin, il a été possible de mettre en évidence l'existence de deux modes distincts de variation dans l'étoile γ^2 Vel (chapitre 4).

Les méthodes utilisées précédemment pour l'étude des structures variables consistaient essentiellement à extraire des structures "individuelles" et de mesurer séparément leurs caractéristiques. Cette méthode avait ceci de subjectif que ces structures "individuelles" étaient définies arbitrairement. Les méthodes introduites dans cette thèse (analyse en ondelettes, fonction de dégradation) permettent plutôt de réaliser une analyse objective, en quantifiant les propriétés du patron *global* dessiné par les structures "individuelles". L'application de la fonction de dégradation dans les chapitres (3) et (4) a, par exemple, permis d'obtenir une estimation relativement fiable des accélérations et temps caractéristiques des sous-pics sans qu'il soit nécessaire de les identifier individuellement. Les résultats du chapitre (2) montrent d'ailleurs clairement que les techniques précédentes étaient sujettes à des erreurs systématiques. À ce propos, les simulations présentées dans le chapitre (3) montrent que les sous-pics variables ne sont pas nécessairement associés à des structures "individuelles" se propageant dans le vent. Chaque sous-pic résultent plus vraisemblablement d'une superposition accidentelle, dans les vitesses projetées sur la ligne de visée, d'un grand nombre d'éléments discrets.

Les techniques numériques développées dans cette thèse permettent d'obtenir une quantification de certaines propriétés des patrons de variabilité. Cependant, les résultats numériques ne sont pas faciles à interpréter directement, dans la mesure où le sens qui doit être donné à une valeur ne se rattache pas de façon évidente aux propriétés physiques du système. Il est apparu que la meilleure méthode d'interprétation des résultats passait par l'*analyse comparative* des données avec des simulations numériques. L'analyse comparative permet de relier indirectement les données à un modèle dont les propriétés sont parfaitement connues.

Or, la mise au point d'un modèle phénoménologique relativement simple est venue montrer que le détail des variations dans les raies d'émission pouvait être reproduit de façon satisfaisante par un vent inhomogène, représenté par un ensemble de structures émissives se propageant dans la direction radiale. Ces simulations ont révélé certaines régularités frappantes qui apparaissent dans les patrons de variabilité, et qui peuvent être directement reliées à des propriétés physiques. Bien que la reproduction du détail des données requière certains ajustements dans les paramètres du modèle, les résultats montrent de façon convaincante qu'un modèle de vent inhomogène est tout à fait indiqué pour l'étude de la variabilité spectrale des étoiles WR.

L'ajustement des paramètres du modèle a permis d'obtenir un certain nombre de contraintes sur la structure inhomogène des vents, de même que sur leur propriétés générales (accélération, symétrie). Le principal résultat de l'analyse comparative concerne la présence de dispersions importantes dans la vitesse locale du vent, de même que les particularités qui y sont associées. La présence de fluctuations dans le champ de vitesse correspondant à plus de dix fois la vitesse du son est étonnante. L'anisotropie dans la dispersion de vitesse suggère que ces gradients ont surtout une orientation radiale, et il est plausible de penser qu'en fait, les dispersions de vitesses supersoniques ne sont orientées que dans cette direction. Ceci corrobore la prédition de Owocki et Rybicky (1991) selon laquelle des perturbations dans les vents stellaires radiatifs doivent dégénérer en chocs hydrodynamiques se propageant uniquement dans la direction radiale. Il semble donc que les données soient en accord qualitatif avec cette dernière hypothèse.

Un problème qui persiste est celui de l'existence possible de fluctuations à plus grande échelle telles que suggérées par les sous-pics plus larges observés dans les raies d'émission de certaines étoiles WR, telles que γ^2 Velorum (chapitre 4). Bien qu'il soit possible d'en modéliser les patrons de variabilité avec un vent

inhomogène, les paramètres qui doivent être utilisés dans le modèle conduisent à certaines incohérences, en particulier dans les temps caractéristiques (chapitre 3). La récurrence qui apparaît nettement dans certains cas (e.g. HD191165) suggère une interprétation sensiblement différente de celle de fluctuations chaotiques à petite échelle dans le vent. L'existence possible d'un lien avec la surface de l'étoile (e.g. Morel *et al.* 1997), laisse supposer qu'un vent stellaire chaud peut souffrir à la fois d'instabilités *provoquées*, et d'instabilités *spontanées*. Il semble que le dernier cas, vraisemblablement responsable de la variabilité stochastique, soit généralisé à tous les vents stellaires chauds, alors que les instabilités provoquées ne se produisent que dans certaines conditions particulières.

5.2 Projets Futurs

Les travaux de cette thèse ont permis de montrer qu'il est possible de tirer un quantité substantielle d'information sur les vents stellaires chauds à partir de la spectroscopie de raies d'émission variables. Grâce aux différentes méthodes numériques qui ont été mises au point, il est maintenant possible d'analyser *systématiquement* des séries temporelles de spectres de raies d'émission, et d'en extraire *rapidement* toute l'information pertinente.

Afin de poursuivre l'étude de la structure des vents stellaires chauds, je propose donc, dans un premier temps, de procéder à un sondage intensif des raies d'émission de toutes les étoiles Wolf-Rayet (et, s'il y a lieu, O, B et LBV) les plus brillantes, afin de procéder à une *classification* du comportement variable de leurs raies d'émission. Ce sondage devrait idéalement inclure une ou plusieurs séries temporelles de spectres à haute résolution et haut rapport signal sur bruit. En particulier, il serait intéressant de rechercher l'existence de sous-pics larges, comme ceux détectés dans γ^2 Vel, et de déterminer (1) si ces variations sont toujours récurrentes (type R) et (2) dans quels cas particuliers elles apparaissent.

Dans un deuxième temps, il serait particulièrement intéressant d'étudier en détail les variations simultanées dans le plus grand nombre possible de raies d'une même étoile, suivant e.g. l'étude préliminaire de Lépine (1996). Si l'on peut estimer la distance de l'étoile à laquelle chaque raie atomique se forme, il devient possible de déterminer de façon plus détaillée la structure inhomogène du vent dans la direction radiale. Ces observations devront être comparées à des simulations semblables à celles présentées dans cette thèse, mais reproduisant les variations simultanées dans plusieurs raies à la fois.

Dans un troisième temps, des indices supplémentaires concernant les variations de type R pourraient être obtenus grâce une étude suivant une méthodologie semblable à celle utilisée ici, c'est à dire la production de simulations à l'aide d'un modèle phénoménologique simple. Ceci permettrait probablement de juger de la géométrie des perturbations de type R, et de tester si l'hypothèse d'une structure en rotation dans le vent est plausible.

Enfin, un projet plus ambitieux serait de mettre au point un modèle hydrodynamique de vent stellaire en 3D incluant les instabilités radiatives. Il faudrait vérifier si l'on peut de nouveau reproduire les patrons de variabilité des raies d'émission. De même, des calculs de transfert radiatif complet permettraient peut-être de mettre en évidence certains effets d'opacité qui n'ont pas pu être étudiés en détail avec le formalisme utilisé dans cette thèse.

Les modèles théoriques d'objets astronomiques élaborés au cours du siècle qui s'achève ont, pour la plupart, été construits sur l'hypothèse de milieux stationnaires et homogènes. Cette approche était nécessaire compte tenu des techniques de calculs utilisées (méthodes analytiques, tables d'arithmétique). Au cours des dernières décennies, la sophistication croissante des méthodes d'observation et l'utilisation massive des ordinateurs a permis d'aborder le problème nettement plus complexe des milieux inhomogènes et non-stationnaires, et conduit à une conscience de la complexité incroyable qui existe dans le milieux astronomiques,

comme partout ailleurs. Heureusement, et cette thèse en témoigne, il est possible de mettre au point des méthodes numériques qui permettent d'identifier symétrie et régularité dans la complexité. Structure complexe mais lois simples: c'est l'espoir d'une compréhension qui se pointe à l'horizon.

RÉFÉRENCES

- Achmad, L., Lamers, H.G.J.L.M., & Pasquini, L. 1997, A&A, 320, 196
- Acker, A., Grosdidier, Y., & Durand, S. 1997, A&A, 317, L51
- Annuk, K. 1990, Acta Astronomica, 40, 267
- Annuk, K. 1991, in: K.A. van der Hucht & B. Hidayat (eds.), Wolf-Rayet Stars and Interrelations with Other Massive Stars in Galaxies, Proc. IAU Symp. No.143, p245.
- Antokhin, I.I., Aslanov, A.A., & Cherepashchuk, A.M. 1982, Soviet Ast.L, 8, 734
- Antokhin, I.I., Kholtygin, A.F., & Cherepashchuk, A.M. 1988, AZh, 65, 558
- Antokhin, I.I., Nugis, T., & Cherepashchuk, A.M. 1992, Soviet Ast., 36(3), 260
- Argoul, F., Arnéodo, A., Elezgaray, J., Grasseau, G., & Murenzi, R. 1989, Phys. Letters A, 135, 327
- Auer, L.H., & Koenigsberger, G. 1994, ApJ, 436, 859
- Balick, B., Rodgers, B., Hajian, A., Terzian, Y., & Bianchi, L. 1996, AJ, 111, 834
- Balona, L.A., Egan, J., & Maranga, F. 1989, MNRAS, 240, 103
- Berghöfer, T.W., & Schmitt, J.H.M.M. 1994, in: A.F.J. Moffat, S.P. Owocki, A.W. Fullerton, & N. St-Louis (eds.), Instability and Variability of Hot-Star Winds, Ap&SS, 221, 309
- Blomme, R., & Runacres, M.C. 1997, A&A, 323, 886
- Brandi, E., Ferrer, O.E., & Sahade, J. 1989, ApJ, 340, 1091

- Brown, J.C., Richardson, L.L., Antokhin, I.I., Robert, C., Moffat, A.F.J., St-Louis, N. 1995, *A&A*, 295, 725
- Brown, J.C., Richardson, L.L., Cassinelli, J.P., & Ignace, R. 1997, *A&A*, 325, 677
- Carpenter, K.G., & Robinson, R.D. 1997, *ApJ*, 479, 970
- Castor, J.I. 1970, *MNRAS*, 149, 111
- Castor, J.I., Abbott, D.C., & Klein, R.I. 1975, *ApJ*, 195, 157
- Castor, J.I., & Lamers, H.G.J.L.M. 1979, *ApJS*, 39, 481
- Castor, J.I., Smith, L.F., Van Blerkom, D. 1970, *ApJ*, 159, 1119
- Cherchneff, I., & Tielens, A.G.G.M., 1995, in: K.A. van der Hucht & P.M. Williams (eds.), *Wolf-Rayet Stars: Binaries, Colliding Winds, Evolution*, Proc. IAU Symp. No.163, p.346
- Cherepashchuk, A.M., Eaton, J.A., & Khaliullin, Kh.F. 1984, *ApJ*281, 774
- Cooper, R.G., & Owocki, S.P. 1994, in: A.F.J. Moffat, S.P. Owocki, A.W. Fullerton, & N. St-Louis (eds.), *Instability and Variability of Hot-Star Winds*, *Ap&SS*, 221, 427
- Cranmer, S.R., & Owocki, S.P. 1996, *ApJ*, 462, 469
- Dalton, W.W., & Sarazin, C.L. 1995, *ApJ*, 448, 369
- Daubechies, I. 1992, *Ten Lectures on Wavelets*, SIAM, Philadelphia
- Drissen, L., Moffat, A.F.J., Bastien, P., Lamontagne, R., & Tapia, S. 1986, *ApJ*, 306, 215
- Drissen, L., Robert, C., Lamontagne, R., Moffat, A.F.J., St-Louis, N., van Weeren, N., & van Genderen, A.M. 1989, *ApJ*, 343, 426
- Drissen, L., St-Louis, N., Moffat, A.F.J., & Bastien, P. 1987, *ApJ*, 322, 888

- Eversberg, T., Lépine, S., & Moffat, A.F.J. 1998a, *ApJ*, 494, 799
- Eversberg, T., Moffat, A.F.J., & Marchenko, S. 1998b, in preparation
- Farge, M. 1992, *Ann. Rev. Fluid Mech.* 24, 395
- Feldmeier, A. 1995, *A&A*, 299, 523
- Feldmeier, A., Puls, J., & Pauldrach, A.W.A. 1997, *A&A*, 322, 878
- Friend, D.B., & Abbott, D.C. 1986, *ApJ*, 311, 701
- Fullerton, A.W. 1990, Ph.D. Thesis, University of Toronto
- Gabler, R., Gabler, A., Kudritzki, R.P., Puls, J., & Pauldrach, A. 1989, *A&A*, 226, 162
- Gayley, K.G., & Owocki, S.P. 1995, *ApJ*, 446, 296
- Gayley, K.G., Owocki, S.P., & Cranmer, S.R. 1995, *ApJ*, 442, 296
- van Genderen, A.M., van der Hucht, K.A., & Bakker, P.R. 1989, *A&A*, 224, 125
- van Genderen, A.M., van der Hucht, K.A., & Steemers, W.J.G. 1987, *A&A*, 185, 131
- van Genderen, A.M., Larsen, I., & van der Hucht, K.A. 1990, *A&A*, 229, 123
- Gill, A.G., & Henriksen, R.N. 1990, *ApJ*, 365, L27
- Gosset, E., Vreux, J.-M. 1987, *A&A*, 178, 153
- Grafener, G., Hamann, W.-R., Hillier, D.J., Koesterke, L. 1998, *A&A*, 329, 190
- Groenewegen, M.A.T., & Lamers, H.J.G.L.M. 1989, *A&AS*, 79, 359
- Haisch, B.M., & Cassinelli, J.P. 1976, *ApJ*, 208, 253

- Hamann, W.-R. 1995, in: K.A. van der Hucht & P.M. Williams (eds.), Wolf-Rayet Stars: Binaries, Colliding Winds, Evolution, Proc. IAU Symp. No.163, p.105
- Hamann, W.-R., & Koesterke, L. 1998, A&A, 333, 251
- Hamann, W.-R., Leuenhagen, U., Koesterke, L., & Wessolowski, U. 1992, A&A, 255, 200
- Hamann, W.-R., & Schwarz, E. 1992, A&A, 261, 523
- Hamann, W.-R., Wessolowski, U., & Koesterke, L. 1994, A&A, 281, 184
- Hartmann, L. 1978, ApJ, 221, 193
- Hartmann, L., & Cassinelli, J.P. 1977, ApJ, 215, 155
- Henriksen, R.N. 1991, ApJ, 377, 500
- Henriksen, R.N. 1994, in: A.F.J. Moffat, S.P. Owocki, A.W. Fullerton, & N. St-Louis (eds.), Instability and Variability of Hot-Star Winds, Ap&SS, 221, 137
- Hillier, D.J. 1987, ApJS, 63, 965
- Hillier, D.J. 1988, ApJ, 327, 822
- Hillier, D.J. 1989, ApJ, 347, 392
- Hillier, D.J. 1991, A&A, 247, 455
- Hillier, D.J. 1995, in: K.A. van der Hucht & P.M. Williams (eds.), Wolf-Rayet Stars: Binaries, Colliding Winds, Evolution, Proc. IAU Symp. No.163, p.116
- Hillier, D.J. 1996, in: J.M. Vreux, A. Detal, D. Fraipont-Caro, E. Gosset & G Rauw (eds.), WR stars in the Framework of Stellar Evolution, Proc. 33rd Liège Int. Astroph. Coll., p.509

- Hillier, D.J., & Miller, D.L. 1998, ApJ, 496, 407
- Hjellming, R.M., & Hiltner, W.A. 1963, ApJ, 137, 1080
- Hogg, D.E. 1989, AJ, 98, 282
- Howarth, I.D., Prinja, R.K., & Massa, D. 1995, ApJ, 452, L65
- Howarth, I.D., & Schmutz, W. 1992, A&A, 261, 503
- van der Hucht, K.A., Conti, P.S., Lundstrom, I., & Stenholm, B. 1981, SSRv, 28, 307
- van der Hucht, K.A., van Genderen, A.M., & Bakker, P.R. 1990, A&A, 228, 108
- van der Hucht, K.A., Schriver, H., Stenholm, B., Lundstrom, I., Moffat, A.F.J., Marchenko, S.V., Seggewiss, W., Setia Gunawan, D.Y.A., Sutantyo, W., van den Heuvel, E.P.J., de Cuypere, J.-P., & Gomez, A.E. 1997, New Astronomy, 2(3), 245
- Ignace, R., Brown, J.C., Richardson, L.L., & Cassinelli, J.P. 1998, A&A, 330, 253
- Jeffers, S., Stiff, T., & Weller, W.G. 1985, AJ, 90, 1852
- Kaper, L., & Henrichs, H.F. 1994, in: A.F.J. Moffat, S.P. Owocki, A.W. Fullerton, & N. St-Louis (eds.), Instability and Variability of Hot-Star Winds, Ap&SS, 221, 115
- Kaper, L., Henrichs, H.F., Nichols, J.S., Snoek, L.C., Volten, H., & Zwarthoed, G.A.A. 1996, A&AS, 116, 257
- Kuhi, L.V. 1973, ApJ, 180, 783
- Lamers, H.J.G.L.M. 1994, in: A.F.J. Moffat, S.P. Owocki, A.W. Fullerton, & N. St-Louis (eds.), Instability and Variability of Hot-Star Winds, Ap&SS, 221, 41

- Lamers, H.J.G.L.M., & Cassinelli, J.P. 1998, *Introduction to Stellar Winds*, Cambridge University Press (in press).
- Lamers, H.J.G.L.M., Cerruti-Sola, M., & Perinotto, M. 1987, ApJ, 314, 726
- Lamers, H.J.G.L.M., Snow, T.P., & Lindholm, D.M. 1997, ApJ, 455, 269
- Lamers, H.J.G.L.M., & Waters, L.B.F.M. 1984, A&A, 138, 25
- Langer, N. 1989, A&A, 210, 93
- Langer, N., Hamann, W.-R., Lennon, M., Najarro, F., Pauldrach, A.W.A., & Puls, J. 1994, A&A, 290, 819
- Lépine, S. 1994, in: A.F.J. Moffat, S.P. Owocki, A.W. Fullerton, & N. St-Louis (eds.), *Instability and Variability of Hot-Star Winds*, Ap&SS, 221, 371
- Lépine, S. 1996, in: J.M. Vreux, A. Detal, D. Fraipont-Caro, E. Gosset & G Rauw (eds.), *WR stars in the Framework of Stellar Evolution*, Proc. 33rd Liège Int. Astroph. Coll., p.253
- Lépine, S., Moffat, A.F.J. 1998, ApJ, submitted (paper II)
- Lépine, S., Moffat, A.F.J., & Henriksen, R.N. 1996, ApJ, 466, 392 (Paper I)
- Lépine, S., Moffat, A.F.J., St-Louis, N., Dalton, M.J., Crowther, P.A., Willis, A.J., & Smith, L. 1998, in preparation
- Le Teuff, Y.H., & Cherchneff, I. 1997, Ap&SS, 251, 389
- Lucy, L.B. 1982, ApJ, 255, 278
- Lucy, L.B., & Solomon, P.M. 1970, ApJ, 159, 879
- Lührs, S. 1997, PASP, 109, 504
- Lundström, I., & Stenholm, B. 1982, in: C. de Loore & A.J. Willis (eds.), *Wolf-Rayet Stars: Observations, Physics, and Evolution*, Proc. IAU Symp. No.99, p.289

- MacFarlane, J.J., & Cassinelli, J.P. 1989, ApJ, 347, 1090
- Maeder, A. 1991, A&A, 242, 93
- Marchenko, S.V., Moffat, A.F.J., Eenens, P.R.J., Hill, G.M., & Grandchamps, A. 1995, ApJ, 450, 811
- Marston, A.P. 1997, ApJ, 475, 188
- Martínez, V.J., Paredes, S., & Saar, E. 1993, MNRAS, 260, 365
- Massa, D., Fullerton, A.W., Nichols, J.S., Owocki, S.P., Prinja, R.K., St-louis, N., Willis, A.J., Altner, B., Bolton, C.T., Cassinelli, J.P., Cohen, D., Cooper, R.G., Feldmeier, A., Gayley, K.G., Harries, T., Heap, S.R., Henriksen, R.N., Howarth, I.D., Hubeny, I., Kambe, E., Kaper, L., Koenigsberger, G., Marchenko, S., McCandliss, S.R., Moffat, A.F.J., Nugis, T., Puls, J., Robert, C., Schulte-Ladbeck, R.E., Smith, L.J., Smith, M.A., Waldron, W.L., & White, R.L. 1995, ApJ, 452, L53
- Massey, P., Niemela, V.S. 1981, ApJ, 245, 195
- McCandliss, S.R. 1988, Ph.D. thesis, University of Colorado, Boulder
- McCandliss, S.R., Bohannan, B., Robert, C., & Moffat, A.F.J. 1994, in: A.F.J. Moffat, S.P. Owocki, A.W. Fullerton, & N. St-Louis (eds.), Instability and Variability of Hot-Star Winds, Ap&SS, 221, 155
- McLean, I.S. 1980, ApJ, 236, 149
- Mihalas D. 1980, Stellar Atmospheres, W.H. Freeman and Co. (eds.), New-York
- Moffat, A.F.J. 1977, A&A, 57, 151
- Moffat, A.F.J. 1995, in: K.A. van der Hucht & P.M. Williams (eds.), Wolf-Rayet Stars: Binaries, Colliding Winds, Evolution, Proc. IAU Symp. No.163, p.213

- Moffat, A.F.J. 1996a, Rev. Mex. A&Ac, 5 (38)
- Moffat, A.F.J. 1996b, in: J.M. Vreux, A. Detal, D. Fraipont-Caro, E. Gosset & G Rauw (eds.), WR stars in the Framework of Stellar Evolution, Proc. 33rd Liège Int. Astroph. Coll., p.199
- Moffat, A.F.J., Drissen, L., Lamontagne, R., & Robert, C. 1988, ApJ, 334, 1038
- Moffat, A.F.J., Lépine, S., Henriksen, R.N., & Robert, C. 1994, Ap&SS, 216, 55
- Moffat, A.F.J., & Marchenko, S. 1996, A&A, 305, L29
- Moffat, A.F.J., Paquin, G., Lamontagne, R., Vogt, N., & Barrera, L.H. 1986, AJ, 91, 1386
- Moffat, A.F.J., & Robert, C. 1992, in: L.Drissen, C. Leitherer & A. Nota (eds.), Nonisotropic and Variable Outflows from Stars, ASP conf. series 22, 203
- Moffat, A.F.J., & Robert, C. 1994, ApJ, 421, 310
- Moffat, A.F.J., & Shara, M.M. 1986, AJ, 92, 952
- Morel, T., St-Louis, N., & Marchenko, S.V. 1997, ApJ, 482, 470
- Morel, T., St-Louis, N., & Marchenko, S.V. 1998a, ApJ, in press
- Morel, T., St-Louis, N., Moffat, A.F.J., Cardona, O., Koenigsberger, G., & Hill, G. 1998b, ApJ, 498, 413
- Nugis, T., & Niedzielski, A. 1995, A&A, 300, 237
- Owocki, S.P. 1994, in: A.F.J. Moffat, S.P. Owocki, A.W. Fullerton, & N. St-Louis (eds.), Instability and Variability of Hot-Star Winds, Ap&SS, 221, 3
- Owocki, S.P. 1998, in: J. Franco & A. Carraminana (eds.), Interstellar Turbulence, Proc. 2nd Guillermo Haro Conference, Mexico, p.310
- Owocki, S.P., Castor, J.I., & Rybicki, G.B. 1988, ApJ, 335, 914

- Owocki, S.P., Cranmer, S.R., & Fullerton, A.W. 1995, ApJ, 453, L37
- Owocki, S.P., & Rybicki, G.B. 1991, ApJ, 368, 261
- Pasquali, A., Langer, N., Schmutz, W., Leitherer, C., Nota, A., Hubeny, I., & Moffat, A.F.J. 1997, ApJ, 478, 340
- Prinja, R.K., Balona, L.A., Bolton, C.T., Crowe, R.A., Fieldus, M.S., Fullerton, A.W., Gies, D.R., Howarth, I.D., McDavid, D., & Reid, A.H.N. 1992, ApJ, 390, 266
- Prinja, R.K., Barlow, M.J., & Howarth, I.D. 1990, ApJ, 361, 607
- Puls, J., Kudridtzki, R.-P., Herrero, A., Pauldrach, A.W.A., Haser, S.M., Lennon, D.J., Gabler, R., Voels, S.A., Vilchez, J.M., Wachter, S., & Feldmeier, A. 1996, A&A, 305, 171
- Puls, J., Owocki, S.P., & Fullerton, A.W. 1993, A&A, 279, 457
- Richardson, L.L., Brown, J.C., & Simmons, J.F.L. 1996, A&A, 306, 519
- Robert, C. 1992, Thèse de Doctorat, Université de Montréal
- Robert, C. 1994, in: A.F.J. Moffat, S.P. Owocki, A.W. Fullerton, & N. St-Louis (eds.), Instability and Variability of Hot-Star Winds, Ap&SS, 221, 137
- Robert, C., Moffat, A.F.J., Bastien, P., Drissen, L., & St-Louis, N. 1989, ApJ, 347, 1034
- Robert, C., Moffat, A.F.J., Drissen, L., Lamontagne, R., Seggewiss, W., Niemela, V., Cerruti, M.A., Barrett, P., Bailey, J., Garcia, J., & Tapia, S. 1992, ApJ, 397, 277
- Runacres, M.C., & Blomme, R. 1994, in: A.F.J. Moffat, S.P. Owocki, A.W. Fullerton, & N. St-Louis (eds.), Instability and Variability of Hot-Star Winds, Ap&SS, 221, 249

- Runacres, M.C., & Blomme, R. 1996, A&A, 309, 544
- Rybicki, G.B., Owocki, S.P., & Castor, J.I. 1990, ApJ, 349, 274
- Schaerer, D., Schmutz, W., & Grenon, M. 1997, ApJ, 484, L153
- Schmutz, W. 1997, A&A, 321, 268
- Schmutz, W., Schweickhardt, J., Stahl, O., Wolf, B., Dumm, T., Gang, T.H., Jankovics, I., Kaufer, A., Lehmann, H., Mandel, H., Peitz, J., & Rivinius, T.H. 1997, A&A, 328, 219
- Schulte-Ladbeck, R.E., Eenens, P.R.J., & Davis, K. 1995, ApJ, 454, 917
- Schulte-Ladbeck, R.E., & van der Hucht, K.A. 1989, ApJ, 337, 887
- Schumann, J.D., & Seggewiss, W. 1975, in: V.E. Sherwood & L. Plaut (eds.), Variable Stars and Stellar Evolution, Proc. IAU Symp. No.67, p.299
- Slezak, E., De Lapparent, V., & Bijaoui, A. 1993, ApJ, 409, 517
- Slezak, E., Durret, F., & Gerbal, D. 1994, AJ, 108, 1996
- Springmann, U. 1994, A&A, 289, 505
- Stevens, I.R., Blondin, J.M., & Pollock, A.M.T. 1992, ApJ, 386, 265
- St-Louis, N., 1995, in: K.A. van der Hucht & P.M. Williams (eds.), Wolf-Rayet Stars: Binaries, Colliding Winds, Evolution, Proc. IAU Symp. No.163, p.388
- St-Louis, N., Dalton, M.J., Marchenko, S.V., Moffat, A.F.J., & Willis, A.J. 1995, ApJ, 452, L57
- St-Louis, N., Drissen, L., Moffat, A.F.J., Bastien, P., & Tapia, S. 1987, ApJ, 322, 888

- St-Louis, N., Hill, G., Moffat, A.F.J., Bartzakos, P., & Antokhin, I. 1996, in: J.M. Vreux, A. Detal, D. Fraipont-Caro, E. Gosset & G Rauw (eds.), WR stars in the Framework of Stellar Evolution, Proc. 33rd Liège Int. Astroph. Coll., p.331
- St-Louis, N., Willis, A.J., & Stevens, I.R. 1993, ApJ, 415, 298
- Szatmáry, K., Vinkó, J., & Gál, G. 1994, A&AS, 108, 377
- Taylor, M. 1990, AJ, 100, 1264
- Thaller, M., 1998, PASP, 110, 636
- Vakili, F., Mourard, D., Bonneau, D., Morand, F., & Stee, P. 1997, A&A, 323, 183
- Veen, P.M., van Genderen, A.M., van der Hucht, K.A., Li, A., & Sterken, C. 1996, in: J.M. Vreux, A. Detal, D. Fraipont-Caro, E. Gosset & G Rauw (eds.), WR stars in the Framework of Stellar Evolution, Proc. 33rd Liège Int. Astroph. Coll., p.583
- Veen, P.M., van Genderen, A.M., van der Hucht, K.A., Li, A., Sterken, C., & Dominik, C. 1998, A&A, 329, 199
- Vreux, J.-M., Gosset, E., Bohannan, B., & Conti, P. 1992, A&A, 256, 148.
- Waldron, W.L., Klein, L. & Altner, B. 1994, ApJ, 426, 725
- Waters, L.B.F.M., & Lamers, H.J.G.L.M. 1984, A&AS, 57, 327
- Wessolowski, U. 1996, in: J.M. Vreux, A. Detal, D. Fraipont-Caro, E. Gosset & G Rauw (eds.), WR stars in the Framework of Stellar Evolution, Proc. 33rd Liège Int. Astroph. Coll., p.343
- Williams, P.M. 1996, in: J.M. Vreux, A. Detal, D. Fraipont-Caro, E. Gosset & G Rauw (eds.), WR stars in the Framework of Stellar Evolution, Proc. 33rd Liège Int. Astroph. Coll., p.135

- Williams, P.M., Beattie, D.H., & Stewart, J.M. 1977, MNRAS, 97, 76
- Williams, P.M., van der Hucht, K.A., Pollock, A.M.T., Florkowski, D.R., van der Woerd, H., & Wamsteker, W.M. 1990, MNRAS, 243, 662
- Willis, A.J. 1991, in: M.K.V. Bappu & J. Sahade (eds.), Wolf-Rayet and High Temperature Stars, Proc. IAU Symp. No.143 (Dordrecht: Kluwer), p.265
- Willis, A.J., Howarth, I.D., Stickland, D.J., & Heap, S.R. 1989, ApJ, 347, 413
- Willis, A.J., Schild, H., & Stevens, I.R. 1995, A&A, 298, 549
- Willis, A.J., & Stevens, I.R. 1996, A&A, 310, 577

REMERCIEMENTS

Les travaux ayant mené à la réalisation de cette thèse ont été rendus possibles grâce au soutien financier du Conseil de Recherches en Sciences Naturelles et en Génie du Canada (CRSNG), et du Fonds pour l'Aide aux Chercheurs et l'Avancement de la Recherche (FCAR).

Je remercie sincèrement Tony Moffat, mon directeur de recherche, pour m'avoir appris à voler de mes propres ailes en prenant le risque calculé de me pousser dans le vide sans parachute. Il est pour moi l'exemple du chercheur ouvert et enthousiaste, jamais à court de questions et d'idées, qui sait s'amuser dans un monde parfois un peu rigide. Merci également à tous les professeurs du département de physique pour leur accueil chaleureux et leur encadrement efficace.

Thanks to Dick Henriksen, my co-director, for his always fruitful ideas and suggestions. I am also grateful to Dr. Stanley Owocki for his encouragements and the interest he showed for my ideas. Thanks also to Drs. John C. Brown, Werner Schmutz, Ian D. Howarth, and Andy Pollock for their constructive criticisms, which stimulated substantial improvements of this work. I am also grateful to Dr. Serguei Marchenko, who showed me the hard work of data reduction.

Merci à tous mes amis et collègues étudiants du Centre de l'Observatoire du Mont-Mégantic pour la camaraderie et la solidarité. Merci particulièrement à Thomas Eversberg pour sa collaboration dans les observations menées au télescope Canada-France-Hawaii. Merci spécial à Jean-Francois pour son humour, pour l'épisode du verglas, pour *Dilbert*, et pour son manuel de L^AT_EX. Merci à

Christian, Loïc, Nadine, Nathalie, Peter, Rémi, Roger, Sébastien, Sylvain, Sonia, Stéphanie, Thierry, Yves, Yvan et tous les autres. Je vous souhaite bonne chance dans votre future carrière.

J'exprime ma gratitude infinie à Pascale Vaillancourt, la femme de ma vie et ma compagne de tous les jours, pour avoir fait ce long chemin à mes côtés en m'encourageant sans relâche. Je la remercie d'avoir toléré mes sautes d'humeur, en particulier dans les derniers milles de cette course folle qu'est la rédaction d'une thèse. Merci aussi à mes parents, Nicole et Pierre, parce que c'est grâce à leur grand cœur et leur ouverture d'esprit que je suis devenu l'homme de sciences que je suis. Merci à mes frères et soeur, François, Alain et Isabelle; je suis fier d'être membre d'un quatuor aussi extraordinaire.

Cette thèse est née en même temps que Laurasia, ma fille chérie. Je lui souhaite de vivre dans un monde où l'émerveillement pour l'univers qui nous entoure sera sans cesse renouvelé, passant de surprise en surprise.